A ROBUST AND AUTOMATIC ELASTIC COMPENSATION METHOD FOR COLLAPSE LOAD DETERMINATION OF STRUCTURES

By

AFSHIN MELLATI

A thesis in fulfillment of the requirements for the degree of

Doctor of Philosophy

School of Civil and Environmental Engineering

The University of New South Wales

Sydney, Australia

August 2018

Thesis/Dissertation Sheet

Surname/Family Name	:	**Mellati**
Given Name/s	:	**Afshin**
Abbreviation for degree as give in the University calendar	:	**PhD**
Faculty	:	**Engineering**
School	:	**School of Civil and Environmental Engineering**
Thesis Title	:	**A robust and automatic elastic compensation method for collapse load determination of structures**

Abstract

This thesis develops a general procedure for a robust and convenient collapse (limit) load determination of engineering structures using the elastic compensation method (ECM), which only involves a series of linear elastic analyses, and therefore is suitable for practical applications.

This research attempts to improve the robustness and automation of the traditional ECM and its modified versions. Two shortcomings of them reported in the literature are presented. Firstly, they use the number of iterations, input by the user, as the convergence criterion due to the presence of the sporadic oscillations with different amplitudes in the limit load curve. This criterion is baseless and might prevent a decent solution to be obtained. Secondly, they need a fine and high-quality mesh to produce acceptable results. Generation of such a mesh for complex structures is time-consuming and often requires tedious human interventions. The first shortcoming is overcome by developing a robust sensitivity-based ECM. It is shown theoretically and confirmed numerically that the use of the sensitivity-based ECM is robust in preventing the oscillations. This scheme provides accurate results by defining the convergence directly on limit loads. The second shortcoming is tackled through the use of the scaled boundary finite element method (SBFEM) and the automatic quadtree (in 2D) and octree (in 3D) mesh generation. Such technique automatically and efficiently handles structures with complex geometries and allows the SBFE discretizations to be constructed from an in-plane solid (2D) or of a solid 3D CAD model.

The combination of the sensitivity-based ECM with the SBFEM leads to an automatic scheme for the collapse load determination of structures. This scheme minimizes the required interference of the user in both mesh generation and analysis parts. However, it may be computationally demanding when uniformly refined meshes are used. To deal with this problem, an adaptive sensitivity-based ECM is proposed. The adaptive scheme generates non-uniform refinements efficiently by the ability of the SBFEM in handling the hanging nodes. This reduces the number of elements while still guaranteeing the required level of accuracy. Therefore, the size of the problem is significantly reduced and hence also the required computational resources.

ORIGINALITY STATEMENT

‘I hereby declare that this submission is my own work and to the best of my knowledge it contains no materials previously published or written by another person, or substantial proportions of material which have been accepted for the award of any other degree or diploma at UNSW or any other educational institution, except where due acknowledgement is made in the thesis. Any contribution made to the research by others, with whom I have worked at UNSW or elsewhere, is explicitly acknowledged in the thesis. I also declare that the intellectual content of this thesis is the product of my own work, except to the extent that assistance from others in the project's design and conception or in style, presentation and linguistic expression is acknowledged.’

Signed ……………………………………………………............

Date ……………………………………………………............

COPYRIGHT STATEMENT

'I hereby grant the University of New South Wales or its agents the right to archive and to make available my thesis or dissertation in whole or part in the University libraries in all forms of media, now or here after known, subject to the provisions of the Copyright Act 1968. I retain all proprietary rights, such as patent rights. I also retain the right to use in future works (such as articles or books) all or part of this thesis or dissertation.
I also authorise University Microfilms to use the 350 word abstract of my thesis in Dissertation Abstract International (this is applicable to doctoral theses only).
I have either used no substantial portions of copyright material in my thesis or I have obtained permission to use copyright material; where permission has not been granted I have applied/will apply for a partial restriction of the digital copy of my thesis or dissertation.'

Signed ....

Date ....14/12/2018..................................

AUTHENTICITY STATEMENT

'I certify that the Library deposit digital copy is a direct equivalent of the final officially approved version of my thesis. No emendation of content has occurred and if there are any minor variations in formatting, they are the result of the conversion to digital format.'

Signed ....

Date ....14/12/2018............................

INCLUSION OF PUBLICATIONS STATEMENT

UNSW is supportive of candidates publishing their research results during their candidature as detailed in the UNSW Thesis Examination Procedure.

Publications can be used in their thesis in lieu of a Chapter if:

- The student contributed greater than 50% of the content in the publication and is the "primary author", ie. the student was responsible primarily for the planning, execution and preparation of the work for publication
- The student has approval to include the publication in their thesis in lieu of a Chapter from their supervisor and Postgraduate Coordinator.
- The publication is not subject to any obligations or contractual agreements with a third party that would constrain its inclusion in the thesis

Please indicate whether this thesis contains published material or not.

☐ *This thesis contains no publications, either published or submitted for publication (if this box is checked, you may delete all the material on page 2)*

☒ *Some of the work described in this thesis has been published and it has been documented in the relevant Chapters with acknowledgement (if this box is checked, you may delete all the material on page 2)*

☐ *This thesis has publications (either published or submitted for publication) incorporated into it in lieu of a chapter and the details are presented below*

CANDIDATE'S DECLARATION

I declare that:

- I have complied with the Thesis Examination Procedure
- where I have used a publication in lieu of a Chapter, the listed publication(s) below meet(s) the requirements to be included in the thesis.

Name	Signature	Date (dd/mm/yy)

ABSTRACT

This thesis develops a general procedure for a robust and convenient collapse (limit) load determination of engineering structures using the elastic compensation method (ECM), which only involves a series of linear elastic analyses, and therefore is suitable for practical applications.

This research attempts to improve the robustness and automation of the traditional ECM and its modified versions. Two shortcomings of them reported in the literature are presented. Firstly, they use the number of iterations, input by the user, as the convergence criterion due to the presence of the sporadic oscillations with different amplitudes in the limit load curve. This criterion is baseless and might prevent a decent solution to be obtained. Secondly, they need a fine and high-quality mesh to produce acceptable results. Generation of such a mesh for complex structures is time-consuming and often requires tedious human interventions. The first shortcoming is overcome by developing a robust sensitivity-based ECM. It is shown theoretically and confirmed numerically that the use of the sensitivity-based ECM is robust in preventing the oscillations. This scheme provides accurate results by defining the convergence directly on limit loads. The second shortcoming is tackled through the use of the scaled boundary finite element method (SBFEM) and the automatic quadtree (in 2D) and octree (in 3D) mesh generation. Such technique automatically and efficiently handles structures with complex geometries and allows the SBFE discretizations to be constructed from an in-plane solid (2D) or of a solid 3D CAD model.

The combination of the sensitivity-based ECM with the SBFEM leads to an automatic scheme for the collapse load determination of structures. This scheme minimizes the required interference of the user in both mesh generation and analysis parts. However, it may be computationally demanding when uniformly refined meshes are used. To deal with this problem, an adaptive sensitivity-based ECM is proposed. The adaptive scheme generates non-uniform refinements efficiently by the

ability of the SBFEM in handling the hanging nodes. This reduces the number of elements while still guaranteeing the required level of accuracy. Therefore, the size of the problem is significantly reduced and hence also the required computational resources.

ACKNOWLEDGEMENT

First and foremost, I like to take this opportunity the express my sincere gratitude and deep appreciation to my main supervisor, professor Chongmin Song. Without his invaluable supports, patience and expert guidance, the completion of this thesis could not be possible. His insight, constructive ideas and advice have given me a better understanding of the philosophy and technique of theoretical research, and thus helped me overcome a number of challenges in the course of doing the research work. I could not thank him enough for all the discussion sessions and countless hours he has invested, despite his busy schedule, to ensure the best quality research possible.

My sincere thanks also go to my joint supervisor, professor Francis Tin-Loi, for all his priceless advice, and continuous support through these years of my PhD study. I would also like to acknowledge my debt to Dr. Sawekchai Tangaramvong, my initial supervisor and my current co-supervisor, for all his helpful discussions and encouragements on my research progress.

I wish to thank Dr. Albert Saputra for his help with the scaled boundary finite element method, and Mr. Junqi Zhang for his assistance in octree mesh generation.

The PhD scholarship supported by the Australian Research Council is also gratefully acknowledged.

Finally, I would like to whole-heartedly dedicate this thesis to my dear parents, Dr. Ahmad Mellati and Mrs Poorandokht Talai, who have always given me continuous support, inspiration and love. To them, I owe my life and my education. I would also like to thank my siblings, Dr. Omid Mellati and Mrs Azita Mellati, for their belief in me and their long-distance supports.

Contents

List of Tables

List of Figures

List of Symbols

$(x_1, x_2, x_3), (x, y, z)$	global coordinates
α	structural safety factor
α^{col}	collapse (limit) load multiplier
α^s, α^k	statically and kinematically admissible load multipliers, respectively
$\bar{\sigma}$	equivalent stress field
$\bar{\sigma}_{\min}, \bar{\sigma}_{\max}$	minimum and maximum equivalent stresses, respectively
$\boldsymbol{\epsilon}$	strain vector
$\boldsymbol{\Lambda}$	eigenvalues from an eigenvalue decomposition
$\boldsymbol{\Phi}$	eigenvectors from an eigenvalue decomposition
$\boldsymbol{\Psi}_\sigma$	stress modes
$\boldsymbol{\sigma}$	stress field, stress state
$\boldsymbol{\sigma}^s, \boldsymbol{\sigma}^k$	statically and kinematically admissible stresses, respectively
Δ	convergence criterion
$\Delta\bar{\boldsymbol{\sigma}}$	stress sensitivity matrix
$\Delta\mathbf{E}$	vector of elastic moduli changes

$\dot{\boldsymbol{\epsilon}}$	strain rate vector
$\dot{\boldsymbol{\sigma}}$	stress rate vector
$\dot{\boldsymbol{q}}$	force rate vector
$\dot{\boldsymbol{u}}$	displacement rate vector
$\dot{D}$	increment of plastic dissipation per the unit volume
$\epsilon_x, \epsilon_y, \epsilon_z, \epsilon_{xy}, \epsilon_{yz}, \epsilon_{xz}$	strain componenets
η, ζ	scaled boundary coordinates on the boundary
κ	plastic property constant
λ	adjustable factor
$(\nabla\bar{\boldsymbol{\sigma}})_{\mathrm{D}}$	diagnal matrix of the stress sensitivity matrix
$(\nabla\bar{\boldsymbol{\sigma}})_{\mathrm{H}}$	hollow matrix of the stress sensitivity matrix
$\bar{\mathbf{F}}_{\mathrm{G}}$	matrix of pseudo forces
$\delta\boldsymbol{\epsilon}, \delta\mathbf{u}$	virtual strains and displacements, respectively
$\mathbf{B}_1, \mathbf{B}_2$	SBFE strain-displacement matrices
$\mathbf{c}$	integration constants
$\mathbf{E}$	vector of elastic moduli of all elements/subdomains
$\mathbf{E}_0, \mathbf{E}_1, \mathbf{E}_2$	coefficient matrices
$\mathbf{F}_{\mathrm{G}}$	global load vector
$\mathbf{H}$	Hessian matrix
$\mathbf{I}$	identity matrix
$\mathbf{K}$	element/subdomain stiffness matrix

$\mathbf{K}_{\mathrm{G}}$	global stiffness matrix
$\mathbf{O}$	null matrix
$\mathbf{q}_0, \mathbf{g}_0$	reference loads
$\mathbf{q}\,(\xi)$	internal nodal forces along the radial direction
$\mathbf{S}_{active}, \mathbf{S}_{non-active}$	active and non-active sets/elements
$\mathbf{u}\,(\xi)$	radial displacement function
$\mathbf{u}_0$	defined kinematic boundary on S_u
$\mathbf{u}_{\mathrm{b}}, \mathbf{q}_{\mathrm{b}}$	displacements and forces on the boundary in SBFEM
$\mathbf{u}_{\mathrm{G}}$	global nodal displacements
$\mathbf{x}_{\mathrm{b}}$	vectors of nodal coordinates
$\mathbf{Z}$	Hamiltonian matrix
$\Delta\bar{\boldsymbol{\sigma}}$	equivalent stress difference vector
$(\nabla\bar{\boldsymbol{\sigma}})_{\mathrm{M}}$	modified stress sensitivity matrix
∇	diffrential operator
$\nabla\mathbf{u}_{\mathrm{G}}$	displacement sensitivity matrix
ν	Poisson's ratio
ϕ^0	point function
σ_0	yield stress in pure tension
σ_m	mean normal stress
σ_n	nominal stress
$\sigma_x, \sigma_y, \sigma_z, \tau_{xy}, \tau_{yz}, \tau_{xz}$	stress componenets

$\sigma_{\mathrm{I}}, \sigma_{\mathrm{II}}, \sigma_{\mathrm{III}}$	principal normal stresses
σ_{arb}	a nonzero arbitrary stress value
σ_N	standard nominal stress of the structure
τ_0	yield stress in pure shear
τ_{max}	maximum shear stress
$\mathbf{D}$	elasticity matrix
$\mathbf{g}$	body force in V
$\mathbf{n}$	outward normal vector
$\mathbf{p^{(n)}}$	stress vector at the point P with outward normal vector $\mathbf{n}$
$\mathbf{q}$	traction on S_t
$\mathbf{S}$	stress deviator tensor
$\mathbf{T^0}$	spherical stress tensor
$\mathbf{T}$	stress tensor
$\mathbf{u}$	general displacement field
θ	the follow-up angle on the GLOSS diagram
$\varepsilon_1, \varepsilon_2$	tolerances
ξ	scaled boundary radial coordinate
$D(\dot{\boldsymbol{\epsilon}})$	enrgy dissipation function related to $\dot{\boldsymbol{\epsilon}}$
E	Young's modulus, elastic modulus
e_α	error in collapse load solution
f	yield function

G	shear modulus
I_1, I_2, I_3	invariants of the stress tensor
K_1, K_2, K_3	invariants of the stress deviator tensor
K_t	stress concentration factor
L	load patten
l_{max}	maximum difference between the division levels of adjacent cells
m', m^0	lower and upper bound multipliers, respectively, in the m_α method
N	shape function
P_L	collapse (limit) load
q	modulus adjustment parameter in the m_α method
R	structural resistance
r	number of iterations
$rmax$	maximum number of iterations
S_u, S_t	boundary regions
$s_x, s_y, s_z, s_{xy}, s_{yz}, s_{xz}$	stress deviator componenets
S_{ratio}	ratio between the maximum and minimum sizes of octree cells
s_Ω	sign function
S_b	seed points on each boundary
S_{max}	maximum allowed number of seed points in a cell

S_m	the ASME code allowable stress
S_{roi}	seed points around each region of interest
SI	stress intensity
T	temperature
t	time
V	volume of the body
V_R	reference volume in the m_α method

Chapter 1

INTRODUCTION

1.1 General

Structural engineering is a sub-discipline of civil engineering which involves the analysis and design of structures, such as buildings, bridges, towers, etc. Structural analysis is the determination of structural responses (i.e. deformations, internal forces, stresses, etc.) due to the loads applied on a structure and its components. Structural design is the economical determinations of the structural components' properties (i.e. suitable materials, section dimensions, etc.) based on the structural responses to ensure the structure performs in such a way to meet some criteria under the applied loads. These criteria are normally known as limit states. The term limit state is used to describe a condition at which a structure or part of a structure ceases to perform its intended function [6]. There are two categories of limit states; serviceability limit state and ultimate limit state (strength). A serviceability limit state is correspondent to a condition beyond which specified service requirements (i.e. deflection, vibration, durability, fire resistance, local deformation, etc.) resulting from the planned utility of the structure are no longer satisfied. The ultimate limit sate is regarded as an inability to sustain any increase in loads [7]. In other words, the ultimate limit state shows the maximum load that the structure can sustain. The ultimate limit state can be described as

$$R \leq \alpha L \tag{1.1}$$

, where R shows the structural resistance and L represents the applied loads. α shows the factor of safety (or safety factor) of the structure under the applied loads. Essentially, the factor of safety shows how much stronger the structure is than it needs to be for an applied load.

For a given load pattern (the spatial distribution of a set of forces), the exact value of the safety factor is different from one structure to another. The safety factor of a structure can be obtained by determining the maximum load that the structure can sustain under the given load pattern. This maximum load is known as the collapse load or the limit load of the structure. The traditional approach to obtain the limit load of a structure is a nonlinear, incremental analysis up to the failure of the modeled structure. This methodology is often computationally very demanding for realistic structures. Additionally, the complexity of the method, specially in defining suitable load steps and iteration controls, usually restricts its engineering applications.

The importance of the safety factor concept in the design and such difficulties of the nonlinear numerical solution have motivated the development of simplified schemes. They include two general kinds of methods; (1) classical limit analysis and (2) iterative linear analyses.

The classical limit analysis which is based on the well-known upper (kinematic) and lower (static) bound theorems is widely used for the direct collapse load determination (e.g. [8, 9, 10]). It is found on the mathematical programming framework and is suitable for sufficiently ductile structures, as it assumes the material behavior as elastic-perfectly plastic. Being path independent and a single-step determination of the collapse load are the main advantages of the classical limit analysis over the nonlinear incremental technique [11]. However, despite its popularity and maturity within research communities over decades, the classical limit analysis does not gain much of interest from practitioners. This is mainly due to their lack of familiarity with the model construction within a generic mathematical programming framework.

Alternatively, methods based on iterative analyses schemes are efficient schemes approximating the limit load using bounding theorems. The materials are assumed to be rigid-perfectly plastic. At each iteration, an elastic stress analysis is performed on the finite element model of the structure. The elastic stiffness properties of the finite elements are systematically adjusted such that the stresses with high intensity are redistributed. The iterations continue until the distribution corresponding to the collapse state is reached.

Various iterative elastic analysis methods have been proposed to perform the limit analysis of structures [12]. In particular, the methods known as elastic compensation method (ECM) and its modified version, modified elastic compensation method (MECM), are developed based on a very simple scheme which make them applicable to many large and complex structures [13, 11, 14, 15, 16, 17] . At each iteration, an arbitrary nominal stress between the maximum and minimum stress is chosen. Then, the finite elements whose stresses sit above the nominal stress are selected and their elastic moduli are scaled down to bring the stresses of the selected elements back to the nominal stress. Ponter et al. [15] showed that this procedure results in a series of analyses which converge to a stress state field on the yield surface if Poisson's ratio is taken as 0.5 (i.e. incompressible material). This condition imposes the required volume conservation in plastic analyses, as the plastic deformations do not change the volume of the material. He mentioned this stress field then can be used along with upper and lower bound theorems to determine the collapse load of structures. ECM is usually referred as a lower bound approach and the upper bound scheme is more often known as linear matching method (LMM). Although the upper bound collapse load given by the LMM is generally more accurate (as the convergence is directly defined on the limit load), the collapse load obtained by the lower bound scheme in the ECM is safer for the design of structures [17]. This is because of the nature of the employed lower bound theorem, which produces conservative computations of the limit load, if its criteria are met.

1.2 Motivation of Research

The use of iterative elastic analyses based on the current ECMs for the determination of collapse loads of structures is quite advantageous. Some of the main merits of this scheme over the other approaches are as follows.

- The use of linear elastic analysis allows the methods to be numerically efficient, even in case of large-size complex (3D) structures.
- Computer software for linear elastic analysis are readily available.
- The method is simple, easy to understand, and applicable to engineering applications, as it only requires the knowledge of linear elastic analysis.
- The use of linear elastic analyses guarantees the existence of a stress state which is in equilibrium with applied loads [18].

The mentioned benefits of the ECM scheme provides the engineers with a simple, efficient, and familiar tool for collapse load determination of practical engineering structures. However, there are some problems which need to be addressed. These problems are either related to the ECM itself or the finite element model on which the ECM is applied.

The main problem is the convergence criterion defined by the method to stop the iterations. The convergence criterion defined by current ECMs is the number of iterations selected by the user as an input [12]. This criterion might not necessarily be sufficient and some trial and error processes are usually required by the user to obtain an approximate solution. The reason for this definition is multiple oscillations of the collapse load with sporadic amplitudes during the iterations, which prevents defining the convergence directly on the limit load. The main reason of the oscillations is rested in the nature of the scheme employed in the ECM when the elastic moduli of finite elements are scaled down; the elastic modulus of each element is reduced individually by a factor without consideration of the other elements whereas the equivalent stresses are computed with contributions of all elements. This approach may eventually lead to the stress overshooting of some elements, preventing the convergence on the limit load. The stress overshooting phenomenon may also affect the level of accuracy of the limit load and the collapse mechanism obtained by the method.

In a finite element model which is utilized for the ECM, the mesh density plays a vital role. Since the behavior of each element is described by one elastic modulus, usually a very fine mesh is needed, specially if a localized plasticity occurs [18]. However, in case of a poor structural discretization, the estimated stress distribution by the method cannot be a good representative of the real, continuous stress distribution in the domain, which is required for the lower bound collapse load calculation. Constructing a high quality fine mesh, specially for 3D structures with sophisticated geometries, often requires tedious human interventions. Additionally, in case of the incompressibility (i.e. Poisson's ratio close to 0.5), the accuracy and robustness of the element itself is of high importance, as the the choice of an unsuitable element will result in numerical difficulties, and can exhibit overly stiff behavior of the structure.

Current research in the area of the limit analysis is primarily motivated by two aims; (a) to develop a new and robust scheme based on the ECM to remove the oscillations, which leads to the convergence directly on limit load, and (b) to remove the mentioned mesh-related challenges to solve the problem more efficiently.

The present study is concerned with both aims. The former will be pursued by developing a novel sensitivity-based ECM which considers the contribution of other elements. In each iteration, the elastic moduli of the selected elements will be altered considering the effect of the change in elastic moduli of the other selected elements. This goal is achieved through the definition of a stress sensitivity matrix. Then, the method predicts the values of equivalent stresses of all elements in the next iteration, and modifies the changes in elastic moduli of elements in case of the stress overshooting. Hence, the stress overshooting will be prevented and the limit load solution can accurately be obtained.

The later will be tackled through the use of the novel scaled boundary finite element method (SBFEM) and the automatic quadtree/octree mesh generation. Firmly established in [19, 20], the SBFEM has simple mesh requirements, a sound theoretical basis and a robust convergent solution for linear elastic analysis. The use of polygon-shaped (in 2D) or polyhedral-shaped (in 3D) SBFEs gives rise to a key algorithm that enables all hanging nodes to be modeled effectively whilst still maintaining the numerical stability [21, 22]. This ability allows the SBFEM to be efficiently combined with quadtree/octree mesh generator schemes [3, 5]. Each cell in the quadtree/octree scheme acts as a polygon/polyhedron where the hanging nodes are behaved as normal corner nodes. The implementation of automatic mesh generator through quadtree/octree schemes, allows the SBFE discretizations to be constructed from an in-plane solid (in 2D problems) or of a solid 3D CAD model (in 3D problems). This technique automatically handles structures with complex geometries (e.g. curved boundaries, holes, etc.) using a modest number of discrete elements, compared to standard finite element methods. This effectively reduces the burden of the fine mesh generation required for the ECM. Additionally, SBFEs do not suffer from the nearly incompressible condition when Poisson's ratios of 0.4999 and smaller are used [3], making it suitable for the ECMs.

The combination of the proposed sensitivity-based ECM with the SBFEM results in an automatic scheme for the collapse load determination of structures. This automatic scheme minimizes the required interference of the user in both mesh generation and analysis parts, and therefore highly reduces the errors which might be caused by the user.

1.3 Objective and Scope of the Study

The main aim of the current research is to contribute to the improvement and development of current methods used for the determination of limit loads of structures. In particular, the primary objective of the work reported herein is to develop a robust scheme based on the ECM that avoids the limit load oscillations often occur in the ECMs. This allows the convergence to be directly defined on limit load curve and eliminates the unfounded need of using the number of iterations as the convergence criterion. Additionally, investigations into improving the automation and convenience of the method through implementing automatic mesh generators will be carried out. Particular emphasis is on the implementation of the SBFEM and the quadtree/octree scheme. This results in an efficient and automatic mesh generation for the analysis of structures in 2D- and 3D-spaces. Additionally, the ability of handling the hanging nodes in SBFEM permits the efficient use of the adaptive refinement, and hence reduces the computational resources required for large-size problems.

The specific measures towards the achievement of the objectives of this thesis are as follows:

1. A full discussion on the ECM and its modifed versions.

2. Investigate the reason for the oscillatory behavior of the ECM and the development of an oscillation-free scheme for the limit load determination by introducing a novel sensitivity-based ECM.

3. Improve the efficiency of both sensitivity-based and traditional ECMs by combining these techniques with SBFEM. This brings the advantages of SBFEM in automatic and adaptive mesh construction, and in handling the condition of incompressibility required in the ECMs.

4. Improve the efficiency of the proposed sensitivity-based ECM in terms of computational resources needed by the use of efficient adaptive SBFEM; the re-

sulting SBFE mesh will have a non-uniform h-refinement pattern, which helps to reduce the number of degrees of freedom (DOFs) required, but still guarantees the required level of accuracy of the solution. As a consequence, the size of the model will be reduced.

1.4 Organization of the Thesis

This thesis deals with improvements on the ECM for computations of the limit load. It consists of 7 chapters, including the introduction. Each chapter begins with a brief review and a more specific introduction of its contents and ends with conclusion remarks. The contents of the chapters are briefly outlined as follows.

In chapter 2, fundamentals for limit load computations are concisely stated. An overview on historical developments on limit load computations is provided. A brief literature review on the nonlinear analysis and classical limit analysis is given which are followed by a detailed and comprehensive literature review on iterative elastic analysis methods, including the ECM. The basis and assumptions used in these methods are covered and merits and drawbacks of each method are discussed.

In chapter 3, the MECM is comprehensively explained. A full discussion on the proper values of Poisson's ratios is provided. The incompressibility and the suitable elements for it are explained. The implementation of the method is presented using the finite element method with the selective integration. Various 2D and 3D numerical examples are then presented and the performance of the method is compared with available results reported in the literature. It also addresses the question whether the collapse load limit computed by the present numerical scheme is a lower bound or an upper bound solution through a mesh refinement study.

Chapter 4 extends the MECM introduced in chapter 3 for the finite element method with the selective integration to the SBFEM. The chapter reviews the formulations that describe the generic SBFE discretization of structures in 2D and 3D spaces. The quadtree and octree mesh generation methods are described. Numerical examples are given to exhibit the performance of the methodology.

Chapter 5 is devoted to the development of a thorough sensitivity-based ECM, which removes the oscillations happening in the ECM and MECM. First, the reason for the oscillations in the limit load is explained and illustrated through a simple example. Then, the sensitivity-based ECM along with its formulations for deriving the sensitivity matrix is discussed in detail for the FEM. Various numerical examples are given to verify the accuracy and robustness of the method.

In chapter 6, the formulation derived for the sensitivity-based ECM with the FEM is extended to the SBFEM. This results in an automatic scheme, in both mesh generation and analysis parts, for the collapse load determination of structures. The formulations are verified through some numerical examples and the results are compared with reported solutions in the literature. In addition, to improve the efficiency of the sensitivity-based ECM, an adaptive refinement approach for 2D problems is discussed. The method utilizes the ability of the SBFEM for handling the hanging nodes without additional refinements. The method is verified using several examples and the results are compared with the solutions obtained by uniform refinement.

Finally, in chapter 7, the conclusions and the key findings of the study are summarized and some various aspects for future research are proposed.

1.5 List of Publications

Some of the materials and results obtained from this thesis have been published or submitted to journals and conference proceedings. They are listed as follows.

1. A. Mellati, S. Tangaramvong, F. Tin Loi, C. Song, Iterative limit analysis of structures within a scaled boundary finite element framework, XIII International Conference on Computational Plasticity, Fundamentals and Applications (COMPLAS XIII). Barcelona, Spain, 2015.

2. A. Mellati, C. Song, F. Tin-Loi S. Tangaramvong, An adaptive elastic scaled boundary finite element approach for limit analysis of structures, 24th Australasian Conference on the Mechanics of Structures and Materials, ACMSM24, Perth, Australia, 2016.

3. A. Mellati, S. Tangaramvong, F. Tin Loi, C. Song, An SBFE iterative elastic analysis approach for limit load determination of structures, submitted to the journal of Engineering Structures.

Chapter 2

FUNDAMENTALS AND THE LITERATURE REVIEW

2.1 Introduction

In chapter 1 different methods for determination of the limit load for structures were shortly discussed. The use of iterative methods, and particularity the ECM, where the elastic moduli of the elements are systematically reduced in a series of linear elastic analyses to simulate stress distributions, was found to be effective as discussed in sections 1.1 and 1.2. The problems with the current ECMs used in the literature were also highlighted in section 1.2 and the measures taken to solve them were discussed in sections 1.2 and 1.3.

In this chapter the fundamental relations/theoretical basis and the relevant literature on methods for limit load determination are more comprehensively reviewed. The fundamentals relations governing the elastic and limit analyses are discussed which are mainly based on the books by Martin [23], Kaliszky [24] and Wong [25]. Different methods for limit load computations are discussed and the merits and drawbacks of each of them are presented. The emphasis is on the simplified methods using linear elastic analysis, and hence they are reviewed in detail.

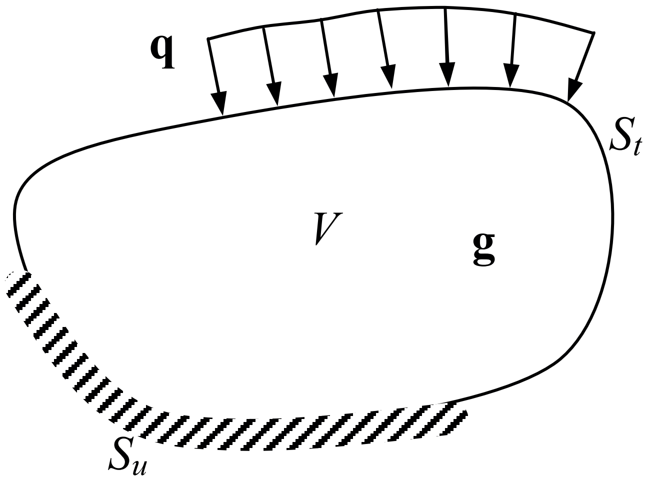

Figure 2.1: Structural model

2.2 Fundamentals

2.2.1 Stress States

This section is based on the book by Kaliszky [24] and the reader is referred to it for further information.

2.2.1.1 Stress tensors

The generic structural model used throughout this thesis (Fig. 2.1) is a bounded domain V consisting of a rigid- or elastic-perfectly plastic material. The boundary of the structure, S, is made of two regions shown as S_u and S_t. On S_t and V the surface forces per unit surface area $\mathbf{q}(\mathbf{x})$ and body forces per unit volume $\mathbf{g}(\mathbf{x})$ are prescribed, where $\mathbf{x}= (\mathrm{x}_1, \mathrm{x}_2, \mathrm{x}_3)$ shows the coordinates of each point in the domain V. The displacements of the points due to the applied forces are shown by $\mathbf{u}= \mathbf{u}(\mathbf{x})$. S_u represents the fixed part of the boundary where the the displacements are prescribed (i.e. $\mathbf{u}= \mathbf{u}^0$).

Consider a section which passes from a point $P(\mathbf{x})$ of the body and is defined by a unit outward normal vector $\mathbf{n}$ (Fig. 2.2). The stress vector $\mathbf{p}^{(\mathrm{n})}$ at the point P

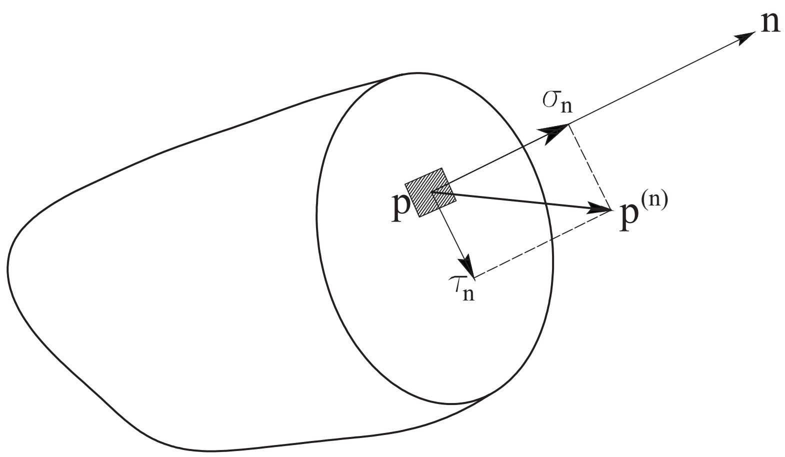

Figure 2.2: A section passing from a point P in the structural body

acting on this section is defined as

$$\mathbf{p}^{(\mathrm{n})} = \lim_{\Delta A \to 0} \frac{\Delta \mathbf{Q}}{\Delta A} \tag{2.1}$$

and shows the stress state of the point P in the section. $\Delta\mathbf{Q}$ is the force acting on the small area ΔA of this section.

The stress vector is a function of the outward normal vector. To completely define the stress states at a point P, the stress vectors related to any section passing from that point should be specified. In other words, the following function F in Eq. (2.2) needs to be derived.

$$\mathbf{p}^{(\mathrm{n})} = F\left(\mathbf{n}\right) \tag{2.2}$$

For this purpose, it is assumed that the stress vectors on the sections perpendicular to Cartesian coordinate axes x_1 (or x), x_2 (or y), and x_3 (or z) are given (Fig. 2.3), and expressed by

$$\begin{aligned} p^{(1)}\left(\sigma_{11}\;\sigma_{12}\;\sigma_{13}\right) &= p^{(x)}\left(\sigma_x\;\tau_{xy}\;\tau_{xz}\right) \\ p^{(2)}\left(\sigma_{21}\;\sigma_{22}\;\sigma_{23}\right) &= p^{(y)}\left(\tau_{yx}\;\sigma_y\;\tau_{yz}\right) \\ p^{(3)}\left(\sigma_{31}\;\sigma_{32}\;\sigma_{33}\right) &= p^{(z)}\left(\tau_{zx}\;\tau_{zy}\;\sigma_z\right). \end{aligned} \tag{2.3}$$

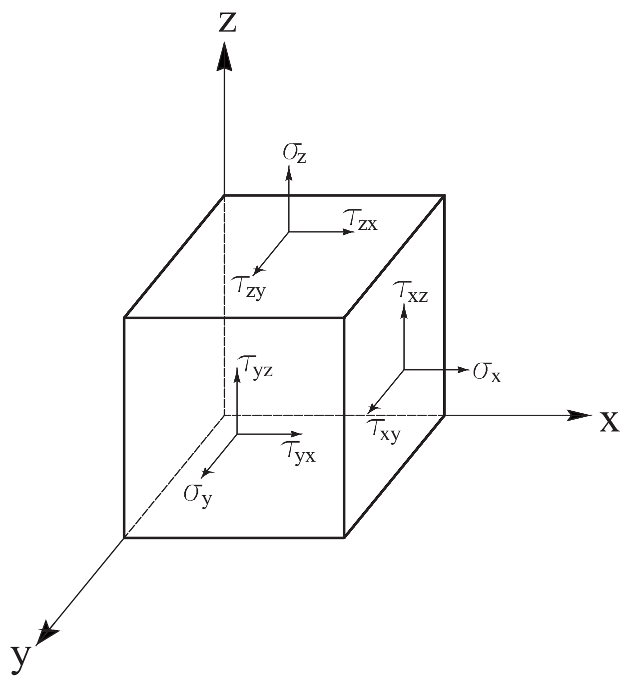

Figure 2.3: Stresses on an infinitesimal cube inside the body

Now the stress vector $\mathbf{p}^{(\mathrm{n})}$ associated with an arbitrary section intersecting with the mentioned sections perpendicular to Catresian coordinate axes, can be obtained by writing the force equilibrium equations as

$$\begin{aligned} p_x^{(\mathrm{n})} &= \sigma_x n_x + \tau_{xy} n_{\mathrm{y}} + \tau_{xz} n_{\mathrm{z}} \\ p_y^{(\mathrm{n})} &= \tau_{yx} n_x + \sigma_y n_y + \tau_{yz} n_z \\ p_z^{(\mathrm{n})} &= \tau_{zx} n_x + \tau_{zy} n_y + \sigma_z n_z. \end{aligned} \tag{2.4}$$

In other words,

$$\mathbf{p}^{(\mathrm{n})} = \mathbf{Tn} \tag{2.5}$$

, where $\mathbf{T}$ is the second order stress tensor, and in the Cartesian system of coordinates is of the form

$$\mathbf{T} = \begin{bmatrix} \sigma_{11} & \sigma_{12} & \sigma_{13} \\ \sigma_{21} & \sigma_{22} & \sigma_{23} \\ \sigma_{31} & \sigma_{32} & \sigma_{33} \end{bmatrix} \equiv \begin{bmatrix} \sigma_x & \tau_{xy} & \tau_{xz} \\ \tau_{\mathrm{yx}} & \sigma_y & \tau_{yz} \\ \tau_{zx} & \tau_{zy} & \sigma_z \end{bmatrix} \equiv \begin{bmatrix} \sigma_{x\mathrm{x}} & \sigma_{x\mathrm{y}} & \sigma_{xz} \\ \sigma_{y\mathrm{x}} & \sigma_{yy} & \sigma_{y\mathrm{z}} \\ \sigma_{zx} & \sigma_{zy} & \sigma_{zz} \end{bmatrix}. \tag{2.6}$$

Additionally, writing the moment equilibrium for the infinitesimal cube displayed in Fig. 2.3 shows the stress tensor is symmetric. That is

$$\begin{aligned}\tau_{xy} &= \tau_{yx}\\ \tau_{yz} &= \tau_{zy}\\ \tau_{xz} &= \tau_{zx}.\end{aligned} \tag{2.7}$$

Therefore, The stress state of a point in 3D space can be shown by six independent scalar components. More often, it is convenient to show these components in a vector (the Voigt notation representation of the stress tensor) of the form

$$\boldsymbol{\sigma} = \left[\sigma_x \; \sigma_y \; \sigma_z \; \tau_{xy} \; \tau_{yz} \; \tau_{xz}\right]^{\mathrm{T}}. \tag{2.8}$$

2.2.1.2 Principal stresses and stress invariants

At each point in a body at least three orthogonal normal vectors $\boldsymbol{l}^{(\mathrm{k})}$, ($k =$ I, II, III) can be found that the associated stress vectors are parallel to the normal vectors. That is

$$\mathbf{p}^{(\mathrm{k})} = \sigma_{\mathrm{k}} \boldsymbol{l}^{(\mathrm{k})}. \tag{2.9}$$

The directions of the normal vectors are known as principal directions and the corresponding coordinate axes are the principal axes (I, II, III). σ_{k} shows the principal (normal) stresses (i.e. σ_{I}, σ_{II}, σ_{III}). The shear stresses on the planes associated with the principal directions are equal to zero by definition.

The principal stresses and directions can be obtained by considering Eqs. (2.4) and (2.9). i.e.

$$\begin{aligned}p_x^{(\mathrm{k})} &= \sigma_{\mathrm{k}} l_x^{(\mathrm{k})} = \sigma_x l_x^{(\mathrm{k})} + \tau_{x\mathrm{y}} l_y^{(\mathrm{k})} + \tau_{xz} l_z^{(\mathrm{k})}\\ p_y^{(\mathrm{k})} &= \sigma_{\mathrm{k}} l_y^{(\mathrm{k})} = \tau_{yx} l_x^{(\mathrm{k})} + \sigma_y l_y^{(\mathrm{k})} + \tau_{yz} l_z^{(\mathrm{k})}\\ p_z^{(\mathrm{k})} &= \sigma_{\mathrm{k}} l_z^{(\mathrm{k})} = \tau_{zx} l_x^{(\mathrm{k})} + \tau_{zy} l_y^{(\mathrm{k})} + \sigma_z l_z^{(\mathrm{k})}.\end{aligned} \tag{2.10}$$

These equations can be rearranged to

$$\begin{aligned}
&(\sigma_x - \sigma_\mathrm{k})\, l_x^{(\mathrm{k})} + \tau_{xy} l_y^{(\mathrm{k})} + \tau_{xz} l_z^{(\mathrm{k})} = 0 \\
&\tau_{yx} l_x^{(\mathrm{k})} + (\sigma_y - \sigma_\mathrm{k})\, l_y^{(\mathrm{k})} + \tau_{yz} l_z^{(\mathrm{k})} = 0 \\
&\tau_{zx} l_x^{(\mathrm{k})} + \tau_{zy} l_y^{(\mathrm{k})} + (\sigma_z - \sigma_\mathrm{k})\, l_z^{(\mathrm{k})} = 0.
\end{aligned} \tag{2.11}$$

For this set of linear equations to have a nontrivial solution for $l_x^{(\mathrm{k})}$, $l_y^{(\mathrm{k})}$, and $l_z^{(\mathrm{k})}$, the determinant of coefficients should be equal to zero. That is

$$\begin{vmatrix} (\sigma_x - \sigma_\mathrm{k}) & \tau_{xy} & \tau_{xz} \\ \tau_{yx} & (\sigma_y - \sigma_\mathrm{k}) & \tau_{yz} \\ \tau_{\mathrm{zx}} & \tau_{\mathrm{zy}} & (\sigma_z - \sigma_\mathrm{k}) \end{vmatrix} = 0. \tag{2.12}$$

Expansion of the determinant leads to the follows equation for σ_k

$$\sigma_\mathrm{k}^3 - I_1 \sigma_\mathrm{k}^2 - I_2 \sigma_\mathrm{k} - I_3 = 0 \tag{2.13}$$

, where

$$\begin{aligned}
I_1 &= \sigma_x + \sigma_y + \sigma_z \\
I_2 &= -\left(\sigma_x \sigma_y + \sigma_y \sigma_z + \sigma_z \sigma_\mathrm{x}\right) + \left(\tau_{\mathrm{xy}}^2 + \tau_{yz}^2 + \tau_{\mathrm{xz}}^2\right) \\
I_3 &= \sigma_\mathrm{x} \sigma_y \sigma_z + 2\tau_{xy}\tau_{\mathrm{yz}}\tau_{xz} - \left(\sigma_x \tau_{yz}^2 + \sigma_y \tau_{xz}^2 + \sigma_z \tau_{xy}^2\right).
\end{aligned} \tag{2.14}$$

The roots of the Eq. (2.13) are the principal stresses shown by σ_I, σ_II, and σ_III. The subscripts of the principal stresses are selected in a way that $\sigma_\mathrm{I} \geq \sigma_\mathrm{II} \geq \sigma_\mathrm{III}$ is met. The coefficients I_1, I_2, and I_3 are called the first, second and third principal invariants of the stress tensor, respectively. They also can be written in the form of principal stresses as

$$
\begin{aligned}
I_1 &= \sigma_{\mathrm{I}} + \sigma_{\mathrm{II}} + \sigma_{\mathrm{III}} \\
I_2 &= -\left(\sigma_{\mathrm{I}}\sigma_{\mathrm{II}} + \sigma_{\mathrm{II}}\sigma_{\mathrm{III}} + \sigma_{\mathrm{III}}\sigma_{\mathrm{I}}\right) \\
I_3 &= \sigma_{\mathrm{I}}\sigma_{\mathrm{II}}\sigma_{\mathrm{III}}.
\end{aligned} \tag{2.15}
$$

Using Eq. (2.4), the principal shear stresses (τ_{I}, τ_{II}, and τ_{III}) acting on the section which consist of one of the principal axes and bisects the angle between the other two principal axes, can also be obtained as follows

$$
\begin{aligned}
\tau_{\mathrm{I}} &= \frac{1}{2}\left(\sigma_{\mathrm{II}} - \sigma_{\mathrm{III}}\right) \\
\tau_{\mathrm{II}} &= \frac{1}{2}\left(\sigma_{\mathrm{I}} - \sigma_{\mathrm{III}}\right) \\
\tau_{\mathrm{III}} &= \frac{1}{2}\left(\sigma_{\mathrm{I}} - \sigma_{\mathrm{II}}\right).
\end{aligned} \tag{2.16}
$$

2.2.1.3 Stress deviator tensor

It is a common approach in plasticity to divide the stress tensor into two parts

$$\mathbf{T} = \mathbf{T}^0 + \mathbf{S} \tag{2.17}$$

, where $\mathbf{T}^0$ defines the spherical stress tensor correspondent to the hydrostatic part of the stress state. It can be written as

$$\mathbf{T}^0 = \begin{bmatrix} \sigma_m & 0 & 0 \\ 0 & \sigma_m & 0 \\ 0 & 0 & \sigma_m \end{bmatrix} \tag{2.18}$$

, where σ_m is called the mean normal stress and is defined as follows

$$\sigma_m = \frac{1}{3}\left(\sigma_x + \sigma_y + \sigma_z\right) = \frac{1}{3}\left(\sigma_{\mathrm{I}} + \sigma_{\mathrm{II}} + \sigma_{\mathrm{III}}\right). \tag{2.19}$$

S is the stress deviator tensor. From Eq. (2.17) it can be expressed as

$$\mathbf{S} = \mathbf{T} - \mathbf{T}^0 = \begin{bmatrix} (\sigma_x - \sigma_m) & \tau_{xy} & \tau_{xz} \\ \tau_{yx} & (\sigma_y - \sigma_m) & \tau_{yz} \\ \tau_{zx} & \tau_{zy} & (\sigma_z - \sigma_m) \end{bmatrix} = \begin{bmatrix} s_x & s_{xy} & s_{xz} \\ s_{yx} & s_y & s_{yz} \\ s_{zx} & s_{zy} & s_z \end{bmatrix}. \quad (2.20)$$

The principal directions are the same for the stress deviator tensor and for the stress tensor. Similar to the section 2.2.1.2, the principal normal stresses of the deviator tensor are denoted by s_{I}, s_{II}, and s_{III} and can be obtained from the following equation

$$s_{\mathrm{k}}^3 - K_1 s_{\mathrm{k}}^2 - K_2 s_{\mathrm{k}} - K_3 = 0 \quad (2.21)$$

, where

$$K_1 = s_x + s_y + s_z = 0$$

$$K_2 = \begin{vmatrix} s_x & s_{xy} \\ s_{yx} & s_y \end{vmatrix} - \begin{vmatrix} s_y & s_{yz} \\ s_{zy} & s_z \end{vmatrix} - \begin{vmatrix} s_z & s_{xy} \\ s_{zx} & s_z \end{vmatrix}$$

$$K_3 = \begin{vmatrix} s_x & s_{xy} & s_{xz} \\ s_{yx} & s_y & s_{yz} \\ s_{zx} & s_{zy} & s_z \end{vmatrix}. \quad (2.22)$$

K_1, K_2, and K_3, do not depend on the chosen coordinate axes and are called the first, second, and third invariants of the stress deviator tensor.

2.2.1.4 Equilibrium equations

The stress state in a body is a function of the coordinates. The nine scalar components of a stress tensor cannot be independent of each others. They need to satisfy some relationships which can be derived from equilibrium equations.

In section 2.2.1.1, it was mentioned that writing the moment equilibrium equations for the infinitesimal cube shown in Fig. 2.3 leads to the symmetricity of the stress tensor shown in Eq. (2.7). Similarly, writing the force equilibrium equations for the same infinitesimal cube with small changes in the stress state leads to the following three differential equilibrium equations

$$\begin{aligned}
&\frac{\partial \sigma_x}{\partial x} + \frac{\partial \tau_{xy}}{\partial y} + \frac{\partial \tau_{xz}}{\partial z} + g_x = 0 \\
&\frac{\partial \tau_{yx}}{\partial x} + \frac{\partial \sigma_y}{\partial y} + \frac{\partial \tau_{yz}}{\partial z} + g_y = 0 \\
&\frac{\partial \tau_{\mathrm{zx}}}{\partial x} + \frac{\partial \tau_{zy}}{\partial y} + \frac{\partial \sigma_{\mathrm{z}}}{\partial z} + g_z = 0.
\end{aligned} \tag{2.23}$$

, where g_x, g_y, and g_z are the body force per unit volume $\mathbf{g}$ components (see Fig. 2.1) in Catresian coordinate axes. These equations are called Cauchy's equilibrium equations. Eqs. (2.23) are only valid for infinitesimal cubes inside the domain and not the infinitesimal neighborhood of a point on the surface on the body. To investigate the equilibrium of a point on the surface of the body, the equilibrium of the infinitesimal tetrahedron made by the coordinate planes and the surface elements in Fig. 2.4 is considered. Then, the following equilibrium equations can be obtained using the Eqs. (2.4)

$$\begin{aligned}
&\sigma_x n_x + \tau_{xy} n_y + \tau_{xz} n_z = q_x \\
&\tau_{yx} n_x + \sigma_y n_y + \tau_{yz} n_z = q_y \\
&\tau_{zx} n_x + \tau_{zy} n_y + \sigma_{\mathrm{z}} n_z = q_{z.}
\end{aligned} \tag{2.24}$$

, where where q_x, q_y, and q_z are the surface forces per unit area ($\mathbf{q}$) components (see Fig. 2.1) in Catresian coordinate axes. These are called the static boundary conditions.

The Eqs. (2.23) and (2.24) can be shown in short form as follows

$$\begin{aligned}
&\nabla \boldsymbol{\sigma} + \mathbf{g} = 0 \qquad \text{in} \quad V, \\
&\boldsymbol{\sigma} \mathbf{n} = \mathbf{q} \qquad \text{on} \quad S_t
\end{aligned} \tag{2.25}$$

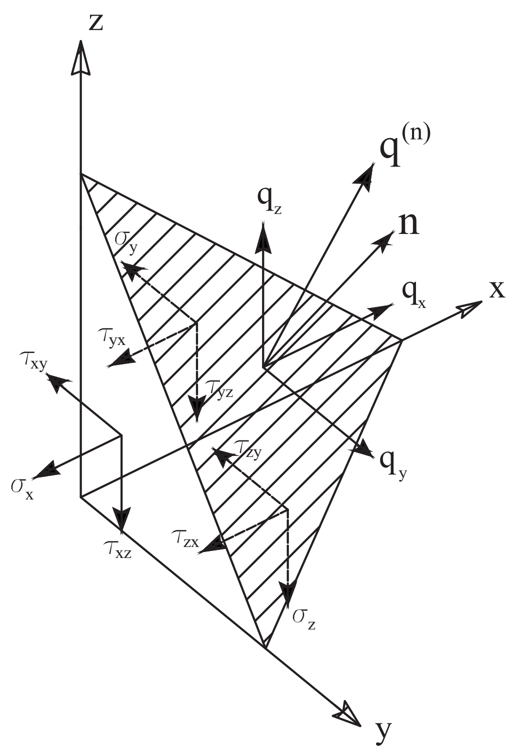

Figure 2.4: The infinitesimal tetrahedron

, where the operator ∇ indicates the differential operator, and is defined as follows

$$\nabla = \begin{bmatrix} \frac{\partial}{\partial x} & 0 & 0 & \frac{\partial}{\partial y} & 0 & \frac{\partial}{\partial z} \\ 0 & \frac{\partial}{\partial y} & 0 & \frac{\partial}{\partial x} & \frac{\partial}{\partial z} & 0 \\ 0 & 0 & \frac{\partial}{\partial z} & 0 & \frac{\partial}{\partial y} & \frac{\partial}{\partial x} \end{bmatrix}. \tag{2.26}$$

A stress field is called an admissible stress field if it satisfies these equilibrium and boundary conditions equations.

2.2.2 Strain States

In the following, it is assumed that the body has continuous deformations. That is, no gaps or overlapping will be seen, and the displacement is only a function of the coordinates. The infinitesimal strain theory is considered where the displacements are assumed infinitesimally smaller than the dimensions of the body. This section is based on the book by Kaliszky [24] and the reader is referred to it for further information.

2.2.2.1 Strain tensor and strain rates

The state of strain at any point in the body can be defined by the strain tensor **E** as follows

$$\mathbf{E} = \begin{bmatrix} \epsilon_{11} & \epsilon_{12} & \epsilon_{13} \\ \epsilon_{21} & \epsilon_{22} & \epsilon_{23} \\ \epsilon_{31} & \epsilon_{32} & \epsilon_{33} \end{bmatrix} = \begin{bmatrix} \epsilon_{x} & \epsilon_{xy} & \epsilon_{xz} \\ \epsilon_{y\mathrm{x}} & \epsilon_{y} & \epsilon_{yz} \\ \epsilon_{zx} & \epsilon_{zy} & \epsilon_{z} \end{bmatrix} = \begin{bmatrix} \frac{\partial u_1}{\partial x_1} & \frac{1}{2}\left(\frac{\partial u_1}{\partial x_2} + \frac{\partial u_2}{\partial x_1}\right) & \frac{1}{2}\left(\frac{\partial u_1}{\partial x_3} + \frac{\partial u_3}{\partial x_1}\right) \\ \frac{1}{2}\left(\frac{\partial u_2}{\partial x_1} + \frac{\partial u_1}{\partial x_2}\right) & \frac{\partial u_2}{\partial x_2} & \frac{1}{2}\left(\frac{\partial u_2}{\partial x_3} + \frac{\partial u_3}{\partial x_2}\right) \\ \frac{1}{2}\left(\frac{\partial u_3}{\partial x_1} + \frac{\partial u_1}{\partial x_3}\right) & \frac{1}{2}\left(\frac{\partial u_3}{\partial x_2} + \frac{\partial u_2}{\partial x_3}\right) & \frac{\partial u_3}{\partial x_3} \end{bmatrix} \tag{2.27}$$

, where u_1, u_2, and u_3 are the displacement components in the Cartesian coordinates axes x_1, x_2, and x_3 at the considered point.

In the theory of plasticity, the strain increments play an important role. Strain increments represent the small changes in strains due to the small changes in a certain parameter in the loading process (i.e. time, iteration, etc.). The strain increment tensor is denoted as follows

$$\mathrm{d}\mathbf{E} = \begin{bmatrix} \mathrm{d}\epsilon_{11} & \mathrm{d}\epsilon_{12} & \mathrm{d}\epsilon_{13} \\ \mathrm{d}\epsilon_{21} & \mathrm{d}\epsilon_{22} & \mathrm{d}\epsilon_{23} \\ \mathrm{d}\epsilon_{31} & \mathrm{d}\epsilon_{32} & \mathrm{d}\epsilon_{33} \end{bmatrix} = \begin{bmatrix} \mathrm{d}\epsilon_{x} & \mathrm{d}\epsilon_{xy} & \mathrm{d}\epsilon_{xz} \\ \mathrm{d}\epsilon_{yx} & \mathrm{d}\epsilon_{y} & \mathrm{d}\epsilon_{yz} \\ \mathrm{d}\epsilon_{zx} & \mathrm{d}\epsilon_{zy} & \mathrm{d}\epsilon_{z} \end{bmatrix} \tag{2.28}$$

, where each entry of it is defined as follows

$$\mathrm{d}\mathbf{E}_{ij} = \frac{1}{2}\left(\frac{\partial \mathrm{d}\mathbf{u}_i}{\partial x_j} + \frac{\partial \mathrm{d}\mathbf{u}_j}{\partial x_i}\right). \tag{2.29}$$

The strain rate tensor, $\dot{\mathbf{E}}$, can be obtained by associating the strain increments to the time increment as follows

$$\dot{\mathbf{E}} = \frac{\mathrm{d}\mathbf{E}}{\mathrm{d}t} = \begin{bmatrix} \dot{\epsilon}_x & \dot{\epsilon}_{xy} & \dot{\epsilon}_{xz} \\ \dot{\epsilon}_{y\mathrm{x}} & \dot{\epsilon}_y & \dot{\epsilon}_{yz} \\ \dot{\epsilon}_{zx} & \dot{\epsilon}_{zy} & \dot{\epsilon}_z \end{bmatrix}. \tag{2.30}$$

By introducing the displacement rate (velocity) as

$$\dot{\mathbf{u}} = \mathbf{v} = \frac{\mathrm{d}\mathbf{u}}{\mathrm{d}t} \tag{2.31}$$

, the strain rates can also be written as

$$\dot{\mathbf{E}}_{ij} = \frac{1}{2}\left(\frac{\partial \dot{\mathbf{u}}_i}{\partial x_j} + \frac{\partial \dot{\mathbf{u}}_j}{\partial x_i}\right). \tag{2.32}$$

2.2.2.2 Kinematic equations

As shown in Eq. (2.27), the strain tensor entries are not independent of each other. The strain tensor is symmetric. That is

$$\mathbf{E}_{ij} = \mathbf{E}_{ji}. \tag{2.33}$$

Therefore, the following relationships can be written as

$$\begin{aligned} \epsilon_x = \frac{\partial u_x}{\partial x},\ \epsilon_y &= \frac{\partial u_y}{\partial y},\ \epsilon_z = \frac{\partial u_z}{\partial z} \\ \epsilon_{xy} = \epsilon_{yx} &= \frac{1}{2}\left(\frac{\partial u_x}{\partial y} + \frac{\partial u_y}{\partial x}\right), \\ \epsilon_{yz} = \epsilon_{zy} &= \frac{1}{2}\left(\frac{\partial u_y}{\partial z} + \frac{\partial u_z}{\partial y}\right), \\ \epsilon_{xz} = \epsilon_{zx} &= \frac{1}{2}\left(\frac{\partial u_x}{\partial z} + \frac{\partial u_z}{\partial x}\right). \end{aligned} \tag{2.34}$$

These relations are known as strain-displacement or kinematic equations. Similar to the stress state and due to symmetricity of the strain tensor, the strain components are more often shown as strain vector $\boldsymbol{\epsilon}$ in the form of

$$\boldsymbol{\epsilon} = [\epsilon_x \; \epsilon_y \; \epsilon_z \; \epsilon_{xy} \; \epsilon_{yz} \; \epsilon_{xz}]^{\mathrm{T}} . \tag{2.35}$$

Similarly, the strain rate vector is defined as

$$\dot{\boldsymbol{\epsilon}} = [\dot{\epsilon}_x \; \dot{\epsilon}_y \; \dot{\epsilon}_{\mathrm{z}} \; \dot{\epsilon}_{xy} \; \dot{\epsilon}_{yz} \; \dot{\epsilon}_{xz}]^{\mathrm{T}} . \tag{2.36}$$

On S_u (see Fig. 2.1) the displacements are prescribed. Therefore, the displacement field should satisfy the kinematic boundary conditions on S_u as follows

$$\mathbf{u} = \mathbf{u}^0. \tag{2.37}$$

The kinematic equations, therefore, in short form can be described as follows

$$\begin{aligned} \mathbf{E}_{ij} &= \frac{1}{2}\left(\frac{\partial \mathbf{u}_i}{\partial x_j} + \frac{\partial \mathbf{u}_j}{\partial x_i}\right) \qquad \text{in} \quad V, \\ \mathbf{u} &= \mathbf{u}^0 \qquad \text{on} \quad S_u. \end{aligned} \tag{2.38}$$

These equations can also be extended to show the strain rate-displacement rate as follows

$$\begin{aligned} \dot{\mathbf{E}}_{ij} &= \frac{1}{2}\left(\frac{\partial \dot{\mathbf{u}}_i}{\partial x_j} + \frac{\partial \dot{\mathbf{u}}_j}{\partial x_i}\right) \qquad \text{in} \quad V, \\ \dot{\mathbf{u}} &= 0 \qquad \text{on} \quad S_u. \end{aligned} \tag{2.39}$$

Similar to the admissible stress fields, the kinematically admissible strain rate and the velocity fields are the ones satisfying the kinematic equation and the kinematic boundary conditions.

2.2.3 Stress-Strain Relations and Material Models

The equilibrium equations (Eqs. (2.25)) and the kinematic equations (Eqs. (2.38) and (2.39)) do not uniquely determine the stresses, strains, and displacements in the domain. To obtain a unique solution, some further equations known as constitutive equations are needed. These equations represent the stress-strain relationship. These equations are based on the material model which has been employed.

Fig. 2.5 shows the linear or multi-linear material models usually assumed to simulate the real stress-strain relations: (a) linear elastic; (b) rigid-perfectly plastic; (c) rigid-plastic hardening; (d) linear elastic perfectly plastic; and (e) linear elastic-plastic hardening. In this study, the material models (a) and (b) are considered. The materials with linear elastic models (a) follow the same linear stress-strain relationships during loading and unloading processes. Therefore, after unloading, no permanent strain remains. For rigid-perfectly plastic materials (b), it is assumed that the elastic deformation is so small that it can be ignored. Although this assumption has some restrictions in its use, its simplicity still has certain merits for the plastic design, and thus is adopted in many design codes (such as European standard, EN 13445-3 [26], for pressure vessel design). Hence, in this thesis, it has been assumed that the material behaves as if the structure does not deform unless it collapses plastically.

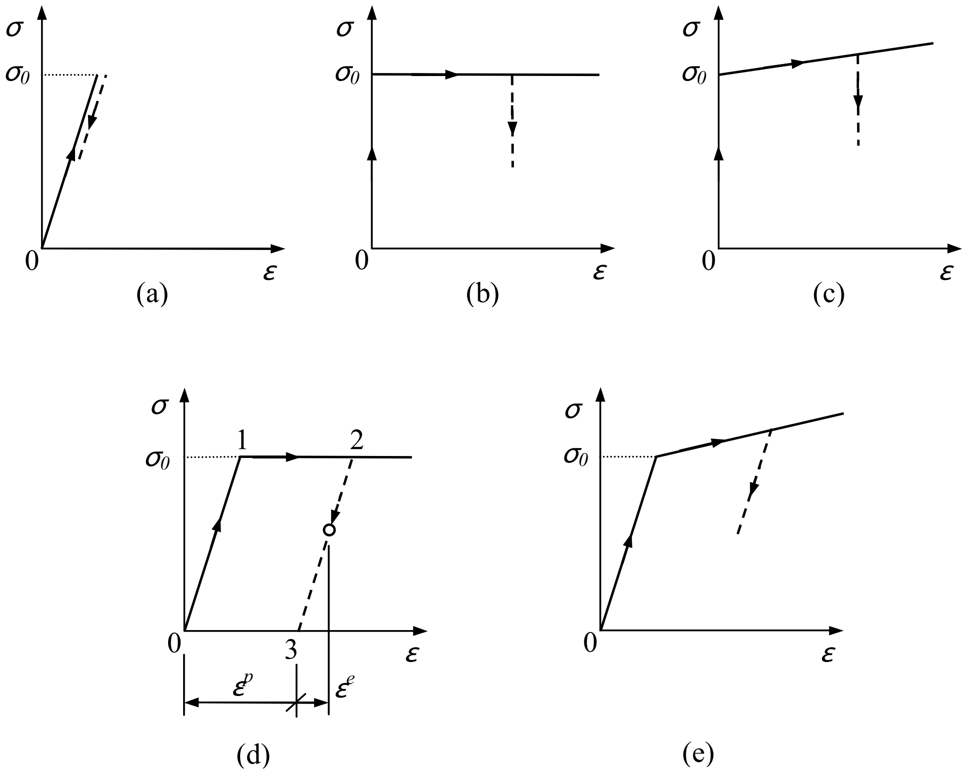

Figure 2.5: Material models; (a) linear elastic (b) rigid-perfectly plastic (c) rigid-plastic hardening (d) linear elastic perfectly plastic and (e) linear elastic-plastic hardening

2.2.4 Constitutive Equations for Linearly Elastic, Isotropic Material

The stress-strain relations for linearly elastic, isotropic material can be described by the Hook's law as follows

$$\begin{gathered}
\epsilon_x = \frac{1}{E}\left[\sigma_x - \nu\left(\sigma_y + \sigma_z\right)\right] \\
\epsilon_y = \frac{1}{E}\left[\sigma_y - \nu\left(\sigma_x + \sigma_z\right)\right] \\
\epsilon_z = \frac{1}{E}\left[\sigma_z - \nu\left(\sigma_x + \sigma_y\right)\right] \\
\epsilon_{xy} = \frac{1}{2G}\sigma_{xy},\ \epsilon_{yz} = \frac{1}{2G}\sigma_{yz},\ \epsilon_{xz} = \frac{1}{2G}\sigma_{xz}
\end{gathered} \tag{2.40}$$

, where E is the Young's modulus or elastic modulus, G is the shear modulus, and ν is the Poisson's ratio of the material. These parameters are dependent on each other and should satisfy the relationship

$$G = \frac{E}{2(1+\nu)}. \tag{2.41}$$

The Hook's law in the matrix form can be written as follows

$$\boldsymbol{\sigma} = \mathbf{D}\boldsymbol{\epsilon} \tag{2.42}$$

, where $\mathbf{D}$ is the elasticity matrix and is defined as

$$\mathbf{D} = \frac{\lambda}{\nu}\begin{bmatrix} (1-\nu) & \nu & \nu & 0 & 0 & 0 \\ \nu & (1-\nu) & \nu & 0 & 0 & 0 \\ \nu & \nu & (1-\nu) & 0 & 0 & 0 \\ 0 & 0 & 0 & (1-2\nu) & 0 & 0 \\ 0 & 0 & 0 & 0 & (1-2\nu) & 0 \\ 0 & 0 & 0 & 0 & 0 & (1-2\nu) \end{bmatrix}. \tag{2.43}$$

Here λ is the Lamé's modulus of material and is defined as

$$\lambda = \frac{\nu E}{(1+\nu)(1-2\nu)}. \tag{2.44}$$

2.2.5 Yield Conditions for Perfectly Plastic Materials

The yield conditions defines the valid range of Hook's law and the constitutive equations when plastic deformation occurs. Consider the uniaxial stress state for the sake of simplicity. The yield function, f, is defined as follows

$$f = \sigma^2 - \sigma_0^2 \tag{2.45}$$

, where σ_0 shows the yield stress of the material. This function expresses two different behaviors of the material; when $f < 0$, it shows the elastic phase of the material and when $f = 0$, it shows the plastic region of the material.

The state $f > 0$ is not stated, as the yield stress σ_0 cannot be exceeded in perfectly plastic materials. Generally, the yield function depends on different factors and can be written as

$$f = f(\boldsymbol{\sigma}, \boldsymbol{\epsilon}, \dot{\boldsymbol{\sigma}}, \dot{\boldsymbol{\epsilon}}, \mathbf{x}, T, t) \tag{2.46}$$

, where $\boldsymbol{\sigma}$, $\boldsymbol{\epsilon}$ are the stress and strain fields, and $\dot{\boldsymbol{\sigma}}$, $\dot{\boldsymbol{\epsilon}}$ are their associated rates defined in subsections 2.2.1 and 2.2.2. T and t represents temperature and time, respectively. However, the yield function is usually simplified to be easy to be implemented; for instance, the medium usually is considered as a homogeneous body and is independent on the temperature and the time. Consequently, the yield function will be independent of the coordinate $\mathbf{x}$, the stress and strain rates ($\dot{\boldsymbol{\sigma}}$,$\dot{\boldsymbol{\epsilon}}$), the temperature T and time t. Additionally, the yield function is path-independent, which means it is independent of deformation field history. As a result, the yield function in Eq. (2.46) can be reduced to be represented only by the stress state in the medium and the material property as

$$f = f(\boldsymbol{\sigma}, \kappa) \tag{2.47}$$

, where κ is the plastic property constant of the material.

When isotropic material is employed, which states that the material properties do not change in different directions, the yield function can be further simplified to be expressed by only the invariants of the stress tensor I_1, I_2, I_3 or principal stresses σ_{I}, σ_{II}, σ_{III} (which are defined in Eqs. (2.14) and (2.15)) as

$$f = f(I_1, I_2, I_3) = f(\sigma_{\mathrm{I}}, \sigma_{\mathrm{II}}, \sigma_{\mathrm{III}}). \tag{2.48}$$

Considering the fact that the hydrostatic pressure normally does not have significant effects on plastic deformations, the addition of hydrostatic stresses to the existing stress states does not affect the occurrence of yielding. Therefore, the yield function can finally be described only in terms of invariants K_2 and K_3 of stress deviator tensor (defined in section 2.2.1.3) as

$$f = f(K_2, K_3, \kappa). \tag{2.49}$$

The yield function in Eq. (2.49) has two important properties; it is closed and convex [24].

The yield function of the materials can be obtained by experimental results and theoretical justifications. In practice, von Mises yield criterion and Tresca yield conditions are the most well-known yield functions utilized for metals, which are stated briefly in the following.

2.2.5.1 The von Mises yield condition

The von Mises yield condition, in its general form, can be stated as

$$f = K_2 - \tau_0^2 = 0. \tag{2.50}$$

Here, τ_0 is the yield stress in pure shear. The second invariant of the stress deviator tensor, K_2, can also be written in terms of invariant stresses or principal stresses. Therefore, the yield function for von Mises condition can be developed to

$$f = \frac{1}{6}\left[(\sigma_x - \sigma_y)^2 + (\sigma_y - \sigma_z)^2 + (\sigma_x - \sigma_z)^2\right] + \tau_{xy}^2 + \tau_{yz}^2 + \tau_{xz}^2 - \tau_0^2 = 0 \tag{2.51}$$

or

$$f = \frac{1}{6}\left[(\sigma_{\mathrm{I}} - \sigma_{\mathrm{II}})^2 + (\sigma_{\mathrm{II}} - \sigma_{\mathrm{III}})^2 + (\sigma_{\mathrm{I}} - \sigma_{\mathrm{III}})^2\right] - \tau_0^2 = 0. \tag{2.52}$$

Eq. (2.52) describes an equation for a cylinder in the principal stress space where the hydrostatic stress lies along the axis of the cylinder (Fig. 2.6).

In case of a uniaxial stress state ($\sigma_{\mathrm{II}} = \sigma_{\mathrm{III}} = 0$), the form of the von Mises yield

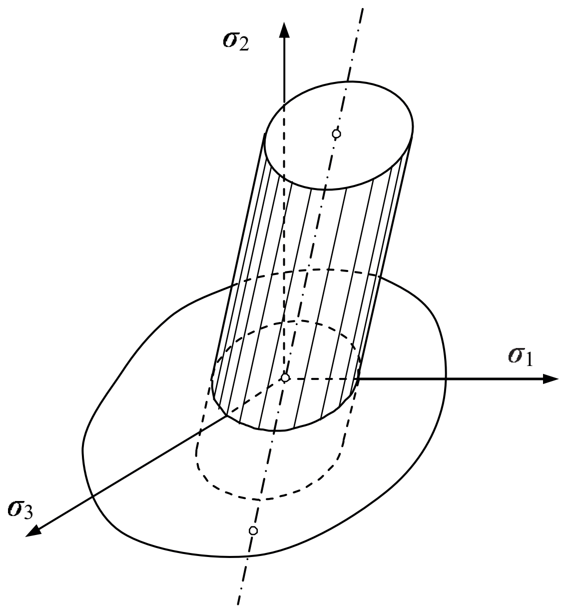

Figure 2.6: The von Mises yield function in principal stress space.

function in Eq. (2.52) can be reduced to

$$f = \frac{1}{3}\sigma_{\mathrm{I}}^2 - \tau_0^2 = 0. \tag{2.53}$$

In this case, the material can also yield when the stress equals the yield stress in pure tension. As a result, the relationship between the yield stress in pure tension and yield stress in pure shear can be derived as

$$\tau_0 = \frac{1}{\sqrt{3}}\sigma_0. \tag{2.54}$$

For two-dimensional problems, two plane states can be considered: plane stress and plane strain states.

In plane stress case, the out of the plane stresses (i.e. $\tau_{xz}, \tau_{yz}, \sigma_z$) or simply σ_{III} are zero everywhere in the body. The use of $\sigma_{\mathrm{III}} = 0$ in Eq. (2.52) leads to

$$f = \sigma_{\mathrm{I}}^2 - \sigma_{\mathrm{I}}\sigma_{\mathrm{II}} + \sigma_{\mathrm{II}}^2 - 3\tau_0^2. \tag{2.55}$$

Alternatively, substituting $\tau_{xz}, \tau_{yz}, \sigma_z$ with zero in Eq. (2.51) and using Eq. (2.54) give

$$f = \sigma_x^2 + \sigma_y^2 - \sigma_x\sigma_y + 3\tau_{xy}^2 - \sigma_0^2 = 0. \tag{2.56}$$

In plane strain case, the out of plane strains (i.e. $\epsilon_{xz}, \epsilon_{yz}, \epsilon_z$) are zero everywhere in the body. However, the stress in principal axis III is not zero. In fact, the deformation condition is met if

$$\sigma_{\mathrm{III}} = \frac{1}{2}\left(\sigma_{\mathrm{I}} + \sigma_{\mathrm{II}}\right), \tag{2.57}$$

so that the tendency for one pair of principal stresses to extend the material along axis III is balanced by the other pair to contract it along this axis [27, 23]. The Eq. (2.57) can also be derived by the use of Prandtl-Reuss constitutive equations [24]. These equations for a rigid-perfectly plastic material can be written in the term of strain rates as follows

$$\begin{aligned} \dot{\epsilon}_x &= \dot{\lambda} s_x \\ \dot{\epsilon}_y &= \dot{\lambda} s_y \\ \dot{\epsilon}_z &= \dot{\lambda} s_z \\ \dot{\epsilon}_{xy} &= \dot{\lambda} s_{xy}, \end{aligned} \tag{2.58}$$

where $\dot{\lambda}$ is the plastic multiplier and $\{s_x,\ s_y,\ s_z,\ s_{xy}\}$ are the stress deviator tensor components defined in section 2.2.1.3 in Eq. (2.20). Since in plane strain case $\epsilon_z = 0$, the third equation can be extended to

$$s_z = \sigma_z - \sigma_m = \sigma_z - \frac{1}{3}\left(\sigma_x + \sigma_y + \sigma_z\right) = 0. \tag{2.59}$$

From Eq. (2.59) it can be derived that the normal stress σ_z is equal to the mean of the other two normal stresses. That is

$$\sigma_z = \sigma_{\mathrm{m}} = \frac{1}{2}\left(\sigma_x + \sigma_y\right). \tag{2.60}$$

As in plane strain condition, $\tau_{xz} = \tau_{yz} = 0$, σ_z also shows a principal stress (σ_{III}), and thus the other principal stresses (σ_{I}, σ_{II}) are parallel to the x, y plane. Hence, the Eq. (2.57) is proved. Substituting σ_{III} from Eq. (2.57) into Eq. (2.52), the von Mises yield function in this case can be reduced to the form of

$$f = (\sigma_{\mathrm{I}} - \sigma_{\mathrm{II}})^2 - 2\tau_0^2 = 0. \tag{2.61}$$

Alternatively, by having τ_{zx}, and τ_{zy} as zeros, and the use of Eq. (2.60) and Eq. (2.54), Eq. (2.51) can be simplified to

$$f = \frac{1}{4}(\sigma_x - \sigma_y)^2 + \tau_{xy}^2 - \frac{\sigma_0^2}{3} = 0. \tag{2.62}$$

2.2.5.2 The Tresca yield condition

The Tresca yield condition states that when the maximum shear stress becomes equal to the yield stress in pure shear, yielding occurs. The Tresca yield function can be written as

$$f = |\tau_{max}| - \tau_0 = 0. \tag{2.63}$$

, where τ_{max} is the maximum shear stress and equals to τ_{II} in Eq. (2.16) when the relationship $\sigma_{\mathrm{I}} \geq \sigma_{\mathrm{II}} \geq \sigma_{\mathrm{III}}$ is satisfied. However, this relationship is not generally known a priori [24]. Therefore, using the Eqs. (2.16) and eliminating the absolute sign in Eq. (2.63), the general form of the Tresca yield condition is as follows

$$\begin{aligned} f_1 &= (\sigma_{\mathrm{I}} - \sigma_{\mathrm{II}})^2 - 4\tau_0^2 = 0 \\ f_2 &= (\sigma_{\mathrm{II}} - \sigma_{\mathrm{III}})^2 - 4\tau_0^2 = 0 \\ f_3 &= (\sigma_{\mathrm{I}} - \sigma_{\mathrm{III}})^2 - 4\tau_0^2 = 0. \end{aligned} \tag{2.64}$$

These equations constitute a hexagonal cylinder in principal stress space. Yielding occurs if at least one of the Eqs. (2.64) is satisfied.

In uniaxial stress state, the principal stresses of σ_{II} and σ_{III} are equal to zero and

Eqs. (2.64) will be reduced to

$$f = \sigma_{\mathrm{I}}^2 - 4\tau_0^2 = 0. \tag{2.65}$$

In this state, the yield condition is reached when the axial stress becomes equal to the yield stress in pure tension. Hence, from Eq. (2.65), one can write

$$\tau_0 = \frac{\sigma_0}{2}. \tag{2.66}$$

In biaxial stress state, two cases are considered; plane stress and plane strain.

In case of plane stress condition, the principal stress in axis 3 is zero. By substituting σ_{III} with zero in Eq. (2.64) and use of Eq. (2.66), the Tresca yield condition can be written as

$$\begin{aligned} f_1 &= \sigma_{\mathrm{II}}^2 - \sigma_0^2 = 0 \\ f_2 &= \sigma_{\mathrm{I}}^2 - \sigma_0^2 = 0 \\ f_3 &= \left(\sigma_{\mathrm{I}}^2 - \sigma_{\mathrm{II}}^2\right) - \sigma_0^2 = 0. \end{aligned} \tag{2.67}$$

In plane strain condition, the Tresca yield function is similar to the von Mises yield condition. Substituting the Eq. (2.57) into Eqs. (2.64) leads to

$$f = \left(\sigma_{\mathrm{I}} - \sigma_{\mathrm{II}}\right)^2 - 4\tau_0^2 = 0 \tag{2.68}$$

, or

$$f = \left(\sigma_x - \sigma_y\right)^2 + 4\tau_{xy}^2 - \sigma_0^2 = 0. \tag{2.69}$$

2.2.5.3 Comparison between the von Mises and Tresca yield conditions

Both the von Mises and Tresca yield conditions are widely used for plasticity of metals. Fig. 2.7 shows the difference of the two yield functions in 2D biaxial principal stress state. As it is illustrated, the Tersca yield condition is engulfed

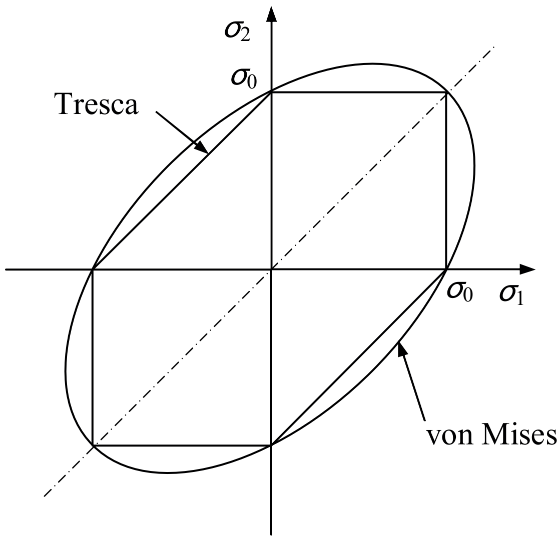

Figure 2.7: von Mises and Tresca yield conditions in biaxial stress states.

with the von Mised yield function. The maximum difference between the two yield functions is 15.5% for any possible stress states [24].

From limit analysis point of view, the former is stated as one nonlinear function in principal stress space, while the latter can be described as three linear functions. Thus, the von Mises function requires less constraints to be described. However, its disadvantage is that the function is nonlinear, whereas the Tresca yield functions are linear. In some cases, such as plane strain condition in biaxial stress state, both functions have an identical form as mentioned before in Eqs. (2.68) and (2.61).

2.2.6 Principle of Virtual Work and Complementary Virtual Work

For rigid-perfectly plastic material, the principles of virtual work and complementary of virtual work is also valid. These principles will be explained in this section.

2.2.6.1 Principle of virtual work

The principle of virtual work exhibits the equilibrium between the external forces applied on the structure and the internal stress field in the body. It demonstrates that the virtual work done by a possible statically admissible stress filed $\boldsymbol{\sigma}$ on any virtual strain filed $\delta\boldsymbol{\epsilon}$ equals the virtual work done by the external forces ($\mathbf{q}$, $\mathbf{g}$) (defined in section 2.2.1.1) on the virtual displacements $\delta\mathbf{u}$ associated with the virtual strains. That is

$$\int_V \boldsymbol{\sigma}\delta\boldsymbol{\epsilon}\mathrm{d}V = \int_{S_t} \mathbf{q}\delta\mathbf{u}\mathrm{d}S_t + \int_V \mathbf{g}\delta\mathbf{u}\mathrm{d}V. \tag{2.70}$$

The principle of virtual power can also be written based on the above equations by substituting virtual strain filed $\delta\boldsymbol{\epsilon}$ and virtual displacement $\delta\mathbf{u}$ by kinematically admissible strain rates $\dot{\boldsymbol{\epsilon}}$ and velocities $\dot{\mathbf{u}}$, respectively. Therefore,

$$\int_V \boldsymbol{\sigma}\dot{\boldsymbol{\epsilon}}\mathrm{d}V = \int_{S_t} \mathbf{q}\dot{\mathbf{u}}\mathrm{d}S_t + \int_V \mathbf{g}\dot{\mathbf{u}}\mathrm{d}V. \tag{2.71}$$

2.2.6.2 Principle of complementary virtual work

The principle of complementary virtual work states that the internal complementary virtual work done by any possible virtual stresses on the kinematically admissible strains is equal to the external complementary virtual work done by the associated virtual forces on the displacements. Considering the fact that virtual forces are zero on the part S_t which has prescribed forces, thus, we can write

$$\int_V \boldsymbol{\epsilon}\delta\boldsymbol{\sigma}\mathrm{d}V = \int_{S_u} \mathbf{u}_0\delta\mathbf{q}\mathrm{d}S_u + \int_V \mathbf{u}\delta\mathbf{g}\mathrm{d}V. \tag{2.72}$$

, where $\mathbf{u}_0$ denotes the defined kinematic boundary on S_u. The principle of complementary virtual work is also known as principle of virtual forces. The principle of complementary virtual power can also be derived as

$$\int_V \boldsymbol{\epsilon}\dot{\boldsymbol{\sigma}}\mathrm{d}V = \int_{S_u} \mathbf{u}_0\dot{\mathbf{q}}\mathrm{d}S_u + + \int_V \mathbf{u}\delta\dot{\mathbf{g}}\mathrm{d}V. \tag{2.73}$$

that describes the works in terms of stress and force rates.

2.2.7 Plastic Limit Analysis

Plastic limit analysis has widely been used by researchers in engineering mechanics. The main purpose of the limit analysis is finding the value of the limit load and its associated safety factor known as limit load multiplier in plastic limit analysis. It can briefly be described as follows. Consider a rigid-perfectly plastic material under the external load distribution of $(\mathbf{q}, \mathbf{g})$. This external load is governed by a proportional load multiplier α and can be written as $\alpha(\mathbf{q}_0, \mathbf{g}_0)$, where $(\mathbf{q}_0, \mathbf{g}_0)$ shows the reference loads. When α is small, the deformations are assumed to be small (which are neglected) and no plastic deformations are occurred. As α increases, some yielding occurs at some point in the structure; however, it is not enough to cause the collapse of the structure. By increasing the load multiplier, the plastic areas are developed in the structure, and finally at some value of the load multiplier, known as the collapse or limit load multiplier, α^{col}, the structure collapses. This process can be depicted by the well-known classical Prandtl's punch problem. Consider a semi-infinite rigid plastic medium under a uniformly distributed vertical force of 2α. Fig. 2.8 shows the geometry and loading of this problem. The plane strain condition and Tresca yield function were adopted. The associated theoretical mechanism is plotted in Fig. 2.9 [24]. By increasing the loads, plastic regions start to develop at the points A and B. However, due to the material rigidity between these local plastic regions, any plastic deformation in the plastic regions are ruled out. As the load increases, the plasticity develops under the load. When the plastic region extends below the entire loading area, the indentation happens and collapse occurs. The plastic area development is plotted in Fig. 2.10, where the plasticity is shown by the reduction in elastic modulus. Due to the symmetric nature of the problem, only the right half is shown. As the load multiplier increases, the plastic zone develops (stages a-l) until the collapse occurs at stage l.

The purpose of the limit analysis is finding the collapse load multiplier and its associated collapse load.

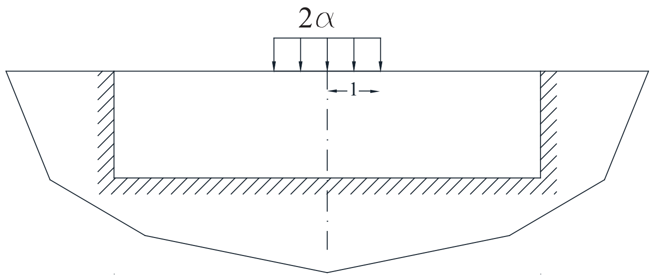

Figure 2.8: Prandtl's punch problem - geometry and loading

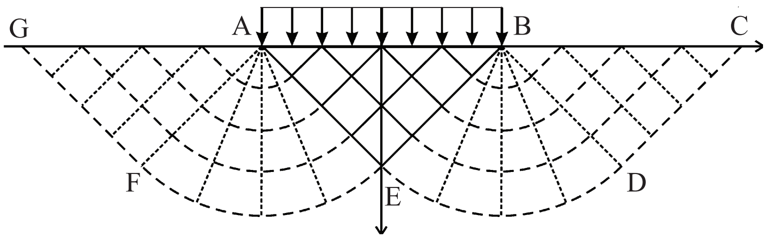

Figure 2.9: The theoretical collapse mechanism for the Prandtl's punch problem

2.2.8 Static Theorem (Lower Bound Theorem)

Any load multiplier α is called a static admissible solution provided that the associated stress field $\boldsymbol{\sigma}^s$ in the body and the force field $\alpha^s(\mathbf{q}_0,\ \mathbf{g}_0)$ applied on the structures satisfy the equilibrium equations

$$\begin{aligned} \nabla\boldsymbol{\sigma}^s + \alpha^s\mathbf{g}_0 = 0 \qquad &\text{in} \quad V, \\ \boldsymbol{\sigma}^s\mathbf{n} = \alpha^s\mathbf{q}_0 \qquad &\text{on} \quad S_t \end{aligned} \tag{2.74}$$

and the yield condition (i.e yield conformity)

$$f(\boldsymbol{\sigma}^s, \kappa) \leq 0. \tag{2.75}$$

at any point in the structure.

The static theorem states that any static admissible limit load multiplier is either less than or equal to the true plastic collapse load multiplier of the structure. That

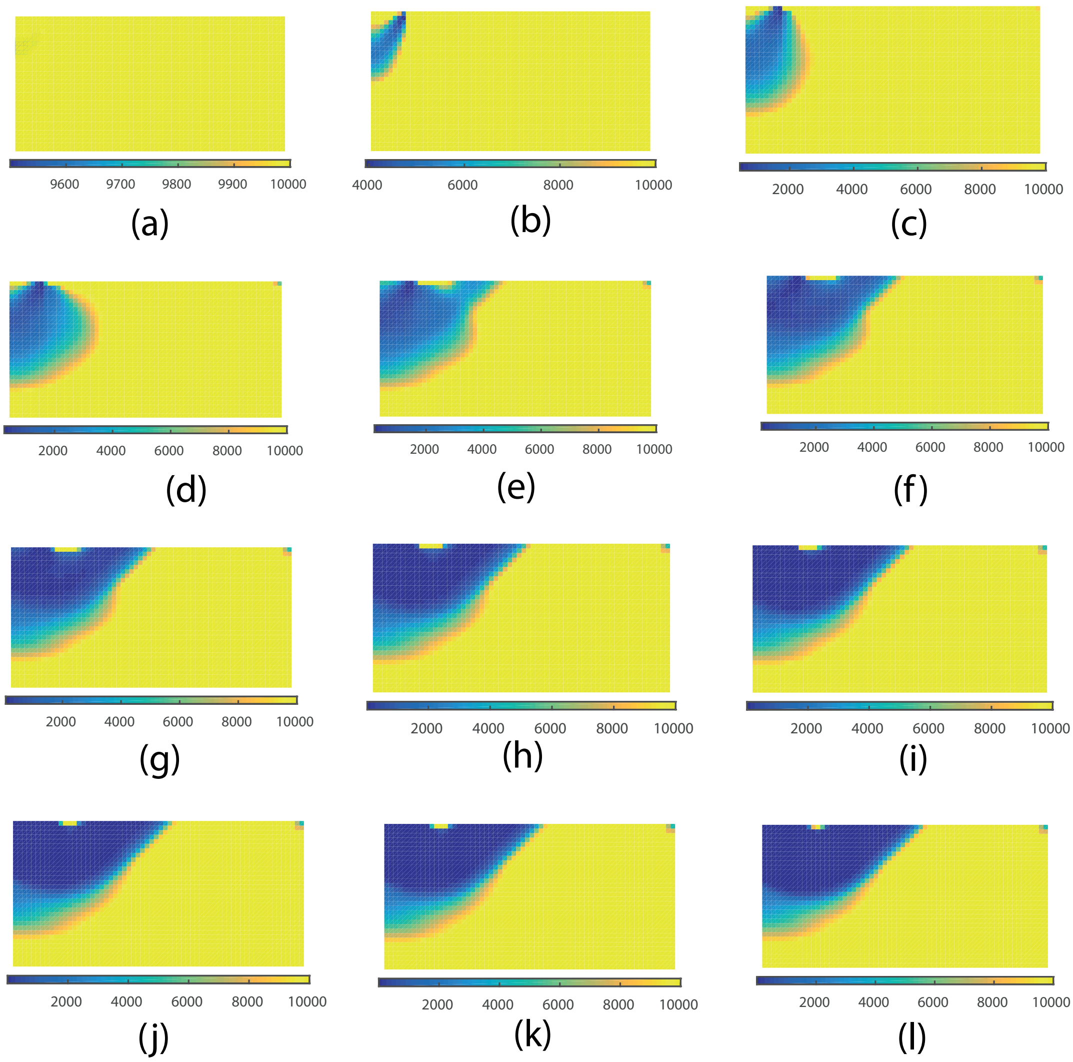

Figure 2.10: The development of plasticity for the Prandtl's punch problem

is,

$$\alpha^s \leq \alpha^{\text{col}}. \tag{2.76}$$

In other words, the collapse load multiplier that is obtained from any collapse mode other than the true one, can be considered conservative when the structure satisfies the equilibrium and yield conformity.

Eq. (2.76) can be proved by applying the principle of virtual power (mentioned in section 2.2.6.1) on a structure where the actual stress $\boldsymbol{\sigma}$ in the body is in equilibrium with the collapse load $\alpha^{\text{col}}(\mathbf{q}_0, \mathbf{g}_0)$. This leads to

$$\int_V \boldsymbol{\sigma}\dot{\boldsymbol{\epsilon}}\mathrm{d}V = \alpha^{\text{col}} \left(\int_{S_t} \mathbf{q}_0 \dot{\mathbf{u}} \mathrm{d}S_t + \int_V \mathbf{g}_0 \dot{\mathbf{u}} \mathrm{d}V \right) \tag{2.77}$$

, where $\dot{\boldsymbol{\epsilon}}$ and $\dot{\mathbf{u}}$ are the kinematically admissible actual strain and displacement rate fields (defined in section 2.2.2.2), respectively. In a similar manner, considering a statically admissible stress field satisfying the yield condition and the force field of $\alpha^s(\mathbf{q}_0, \mathbf{g}_0)$, the principle of virtual power can be written as

$$\int_V \boldsymbol{\sigma}^s\dot{\boldsymbol{\epsilon}}\mathrm{d}V = \alpha^s \left(\int_{S_t} \mathbf{q}_0 \dot{\mathbf{u}} \mathrm{d}S_t + \int_V \mathbf{g}_0 \dot{\mathbf{u}} \mathrm{d}V \right). \tag{2.78}$$

Subtracting Eq. (2.77) from Eq. (2.78) leads to

$$\int_V (\boldsymbol{\sigma} - \boldsymbol{\sigma}^s)\dot{\boldsymbol{\epsilon}}\mathrm{d}V = \left(\alpha^{\text{col}} - \alpha^s\right) \left(\int_{S_t} \mathbf{q}_0 \dot{\mathbf{u}} \mathrm{d}S_t + \int_V \mathbf{g}_0 \dot{\mathbf{u}} \mathrm{d}V \right). \tag{2.79}$$

Considering the convexity of the yield surface and the normality rule, which states that the plastic strain increments vector must coincide with the outward normal vector of the yield surface [24], we can write

$$(\boldsymbol{\sigma} - \boldsymbol{\sigma}^s)\dot{\boldsymbol{\epsilon}} \geq 0, \tag{2.80}$$

at every point in the body. Eq. (2.80) is obvious from the Fig. 2.11, as the angle ϕ between the vectors $(\boldsymbol{\sigma} - \boldsymbol{\sigma}^s)$ and $\dot{\boldsymbol{\epsilon}}$ cannot be larger than 90°. Larger angles

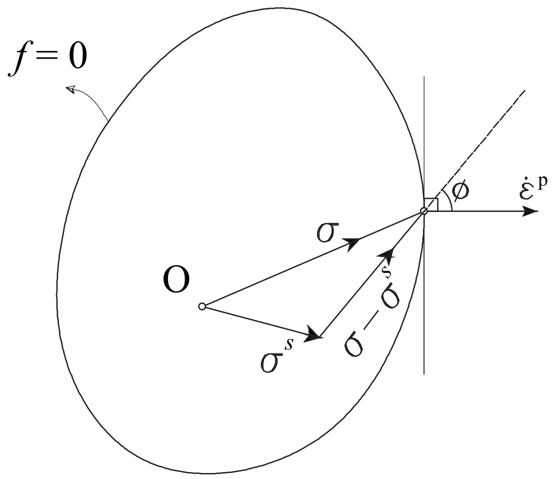

Figure 2.11: Convexity of the yield surface and normality rule - lower bound theorem

contradict either the convexity of the yield surface or the normality rules (Fig. 2.12).

Consequently, the right hand side of the Eq. (2.79) should also be positive, i.e.

$$\left(\alpha^{\mathrm{col}} - \alpha^{s}\right)\left(\int_{S_t} \mathbf{q}_0 \dot{\mathbf{u}} \mathrm{d}S_t + \int_V \mathbf{g}_0 \dot{\mathbf{u}} \mathrm{d}V\right) \geq 0. \tag{2.81}$$

Here, the second bracket shows the work done by the external loads on the displacement rates of the body and cannot be negative by its definition. As a result, the Eq. (2.76) is proved.

2.2.9 Kinematic Theorem (Upper Bound Theorem)

Any load multiplier α^k is called a kinematically admissible load multiplier if it satisfies

$$\alpha^k \left(\int_{S_t} \mathbf{q}_0 \dot{\mathbf{u}}^k \mathrm{d}S_t + \int_V \mathbf{g}_0 \dot{\mathbf{u}}^k \mathrm{d}V\right) \geq \int_V \boldsymbol{\sigma}^k \dot{\boldsymbol{\epsilon}}^k \mathrm{d}V, \tag{2.82}$$

and

$$\int_{S_t} \mathbf{q}_0 \dot{\mathbf{u}}^k \mathrm{d}S_t + \int_V \mathbf{g}_0 \dot{\mathbf{u}}^k \mathrm{d}V \geq 0 \tag{2.83}$$

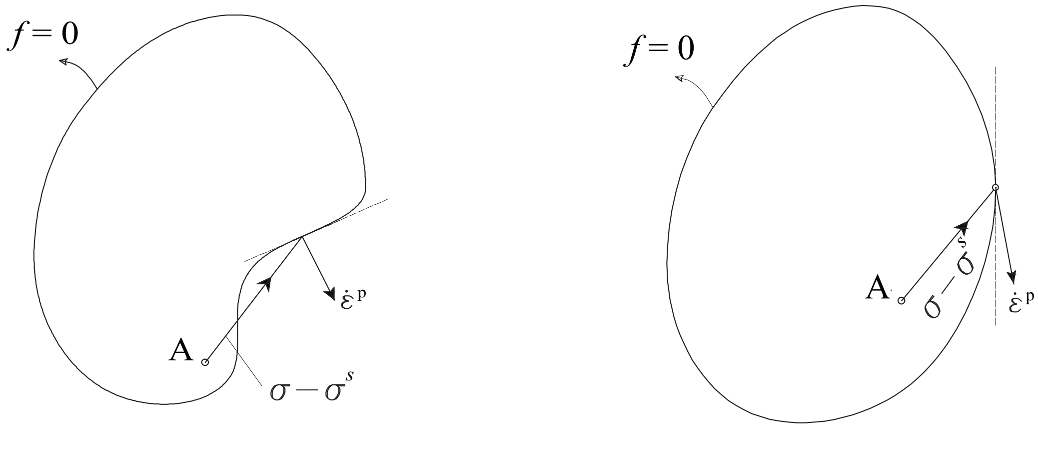

(a) (b)

Figure 2.12: Contradictory examples (a) lack of convexity of the yield surface (b) lack of normality rule

, where $\dot{\boldsymbol{\epsilon}}^k$ and $\dot{\mathbf{u}}^k$ are the kinematically admissible plastic strain rate and velocity, respectively., which are defined in section 2.2.2.2. $\boldsymbol{\sigma}^k$ is the stress field associated with $\dot{\boldsymbol{\epsilon}}^k$ and meets yield conformity anywhere in the domain.

The kinematic theorem states that any kinematically admissible load multiplier is either greater than or equal to the collapse load multiplier

$$\alpha^k \geq \alpha^{\mathrm{col}}. \tag{2.84}$$

In other words, the true collapse load multiplier is the smallest value between all the load multipliers obtained from all the possible cases of the collapse mechanisms for the structure.

Inequality (2.84) can be proved by applying the principal of virtual power (section 2.2.6.1) for an arbitrary kinematically admissible strain rate $\dot{\boldsymbol{\epsilon}}^k$ and velocity $\dot{\mathbf{u}}^k$. Considering the actual stress field as $\boldsymbol{\sigma}$ which maintains equilibrium with the plastic limit load, we can write

$$\alpha^{\mathrm{col}}\left(\int_{S_t} \mathbf{q}_0 \dot{\mathbf{u}}^k \mathrm{d}S_t + \int_V \mathbf{g}_0 \dot{\mathbf{u}}^k \mathrm{d}\,V\right) = \int_V \boldsymbol{\sigma}\dot{\boldsymbol{\epsilon}}^k \mathrm{d}\,V. \tag{2.85}$$

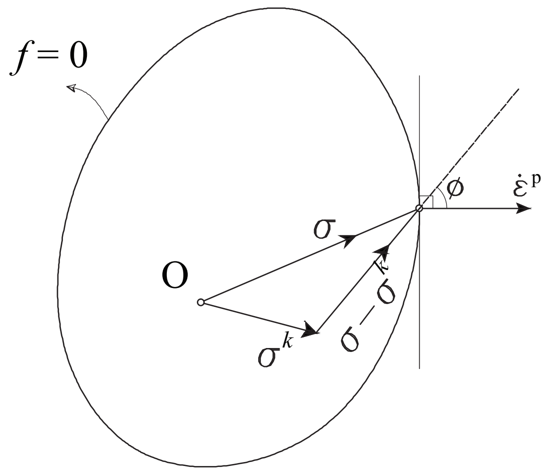

Figure 2.13: Convexity of the yield surface and normality rule - upper bound theorem

Subtracting Eq. (2.82) from Eq. (2.85) results in

$$\left(\alpha^k - \alpha^{\mathrm{col}}\right)\left(\int_{S_t} \mathbf{q}_0 \dot{\mathbf{u}}^k \mathrm{d}S_t + \int_V \mathbf{g}_0 \dot{\mathbf{u}}^k \mathrm{d}\,V\right) \geq \int_V (\boldsymbol{\sigma}^k - \boldsymbol{\sigma})\dot{\boldsymbol{\epsilon}}^k \mathrm{d}\,V. \tag{2.86}$$

By the convexity of the yield function and the normality rule, we can write

$$(\boldsymbol{\sigma}^k - \boldsymbol{\sigma})\dot{\boldsymbol{\epsilon}}^k \geq 0, \tag{2.87}$$

as can be seen from Fig. 2.13. Consequently, the following relation can be obtained

$$\left(\alpha^k - \alpha^{\mathrm{col}}\right)\left(\int_{S_t} \mathbf{q}_0 \dot{\mathbf{u}}^k \mathrm{d}S_t + \int_V \mathbf{g}_0 \dot{\mathbf{u}}^k \mathrm{d}\,V\right) \geq 0. \tag{2.88}$$

Considering the Eqs. (2.83) and (2.88) the kinematic theorem is proved.

In summary, the limit load multiplier is the largest value among all statically admissible load multipliers and the smallest value among all kinematically admissible load multipliers. Therefore, the following relation can be written

$$\alpha^{\mathrm{col}} = \max \alpha^{\mathrm{s}} = \min \alpha^{\mathrm{k}}. \tag{2.89}$$

It is obvious that there are three ways to calculate the limit load multiplier:

1. find the value satisfying Eq. (2.76), which is a lower bound limit load multiplier.

2. find the value satisfying Eq. (2.84), which is an upper bound limit load multiplier.

3. find the value satisfying Eqs. (2.76) and (2.84) simultaneously, which is a dual value.

The first approach is known as a lower bound scheme. The second one is the upper bound scheme, and the third approach is the basis for establishing a dual formulation of the limit analysis.

2.3 Incremental Nonlinear Finite Element Method

The finite element method (FEM) [28] was initially introduced by practitioners rather that mathematicians using abstract methods. Its concept is based on subdividing the body under the load to some smaller shapes or finer finite dimensions which are so-called “finite elements”. The original body is then reproduced by the assemblage of these finite elements connected at some joints called “nodes”. Fig. 2.14 and Fig. 2.15 illustrate these two concepts for 2D and 3D structures, respectively. The unknown field quantities over the elements can be interpolated in a piece-wise fashion from the known field values at nodes using the “shape functions”. The best field values at nodes is usually obtained through minimizing a function such as total energy. The minimization is done through solving a set of algebraic equations for field variables at nodes. By having the nodal values, and the use of shape functions, the element field quantities, such as stresses and strains, are computed.

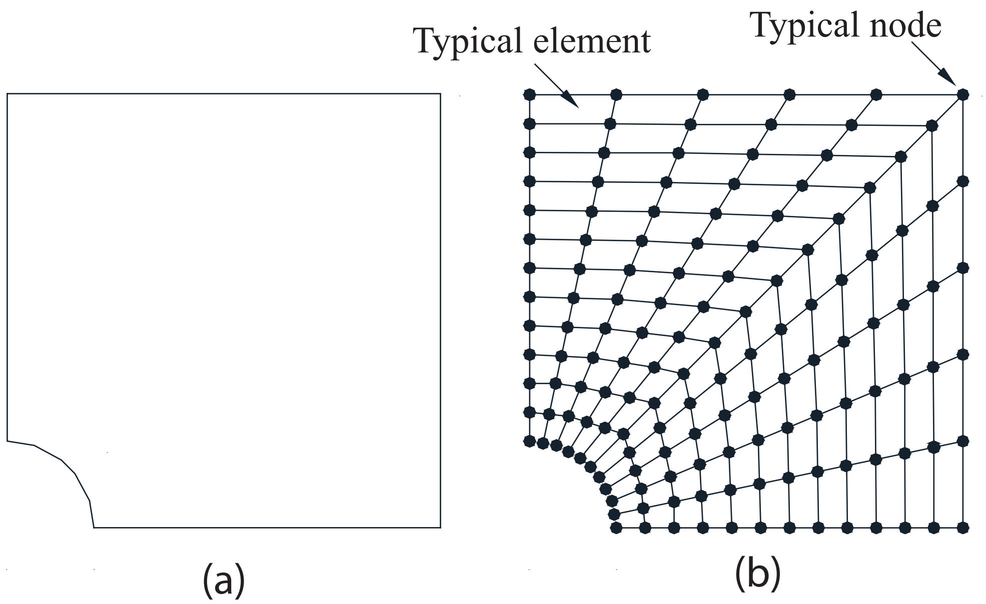

Figure 2.14: A 2D structure (a) geometry (b) the associated FE model

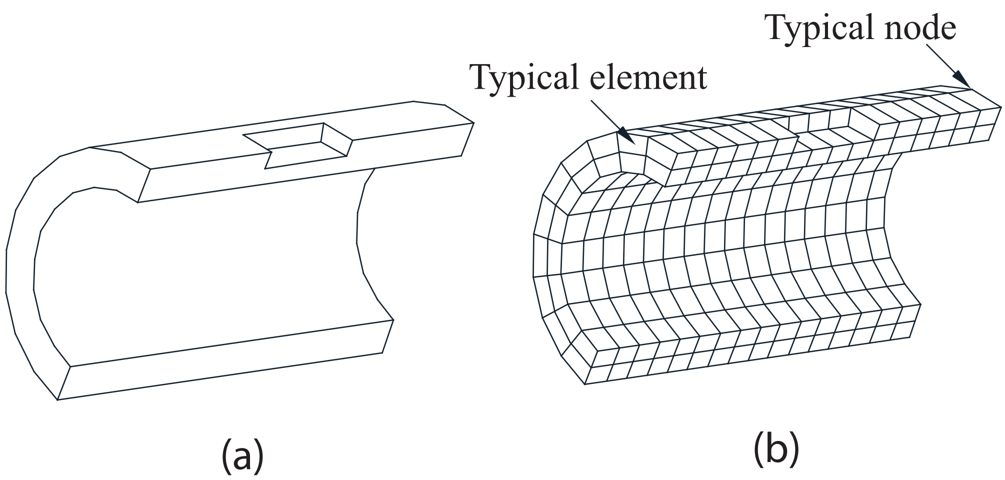

Figure 2.15: A 3D structure (a) geometry (b) the associated FE model

In incremental nonlinear finite element analysis (FEA) [29, 30, 31], the external load is incrementally increased up to failure of the structure. At each load increment, which is known as time step, the equilibrium between the external loads and the internal loads at nodes is satisfied through a series of linear analyses.

The most outstanding feature of the nonlinear FEM is its generality and robustness [29, 30, 31]; for the inelastic problems, due to the nonlinear nature of the problem, the analytical solution is difficult to obtain and for complex cases, such as three-dimensional cases, it is practically impossible to solve. In nonlinear FEM, the material is assumed to be elasto plastic and the hardening and even the softening behavior of the material can be taken into consideration. A complete solution for the monotonic increasing load is determined. The analysis continues until the failure of the structure; the load where the uncontained plastic flow happens is the limit load.

Additionally, one of the most advantageous capabilities of the incremental nonlinear FEA, in comparison to the other limit analysis techniques, is providing useful and comprehensive information on the behavior of the structure up to its failure in a complete package. This information can be important in the design of structures. In particular, a full nonlinear FEA can produce the correct deformations that are needed for designs based on serviceability criteria, whereas some other limit load analysis methods may not be able to provide such accurate information on the deformation of structures.

Aside from the mentioned merits of the method, the incremental nonlinear FEM has its own disadvantages; it is more demanding than its comparable limit analysis technique in terms of computational resources, definition of the material models, and user's knowledge and expertise.

Firstly, the necessity of performing the analysis incrementally and in an iterative manner, due to the dependence of the method on the loading history, makes the incremental nonlinear FEM computationally expensive, specifically for large-size problems (i.e. 3D problems). A high amount of time and computational resources are needed for carrying out the iterations and storage of the intermediate results.

Secondly, the nonlinear FEM is dependent on the sound definition of material properties under all loading conditions and the exact inelastic flow rule. The material constitutive relationship should be precisely defined before the analysis. At initial stages of the design, this may not be the case.

Convergence of the solution could also be burdensome in some cases. As the solution approaches the limit load, achieving the convergence becomes more and more difficult by spreading the plastic zone in the structure. A large load step may produce convergence failure and lead to sudden changes in the load deflection curve. There are some guidelines for the proper definition of convergence criteria and tolerances, but the user's experience and expertise are usually needed for obtaining a good solution.

The mentioned drawbacks of the incremental nonlinear FEM motivated the researchers to develop simplified approaches to find the limit load solutions. These simplified solutions contain two general methods; the classical limit analysis based on mathematical programming and methods based on linear elastic analyses.

2.4 Classical Limit Analysis by Mathematical Programming

By combining the mathematical programming method and finite element method, the classical limit analysis [32, 33, 8] was developed based on the lower and upper bound theorems mentioned in sections 2.2.8 and 2.2.9, respectively. The classical limit analysis can be divided into two groups based on the type of the mathematical programming method used. The first approach is to use a linearized yield function and treat the limit analysis problem as a linear programming (LP) method [8]. The other approach is the nonlinear programming (NLP) method, which utilizes the nonlinear yield condition and higher order approximations for the stress and velocity fields. In both cases, the numerical formulation of the limit analysis is described as an optimization problem. In this problem, the objective function is either maximized or minimized subjected to some equality and inequality constraints. In the following, this optimization problem under both static and kinematic approaches are formulated.

2.4.1 Static Limit Analysis

The static limit analysis is formulated as finding the maximum load multiplier, α, such that the equilibrium (Eq. (2.74)) and yield condition (Eq. (2.75)) are simultaneously satisfied. That is

$$\begin{gathered} \alpha^{\mathrm{col}} = \max \alpha \\ \text{subject to} \\ \nabla \boldsymbol{\sigma} + \alpha \mathbf{g}_0 = 0 \qquad \text{in} \quad V, \\ \boldsymbol{\sigma} \mathbf{n} = \alpha \mathbf{q}_0 \qquad \text{on} \quad S_t \\ f(\boldsymbol{\sigma}, \kappa) \leq 0. \end{gathered} \tag{2.90}$$

2.4.2 Kinematic Limit Analysis

In case of the limit load analysis, the Eq. (2.71) can be written in the following form

$$\alpha \left(\int_{S_t} \mathbf{q} \dot{\mathbf{u}} \mathrm{d} S_t + \int_V \mathbf{g} \dot{\mathbf{u}} \mathrm{d}\, V \right) = \int_V \boldsymbol{\sigma} \dot{\boldsymbol{\epsilon}} \mathrm{d}\, V = \int_V D \left(\dot{\boldsymbol{\epsilon}} \right) \mathrm{d}\, V. \tag{2.91}$$

, where $D\left(\dot{\boldsymbol{\epsilon}}\right)$ is the energy dissipation function related to $\dot{\boldsymbol{\epsilon}}$. Therefore

$$\alpha = \frac{\int_V D\left(\dot{\boldsymbol{\epsilon}}\right) \mathrm{d}\, V}{\int_{S_t} \mathbf{q} \dot{\mathbf{u}} \mathrm{d} S_t + \int_V \mathbf{g} \dot{\mathbf{u}} \mathrm{d}\, V}. \tag{2.92}$$

The kinematically admissible fields $\dot{\boldsymbol{\epsilon}}$ and $\dot{\mathbf{u}}$ can be normalized such that

$$\int_{S_t} \mathbf{q}\dot{\mathbf{u}}\mathrm{d}S_t + \int_V \mathbf{g}\dot{\mathbf{u}}\mathrm{d}V = 1. \tag{2.93}$$

The kinematic limit analysis can be formulated as finding the maximum limit load multiplier α based on Eqs. (2.92) and (2.93) such that $\dot{\boldsymbol{\epsilon}}$ and $\dot{\mathbf{u}}$ satisfies the kinematic equation and the kinematic boundary conditions mentioned in section 2.2.2.2 [23]. That is

$$\begin{gathered}
\alpha^{\mathrm{col}} = \min \alpha \\
\text{subject to} \\
\int_{S_t} \mathbf{q}\dot{\mathbf{u}}\mathrm{d}S_t + \int_V \mathbf{g}\dot{\mathbf{u}}\mathrm{d}V = 1 \\
\dot{\mathbf{E}}_{ij} = \frac{1}{2}\left(\frac{\partial \dot{\mathbf{u}}_i}{\partial x_j} + \frac{\partial \dot{\mathbf{u}}_j}{\partial x_i}\right) \qquad \text{in} \quad V \\
\dot{\mathbf{u}} = 0 \qquad \text{on} \quad S_u.
\end{gathered}$$

Recent works [34, 35, 36, 37, 38] have been done to overcome the limitations underlying the classical limit analysis (viz. the main ones being rigid perfect plasticity, associativity and small deformations). The focus is on the development of a so-called extended approach that can tackle various nonstandard conditions underpinning practical engineering applications. For instances, the inclusion of elastoplastic (strain hardening and/or softening) material properties [34, 35] and/or geometric nonlinearity of structures [39] has been furnished through the formulations and solutions of a challenging (nonconvex and/or nonsmooth) mathematical programming problem with equilibrium constraints [40]. Moreover, the limit analysis of structures with non-associative constitutive responses (e.g. Coulomb's frictional contacts and cohesive fracture interfaces) has been presented in [41, 42, 43, 36, 37, 38].

Despite of its popularity and maturity within research communities over decades, the classical limit analysis does not gain much of interest from practitioners.

This is mainly due to their lack of familiarity of the classical limit analysis model construction within a generic mathematical programming framework. Furthermore, this method is usually applied to 2D problems and relatively simple 3D problems due to the computational time and resources required. This motivates the use of iterative methods based on the linear analysis.

2.5 Iterative Methods Based on the Linear Elastic Analysis

The iterative methods based on the linear elastic analysis are simplified methods which uses the finite element analysis and a series of the linear elastic analysis. In these methods, the effect of the plastic flow on the stiffness of the structure is considered by altering the elastic moduli of elements. Hence, these methods are often known as elastic modulus adjustment procedures (EMAPs)

EMAP was firstly introduced by Jones and Dhalla [44] for the classification of clamp-induced stresses in thin-walled strait pipes. The method was named adjusted secant for piping (ASP), as the inelastic effects in pipes are simulated by a modified secant modulus of material. The key purpose of the ASP is to discern trends of the simulated inelastic response near structural discontinuities, so that the discontinuity of stresses can be properly classified to satisfy the requirement of the American society of mechanical engineers (ASME) code [45].

Marriott [46] modified ASP to estimate the lower bound limit load. He mentioned the modulus adjustment technique by the finite element analysis generates a statically admissible stress field which can be used for lower limit load approximations. In this scheme, the first elastic analysis at the first iteration, $r = 1$, adopts the initial given elastic modulus of the material for all elements. In the next iteration, $r+1$, all the elements whose stress intensities, (SI), sit above the ASME code allowable stress (S_m), are selected and their elastic moduli are adjusted according to

$$E_i^{r+1} = E_i^r \times \frac{S_m}{SI_i} \tag{2.94}$$

, where E_i^{r+1} is the modified elastic modulus of the element i. The process is repeated until the maximum stress intensity converges to some value which can be less or greater than S_m. The load multiplier at each iteration, α^r, can be obtained as

$$\alpha^r = \frac{\sigma_0}{\sigma_{\max}^r} \tag{2.95}$$

, where σ_0 is the yield stress, and $\sigma_{\max}^r$ represents the maximum equivalent stress at iteration r.

Marriott showed that the mentioned procedure leads to a distribution of stresses which does not entirely characterize the actual stress distribution happening in the nonlinear analysis; however, it could be used to approximate the inelastic solutions.

The advent of EMAP enabled engineers to simulate the nonlinear solution of large-size problems with limited computing resources. This is the key reason that EMAP has attracted much interest from researches. So far, a number of EMAPs have been developed which can be classified as the following four groups.

(1) Stress classifications; this includes the ASP method and Marriott's procedure, which were introduced for stress classifications.

(2) Local inelastic analysis; this covers the problems with local plasticity, such as the approximation of stress and strains at notches. The related EMAPs are the generalized local stress and strain (GLOSS) method by Seshadri et al. [47, 48, 49] and the modulus adjustment and redistribution of stress (MARS) method by Babu [50, 51]. In these schemes, the elastic moduli of the elements sitting above the yield stress are systematically modified through some iterations.

(3) Limit analysis; the EMAPs for limit analysis include GLOSS R-node method, the variational m_α multiplier technique and the elastic compensation method.

(4) Shakedown and ratchet analysis; this includes the methods introduced by Mackenzie and Boyle [52] and Mackenzie et al. [53]. Further development of these

methods is made by Ponter et al. and Chen and Ponter [15, 54, 55, 56, 57, 58, 59].

As the focus of this research is on the limit analysis by iterative methods, all the major EMAPs for the determination of the limit load are explained in follows.

2.5.1 R-Node Method

2.5.1.1 General concept

Seshadri et al. [48, 60] suggested a procedure based on the elastic moduli adjustment procedures which uses the concept of r-nodes, from the creep design, rather than the lower bound theorem to obtain the limit load. The r-node method is based on two linear analyses. In first elastic analysis, the stress of all elements are obtained based on the specific material properties of the structure. Next, the elastic moduli of all elements will be individually modified such that the stresses are scaled to an arbitrary stress. In the second analysis, the new equivalent stresses for all elements are computed; those elements whose equivalent stresses remain unchanged during the two analysis are treated as r-nodes and are statistically determinate. The r-node stresses are then considered as reference stresses and associated with the limit load of the structure.

2.5.1.2 Redistribution nodes and plastic collapse

In creep solution of beams, Schulte [61] noticed that as the solution progressed from the initial elastic stage to the final plastic stage, there are some points in the cross section at which the stress hardly varies. Marriott and Leckie [62] named these locations as “skeletal points”. Seshadri and Marriott [63] later extended the skeletal point concept to a more general inelastic material behavior and showed that the skeletal points can be thought of as nodes of the redistribution of stresses (r-nodes). The r-node stresses can be considered load controlled and are statically determinate. When plastic stage occurs, which involves the entire cross section, the stress at r-nodes remain constant while the stress at other statically indeterminate

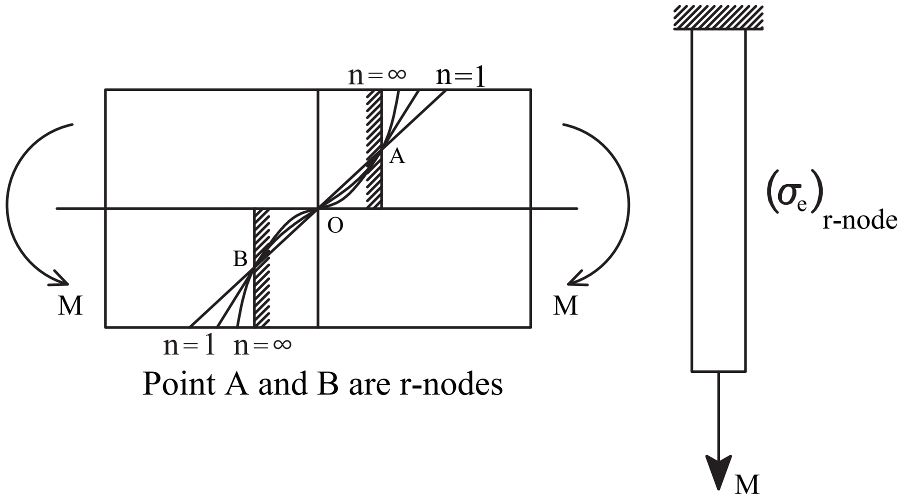

Figure 2.16: R-nodes in a beam subjected to bending.

points undergo a redistribution.

Consider a beam which is subjected to a bending moment, where the stress-strain relationship of the material is given by

$$\epsilon = B\sigma^n. \tag{2.96}$$

Here, B and n are material parameters, where $n = 1$ represents the elastic stage and $n \to \infty$ corresponds to perfect plasticity. Fig. 2.16 shows different stress distributions for various values of n. R-nodes can be designated from the intersection of stress distributions for $n = 1$ and $n \to \infty$. The stress distributions for all other points pass through the r-nodes. The r-nodes can be considered by a uniaxial bar with the given material properties.

As the stresses of r-nodes (i.e. $(\sigma_e)_{r-node}$) are statically determinate, they are proportional to the applied loads (P). That is

$$(\sigma_e)_{r-node} = \gamma P \tag{2.97}$$

, where γ is the constant of proportionality. The collapse happens when the stress at r-nodes reaches the yield stress. i.e.

$$\sigma_0 = \gamma P_L \tag{2.98}$$

, where σ_0 is the yield stress and P_L represents the limit load. Therefore, the limit load can be obtained as

$$P_L = P\frac{\sigma_0}{(\sigma_e)_{r-node}} \tag{2.99}$$

For structures which need multiple plastic hinges to be formed in order to collapse, a multi-bar model can be employed to simulate the collapse process. The model allows the loads to be transferred to proper bars until the collapse occurs. The combined r-node effective stress, $\bar{\sigma}_n$, is defined as

$$\bar{\sigma}_n = \frac{\sum\limits_{j=1}^{N} \sigma_{nj}}{N} \tag{2.100}$$

, where σ_{nj} is the j^{th} r-node stress and N is the number of r-nodes. The limit load, therefore, can be obtained as

$$P_L = P\frac{\sigma_0}{\bar{\sigma}_n}. \tag{2.101}$$

2.5.1.3 Limit load determination using r-nodes method

The r-node method can be implemented as follows [64].

- A linear elastic analysis for a given load is performed based on the specific material properties.

- The elastic moduli of all the elements are modified according to the following equation

  $$E_e = E_0\frac{\sigma_{arb}}{\sigma_e} \tag{2.102}$$

  , where E_e is the new elastic modulus of the element e and E_0 is the initial elastic modulus of all the elements. σ_{arb} is an arbitrary nonzero value and σ_e is the equivalent stress of the element.

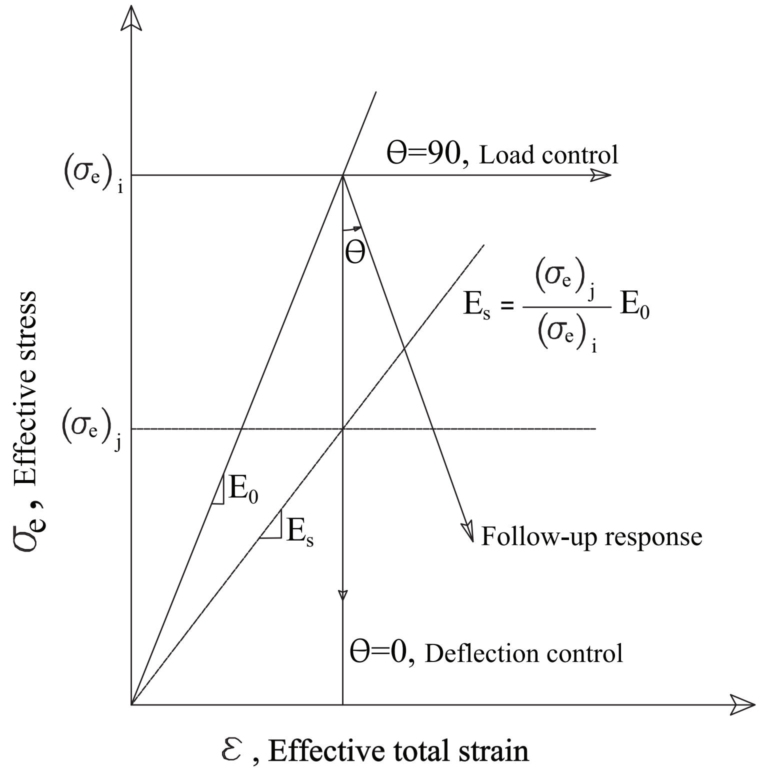

Figure 2.17: The GLOSS diagram [1].

- The second linear analysis is carried out using the modified elastic moduli of the elements.
- Based on the two analyses, the follow up angle θ on the GLOSS diagram can be determined for each element (Fig. 2.17). R-nodes are the elements whose associated follow up angles is 90 degrees.
- The r-node stresses are then treated as reference stresses. The effective r-node stress is determined from Eq. (2.100) and the limit load of the structure is obtained from Eq. (2.101).

2.5.1.4 Discussion of the R-node method

Although the conceptual model for r-nodes has been developed by Mangalaramanan [65], the concept of r-nodes in creep design and its extension in the limit analysis is not fully understood [2, 12]. The R-node detection is generally straightforward for a simple structure such as a beam or a cylinder; however, for more complex structures such as three-dimensional structures, it becomes difficult and is relied on practical experiences. This undermines the robustness of the method and makes the determination of the limit load indirect.

2.5.2 m_α Multiplier Method

To remove the hassles of the r-node method for more complex structures, Seshadri and Mangalaramanan [2] proposed the m_α multiplier method based on the variational theorem of Mure et al. [66]. As stated before, yield conformity necessitates the statically admissible stress field to lie inside the yield surface. Mure et al. made this constraint more straightforward by introducing the concept of "integral mean of yield" into the variational theorem. This allows the stress distributions to be used for estimating the upper and lower bounds of the limit load. The "integral mean of yield" is written as

$$\int_V \mu^0 \left(f(s_{ij}^0) + \left(\phi^0\right)^2 \right) dV. \tag{2.103}$$

Here, s_{ij}^0 is the deviatoric tensor (defined in 2.2.1.3) related to the statically admissible stress field and $\mu^0 \geq 0$. ϕ^0 is a point function which assumes to be zero at yield and a positive value below yield. By satisfying Eq. (2.103) and through implementing variational principles, lower bound and upper bound multipliers, namely m' and m^0 respectively, can be obtained using two linear elastic analyses. The first elastic analysis corresponds to a conventional linear elastic analysis based on the uniform material properties of the structure. The second linear analysis involves the modifications on the elastic modulus of all elements based on the following formulation:

$$\left(E_s\right)_e = E_0 \left(\frac{\sigma_{arb}}{\sigma_e} \right)^q \tag{2.104}$$

, where $\left(E_s\right)_e$ is the new elastic modulus of the element e and E_0 is the initial elastic modulus of all the elements. σ_{arb} is an arbitrary nonzero value and σ_e is the equivalent stress of the element. q is the modulus adjustment parameter and normally is taken as 1, but can be less than 1 in case of sensitive pressure components. The upper and lower bound multipliers can be obtained as follows

$$m^0 = \frac{\sigma_y \sqrt{V}}{\sqrt{\sum\limits_{k=1}^{N} (\sigma_{ek})^2 \Delta V_k}} \tag{2.105}$$

$$m' = \frac{2m^0 \sigma_y^2}{\sigma_y^2 + (m^0)^2 (\sigma_M^0)^2} \tag{2.106}$$

, where k represents the element number and N is the total number of elements. σ_y is the yield stress, σ_{ek} is the effective stress of element k, and σ_M^0 is the maximum equivalent stress in the structure. V is the total volume of structure and ΔV_k shows the volume of element k.

The lower bound multiplier based on Eq. (2.106) will be overestimated when the plastic collapse occurs over a localized region of the structure. This is due to the fact that Eq. (2.106) is based on the total volume of the structure. The corresponding upper bound m' will be consequently underestimated. Seshardi and Mangalaramanan [2] addressed this issue, and defined the new concept of reference volume based on the theorem of nesting surfaces [67, 68]. With the idea of "leap-frogging" to the limit state, they proposed an improved upper bound multiplier which can be obtained based on the following formulation

$$m^0(V_R) = \frac{\sigma_y \sqrt{V_R}}{\sqrt{\sum\limits_{k=1}^{\alpha} (\sigma_{ek})^2 \Delta V_k}} \tag{2.107}$$

, where V_R ($V_R \leq V$) is the reference volume introduced to identify the "kinematically active" portion of the structure participating in the plastic response. The reference volume can be obtained by plotting the variations of m_1^0 and m_2^0 corresponding to the first and second linear elastic analyses (Fig. 2.18). The reference volume is the volume at which the two curves intersects (i.e. $m_1^0(V_R) = m_2^0(V_R)$). α in Eq. (2.107) can be obtained by arranging the elements in the descending order

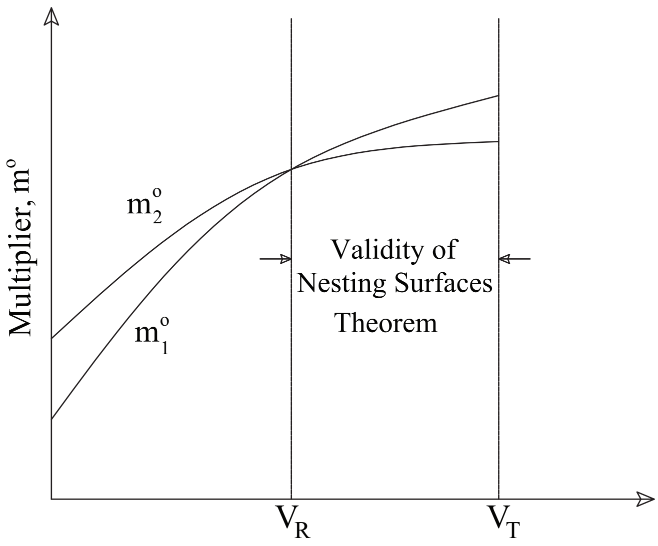

Figure 2.18: Identification of reference volume [2].

of their energy dissipations (i.e. $(\sigma_{ek})^2 \Delta V_k$). α ($\alpha \leq N$) is the number of elements with highest amount of dissipation energy which theoretically satisfy

$$V_R = \sum_{j=1}^{\alpha} \Delta V_k. \tag{2.108}$$

The phrase "m_α method" also refers to the use of these α elements that contributes to the identification of the reference volume.

The m_α multiplier method can also be performed on the basis of iterative iterations, where Eq. (2.104) is used for elastic modulus modifications at each iterations [49]. This allows a better estimation of load multipliers as the number of iterations increase. In this case, the lower bound multiplier at each iteration can be determined as

$$m'(\zeta) = \frac{2m^0(\zeta)\sigma_y^2}{\sigma_y^2 + (m^0(\zeta))^2 (\sigma_M^0(\zeta))^2}. \tag{2.109}$$

, where ζ represents the iteration number. The convergence of the upper and lower bounds within the successive linear elastic iterations is schematically shown in Fig. 2.19.

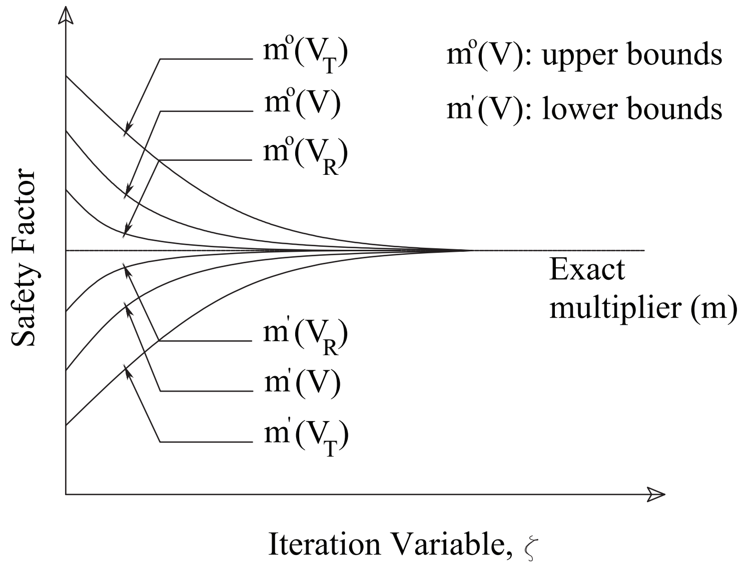

Figure 2.19: Schematic convergence of upper and lower limit load multipliers [2].

2.5.3 Elastic Compensation Method

Meckenzie et al. [13, 69, 11], Nadarajah et al. [70] and Shi et al. [71] developed a straightforward iterative method for the collapse load determination named as the elastic compensation method (ECM). It is based on a series of linear elastic finite element analyses where the elastic moduli of highly stressed elements are reduced and those of low stressed elements are increased.

For a structure with an isotropic homogeneous material with the yield stress of σ_0 under the nominal load set $\boldsymbol{P}_{\rm d}$, initially a finite element model is constructed and a linear elastic analysis is performed as the first iteration (r=1, where r denotes the iteration number). From the stress responses, the maximum equivalent stress (i.e by use of von Mises or Tresca yield criteria) for each element, i, is obtained, namely $\bar{\sigma}_i^r$. A series of linear elastic analyses are then performed where the elastic moduli of elements in the next iterative step (r+1) are adjusted by

$$E_i^{r+1} = E_i^r \frac{\sigma_n^r}{\bar{\sigma}_i^r}, \quad i = 1,\, 2,\, \dots \tag{2.110}$$

, where E_i^r is the elastic modulus of the element i at the current iteration and E_i^{r+1} is the elastic modulus used in the next iteration. σ_n^r is an arbitrary nominal stress

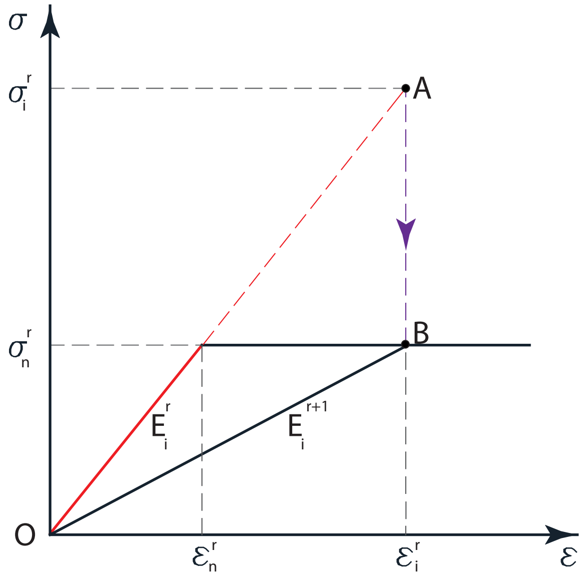

Figure 2.20: Elastic modulus modification in ECM - FSM.

often defined as

$$\sigma_n^r = \frac{\bar{\sigma}_{\max}^r + \bar{\sigma}_{\min}^r}{2} \tag{2.111}$$

, where $\bar{\sigma}_{\max}^r$ and $\bar{\sigma}_{\min}^r$ are the maximum and minimum equivalent stresses within the domain. This modification of the elastic modulus of an element is known as the fixed strain method (FSM) and schematically depicted in Fig. 2.20.

At the end of the iterations, an admissible stress field and a kinematically strain field is produced which can be used with both the lower bound (section 2.2.8) and upper bound (section 2.2.9) theorems as follows.

2.5.3.1 Lower bound limit load

The lower bound limit load requires a statically admissible stress field which satisfies the yield conformity in order to define a lower bound limit load. The ECM generates a series of stress fields which are in equilibrium with external forces. As all the analyses are linear, the algorithm ensures the yield conformity for each analysis iteration by adjusting the applied forces with a load multiplier α^r defined as

$$\alpha^r = \frac{\sigma_0}{\bar{\sigma}_{\max}^r}. \tag{2.112}$$

The ECM is performed for r=1 to a iterations, and it selects the maximum value of load multipliers α^r for all a iterations as the plastic collapse load multiplier, α^{col}. That is

$$\alpha^{\mathrm{col}} = \max(\alpha^r), \quad r = 1,\, 2,\, \ldots, a \tag{2.113}$$

2.5.3.2 Upper bound limit load

To apply the upper bound theorem, the kinematically admissible strain and deformation fields are required. The ECM automatically generates these strain and deformation modes. Recalling the Eq. (2.92), the upper bound collapse load multiplier can be obtained from

$$\alpha = \frac{\int_V \dot{D}\mathrm{d}V}{\int_{S_t} \mathbf{q}\dot{\mathbf{u}}\mathrm{d}S_t + \int_V \mathbf{g}\dot{\mathbf{u}}\mathrm{d}V} \tag{2.114}$$

, where $\dot{D}$ is the increment of plastic dissipation per the unit volume, and for the von Mises yield condition is as follows

$$\dot{D} = \sigma_0 \sqrt{\frac{2}{3}\,(\dot{\epsilon}_1^2 + \dot{\epsilon}_2^2 + \dot{\epsilon}_3^2)}. \tag{2.115}$$

The calculation of the work term can be done by invoking the linear elastic nature of the solution [12]. Since the external work done is equal to the elastic strain energy calculated in the finite element analysis, the upper bound multiplier at each iteration r can be calculated as

$$\alpha^r = \frac{\int_V \dot{D}\mathrm{d}V}{\int_V \boldsymbol{\sigma}\dot{\boldsymbol{\epsilon}}\mathrm{d}V}. \tag{2.116}$$

In a series of a iterations, the best estimate of upper collapse load multiplier is the lowest of upper bound multipliers. That is

$$\alpha^{\mathrm{col}} = \min(\alpha^r), \quad r = 1,\, 2,\, \ldots, a. \tag{2.117}$$

2.5.3.3 Theoretical justifications and discussion

Ponter and Carter [15] provided a more rigorous interpretation of the ECM by implementing a similar scheme to it, where the shear modulus, G, of elements is systematically modified rather than the elastic modulus. They identified an important feature of the procedure for limit analysis. They showed that the mentioned iterative procedure results in a monotonically reducing upper bound which converges to the exact limit load solution for von Mises material, providing an incompressible material is used (i.e. Poisson's ratio is 0.5) and elastic solutions are evaluated exactly. For the finite element solutions, the produced upper bound limit load converges to the least upper bound corresponding to the class of displacement and strain fields permitted by the finite element formulation. In this case and in the sense of the lower bound limit load, the solutions provided by the ECM reported in section 2.5.3.1, are more precisely lower bounds to the upper bounds, namely pseudo-lower bounds.

Additionally, Ponter and Carter added a fresh insight to the nature of iterative process and showed that the strain field corresponding to a spatial variation of the shear modulus can be found from the solution to a nonlinear mathematical programming problem. The difference is that, unlike the computationally expensive mathematical programming methods, there is no need of a search on a global functional; the ECM prescribes an explicit search direction by adjusting the elastic modulus in such a way that the equivalent stresses are factored to some nominal stress.

Although the upper bound collapse load given by the ECM may generally be more accurate (as it is monotonically reducing [15]), the lower collapse load may be of more importance as it is safer (providing that the requirements needed for the lower bound theorem are completely satisfied). Therefore, the implementation of the ECM via the lower bound scheme results in a safe, yet close to the exact collapse load solution. Hence, in this thesis the focus is on the lower bound ECM.

The lower bound ECM reported in section 2.5.3.1 is shown to provide sufficiently accurate results for simple structures, specially for pressure vessels [13, 11, 14]; however, for more complex structures, such as the structures containing flaws, the analyses might abort before a better solution is obtained. This is due to the numerical singularity arising from the excessive increase of the elastic modulus of the elements whose equivalent stresses are approaching zero [16, 17]. In addition, the convergence criterion defined by the ECM is the number of iterations which might not be sufficient. The reason for this definition is the multiple oscillations happening during the iterations. Chen et al. [17] by implementing the Banach's contraction mapping theorem in mathematical analysis discussed the convergence problem of the ECM. They demonstrated that a good limit load solution can be obtained only when iterative elastic modulus adjustments are contraction mappings.

Yang et al. [16] and Chen et al. [17] proposed two modified elastic compensation methods (known as MECM and $\mathrm{K_t}$ECM respectively) which just allow the reduction of the elastic modulus to improve the convergence of the ECM. Therefore, they amended the Eq. (2.110) to

$$E_i^{r+1} = \begin{cases} E_i^r \frac{\sigma_n^r}{\bar{\sigma}_i^r}, & \text{for } \sigma_i^r > \sigma_n^r \\ E_i^r, & \text{for } \sigma_i^r \leq \sigma_n^r \end{cases} \tag{2.118}$$

, where only the elastic moduli of elements whose equivalent stresses are bigger than the nominal stress are decreased; the elastic moduli for the other elements remain unchanged. In addition, they introduced an adjustable factor, λ, to the definition of σ_n^r in order to ensure that only the elastic moduli of highly stressed elements are being modified. The nominal stress is defined as

$$\sigma_n^r = \bar{\sigma}_{\max}^r - \lambda\left(\bar{\sigma}_{\max}^r - \bar{\sigma}_{\min}^r\right), \quad \lambda \in (0,\, 1). \tag{2.119}$$

They asserted that while small value of λ increases the computational precision, it is more time-consuming. On the other hand, a large value of λ may lead to a reduction in accuracy level. Yang et al. suggested $\lambda = 0.4$ for limit analysis of nozzle-to-cylinder junctions [16]. Chen et al. [17] associated λ with the stress concentration factor (K_t) of the structure, which is defined as

$$K_t = \frac{\bar{\sigma}^r_{\max}}{\sigma^r_N} \tag{2.120}$$

, where σ^r_N is the standard nominal stress of the structure. It is usually defined in three forms [17]; (1) the mean stress of the net section at the stress concentration area; (2) the mean stress of the unreduced section; (3) the stress of the associated point away from the stress concentration region. λ is then defined as

$$\lambda = \frac{1}{1 + K_t} \tag{2.121}$$

Yang et al. [16] and Chen et al. [17] showed the modified ECMs can generally give a better estimation of the collapse load for complex structures, specially for structures with flaws. However, they do not completely resolve the oscillation problem; when Eq. (2.121) is used for λ, the lack of a unique definition for the standard nominal stress for a structure leads to different values for λ and, therefore, different collapse loads. In addition, the Eq. (2.121) may produce very small value of λ. In this case, the procedure not only highly increases the computational time, but also might lead to a wrong convergence, as the changes in the associated load multipliers are significantly small too. Yang et al. [16] and Chen et al. [17] also did not consider the condition of incompressibility for their numerical examples. This might not be a major issue for some examples, but can be in highly constraint problems, such as limit analysis for cracked components [12].

For further improving the convergence of the ECM, Adibi-Asl et al. [72] proposed a new scheme for adjusting the elastic moduli in the ECM by implementing the strain energy equilibrium principle [73]. The principle assumes that the strain energy in an element before performing the rth iteration is equal to the sum of the strain

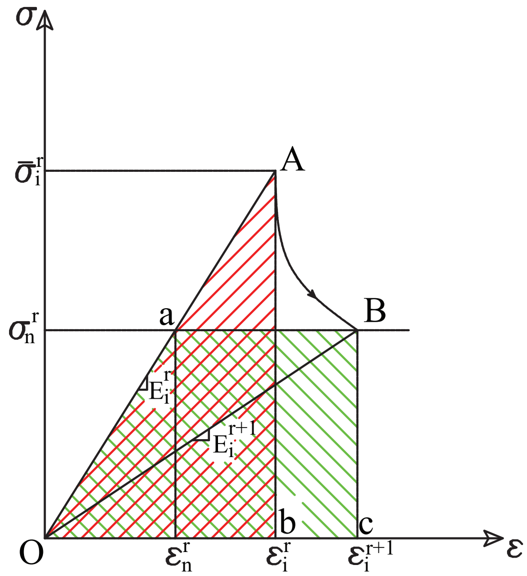

Figure 2.21: Strain energy equilibrium principle scheme.

energies remained and dissipated in the element after the rth iteration (Fig.2.21). Hence, the new point B can be determined by equalizing the area of the triangle AOb with that of the quadrelateral $BaOc$. Therefore, by considering the linear relationships between stresses and strains based on Hook's law (section 2.2.4), the elastic modulus for the elements sitting above the nominal stress can be modified as follows

$$E_i^{r+1} = E_i^r \frac{2\left(\sigma_n^r\right)^2}{\left(\bar{\sigma}_i^r\right)^2 + \left(\sigma_n^r\right)^2}. \tag{2.122}$$

Based on this scheme, Yu and Yang [74] and Yang et al. [75] extended the ECM to shell structures and truss and framed structures, respectively. However, these modified schemes still use the number of iterations, input by the user, as the convergence criterion. As discussed in chapter 1 and in section 1.2, this is due to the oscillations in load multipliers with different amplitudes which might happen during the iterations. These oscillations do not allow the convergence to be defined on limit load solutions. The main reason is rooted in the modification scheme implemented in the ECM; at each iteration, the stiffness of the elements is discretely modified at the individual element level and without considering the contribution of other elements. However, in the next iteration, the stresses are computed with considering the effects of all elements. This causes a discontinuous stress distribution that estimates but never replicates the smooth limit state stress field [12]. This concept will be further investigated in chapter 5 of this thesis.

Another problem associated with the ECM is its inherent degree of over-conservatism when the lower bound scheme is implemented. This is due to the use of the maximum equivalent stress of an element, rather than an averaged equivalent stress, for modification of its elastic modulus. Although this approach satisfies the yield conformity better, it might underestimate the collapse load of the structure. Additionally, the use of the maximum equivalent stress of an element as the stress representative of an element, may even exacerbate the oscillations occurring in load multipliers of the structure. This is due to the fact that the averaged equivalent stress of an element, as a representative of stress filed of the element, is more similar to the smooth stress field within the element than the maximum equivalent stress of the element.

2.6 Concluding Remarks

In the limit analysis, the EMAPs for determination of the collapse load of structures are direct, simple and applicable to complex structures compared to other methods; the incremental nonlinear FEA is costly and laborious and the classical limit analysis is complex for engineers without the mathematical programming familiarity. Among the EMAPs for the limit analysis, the ECM provides a better lower bound performance than the r-node method and is simpler than the m_α- method. Therefore, there are adequate incentives for further development of ECM, not only to extend its applications to other structures through automated mesh generation scheme, but also to improve the basic formulation of the method.

The following chapter provides a detailed implementation of the modified elastic compensation method (MECM). In particular, the well-known FEM is used for performing the linear elastic analyses.

Chapter 3

THE MECM FOR COLLAPSE LOAD DETERMINATION OF STRUCTURES USING FINITE ELEMENT METHOD

3.1 Introduction

This chapter explains the implementation of the modified ECM (MECM) as an efficient limit load determination scheme for a range of 2D and 3D ductile structures. The organization of this chapter is as follows. In section 3.2, the MECM is comprehensively described and its implementation via the well-known FEM is explained. In section 3.3, the effect of Poisson's ratio on the collapse load multiplier is investigated through an example. To consider the effect of incompressiblity, the robust mixed finite element method [76, 77, 78] is used, and it is shown that the true estimation of the collapse load is obtainable providing the condition of incompressibility (or nearly incompressible condition) is satisfied. Section 3.4 shows the performance of the finite element method and explains that the very widely-used low order displacement-based finite elements along with the selective integration scheme can be used in the MECM. Section 3.5 illustrates the performance of the MECM within FEM by selective integration scheme through implementing the method on a range of 2D benchmarks and 3D structures. This section also seeks the answer to the question whether the collapse load limit computed by the present numerical scheme shows a lower bound or upper bound on the analytical solution. In essence, the computed numerical examples illustrate that all of the collapse load results tend to converge to the lower bound limits when a sufficient number of structural discretization has been attained. Section 3.6 summarizes the concluding remarks.

3.2 MECM Implementation

The MECM performs an iterative elastic analysis of sufficiently ductile structures that are modeled within the finite element framework to determine the maximum load capacity at plastic collapse. The method involves a lower-bound limit analysis theorem. The generic idea is trivial in that a series of elastic finite element analyses are iteratively processed. At the end of each iteration r, the computed statically admissible stress resultants are collected to calculate the corresponding load factor α^r that complies with the plastic capacity of materials employed. At the beginning of the next iteration $r+1$, the stress resultants are collected to systematically adjust the elastic stiffnesses of critical elements. The procedures are repeated until the predefined maximum number of iterations ($rmax$) has been reached. The collapse load multiplier (α^{col}) is selected as the maximum of the statically admissible load factors computed over all analysis computations. The structural system is suitably discretised into n finite elements and d degrees of freedom. Each finite element contains g integration points. The ECM numerical analysis determines the collapse load factor α^{col} that can be safely sustained by the structure under monotonically applied forces $\alpha\mathbf{F}_{\mathrm{G}} \in R^d$, where $\mathbf{F}_{\mathrm{G}} \in R^d$ is a vector of global nodal forces. The approach enforces the stress resultants at all integration points of an element $j = 1$ to g to comply with the failure conditions imposed by the specific material properties, such as the von Mises (M) and Tresca (T) yield criteria explained in sections 2.2.5.1 and 2.2.5.2 respectively, in 2D (or 3D) space as follows.

- **2D plane strain**

  From Eqs. (2.62) and (2.69):

$$\left(\bar{\sigma}_{i,j}^{r}\right)_M = \sqrt{\frac{3}{4}\left\{\left(\sigma_x - \sigma_y\right)^2 + 4\tau_{xy}^2\right\}} \tag{3.1}$$

$$\left(\bar{\sigma}_{i,j}^{r}\right)_T = \sqrt{\left(\sigma_x - \sigma_y\right)^2 + 4\tau_{xy}^2} \tag{3.2}$$

- **2D plane stress**

  From Eqs. (2.56) and (2.67):

$$\left(\bar{\sigma}_{i,j}^{r}\right)_M = \sqrt{\left(\sigma_x - \sigma_y\right)^2 + \sigma_x\sigma_y + 3\tau_{xy}^2} \tag{3.3}$$

$$\left(\bar{\sigma}_{i,j}^{r}\right)_T = \max\left(|\sigma_{\mathrm{I}}|, |\sigma_{\mathrm{II}}|, |\sigma_{\mathrm{I}} - \sigma_{\mathrm{II}}|\right) \tag{3.4}$$

- **3D space**

  From Eqs. (2.51) and (2.54) for von Mises condition, and from Eqs. (2.64) and (2.65) for Tresca condition:

$$\left(\bar{\sigma}_{i,j}^{r}\right)_M = \sqrt{\sigma_x^2 + \sigma_y^2 + \sigma_z^2 - \sigma_x\sigma_y - \sigma_y\sigma_z - \sigma_x\sigma_z + 3\left(\tau_{xy}^2 + \tau_{xz}^2 + \tau_{yz}^2\right)} \tag{3.5}$$

$$\left(\bar{\sigma}_{i,j}^{r}\right)_T = \max\left(|\sigma_{\mathrm{I}} - \sigma_{\mathrm{II}}|, |\sigma_{\mathrm{II}} - \sigma_{\mathrm{III}}|, |\sigma_{\mathrm{III}} - \sigma_{\mathrm{I}}|\right). \tag{3.6}$$

In above equations $\sigma_x, \sigma_y, \sigma_z, \tau_{xy}, \tau_{xz}, \tau_{yz}$ and $\sigma_{\mathrm{I}}, \sigma_{\mathrm{II}}, \sigma_{\mathrm{III}}$ are the standard sets of stress tensors and principal stresses explained in sections 2.2.1.1 and 2.2.1.2, respectively; $\bar{\sigma}_{i,j}^{r}$ shows the equivalent stress resultant at the integration point j of the element i at the iteration r. Different material laws can be enforced by simply defining the stress resultants, such as ones given in Eqs. (3.1) to (3.6).

At the beginning of each subsequent iteration $r + 1$, the stress redistribution of some critical elements i is implemented by systematically adjusting stiffness properties (i.e. Young's modulus) of an elastic body. The critical elements contain the averaged stress resultants $\bar{\sigma}_i^r$ (where $\bar{\sigma}_i^r = \sum_{j=1}^{g} \bar{\sigma}_{i,j}^r / g$) computed in the current iteration r that are greater than the nominal value σ_n^r, and the corresponding elastic stiffnesses are modified by

$$E_i^{r+1} = \begin{cases} E_i^r \frac{\sigma_n^r}{\bar{\sigma}_i^r}, & \text{if } \bar{\sigma}_i^r > \sigma_n^r \\ E_i^r, & \text{if } \bar{\sigma}_i^r \leq \sigma_n^r \end{cases} \tag{3.7}$$

, where

$$\sigma_n^r = \bar{\sigma}_{\max}^r - \lambda \left(\bar{\sigma}_{\max}^r - \bar{\sigma}_{\min}^r \right) \tag{3.8}$$

$\lambda \in (0, 1)$ is a modification factor; and $\bar{\sigma}_{\max}^r$ and $\bar{\sigma}_{\min}^r$ are the maximum and minimum stress resultants developed in iteration r in the whole structure, namely $\bar{\sigma}_{\max}^r = \max\left(\bar{\sigma}_i^r\right)$ and $\bar{\sigma}_{\min}^r = \min\left(\bar{\sigma}_i^r\right)$ for all $i = 1$ to n elements, respectively.

The factor λ plays an important role, in which its smaller value admits a fewer number of elements with elastic stiffness adjustment. Whilst a good convergence to the collapse load solution is expected, the method employing the smaller value of λ is likely to experience a larger number of numerical simulations for solution convergence. Vice versa, the higher value of λ results in the a higher number of elements entering elastic stiffness modifications, and hence less computing effort. The analysis with a higher λ value, however, does not consistently guarantee a good numerical stability and accuracy of the collapse load limit [16, 17]. This matter is further discussed in section 3.5 and illustrated in figures 3.11, 3.17, 3.23, 3.28, 3.33, and 3.40.

Of the conditions underpinning the lower bound limit analysis theorem is the yield conformity over the whole structural system. Numerically, the plastic material properties are enforced solely at some predefined critical locations, namely integration points for each of the finite elements. The proposed algorithm imposes such conditions by determining the associated (positive scalar) load factor of $\alpha^r = \sigma_0 / \bar{\sigma}_{\max}^r$ that adjusts the magnitude of stresses to lie within the maximum allowable yield stress σ_0, where $\bar{\sigma}^r_{\max}$ is the maximum stress resultant of the whole structure at iteration r. This ensures that the statically admissible stress resultants satisfy the allowable yield limit σ_0. Therefore, for the total number (viz. $rmax$) of iterative elastic analyses, the lower bound limit analysis determines the collapse load limit α^{col} of the structure by maximizing the load factor α^r, namely $\alpha^{\text{col}} = \max\{\alpha^r | r = 1, \ldots, rmax\}$.

The pseudo code summarizing key steps underlying the MECM is prescribed below:

Step 0: Initialization

- At iteration $r = 0$, initialize: maximum number of iterations $rmax$, $\lambda \in (0,\, 1)$, yield limit σ_0, and elastic Young's modulus for all $i = 1$ to n finite elements.
- Construct a finite element model, and assemble the global nodal forces vector and global stiffness matrix associated with 2D (or 3D) structure.

Step 1: Iterative elastic analyses

- For $r = 1$ to $rmax$
  - Perform an elastic analysis
  - Determine the equivalent stress resultants using Eqs. (3.1) to (3.6) and the averaged stress resultants $\bar{\sigma}^r_i$ and $\bar{\sigma}^r_{\max}$.
  - Update the elastic modulus E^r_i for all elements using Eqs. (3.7) and (3.8).
  - Compute the load multiplier $\alpha^r = \sigma_0 / \bar{\sigma}^r_{\max}$.
- end

Step 2: Termination

- Determine the collapse load $\alpha^{\mathrm{col}} = \max\{\alpha^r | r = 1, \ldots, rmax\}$.

It is useful to make some additional remarks regarding the MECM algorithm used in this thesis.

(1) The selection of both the modification parameter λ and the maximum number of numerical iterations $rmax$ is problem dependent. Our numerical experience indicates that the values of $\lambda = 0.05$ and $rmax = 300$ give accurately enough convergence to the collapse load solutions computed for all examples tested in section 3.5; however, a better convergence can be achieved by using lower values of λ and higher values of $rmax$ (please refer to section 3.5 and figures 3.11, 3.17, 3.23, 3.28, 3.33, and 3.40).

(2) In the original ECM and its modified versions, the maximum stress resultant between the integration points of an element is taken as the representative stress resultant of the element. The main purpose of this selection is to satisfy the yield conformity better in the domain. However, as indicated in chapter 2, this action makes a larger gap between a real smooth stress field within an element and the stress resultant used as the representative of the elements. A larger gap leads to more oscillations in the load multiplier curve. Additionally, adjusting the elastic modulus of an element based on its maximum equivalent stress might be over-conservative. In this thesis, to make the simulated stress field in an element closer to the real stress field in it, the averaged stress resultants of integration points is taken as the representative of the stress resultant of the element. In this case, the yield conformity will be satisfied better in the domain by refining the mesh.

(3) The MECM stated herein is straightforward and thus ideal for computer programming. Mackenzie et al. [79, 12] developed the original ECM method to work with the ANSYS program using APDL macrolanguage to automate the procedure. The user inputs the material properties and the number of iterations. The program runs the ECM and prints a summary of results, and highlights the maximum lower limit load solution computed. The advantage of using commercial software such as ANSYS is that the extensive library of element types, pre-processors and

post-processors is available. However, there is the disadvantage that it is not possible to change the standard procedures within such codes. The implementation involves the solution of a sequence of linear problems where the material moduli are changed at each iteration according to the algorithm equations. At each iteration, the element stiffness matrices for all elements are constructed and assembled to generate the structural stiffness matrix. Generation of element stiffness matrices is time-consuming and not needed at each iteration. As the analyses are linear, these matrices can be computed by factoring the previously computed element stiffness matrices at the first iteration. Therefore, in this thesis, the MATLAB environment is utilized for programming the MECM. In this way, the element stiffness matrices are computed only once in the first iteration, and then stored. In the subsequent iterations, their factored matrices will be used for assembling the total stiffness matrix. This increases the efficiency of the method.

(4) The mentioned MECM algorithm leads to the collapse load multiplier providing the incompressible (or nearly incompressible) condition is implemented (i.e Poisson's ratio, $\nu = 0.5$) [80, 81]. Although the MECMs proposed by Yang and Chen [16, 17] do not consider this condition, the use of Poisson's ratios highly less than 0.5 might be problematic, and could be a major issue in highly constraint problems. In next section, the effect of Poisson's ratio on a very well-known Prandlt's punch problem is discussed.

3.3 Poisson's Ratio Effect

As illustrated before, the ECM uses a series of linear elastic analyses where the elastic moduli of elements are systematically modified at each iteration to simulate the stress distribution. Ponter et al. [54, 15, 81] showed that this procedure will converge to stress states on the yield surface if Poisson's ratio is 0.5 to reflect plastic incompressibility. They proved that a sufficient condition for convergence of upper bound limit load solution is provided by the requirement that the complementary energy surface for the linear material defined by the elastic modulus, must either coincide with the yield surface or lie outside it. They concluded that for the von Mises yield condition the complementary energy surface coincides with the yield surface when Poisson's ratio $\nu = 0.5$, but for $\nu < 0.5$ it lies within the yield surface and contravenes the conditions of the convergence proof. Though the convergence proof they made is for the upper bound solution, the necessity of incompressibility is found to be vital for the lower bound limit load solution too. This is due to the fact that the condition of incompressibility in linear analyses (i.e. the use of Poisson's ratio as 0.5) imposes the required volume conservation in plastic analyses, as the plastic deformations do not change the volume of the material [23].

To further investigate the effect of the Poisson's ratio on the lower bound limit load solution, in this section, the behavior of the MECM under different Poisson's ratios is investigated through studying the very well-known Prandtl's punch problem defined in chapter 2 in section 2.2.7. The classical plane strain problem consisting of a semi-infinite rigid plastic medium under a uniformly distributed vertical force of 2α is shown in Fig. 3.1a. The dimensions were taken large enough to simulate the semi-infinite condition. This does not allow the boundaries to affect the collapse mechanism. The sufficiency of the dimensions were tested in another example, where the mesh size was kept the same, but the dimensions were increased. It was concluded that the same results were obtained, signifying the adequacy of the dimensions. The perfectly plastic Tresca material was adopted. The elastic modulus was given as $E = 10000$ whose unit is the same as stress unit. The analytical ratio of the collapse load multiplier to the yield stress (i.e. $\frac{\alpha^{col}}{\sigma_0}$) is 2.5708. In view of the symmetry in geometry and loading involved in this problem, only half of the structure was modeled (Fig. 3.1b). To properly cover all ranges of Poisson's ratios including the nearly incompressible condition, the model was constructed from mixed finite elements of Capsoni and Corradi [76, 77], which allows accurate solutions even for nearly incompressible material.

The MECM using $\lambda = 0.05$ and 300 iterations for various Poisson's ratios was

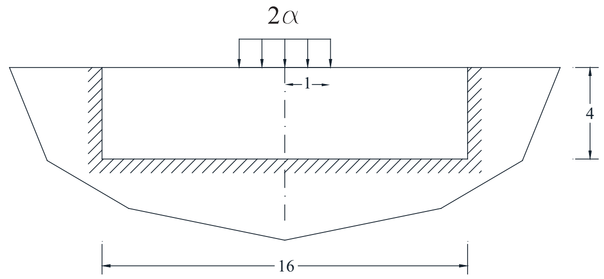

(a)

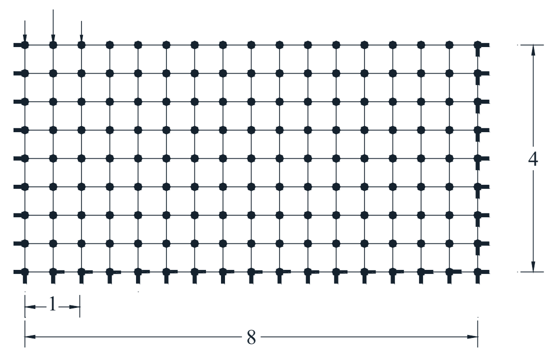

(b)

Figure 3.1: Prandtl's punch problem (a) geometry and loading and (b) mixed finite element model, where thick solid lines denote nodal restrained directions

carried out on a sufficiently fine mesh (i.e 32768 mixed-elements, 33153 nodes, and 66306 degree of freedoms (DOFs)). The reason that this mesh is chosen as an adequately fine mesh is later explained through a convergence study at the end of this section. The results are shown in Table 3.1. Fig. 3.2 also shows the variation of limit loads. As can be seen from the Table 3.1, the values of Poisson's ratio equal to or higher than 0.499 lead to adequately accurate limit load solutions. A value higher than 0.45, for this example, can also be used for appropriate estimations of the collapse load; however, the values less than 0.45 lead to a convergence of wrong limit load values. This conveys the importance of employing the incompressibility in MECM.

A convergence study on the mesh size is also performed on this problem with Poisson's ratio of 0.499. The mixed finite elements were uniformly refined to produce a range of coarse to fine meshes. At each refinement level, each element is subdivided into four similar elements. This allows the uniform refinement. The

Table 3.1: Collapse load solutions for different Poisson's ratios

Poisson's ratio (ν)	$\alpha^{\mathrm{col}}/\sigma_0$	error %
0	1.2315	-52.10
0.1	1.2680	-50.68
0.2	1.3248	-48.47
0.3	1.5435	-39.96
0.4	2.1726	-15.49
0.45	2.5625	-0.32
0.49	2.5725	0.07
0.499	2.5742	0.13
0.4999	2.5798	0.35
0.49999	2.5798	0.35
0.499999	2.5798	0.35

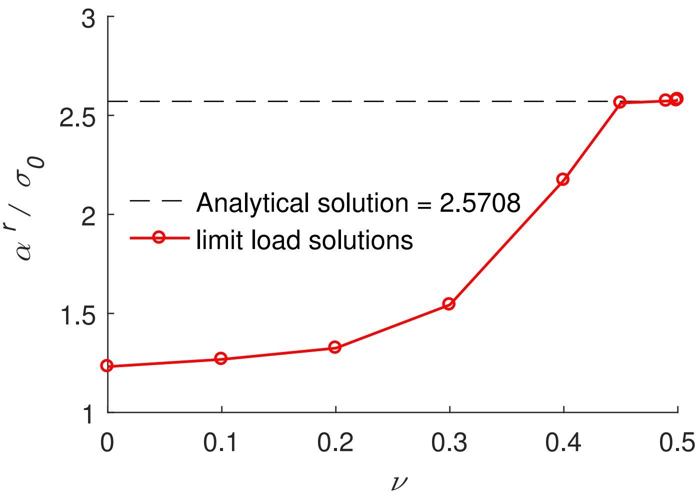

Figure 3.2: Variation of the collapse load multiplier with Poisson's ratio

Table 3.2: The collapse load solutions of the Prandtl's punch problem for different mixed FE discretization using the MECM

No. of elements (NE)	element mesh size (h)	$\frac{\alpha^{\text{col}}}{\sigma_0}$	error%
32	1.00000	3.1679	23.23
128	0.25000	2.8471	10.75
512	0.06250	2.6946	4.82
2048	0.01563	2.61845	1.85
8192	0.00391	2.5918	0.82
32768	0.00098	2.5798	0.35

results are shown in Table 3.2, where the errors between the final solutions and the analytical value ($\frac{\alpha^{\text{col}}}{\sigma_0} = 2.5708$) are also derived. The normalized ratio of the collapse load multipliers to the yield stress is also plotted versus different number of elements in Fig. 3.3. The convergence shows that the mesh with 32768 mixed finite elements, used for investigation of the Poisson's ratio on the collapse load multiplier, is reasonably fine.

3.4 Selective Integration Technique for Finite Element Implementation of MECM

Low order standard displacement-based finite elements are preferred and used widely in engineering structural analysis due to their simplicity and data sparsity; However, for incompressible or nearly incompressible media, numerical difficulties limit their usage. There has been a long history of attempts to develop accurate finite element formulation for these media [82]. In particular, the reduced and selective integration procedures found to be effective when incompressible medium is targeted [83]; however, the use of reduced integration scheme may lead to spurious modes [84] and thus the selective integration scheme is preferred. In this method, the element stiffness matrix is divided into the volumetric and deviatoric (described in section 2.2.1.3) terms. A lower order integration is only performed on the volumetric term and the deviatoric term is fully integrated.

The aim of this section is to show the performance of MECM when low order

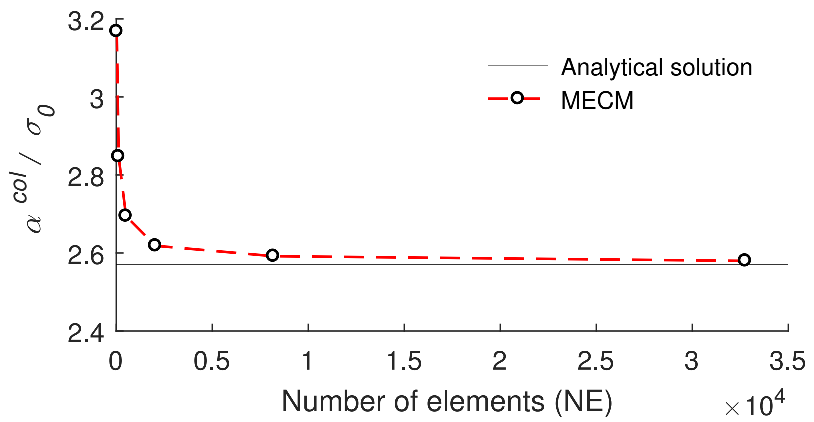

(a)

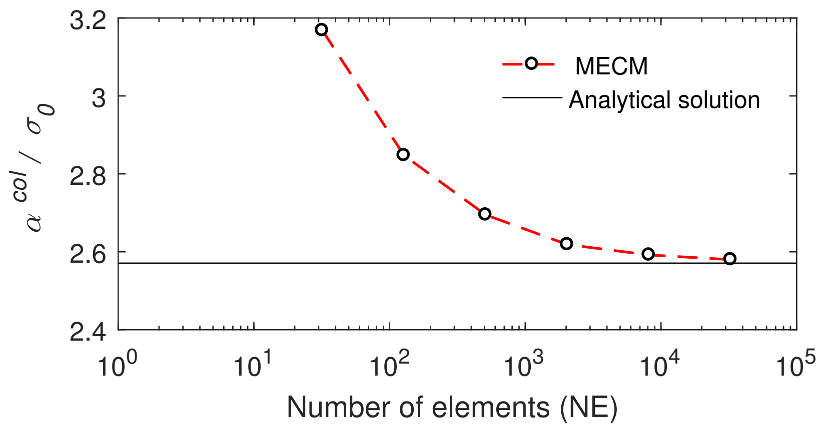

(b)

Figure 3.3: Variation of the collapse load solution with the number of elements for the Prandtl's punch problem using the MECM and mixed FEM (a) natural scale (b) logarithmic scale

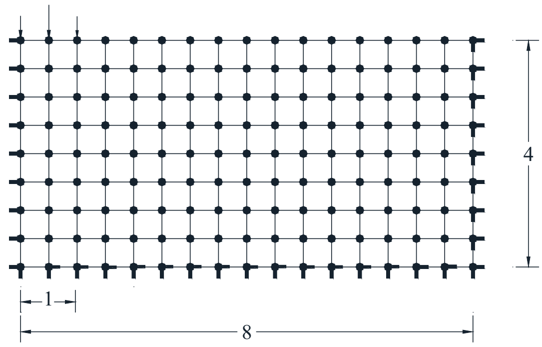

Figure 3.4: Finite element model with selective integration

finite elements with the selective integration scheme are used. For this purpose, the same Prandtl's punch problem discussed in section 3.3 is considered, as its true collapse load solution is highly dependent on the right choice of Poisson's ratio. The structure was modeled using the four-node low order finite elements with the selective integration (Fig. 3.4). The MECM using $\lambda = 0.05$ and 300 iterations for various Poisson's ratios was carried out on a very fine mesh (i.e 32768 elements, 33153 nodes, and 66306 DOFs). The convergence study performed in section 3.5.1.1 validates that the chosen mesh is reasonably fine enough. The results are tabulated in Table 3.3, where the errors between the final solutions and the analytical value ($\frac{\alpha^{col}}{\sigma_0} = 2.5708$) are also derived. Fig. 3.5 also shows this variation of limit loads. The final results show that the collapse load solutions are in good agreement with the analytical solution when Poisson's ratios of 0.499 and higher are used. Poisson's ratios of 0.45-0.499 also can lead to acceptable collapse loads for this example.

3.5 Numerical Examples

A number of numerical examples are provided to illustrate applications of the MECM using the FEM with selective integration scheme that can capture the collapse load and stress distributions at the failure of ductile structures. The examples cover not only 2D in-plane (benchmark) examples, but also 3D structures. In all examples, the nearly incompressible condition was considered by using the Poisson's ratio $\nu = 0.499$. The numerical examples show that this value should be close enough to

Table 3.3: Collapse load solutions for different Poisson's ratios using FEM with selective scheme

Poisson's ratio (ν)	$\alpha^{\mathrm{col}}/\sigma_0$	error %
0	1.2316	-52.09
0.1	1.2681	-50.67
0.2	1.3318	-48.19
0.3	1.5542	-39.55
0.4	2.1600	-15.98
0.45	2.5456	-0.98
0.49	2.5625	-0.32
0.499	2.5676	-0.12
0.4999	2.5683	-0.10
0.49999	2.5683	-0.10
0.499999	2.5683	-0.10

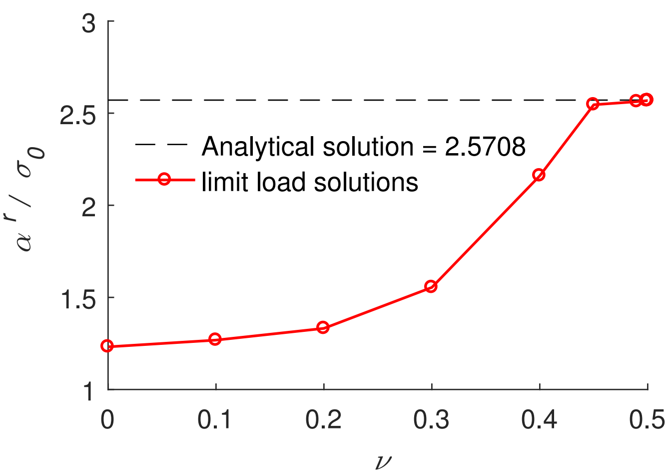

Figure 3.5: Variation of collapse load multiplier with Poisson's ratio using FEs with selective scheme

0.5 to provide sufficiently accurate collapse load solutions. Plasticity was conformed solely at Gauss's integration points. In all examples, $\lambda = 0.05$ and $rmax = 300$ were considered. The analysis procedures were implemented within a MATLAB programming environment.

3.5.1 2D In-plane Structures

3.5.1.1 Prandtl's punch problem

The first example concerns the Prandtl's punch problem of a flexible footing discussed in section 2.2.7 and used in sections 3.3 and 3.4 for validation of the incompressiblity condition. This problem is challenging because of the strong discontinuity that occurs at the footing edge, leading typically to high computational costs [85, 78, 86]. This classical plane strain problem consisting of a semi-infinite rigid plastic medium under a uniformly distributed vertical force of 2α is shown in Fig. 3.6a. The dimensions were taken sufficiently large to simulate the semi-infinite condition. The perfectly plastic Tresca material was adopted. The elastic modulus was taken as $E = 10000$ whose unit is the same as the stress unit. The analytical solution of the ratio of the collapse load multiplier to the yield stress (i.e. $\frac{\alpha^{\text{col}}}{\sigma_0}$) is 2.5708. In view of the symmetry in the geometry and loading involved in this problem, only half of the structure was modeled using four-node low order finite elements and the selective integration procedure was used to simulate the nearly incompressible condition. Fig. 3.6b displays the schematic model used in this study, where each element shown was subdivided into 16 similar elements (i.e. 2048 elements). The actual obtained model is plotted in Fig. 3.6c.

The MECM was successfully performed and the plot of the ratio of load multipliers to the yield stress $\frac{\alpha^r}{\sigma_0}$ collected at all analysis iterations r is displayed in Fig. 3.7. As can be seen, due to the crudity of the mesh, the yield conformity as a requirement for the lower bound theorem is not completely satisfied and thus the solution exceeds the analytical solution after some iterations [80] and converges to

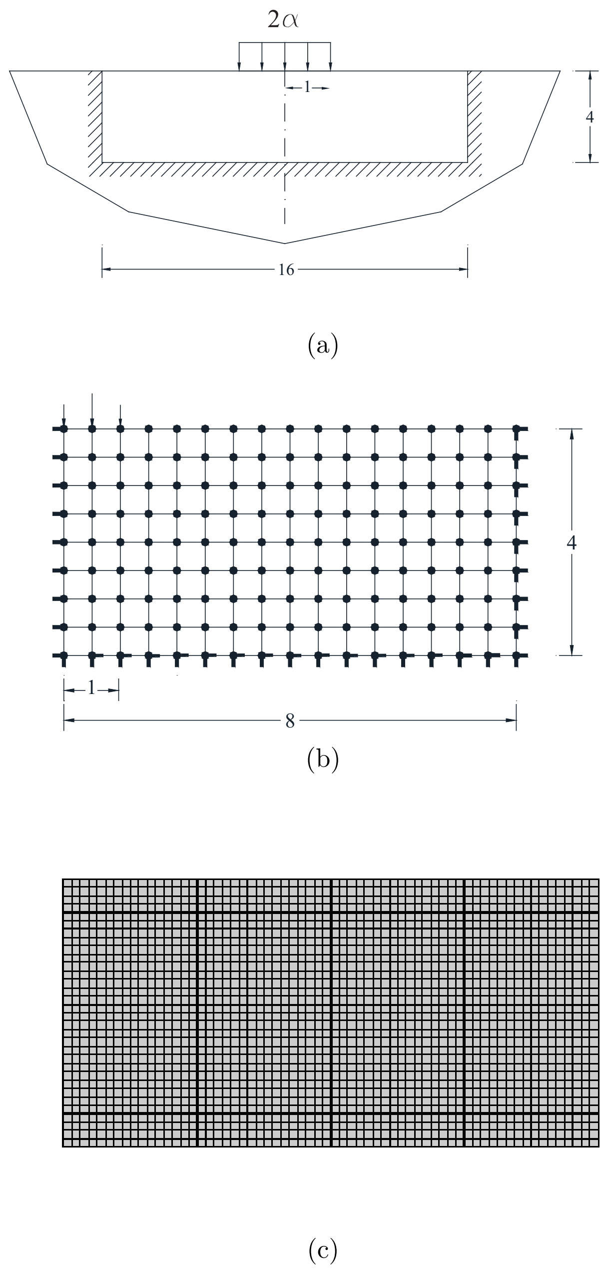

Figure 3.6: Prandtl's punch problem (a) geometry and loading and (b) schematic finite element model, where thick solid lines denote nodal restrained directions (c) actual finite element model

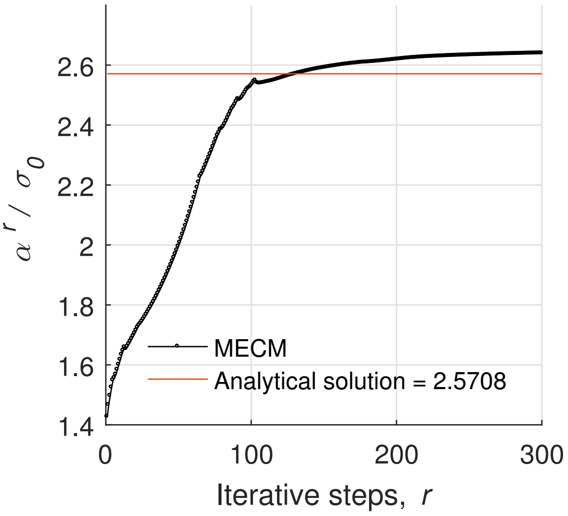

Figure 3.7: The MECM iterative scheme for the Prandtl's punch problem with 2048 finite elements

its maximum value after 300 iterations. This trend shows that although the MECM is a lower bound scheme, it does not produce strict lower bound solutions unless sufficient number of elements is used. The ratio of the collapse load multiplier to the yield stress $\frac{\alpha^{\mathrm{col}}}{\sigma_0}$ was obtained as 2.6392. The error compared to the analytical solution is 2.66% .

The plots of the stress and elastic modulus distributions corresponding to the collapse load solution are displayed in Fig. 3.8, which agree well with the analytical collapse mechanism discussed in section 2.2.7 and the collapse mechanisms reported in the literature (e.g. [87]). The scaled displacement field is also displayed in Fig. 3.9. Fig. 3.10 also shows the sequences of developments of plastic areas, where the elastic moduli of the highly loaded elements have been iteratively reduced. At the end of the iterations, the smallest values of elastic moduli belong to the elements contributing to the collapse mechanism.

The diagram in Fig. 3.11 presents the relationship between the number of iterations and the ratio of load multipliers to the yield stress $\frac{\alpha^r}{\sigma_0}$ for different values of λ (viz. ranging from 0.05 to 0.5). In this figure, it is illustrated that the analysis with a high value of λ (e.g. values equal or higher than 0.2) may quickly attain the collapse load limit, but later experience some numerical instabilities (i.e. oscillation

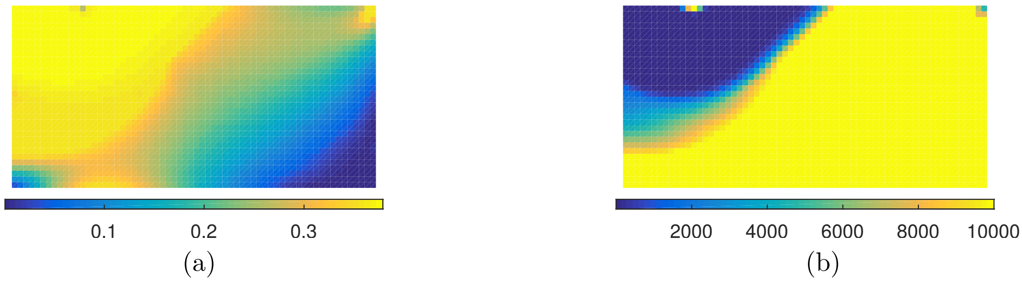

Figure 3.8: Stress and elastic modulus distributions for the Prandtl's punch problem using the MECM and FEM (a) stress distribution (b) elastic modulus distribution

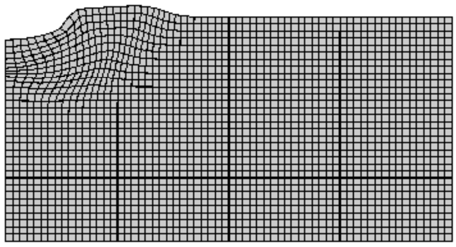

Figure 3.9: The schematic displacement field for the Prandtl's punch problem using the MECM and FEM

of the α^r responses) in the algorithm leading to solution divergence. The reason of the shown oscillations is the stress overshooting which will be discussed in chapter 5. The analysis with a small λ value (e.g. values less than 0.2) provides a better chance to obtain good (numerically stable) convergence of the solution, but often requires a sufficiently large number of numerical iterations. This leads to more computing effort for the load limit to converge. The choice of $\lambda = 0.05$ and $rmax = 300$ has led to an acceptable convergence in this example.

Finally, the influence of the total number of elements on the accuracy of the collapse load solution (mesh study) was investigated. The FEM was uniformly refined for different (ranging from coarse to fine) numbers of elements. At each refinement step, each element was subdivided into four similar elements to guarantee the uniform refinement. The results are presented in Table 3.4. The ratio of load multipliers to the yield stress with respect to variation of the number of elements are also plotted in Fig. 3.12. As seen, the values of collapse load multipliers generally decrease

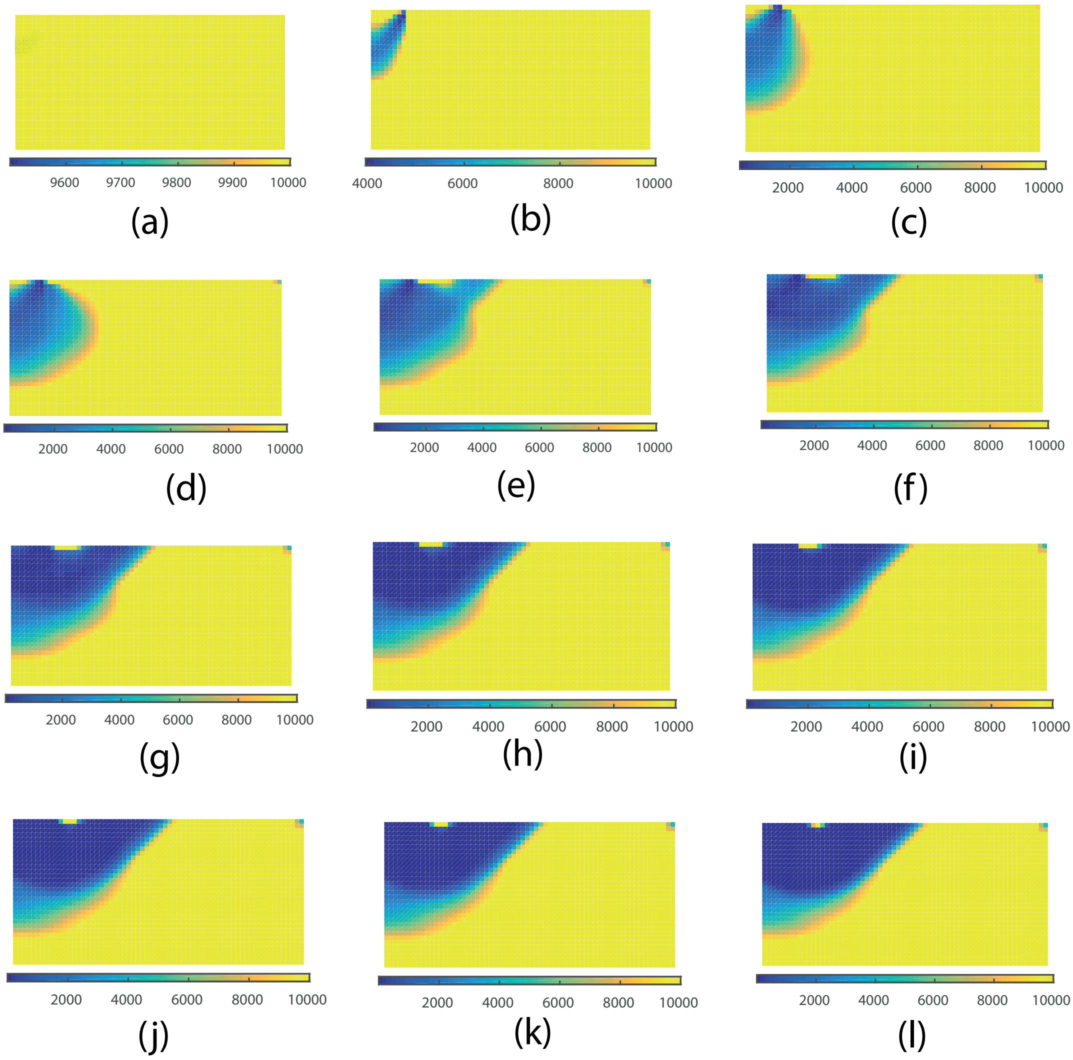

Figure 3.10: The mechanism development for the Prandtl's punch problem using the MECM and FEM

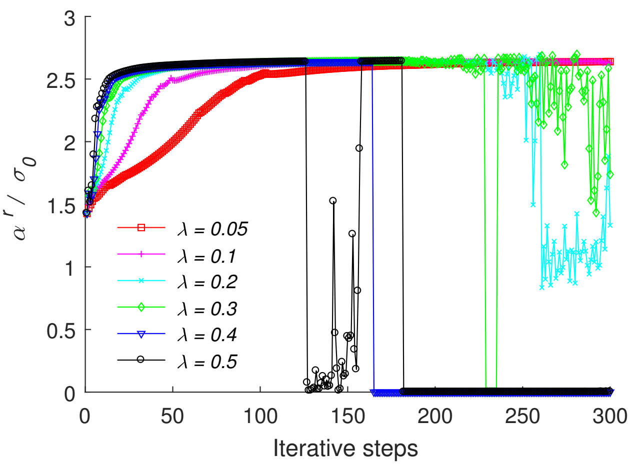

Figure 3.11: Variation of collapse load solutions with λ for the Prandtl's punch problem using the MECM and FEM

Table 3.4: The collapse load solutions of the Prandtl's punch problem for different FE discretization using the MECM

No. of elements (NE)	element mesh size (h)	$\frac{\alpha^{col}}{\sigma_0}$	error%
32	1.00000	3.1926	24.19
128	0.25000	2.8589	11.21
512	0.06250	2.7092	5.38
2048	0.01563	2.6392	2.66
8192	0.00391	2.5935	0.88
32768	0.00098	2.5676	-0.12

to a value below the analytical solution by reducing the mesh size (increasing the number of elements). This shows the importance of mesh density in the ECM. As only one elastic modulus is defined for each element, a fine mesh is usually required if the localized plasticity occurs [18]. If the mesh is too coarse, the estimated stress field cannot represent the real continuous stress filed which is vital for the lower bound application, and usually causes the load capacity of the structure to be overestimated. Additionally, increasing the number of integration points in the domain, as the byproduct of discretization, leads to a better yield conformity and, therefore, better limit load solutions. This emphasizes that although the MECM is a lower bound scheme (see Fig. 3.7), it is not a strict lower bound method. In fact, the strict lower bound solutions can be obtained only if sufficient number of elements is used.

3.5.1.2 Double-edge notched specimen

This problem is a popular benchmark test used for elastoplastic analysis procedures. It was first introduced by Nagtegaal et al. [88] to illustrate locking and later studied in [89, 90]. The structure in Fig. 3.13a consists of a rectangular specimen with two thin notches under a reference load consisting of in-plane tensile stresses 2α. The perfectly plastic von Mises material was adopted. The elastic modulus was given as $E = 70$ whose unit is the same as stress unit. The reported ratio of the collapse load multiplier to the yield stress (i.e. $\frac{\alpha^{col}}{\sigma_0}$) is 4.6749. Due to symmetry, only a quarter of the tensile specimen was modeled using finite elements. The schematic figure of

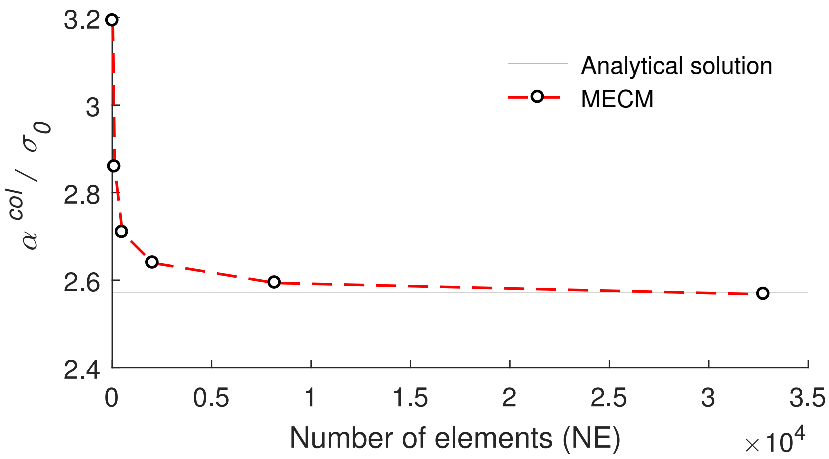

(a)

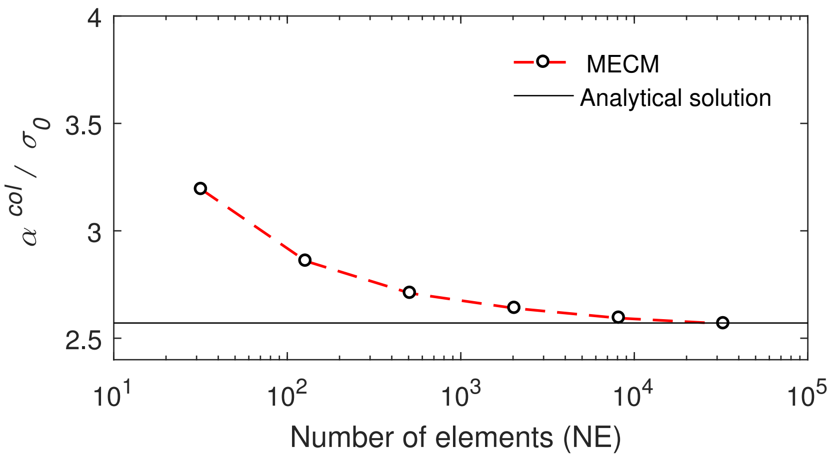

(b)

Figure 3.12: Variation of the collapse load solution with the number of elements for the Prandtl's punch problem using the MECM and FEM (a) natural scale (b)logarithmic scale

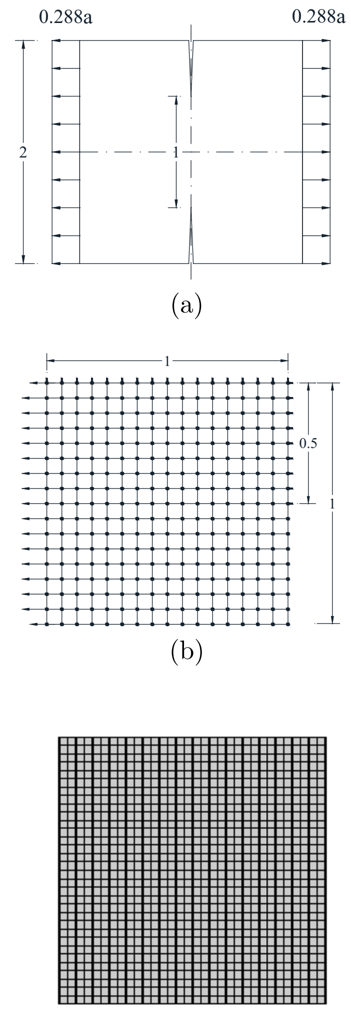

(a)

(b)

(c)

Figure 3.13: Double-edge notched specimen (a) geometry and loading and (b) schematic finite element model, where thick solid lines denote nodal restrained directions (c) actual finite element model

the model is shown in Fig. 3.13b, where each element was subdivided into 4 similar elements. In total, 1024 elements, 1089 nodes and 2178 DOFs were considered. Fig. 3.13c displays the actual employed mesh after these subdivisions.

The MECM was implemented on the model and the ratio of the collapse load multiplier to the yield stress $\frac{\alpha^{col}}{\sigma_0}$ of 4.765 was obtained, which is some 1.937% higher than the reported solution. Fig. 3.14 displays the variations of $\frac{\alpha^{col}}{\sigma_0}$ with the number of iterations.

Additionally, Fig. 3.15 shows the corresponding stress and elastic modulus distributions at the collapse load solution, which both agree well with the reported

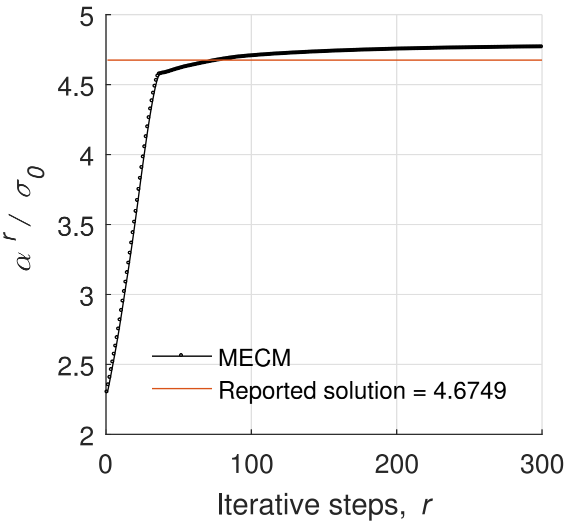

Figure 3.14: The MECM iterative scheme for the double-edge notched specimen with 1024 finite elements

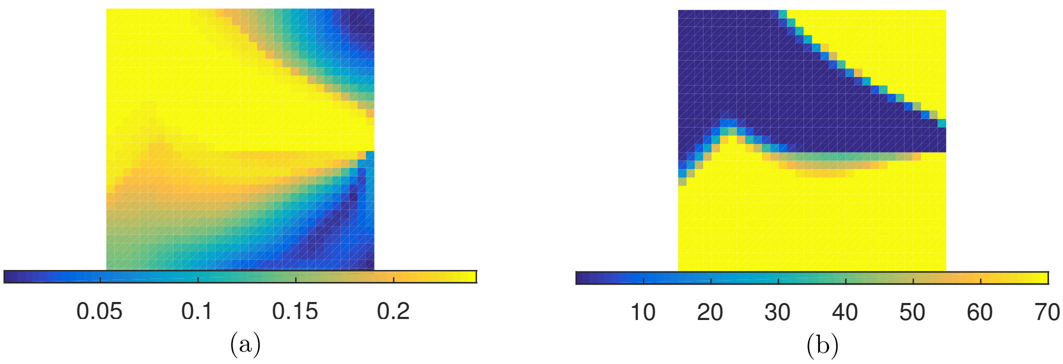

Figure 3.15: Stress and elastic modulus distributions of the double-edge notched specimen using the MECM and FEM (a) stress distribution (b) elastic modulus distribution

mechanism [87]. The schematic displacement field showing the collapse mechanism is also depicted at Fig. 3.16

The effect of λ on the collapse load solutions for the current mesh and a finer mesh (with 4096 elements) was studied and the results are plotted in Fig. 3.17. As illustrated, the higher values of λ resulted in a faster convergence (for the coarser mesh (a)), however, they diverged in later iterations due the numerical instability. This prevented a better solution to be obtained. For the finer mesh (b), the use of higher values of λ (such as 0.4 and 0.5) could not even give a relative convergence due to the oscillations of α^r responses. In both cases, use of the proposed value of $\lambda = 0.05$ led to an acceptable convergence and numerical stability.

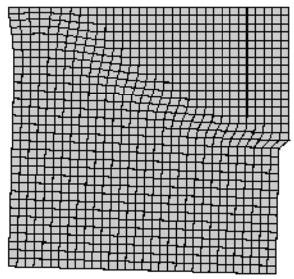

Figure 3.16: The schematic displacement field of the double-edge notched specimen using the MECM and FEM

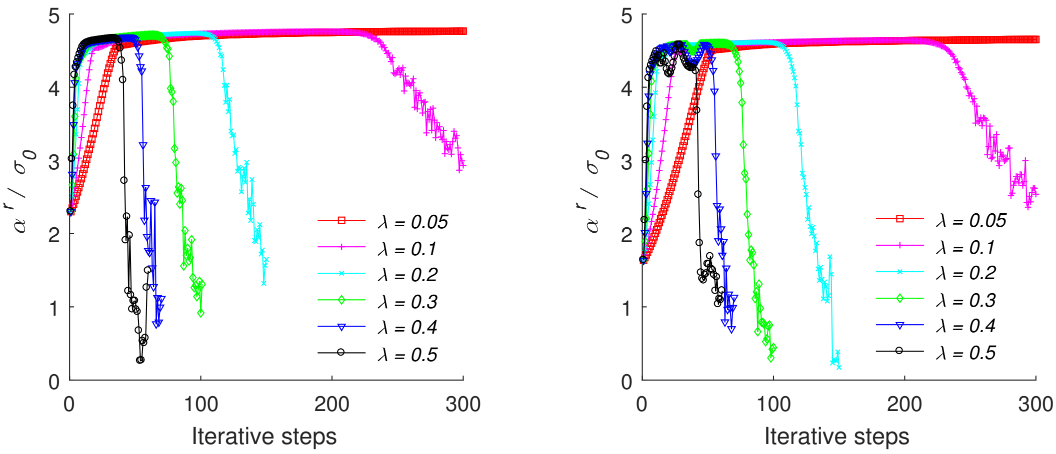

(a) (b)

Figure 3.17: Variation of the collapse load solution with λ for the notched problem using the MECM and FEM (a) 1024 elements (b) 4096 elements

Table 3.5: The collapse load solutions of the double-edge notched specimen for different FE discretization using the MECM

No. of elements (NE)	element mesh size (h)	$\frac{\alpha^{\text{col}}}{\sigma_0}$	error%
4	0.5	7.2551	55.19
16	0.25	5.8807	25.79
64	0.125	5.3004	13.38
256	0.0625	4.9424	5.72
1024	0.03125	4.7654	1.94
4096	0.01563	4.6543	-0.44
16384	0.00781	4.5885	-1.85
65536	0.00391	4.5556	-2.55

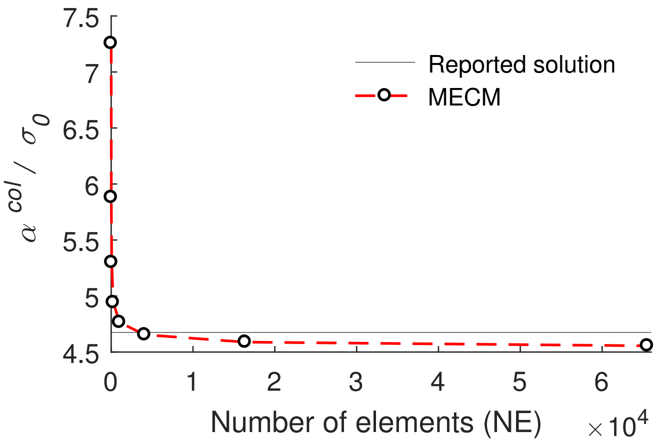

Figure 3.18: Variation of the collapse load solution with the number of elements for the notched specimen using the MECM and FEM

The effect of the number of elements on the accuracy of the collapse load is investigated through the mesh study on the problem. Eight models were considered and the number of elements were uniformly increased from a very coarse mesh to the finest mesh. At each refinement step, each element was subdivided into four similar elements to guarantee the uniform discretization. The results are tabulated in Table 3.5 and illustrated in Fig. 3.18. As expected, the collapse load monotonically decreased to a value below the reference solution by increasing the number of elements. It should be noticed that no justification about the trend of the solutions (i.e. lower bound solutions or strict lower bound solutions) can be provided in this example, as the results are compared with the available reported solution in the literature and not the analytical one.

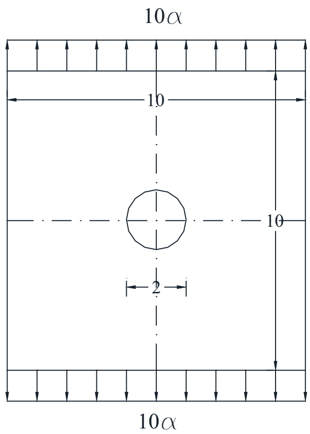

(a)

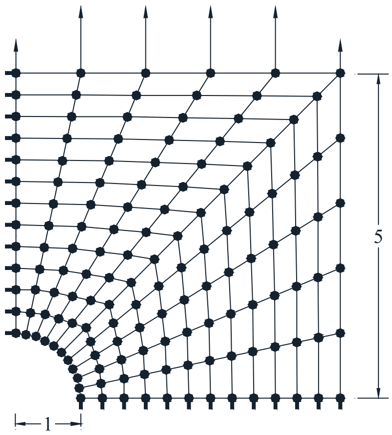

(b)

Figure 3.19: Perforated plate problem (a) geometry and loading and (b) finite element model, where thick solid lines denote nodal restrained directions

3.5.1.3 Perforated plate problem

The third example involves a plane stress square plate perforated with a central circular hole [86, 90, 87] as in Fig. 3.19a. The structure was subjected to the uniformly tensile forces of 10α. The perfectly plastic von Mises material was adopted. The elastic modulus was given as $E = 10000$ whose unit is the same as the stress unit. The analytical ratio of the collapse load multiplier to the yield stress (i.e. $\frac{\alpha^{\text{col}}}{\sigma_0}$) is 0.8. Due to symmetry, only a quarter of the plate was modeled using finite elements (Fig. 3.19b). Totally, 120 finite elements, 143 nodes and 286 DOFs were employed.

The MECM was performed on the finite element model and $\frac{\alpha^{\text{col}}}{\sigma_0}$ was computed as 0.8165 (some 2.06% higher than the analytical solution). The iterative scheme is shown in Fig. 3.20. As can be seen, the drop at the iteration 70 prevented the scheme

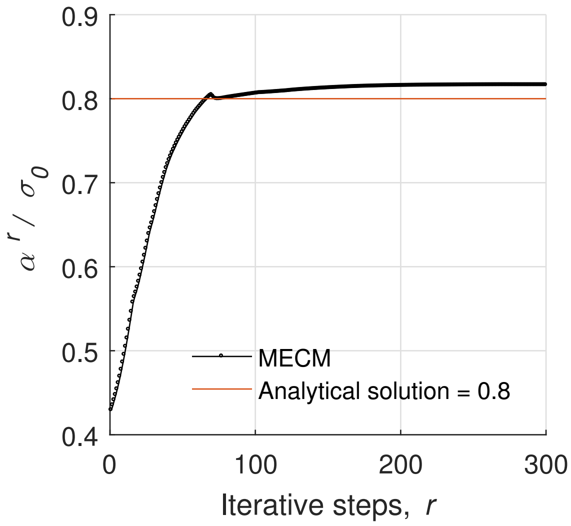

Figure 3.20: The MECM iterative scheme for the perforated plate with 120 finite elements

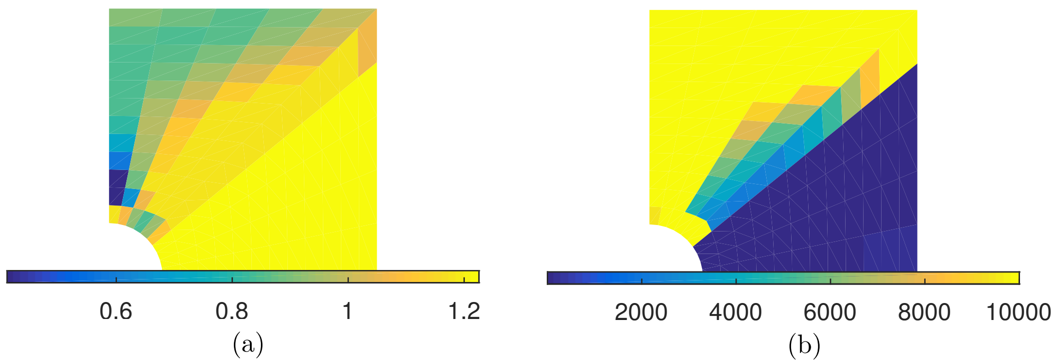

Figure 3.21: Stress and elastic modulus distributions of the perforated plate using the MECM and FEM (a) stress distribution (b) elastic modulus distribution

to define the convergence of the collapse load multiplier. In another note, this figure shows that although the MECM is a lower bound scheme, it is not a strict lower bound method. The strict lower bound solution is only obtained if sufficient number of elements is used to satisfy yield conformity. This matter is further discussed in convergence study of the example.

The stress and elastic modulus distributions corresponding to the last iteration are plotted in Fig. 3.21, which agree well with the reported mechanism [87]. The schematic deformed structure is also plotted in Fig. 3.22.

The variation of the collapse load solution with λ was also investigated for the current mesh and one mesh finer (600 elements) and the results are plotted in Fig.

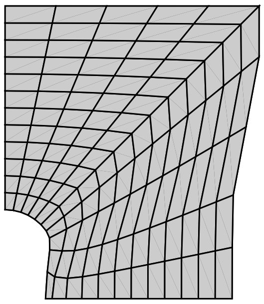

Figure 3.22: The schematic displacement field of the perforated plate using the MECM and FEM

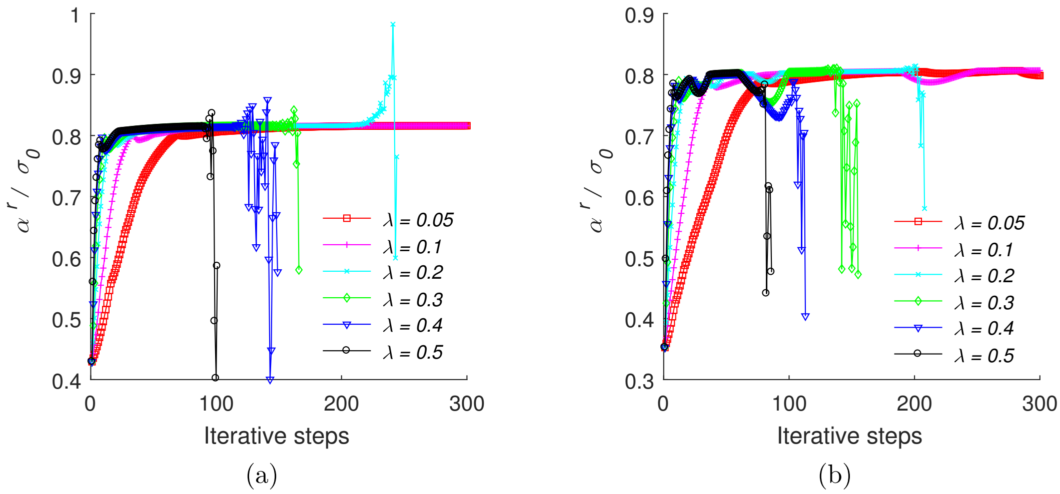

Figure 3.23: Variation of the collapse load solution with λ for the perforated problem using the MECM and FEM (a) 120 elements (b) 600 elements

3.23. As seen, for the coarser mesh, a rough collapse load limit was quickly obtained for higher values of λ, but the the numerical instabilities led the solution to diverge in the later iterations and prevented a better collapse load solution to be obtained. For the finer mesh, the oscillations increased for high values of λ, and the divergence occurred before a better collapse load is obtained. In both cases, the proposed value of $\lambda = 0.05$ led to an acceptable convergence and numerical stability.

The mesh study on the perforated problem was also carried out, where finite element models were constructed for a range of coarse to fine meshes. The results are reported in Table 3.6, where $\frac{\alpha^{\mathrm{col}}}{\sigma_0}$ is reduced to a safe value below the analytical solution by increasing the number of elements. Fig. 3.24 also shows these variations. This figure shows that the strict lower bound solution for the MECM is obtainable

Table 3.6: The collapse load solutions of the perforated plate for different discretizations using the MECM

No. of elements (NE)	$\frac{\alpha^{\mathrm{col}}}{\sigma_0}$	error%
120	0.8165	2.06
600	0.8066	0.82
2080	0.8022	0.27
8320	0.7997	-0.04
33280	0.7983	-0.21

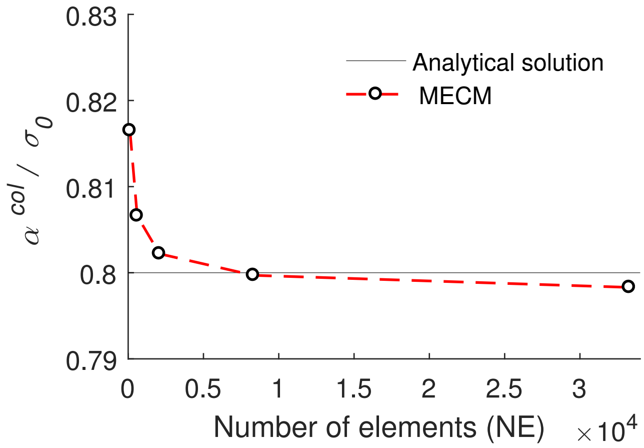

Figure 3.24: Variation of the collapse load solution with the number of elements for the perforated plate problem using the MECM and FEM

only if sufficient number of elements is used to satisfy the yield conformity.

3.5.2 3D Structures

The MECM can also compute the collapse load limits of 3D structures. The three examples presented in this section are the well-known thick cylinder under uniform pressure [16], the pressurized hollow sphere [91], and the pipeline with defected surface [86]. For all the examples, the von Mises (perfectly plastic) materials were employed and the Poisson's ratio was taken as 0.499. Low order 8 node elements (brick elements) with selective integration were employed.

3.5.2.1 Thick cylinder

To evaluate the performance of the MECM, first, a thick cylinder under internal pressure is considered. The geometry and mesh are shown in Fig. 3.25. The

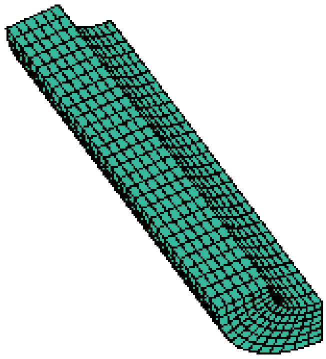

Figure 3.25: The geometry and finite element model of the thick cylinder

geometry and material properties were taken as follows:

- Outer radius: $R = 200$ mm
- Inner radius: $r = 100$ mm
- Length of thick cylinder:$L = 700$ mm
- Elastic modulus: $E = 209$ GPa
- Yield stress: $\sigma_0 = 276$ MPa

The analytical solution of the problem is 220.9 MPa obtained from

$$\alpha^{\mathrm{col}} = \frac{2}{\sqrt{3}}\sigma_0 \ln\left(\frac{R}{r}\right) \tag{3.9}$$

, which gives the ratio of the collapse load multiplier to the yield stress (i.e. $\frac{\alpha^{\mathrm{col}}}{\sigma_0}$) as 0.8004.

The MECM was performed on the finite element mesh (Fig. 3.25) with 2016 elements, 2639 nodes and 7917 DOFs. The value of $\frac{\alpha^{\mathrm{col}}}{\sigma_0}$ was computed as 0.8020 which is some 0.25% higher than the analytical solution. Fig. 3.26 shows the iterative procedure for the problem. The corresponding stress and elastic modulus distributions for the last iteration are plotted in Fig. 3.27.

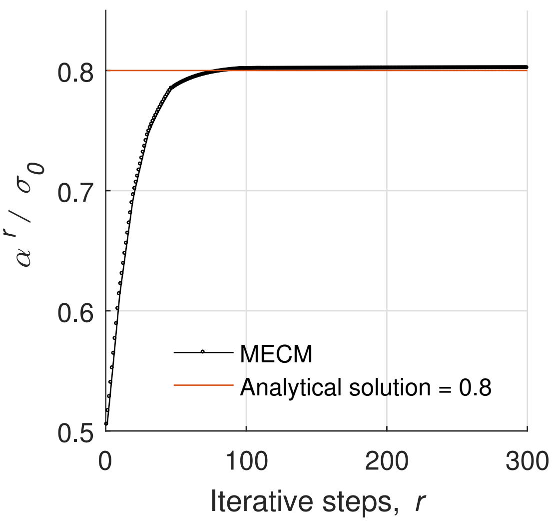

Figure 3.26: The MECM iterative scheme for the thick cylinder with 2016 finite elements

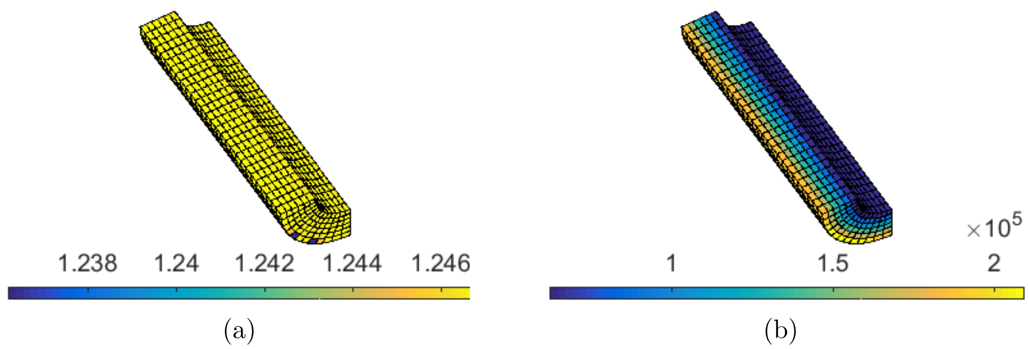

Figure 3.27: Stress and elastic modulus distributions of the thick cylinder using the MECM and FEM (a) stress distribution (b) elastic modulus distribution

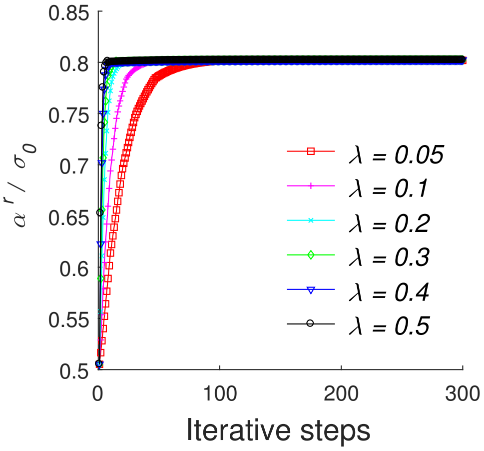

(a)

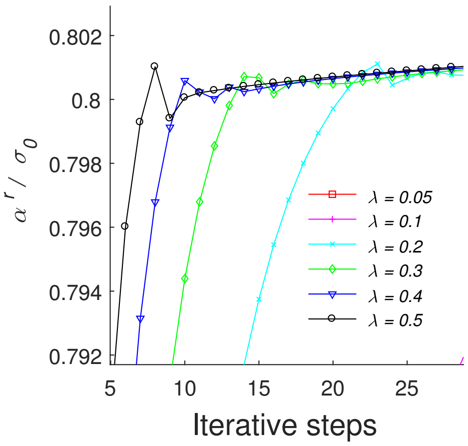

(b)

Figure 3.28: Variation of the load multiplier solutions with λ for the thick cylinder with 2016 elements using the MECM and FEM (a) normal version (b) magnified version

Table 3.7: The collapse load solutions of the thick cylinder for different discretization using the MECM and FEM

No. of elements (NE)	$\frac{\alpha^{col}}{\sigma_0}$	error%
252	0.8074	0.87
756	0.8056	0.66
2016	0.8020	0.20
4725	0.8015	0.14
36288	0.8002	-0.02

The variation of the normalized load multipliers with respect to λ was also studied for the current mesh and the results are shown in Fig. 3.28. As seen in Fig. 3.28a, almost for all values of λ an acceptable level of convergence is obtained. However, as it is emphasized in Fig. 3.28b, where the same results in Fig. 3.28a are magnified, there is still some oscillations for higher values of λ.

The variation of the collapse load limit with the the number of elements was also investigated, and the associated results are tabulated in Table 3.7. Fig. 3.29 also shows these variations. As illustrated, by increasing the number of elements, the collapse load solution decreased to a value below the analytical solution. This trend illustrates that the MECM is a lower bound scheme (see Fig. 3.26), but not a strict lower bound method. In fact, a strict lower bound solution can be obtained only if sufficient number of elements is employed.

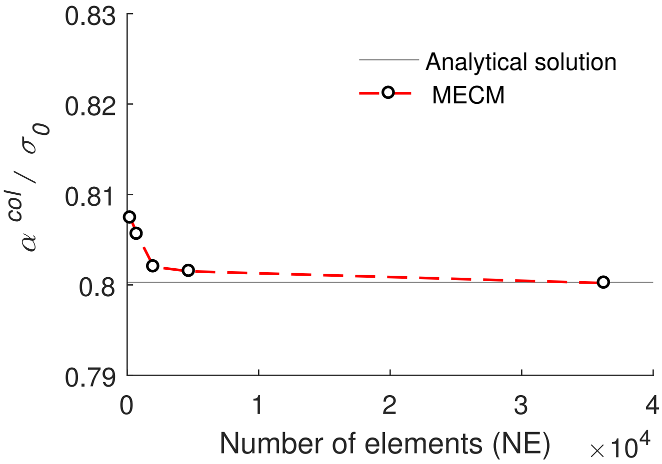

Figure 3.29: Variation of the collapse load solution with the number of elements for the thick cylinder problem using the MECM

3.5.2.2 Hollow sphere

The second 3D example considers a homogeneous hollow sphere with an internal radius a, and external radius b, which is subjected to a uniform internal pressure. The geometry and the corresponding finite element model are illustrated in Fig. 3.30. Due to the symmetric nature of the problem, only one-eights of the problem was modeled, where 2916 elements, 3523 nodes and 10569 DOFs were employed. The geometry and material properties were taken as follows:

- Outside radius: $b = 6$ mm
- Inside radius: $a = 2$ mm
- Elastic modulus: $E = 10000$ MPa
- Yield stress: $\sigma_0 = 1$ MPa

The analytical solution of the problem is 220.9 MPa obtained from

$$\alpha^{\text{col}} = 2\sigma_0 \ln\left(\frac{b}{a}\right) \tag{3.10}$$

, which gives the ratio of the collapse load multiplier to the yield stress (i.e. $\frac{\alpha^{\text{col}}}{\sigma_0}$) as 2.197.

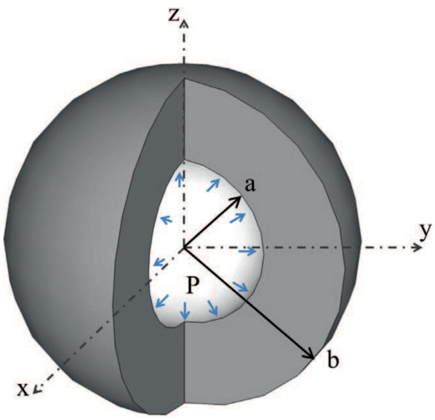

(a)

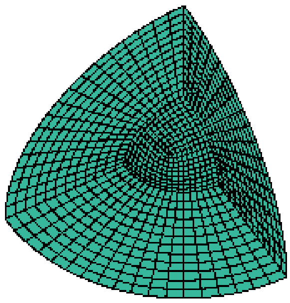

(b)

Figure 3.30: The hollow sphere problem (a) geometry (b) finite element model

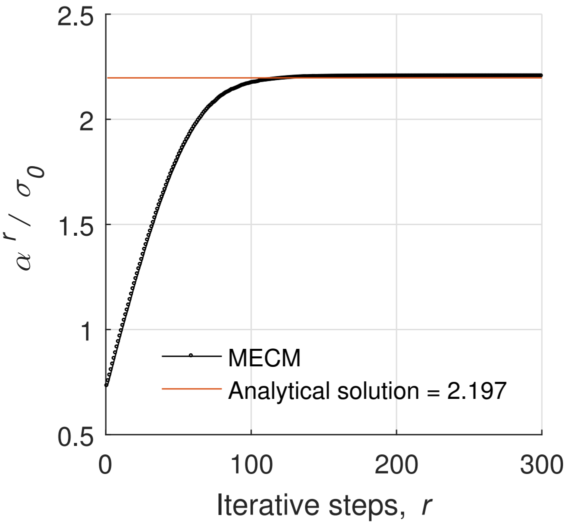

Figure 3.31: The MECM iterative scheme for the hollow sphere with 2916 finite elements

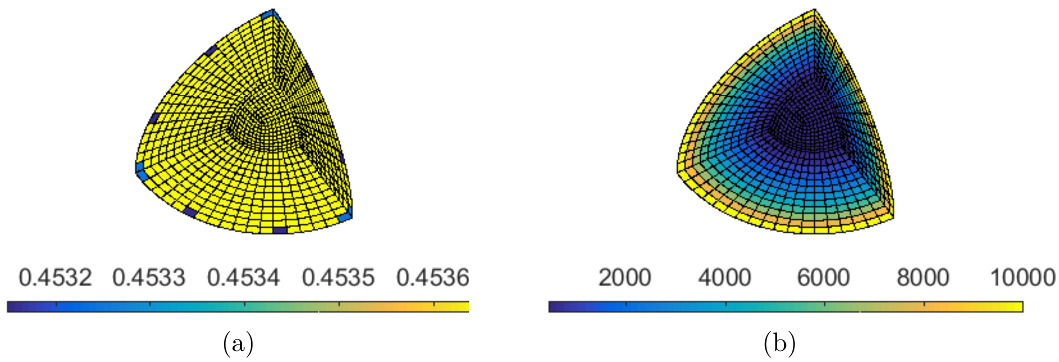

Figure 3.32: Stress and elastic modulus distributions of the hollow sphere problem using the MECM and FEM (a) stress distribution (b) elastic modulus distribution

The MECM was implemented on the finite element model and the $\frac{\alpha^{\mathrm{col}}}{\sigma_0}$ was obtained as 2.2044, which is only 0.34% higher than the analytical solution. Fig. 3.31 shows the iterative procedure for the first 300 iterations, where the lower bound scheme of the MECM is shown. The corresponding stress and elastic modulus distributions for the last iteration are also plotted in Fig. 3.31.

The effect of the parameter λ on the variation of the normalized load multipliers is also studied on the current mesh, and the results are shown in Fig. 3.33. As seen, the convergence is obtained for all values of λ. This matter indicates that for simple 3D structures such as hollow spheres, the ECM can be accurate and efficient.

The influence of the number of elements on the collapse load solution is shown

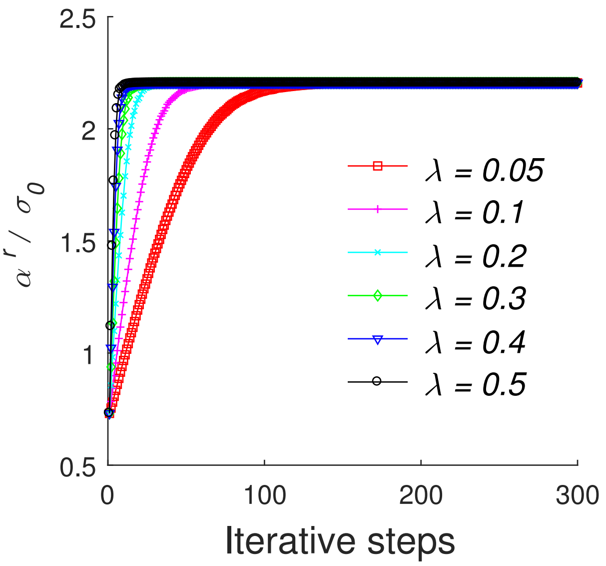

Figure 3.33: Variation of load multiplier solutions with λ for the hollow sphere problem using the MECM and FEM

Table 3.8: The collapse load solutions of the hollow sphere for different FE discretizations using the MECM

No. of elements (NE)	$\frac{\alpha^{col}}{\sigma_0}$	error%
252	2.2537	2.58
864	2.21	0.59
2916	2.2044	0.34
6912	2.199	0.09

in Table 3.8 and Fig. 3.34. As illustrated, by increasing the number of elements, the collapse load solution has been reduced and become closer to the analytical solution. This illustrates that although the MECM is a lower bound scheme, it is not a strict lower bound method.

3.5.2.3 Defected pipeline

The pipeline with defected surface shown in 3.35 was simultaneously subjected to a uniform internal pressure of $P = 1$ MPa and a uniform axially compression force of $P_N = \pi R_i^2 P$ kN, where R_i is the inner radius of the pipeline ($R_i = 50$mm), and the pipe thickness is 20 mm. The von Mises material properties employed were $E = 207$ GPa, and $\sigma_0 = 200$ MPa. Two finite element discretization models (Fig. 3.36) were considered, namely a courser mesh case a (viz. consisting of 316 elements, 558 nodes

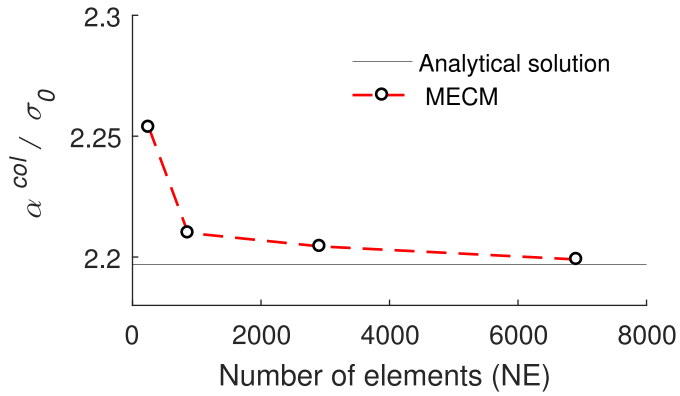

Figure 3.34: Variation of the collapse load solution with the number of elements for the hollow sphere problem using the MECM and FEM

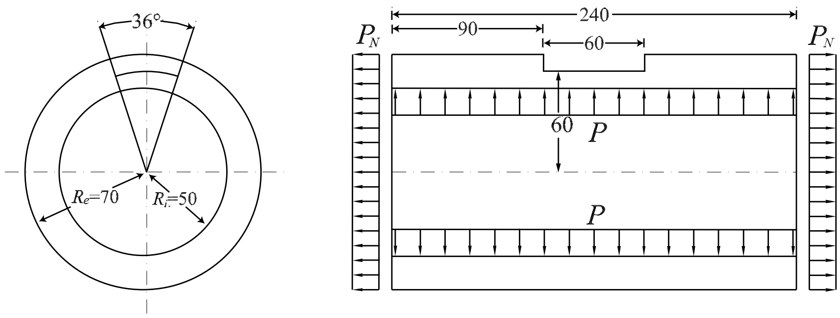

Figure 3.35: Defected pipeline - geometry and loading

and 1674 DOFs) and a finer mesh case b (with 2528 elements, 3437 nodes, and 10311 DOFs).

The MECM successfully computed the collapse load solutions of $\alpha^{\text{col}} = 73.49$ in case a and $\alpha^{\text{col}} = 68.1126$ in case b. Fig. 3.37 shows the employed iterative scheme for case b. The proposed approach provides good accuracy of the collapse load results, as the solutions computed agree well with the reference values reported from various numerical algorithms, namely $\alpha^{\text{col}}_{ref} = 64.05$ using the incremental method [92], $\alpha^{\text{col}}_{ref} = 67.13$ using the kinematic method [86], and $\alpha^{\text{col}}_{ref} = 63.42$ using the static method [92]. The diagrams in Fig. 3.38 depict the von Mises stress and elastic moduli distributions computed at α^{col} for case b. The schematic collapse mechanism associated to α^{col} is also plotted for case b in Fig. 3.39.

The influence of the parameter λ is also studied for this example for the case b. Fig. 3.40 shows the variation of the normalized load multipliers over the iterations

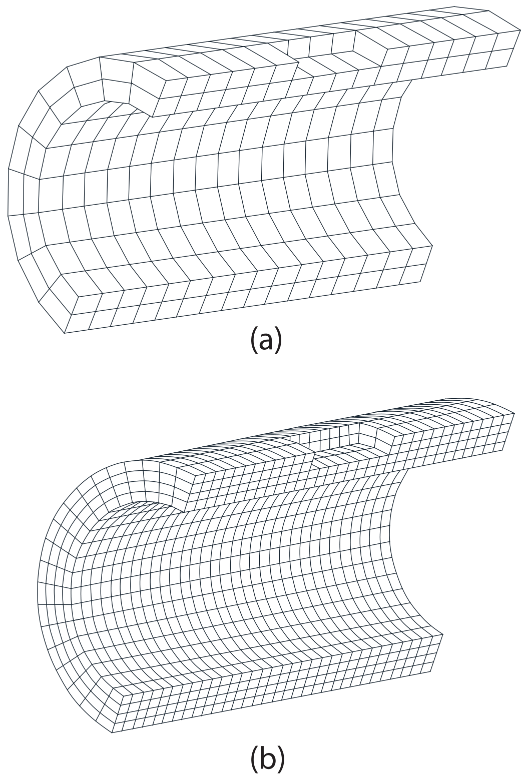

Figure 3.36: Finite element models of the defected pipeline a) case a b) case b

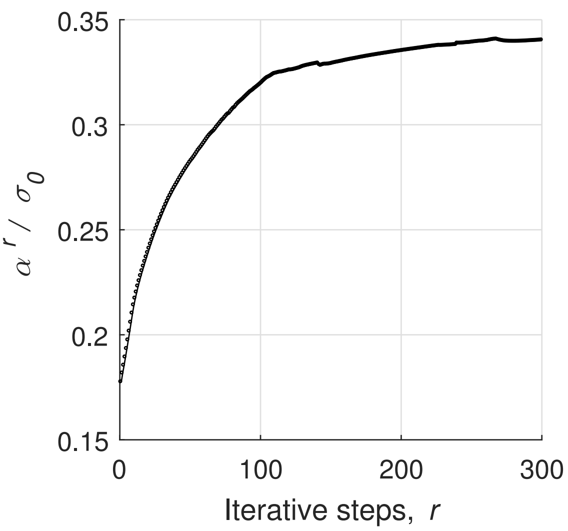

Figure 3.37: The MECM iterative scheme for the defected pipeline with 2528 finite elements

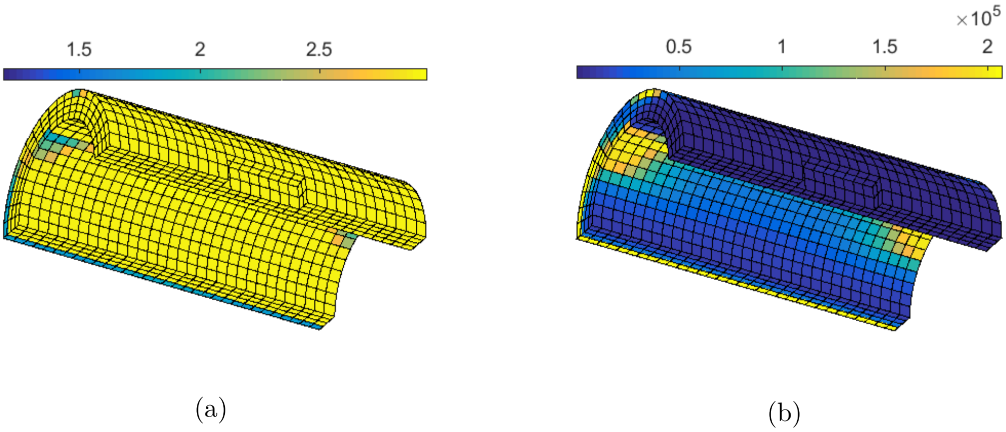

Figure 3.38: Stress and elastic modulus distributions of the defected pipeline problem (case b) using the MECM and FEM (a) stress distribution (b) elastic modulus distribution

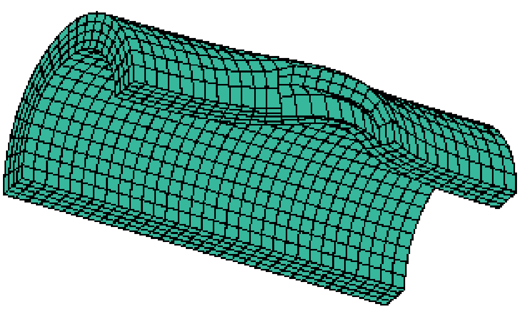

Figure 3.39: The collapse mechanism for the defected pipeline using the MECM and FEM

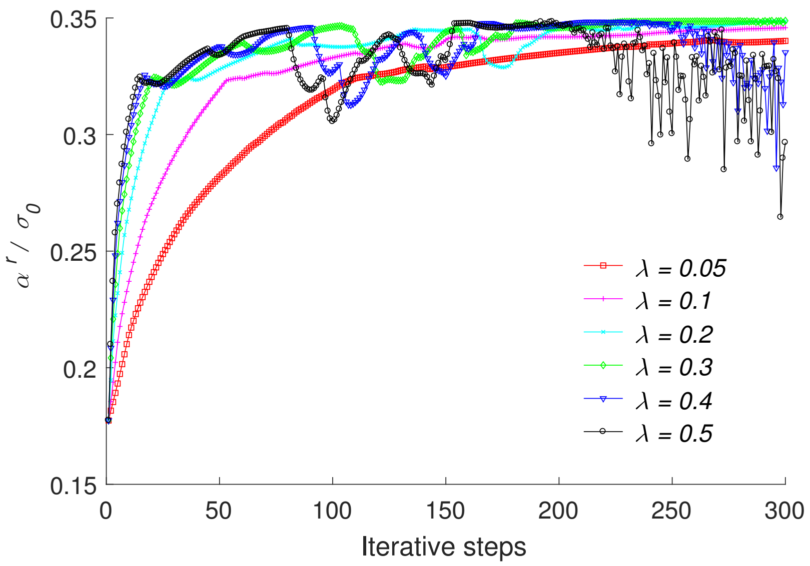

Figure 3.40: Variation of load multiplier solutions with λ for the defected pipeline problem (case b) using the MECM and FEM

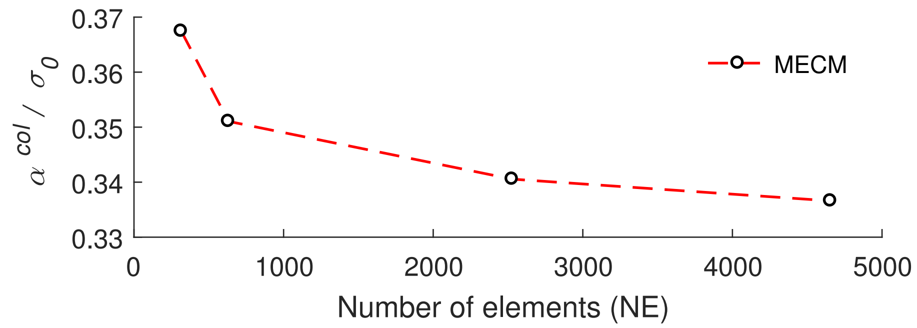

Figure 3.41: Variation of the collapse load solution with the number of elements for the defected pipeline using the MECM and FEM

for different values of λ. As seen, the oscillations are increased for high values of λ, and the divergence occurred before a better collapse load is obtained. The choice of $\lambda = 0.05$, however, leads to an acceptable level of accuracy for this example.

The variation of the normalized collapse load solution with respect to the number of elements is shown in Fig. 3.41. As seen, by increasing the number of elements, the collapse load solution is decreased. However, as the analytical solution is not available for this example, no justification about the trend of the solution (i.e. a lower bound solution or a strict one) can be done.

3.6 Concluding Remarks

In this chapter, the implementation of the MECM for a range of 2D and 3D problems was explained. In particular, the importance of the value of the Poisson's ratio in the MECM procedure was studied through an example and use of mixed finite element. It was emphasized that the incompressibility is vital for a true collapse load solution. It was illustrated that the use of Poisson's ratio less than 0.45 may lead to a wrong convergence in the MECM. The value of $\nu = 0.499$ was shown to be close enough to 0.5 to satisfy the nearly incompressible condition.

The use of the finite element method in the MECM was evaluated and it was shown that the popular widely-used low order displacement-based finite elements can be used along with the MECM when selective integration scheme is applied to evaluate the element stiffness matrices under nearly incompressible condition. The performance of this scheme was validated for a range of 2D benchmarks and 3D structures. The analysis procedures were implemented within a MATLAB programming environment, allowing the element stiffness matrices to be computed only once in the first iteration, and then stored. In the subsequent iterations, their factored matrices were used for assembling the total stiffness matrix. This increases the efficiency of the method.

The numerical examples illustrated that all of the estimated collapse load results tend to converge to the lower bound limits when a sufficient number of structural discretization has been attained. This emphasizes the importance of using a high quality fine mesh along with the scheme. Constructing a high quality fine mesh, specially for 3D structures, often requires tedious human interventions and is time-consuming. The next chapter illustrates the use of SBFEM, which allows the user to incorporate the automatic mesh constructions using quadtree and octree algorithms for the analysis of structures in 2D and 3D spaces.

Chapter 4

THE MECM FOR COLLAPSE LOAD DETERMINATION OF STRUCTURES USING THE SCALED BOUNDARY FINITE ELEMENT METHOD

4.1 Introduction

The success of the MECM depends on the precision and quality of the structural discrete model employed during elastic analyses, as poor structural discretization will lead to overestimation of the collapse load solution as discussed in the last chapter. Constructing a high quality mesh, specially for 3D structures, often requires tedious human efforts and is time-consuming. Even for semi-automatic procedures, it is tedious, error prone and does not contain safeguards to ensure the validity of the discretization for the medium of interest.

The automatic mesh generation has been a topic of active research for decades [93, 94, 95, 96]. In 2D structures, quadtree decomposition has been widely utilized

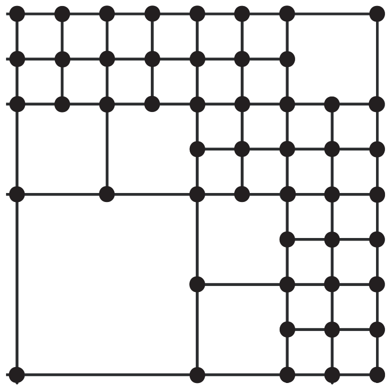

Figure 4.1: Hanging nodes in a quadtree mesh [3]

in the automatic mesh generation [97, 98, 99] due to its simplicity, efficiency and ability in achieving rapid and smooth transitions of element sizes between region of mesh refinements. Employment of the quadtree approach within the scheme of the finite element, however, is not widespread. The main reason for this is the presence of hanging nodes, shown in Fig. 4.1 as filled circles. The hanging nodes cause displacement incompatibility between the adjacent elements. Special treatments of the hanging nodes are necessary in a finite element analysis.

In 3D spaces, techniques to reduce the burden on automatic mesh generation from the computer-aided design (CAD) models have been extensively researched. Hughes et al. [100] first proposed the idea of the isogeometric analysis (IGA) and used NURBS (non-uniform rational B-splines) to construct the basis functions of the solution. The key advantage of the IGA is that there is no need of meshing, which leads to a seamless integration of analysis and engineering design. Kim et al. [101] made the IGA method available for the analysis of complex surfaces by adding the trimming techniques to the method. Bazilevs et al. [102] further improved the IGA by employing the T-splines as a replacement of NURBS. T-splines allow local refinement and watertight combination of parts, which is more versatile in presenting CAD models. The IGA concept has been used to resolve many problems such as structural vibrations [103], large deformations [104], and fluid-structure interactions [105].

With respect to the representation of the geometry, the standard tessellation language (STL) has been widely supported in the present CAD industry. This is due to its unique use in 3D printing and rapid prototyping [106, 107]. The advantage of STL is its simplicity. For an STL model only unstructured triangular facets are required, which can be ill-shaped, overlapping, and self intersecting. This simplicity has made its applications even wider than NURBS. This drew the attention of the mesh generation community to develop automatic mesh generators from the STL model. So far, a number of surface re-meshing methods have been developed to generate computational meshes from STL models for the FEM [108, 109]. However, these methods are dependent on the characteristics of the STL models, and require surfaces which are manifold, watertight, not overlapping, and not self-intersecting. Otherwise, mesh repairing technique [110] should be performed which is a challenging and non-trivial topic. Additionally, even if high-quality triangular surfaces can be generated, the corresponding mesh is tetrahedral, and inferior to hexahedral mesh concerning the stress analysis accuracy required for the ECM/MECM. Until now, the well-known commercial FE software (e.g. ANSYS and Abaqus) cannot robustly perform analyses on STL models.

In 3D problems, similar to 2D quadtree technique, octree structure has been used for the purpose of the automatic mesh generation; however, the application of this efficient algorithm is relatively rare due to the difficulty of handling the hanging nodes by the FEM [111].

To reduce the burden of the mesh generation in producing reasonably fine meshes required for the MECM, in this chapter, the scaled boundary finite element method (SBFEM) is employed to be used along with the MECM. Firmly established in [19, 20], the SBFEM has simple mesh requirements, a sound theoretical basis and a robust convergent solution for the linear elastic analysis. The use of polygonal-shaped (in 2D) [21, 22, 3] or polyhedral-shaped (in 3D) [5, 112] SBFEs enables all hanging nodes to be modeled effectively whilst still maintaining the numerical stability. This feature is the main advantage of using the SBFEM over the FEM and iso-geometric FEM in this study. Therefore, the automated quadtree/octree algorithms can be incorporated directly within the SBFE framework. This allows the SBFE discretization to be constructed from an in-plane solid (in 2D problems) or of a solid 3D CAD model (in 3D problems). The use of the subdomains (analogous to elements in the FEM) with polygonal/polyhedral shapes and of an arbitrary number of edges/faces automatically and efficiently handles the structures with complex geometries (e.g. curved boundaries, holes, etc.), and minimizes the user interference and its associated errors in mesh generation part. Additionally, the performance of the SBFEM under the nearly incompressible condition is sufficiently accurate without any specific treatment [113], which makes it suitable for MECM.

This chapter is organized as follows. First, in section 4.2, the important formulation for the SBFEM are explained for 2D and 3D structures. Then, in section 4.3, the automated mesh generation for 2D and 3D domains are discussed using the quadtree and octree algorithms, respectively. In section 4.4, the use of the MCEM along with the SBFEM for the determination of the collapse load of a structure is proposed, and its implementation is described. The application of the proposed scheme to some 2D benchmarks and 3D structures are shown in section 4.5 to highlight its performance. The conclusion and remarks are summarized in section 4.6 of this chapter.

It is acknowledged that some of the materials used in this chapter are used in publications/submissions 1 and 3 mentioned in section 1.5.

4.2 Scaled Boundary Finite Element Formulation

This section reviews the SBFEM formulations [19, 20, 114, 112] of structures in 2D (and 3D) spaces. The relations are based on the assumptions of geometric linearity and elastic material properties.

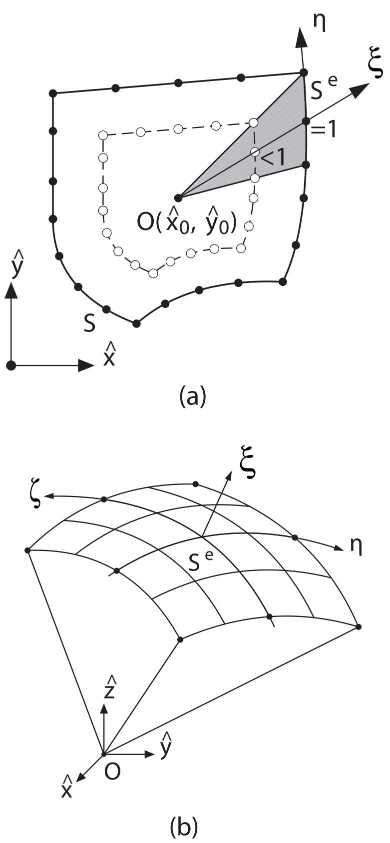

Figure 4.2: Generic SBFE subdomain (a) 2D case, (b) 3D case

For clarity of the following expressions, a generic polygon-type SBFE subdomain [115, 19, 20] is considered in Fig. 4.2, where a scaling centre "O" is defined at a location directly visible from the whole boundary of the subdomain. The boundary is divided into line elements (see Fig. 4.2a). The geometry of the 2D domain is expressed in a 2D curvilinear scaled boundary coordinates (η, ξ) . For a 3D subdomain, the boundary is divided into doubly-curved surface elements (Fig. 4.2b). The 3D scaled boundry coordinates (η, ζ, ξ) are introduced.

The geometry of the boundary along a circumferential direction is described using standard shape functions, namely $N(\eta)$ for $-1 \leq \eta \leq 1$ and $N(\eta, \zeta)$ for $-1 \leq \eta \leq 1$ and $-1 \leq \zeta \leq 1$ in 2D and 3D spaces, respectively. The dimensionless radial coordinate ξ describes the subdomain by scaling the boundary between the scaling center (where $\xi = 0$) and the boundary ($\xi = 1$).

The coordinate transformation between the Cartesian (x, y) and (x, y, z) coordinates and the local scaled boundary coordinate systems (η, ξ) and (η, ζ, ξ) are given by the scaled boundary transformation equations [115], viz.

- In a 2D space

$$\begin{aligned} x(\xi,\eta) &= \xi \mathbf{x}_\mathrm{b}(\eta) = \xi \mathbf{N}(\eta)\,\mathbf{x}_\mathrm{b} \\ y(\xi,\eta) &= \xi \mathbf{y}_\mathrm{b}(\eta) = \xi \mathbf{N}(\eta)\,\mathbf{y}_\mathrm{b} \end{aligned} \tag{4.1}$$

- In a 3D space

$$\begin{aligned} x(\xi,\eta,\zeta) &= \xi \mathbf{x}_\mathrm{b}(\eta,\zeta) = \xi \mathbf{N}(\eta,\zeta)\,\mathbf{x}_\mathrm{b} \\ y(\xi,\eta,\zeta) &= \xi \mathbf{y}_\mathrm{b}(\eta,\zeta) = \xi \mathbf{N}(\eta,\zeta)\,\mathbf{y}_\mathrm{b} \\ z(\xi,\eta,\zeta) &= \xi \mathbf{z}_\mathrm{b}(\eta,\zeta) = \xi \mathbf{N}(\eta,\zeta)\,\mathbf{z}_\mathrm{b} \end{aligned} \tag{4.2}$$

, where $\{x(\xi,\eta)\ y(\xi,\eta)\}$ and $\{x(\xi,\eta,\zeta)\ y(\xi,\eta,\zeta)\ z(\xi,\eta,\zeta)\}$ are the coordinates of a point in the subdomain in 2D and 3D spaces, respectively. $\mathbf{x}_\mathrm{b} = [x_1\, x_2\, \ldots\, x_Q]^\mathrm{T}$ and $\mathbf{y}_\mathrm{b} = [y_1\, y_2\, \ldots\, y_Q]^\mathrm{T}$ (in Eq. (4.1)) are the vectors containing the nodal coordinates on each line elements, and $\mathbf{x}_\mathrm{b} = [x_1\, x_2\, \ldots\, x_Q]^\mathrm{T}$, $\mathbf{y}_\mathrm{b} = [y_1\, y_2\, \ldots\, y_Q]^\mathrm{T}$, and $\mathbf{z}_\mathrm{b} = [z_1\, z_2\, \ldots\, z_Q]^\mathrm{T}$ (in Eq. (4.2)) are the vectors containing the nodal coordinates on each surface elements. The subscript Q is the total number of nodes on the line elements (in 2D) or on the surface elements (in 3D). $\mathbf{N}(\eta)$ and $\mathbf{N}(\eta,\zeta)$ are the shape function matrices, which are defined as follows:

- In a 2D space

$$\mathbf{N}(\eta) = [N_1(\eta),\ N_2(\eta),\ \ldots,\ N_Q(\eta)] \tag{4.3}$$

- In a 3D space

$$\mathbf{N}(\eta,\zeta) = [N_1(\eta,\zeta),\ N_2(\eta,\zeta),\ \ldots,\ N_Q(\eta,\zeta)]\,. \tag{4.4}$$

For a generic SBFE subdomain, the displacement field adopts

- In a 2D (ξ, η) coordinate system

$$\mathbf{u}(\xi, \eta) = \mathbf{N}_{\mathbf{u}}(\eta)\, \mathbf{u}(\xi) \tag{4.5}$$

- In a 3D (ξ, η, ζ) coordinate system

$$\mathbf{u}(\xi, \eta, \zeta) = \mathbf{N}_{\mathbf{u}}(\eta, \zeta)\, \mathbf{u}(\xi) \tag{4.6}$$

, where $\mathbf{N}_{\mathbf{u}}(\eta)$ and $\mathbf{N}_{\mathbf{u}}(\eta, \zeta)$ are the interpolation shape functions and defined as

- In a 2D space

$$\mathbf{N}_{\mathbf{u}}(\eta) = [N_1 \mathbf{I}(\eta),\ N_2 \mathbf{I}(\eta),\ \ldots,\ N_Q \mathbf{I}(\eta)] \tag{4.7}$$

- In a 3D space

$$\mathbf{N}_{\mathbf{u}}(\eta, \zeta) = [N_1 \mathbf{I}(\eta, \zeta),\ N_2 \mathbf{I}(\eta, \zeta),\ \ldots,\ N_Q \mathbf{I}(\eta, \zeta)]\,. \tag{4.8}$$

$\mathbf{I}$ represents a 2×2 identity matrix in 2D spaces and a 3×3 identity matrix in 3D spaces. $\mathbf{u}(\xi)$in Eqs. (4.5) and (4.6) is the radial displacement function and is obtained by solving the scaled boundary finite element equations in displacement[115]:

$$\mathbf{E}_0 \xi^2 \mathbf{u}(\xi)_{,\xi\xi} + \left((s-1)\mathbf{E}_0 - \mathbf{E}_1 + \mathbf{E}_1^{\mathrm{T}}\right) \xi \mathbf{u}(\xi)_{,\xi} + \left((s-2)\mathbf{E}_1^{\mathrm{T}} - \mathbf{E}_2\right) \mathbf{u}(\xi) = 0 \tag{4.9}$$

, where $s = 2$ and 3 in 2D and 3D spaces, respectively. The coefficient matrices are as follows:

- In a 2D space

$$\mathbf{E}_0 = \int_{-1}^{+1} \mathbf{B}_1^{\mathrm{T}}(\eta)\, \mathbf{D} \mathbf{B}_1(\eta)\, |\mathbf{J}(\eta)| d\eta \tag{4.10}$$

$$\mathbf{E}_1 = \int_{-1}^{+1} \mathbf{B}_2^{\mathrm{T}}(\eta)\, \mathbf{D} \mathbf{B}_1(\eta)\, |\mathbf{J}(\eta)| d\eta \tag{4.11}$$

$$\mathbf{E}_2 = \int_{-1}^{+1} \mathbf{B}_2^{\mathrm{T}}(\eta)\, \mathbf{D} \mathbf{B}_2(\eta)\, |\mathbf{J}(\eta)| d\eta \tag{4.12}$$

- In a 3D space

$$\mathbf{E}_0 = \int_S \mathbf{B}_1^{\mathrm{T}}(\eta,\zeta)\,\mathbf{D}\mathbf{B}_1(\eta,\zeta)\,|\mathbf{J}(\eta,\zeta)|d\eta d\zeta \tag{4.13}$$

$$\mathbf{E}_1 = \int_S \mathbf{B}_2^{\mathrm{T}}(\eta,\zeta)\,\mathbf{D}\mathbf{B}_1(\eta,\zeta)\,|\mathbf{J}(\eta,\zeta)|d\eta d\zeta \tag{4.14}$$

$$\mathbf{E}_2 = \int_S \mathbf{B}_2^{\mathrm{T}}(\eta,\zeta)\,\mathbf{D}\mathbf{B}_2(\eta,\zeta)\,|\mathbf{J}(\eta,\zeta)|d\eta d\zeta \tag{4.15}$$

In above equations, $\mathbf{D}$ is the material constitutive matrix. $\{\mathbf{B}_1(\eta), \mathbf{B}_2(\eta)\}$ and $\{\mathbf{B}_1(\eta,\zeta), \mathbf{B}_2(\eta,\zeta)\}$ are the SBFEM strain-displacement matrices in 2D and 3D respectively. $|\mathbf{J}(\eta)|$ and $|\mathbf{J}(\eta,\zeta)|$ are the Jacobians on the boundary required for coordinate transformation in 2D and 3D spaces.

The internal nodal forces along the radial direction are expressed as

$$\mathbf{q}(\xi) = \xi^{s-2}\left(\mathbf{E}_0\xi\mathbf{u}(\xi)_{,\xi} + \mathbf{E}_1^{\mathrm{T}}\mathbf{u}(\xi)\right). \tag{4.16}$$

Further, formulating the two Eqs. (4.9) and (4.16) as the first-order ordinary differential system with twice the number of unknowns results in

$$\xi\mathbf{X}(\xi)_{,\xi} = -\mathbf{Z}\mathbf{X}(\xi) \tag{4.17}$$

, where the variable $\mathbf{X}(\xi)$ is defined as

$$\mathbf{X}(\xi) = \left[\xi^{+0.5(s-2)}\mathbf{u}(\xi) \quad \xi^{-0.5(s-2)}\mathbf{q}(\xi)\right]^{\mathrm{T}}. \tag{4.18}$$

$\mathbf{Z}$ is the Hamiltonian matrix as follows

$$\mathbf{Z} = \begin{bmatrix} \mathbf{E}_0^{-1}\mathbf{E}_1^{\mathrm{T}} - 0.5(s-2)\mathbf{I} & -\mathbf{E}_0^{-1} \\ \mathbf{E}_1\mathbf{E}_0^{-1}\mathbf{E}_1^{\mathrm{T}} - \mathbf{E}_2 & -\left(\mathbf{E}_1\mathbf{E}_0^{-1} - 0.50.5(s-2)\mathbf{I}\right) \end{bmatrix} \tag{4.19}$$

, and $\mathbf{I}$ is an identity matrix of appropriate size.

The scaled boundary finite-element equation is solved with the eigenvalue method. The formal solution of $\mathbf{X}(\xi)$ can be considered as

$$\mathbf{X}(\xi) = \xi^{-\lambda_i}\mathbf{\Phi}_i. \tag{4.20}$$

Substituting Eq. (4.20) into Eq. (4.17) results in the eigenproblem of matrix $\mathbf{Z}$

$$\mathbf{Z}\mathbf{\Phi}_i = \lambda_i\mathbf{\Phi}_i \tag{4.21}$$

with the eigenvalue λ_i and eigenvectors $\mathbf{\Phi}_i$, where if λ_i is an eigenvalue of $\mathbf{Z}$ matrix, $-\lambda_i$ is also an eigenvalue. If the translational motions, denoted as $\mathbf{u}_t$, are not constrained, the vector $\mathbf{\Phi}_t$ corresponding to the translational motion is formed as

$$\mathbf{\Phi}_t = \begin{Bmatrix} \mathbf{u}_t \\ 0 \end{Bmatrix}. \tag{4.22}$$

It can be proved [114] that $\mathbf{\Phi}_i$ is an eigenvector of $\mathbf{Z}$, and its corresponding eigenvalues are

$$\lambda_t = \pm 0.5\left(s-2\right). \tag{4.23}$$

In three dimensions, $\lambda_t = \pm 0.5$, and no zero eigenvalues exist in Eq. (4.21). Between $2n$ eigenvalues of $\mathbf{Z}$, n of them are with positive real parts and n of them are with negative real parts. In two dimensional problems, $\lambda_t = 0$ is concluded from Eq. (4.23). Each translational motions is corresponding to a pair of zero eigenvalues. Here, to facilitate the solution procedure, the zero eigenvalues are removed by substituting $\mathbf{E}_2$ with $\mathbf{E}_2 + \varepsilon\mathbf{I}$, where ε is a highly small value with the same dimensions of $\mathbf{E}_2$. This action separates the eigenvalues into two two groups of equal sizes and based on the signs of their real parts [114].

The eigenvalue decomposition of $\mathbf{Z}$ gives

$$\mathbf{Z}\mathbf{\Phi} = \mathbf{\Phi}\mathbf{\Lambda} = \begin{bmatrix} \mathbf{\Phi}_{\mathrm{u}}^{(\mathrm{n})} & \mathbf{\Phi}_{\mathrm{u}}^{(\mathrm{p})} \\ \mathbf{\Phi}_{\mathrm{q}}^{(\mathrm{n})} & \mathbf{\Phi}_{\mathrm{q}}^{(\mathrm{p})} \end{bmatrix} \begin{bmatrix} \mathbf{\Lambda}^{(\mathrm{n})} & 0 \\ 0 & \mathbf{\Lambda}^{(\mathrm{p})} \end{bmatrix}. \tag{4.24}$$

$\mathbf{\Lambda}^{(\mathrm{n})}$ and $\mathbf{\Lambda}^{(\mathrm{p})}$ are the eigenvalue matrices, whose real parts are negative and positive, respectively. $\mathbf{\Phi}_{\mathrm{u}}^{(\mathrm{n})}$ and $\mathbf{\Phi}_{\mathrm{q}}^{(\mathrm{n})}$ are the eigenvectors of $\mathbf{\Lambda}^{(\mathrm{n})}$, and $\mathbf{\Phi}_{\mathrm{u}}^{(\mathrm{p})}$ and $\mathbf{\Phi}_{\mathrm{q}}^{(\mathrm{p})}$ are the eigenvectors of $\mathbf{\Lambda}^{(\mathrm{p})}$.

The bounded domain is considered, where the associated eigenvalues retain only the negative real parts, satisfying the condition of finite displacements at the scaling center "O". Hence, substituting Eq. (4.24) into Eq. (4.17) provides the solutions of displacements and nodal internal forces as follows

$$\mathbf{u}(\xi) = \mathbf{\Phi}_{\mathrm{u}}^{(\mathrm{n})} \xi^{-(\mathbf{\Lambda}^{(\mathrm{n})}+0.5(s-2)\mathbf{I})} \mathbf{c}^{(\mathrm{n})}, \tag{4.25}$$

$$\mathbf{q}(\xi) = \mathbf{\Phi}_{\mathrm{q}}^{(\mathrm{n})} \xi^{-(\mathbf{\Lambda}^{(\mathrm{n})}-0.5(s-2)\mathbf{I})} \mathbf{c}^{(\mathrm{n})} \tag{4.26}$$

, where $\mathbf{c}^{(\mathrm{n})}$ is integration constants. The solutions of Eqs. (4.25) and (4.26) on the boundary ($\xi = 1$) of the subdomain, that is $\mathbf{u}_{\mathrm{b}} = \mathbf{u}(\xi = 1)$ and $\mathbf{q}_{\mathrm{b}} = \mathbf{q}(\xi = 1)$, can be written as

$$\mathbf{u}_{\mathrm{b}} = \mathbf{\Phi}_{\mathrm{u}}^{(\mathrm{n})} \mathbf{c}^{(\mathrm{n})}, \tag{4.27}$$

$$\mathbf{q}_{\mathrm{b}} = \mathbf{\Phi}_{\mathrm{q}}^{(\mathrm{n})} \mathbf{c}^{(\mathrm{n})}. \tag{4.28}$$

The stiffness matrix of each subdomain, $\mathbf{K}$, can be formulated in terms of $\mathbf{u}_{\mathrm{b}}$ and $\mathbf{q}_{\mathrm{b}}$ (defined in Eqs. (4.27) and (4.28)) as

$$\mathbf{q}_{\mathrm{b}} = \mathbf{K}\mathbf{u}_{\mathrm{b}}. \tag{4.29}$$

Using Eqs. (4.27) and (4.28), $\mathbf{K}$ can be also written as

$$\mathbf{K} = \mathbf{\Phi}_{\mathrm{q}}^{(\mathrm{n})} \left(\mathbf{\Phi}_{\mathrm{u}}^{(\mathrm{n})}\right)^{-1}. \tag{4.30}$$

Having all the stifness matrices of all subdomains, the global stiffness matrix of the domain can be obtained by the assembly of all subdomain's stiffness matrices in the same way as the FEM to be used in the following global equation

$$\mathbf{K}_{\mathrm{G}}\mathbf{u}_{\mathrm{G}} = \mathbf{F}_{\mathrm{G}}. \tag{4.31}$$

Here, $\mathbf{K}_{\mathrm{G}}$ is the global stiffness matrix, $\mathbf{F}_{\mathrm{G}}$ is the global nodal force vector and $\mathbf{u}_{\mathrm{G}}$ is the global nodal displacements of the whole domain. After enforcing the boundary conditions, a system of linear equations is solved (similar to the FEM) to obtain the global nodal displacements $\mathbf{u}_{\mathrm{G}}$.

The nodal displacement on the boundary $\mathbf{u}_{\mathrm{b}}$ of a subdomain is extracted from the global displacements $\mathbf{u}_{\mathrm{G}}$ according to the connectivity of the elements. Thereafter, the integration constants $\mathbf{c}^{(\mathrm{n})}$ in Eqs. (4.25) and (4.26) can be determined from the nodal displacements as

$$\mathbf{c}^{(\mathrm{n})} = \left(\boldsymbol{\Phi}_{\mathrm{u}}^{(\mathrm{n})}\right)^{-1} \mathbf{u}_{\mathrm{b}}. \tag{4.32}$$

For each SBFE subdomain, the stresses are computed at an element level using the Hooke's law (section 2.2.4) and the strain-displacement relationship, and defined by

- In a 2D space

$$\boldsymbol{\sigma}\left(\xi,\eta\right) = \mathbf{D}\left(\mathbf{B}_1\left(\eta\right)\mathbf{u}\left(\xi\right)_{,\xi} + \frac{1}{\xi}\mathbf{B}_2\left(\eta\right)\mathbf{u}\left(\xi\right)\right) \tag{4.33}$$

- In a 3D space

$$\boldsymbol{\sigma}\left(\xi,\eta,\zeta\right) = \mathbf{D}\left(\mathbf{B}_1\left(\eta,\zeta\right)\mathbf{u}\left(\xi\right)_{,\xi} + \frac{1}{\xi}\mathbf{B}_2\left(\eta,\zeta\right)\mathbf{u}\left(\xi\right)\right). \tag{4.34}$$

Substituting Eq. (4.25) into Eqs. (4.33) and (4.34) yields

- In a 2D space

$$\boldsymbol{\sigma}\left(\xi,\eta\right) = \boldsymbol{\Psi}_{\sigma}\left(\eta\right)\xi^{-\left(\boldsymbol{\Lambda}^{(\mathrm{n})}+\mathbf{I}\right)}\mathbf{c}^{(\mathrm{n})} \tag{4.35}$$

- In a 3D space

$$\boldsymbol{\sigma}\left(\xi,\eta,\zeta\right)=\boldsymbol{\Psi}_{\sigma}\left(\eta,\zeta\right)\xi^{-\left(\boldsymbol{\Lambda}^{(\mathrm{n})}+1.5\mathbf{I}\right)}\mathbf{c}^{(\mathrm{n})} \tag{4.36}$$

, where

$$\boldsymbol{\Psi}_{\sigma}\left(\eta\right)=\mathbf{D}\left(-\mathbf{B}_{1}\left(\eta\right)\boldsymbol{\Phi}_{\mathrm{u}}^{(\mathrm{n})}\boldsymbol{\Lambda}^{(\mathrm{n})}+\mathbf{B}_{2}\left(\eta\right)\boldsymbol{\Phi}_{\mathrm{u}}^{(\mathrm{n})}\right), \tag{4.37}$$

$$\boldsymbol{\Psi}_{\sigma}\left(\eta,\zeta\right)=\mathbf{D}\left(-\mathbf{B}_{1}\left(\eta,\zeta\right)\boldsymbol{\Phi}_{\mathrm{u}}^{(\mathrm{n})}\left(\boldsymbol{\Lambda}^{(\mathrm{n})}+0.5\mathbf{I}\right)+\mathbf{B}_{2}\left(\eta,\zeta\right)\boldsymbol{\Phi}_{\mathrm{u}}^{(\mathrm{n})}\right) \tag{4.38}$$

define stress modes associated with structures in 2D and 3D geometry systems, respectively.

4.3 Automatic Mesh Generation Using the SBFEM

4.3.1 Polygonal Quadtree Mesh Generation

For the structural system that can be defined in a 2D space, the structural discrete model adopts the computationally advantageous quadtree mesh generation technique using polygon-shaped SBFEs [3]. Such methodology provides a rapid and automated procedure to discretize structures with (complex) 2D geometries.

The algorithmic implementation of the quadtree SBFE model is summarized in Fig. 4.3, where S_{max} is the maximum allowed number of seed points in a cell, S_b seed points on each boundary, and S_{roi} seed points around each region of interest, and l_{max} the maximum difference between the division levels of adjacent cells. In this scheme, the geometry information of the whole structural system is controlled by the signed distance function. The function of a point $\mathrm{X} \in \mathrm{R}^2$ within a SBFE subdomain Ω is graphically described in Fig. 4.4, and its mathematical description is given by

$$d_{\Omega}\left(x\right)=s_{\Omega}\left(x\right)\min_{y\in\partial\Omega}||x-y||, \tag{4.39}$$

, where $\partial\Omega$ represents the boundary of the subdomain, $||x-y||$ is the Euclidean norm in R^2 with $y \in \partial\Omega$, and $s_{\Omega}\left(x\right)$ the sign function (namely –1 inside the subdomain or

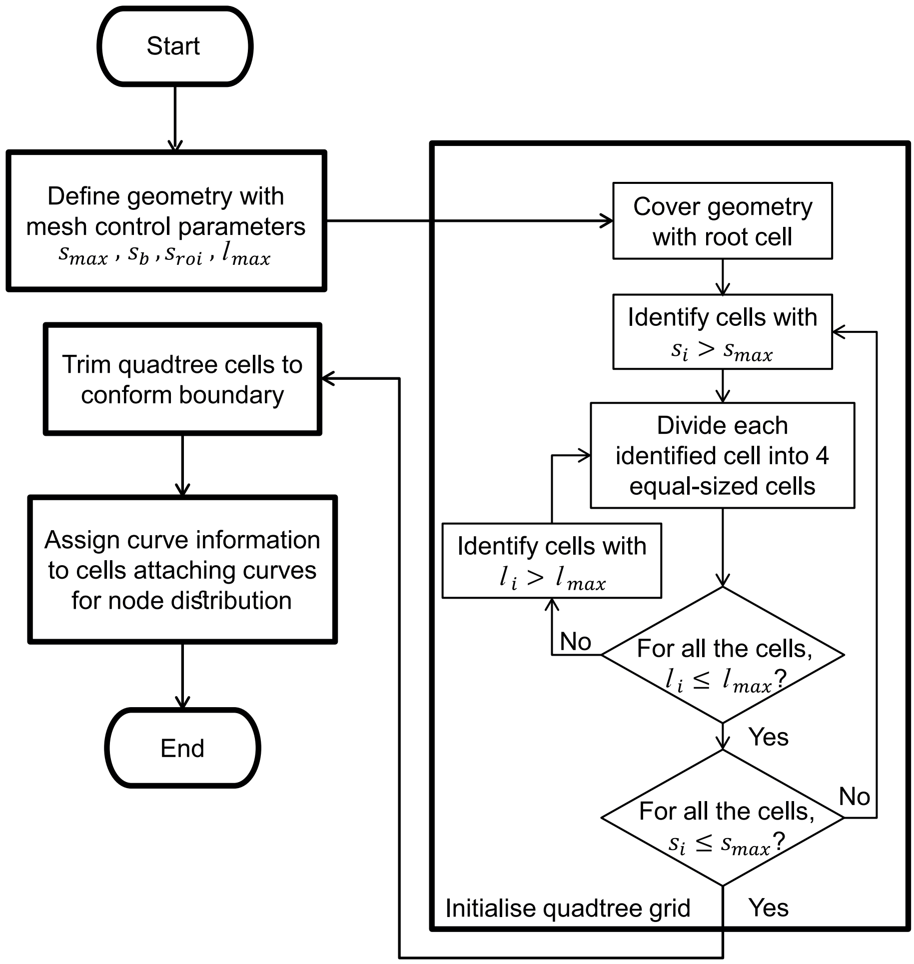

Figure 4.3: Flowchart for quadtree mesh generation procedures

1 otherwise). Boolean operations are employed to implement the complex geometry of the structure concerned [116].

A series of seed points are predefined to control the local density and quality of the quadtree cells adopted in the boundary. The entire domain is initially covered by a single square, called root cell. The root cell is divided into 4 square cells, provided that the number of seed points S_i is larger than the maximum allowable limit of the corresponding cell, S_{max}. This process is iteratively performed until the number of seed points of all cells are less than a predefined value. At each iteration, the cell with the high division level between the contiguous cells, namely $l_i > l_{max}$, is subdivided. The diagram in 4.5 illustrates this recursive process used to obtain an initial grid in 4.5b of a square plate with a circular perforation (Fig. 4.5a). In Fig. 4.5b, the initial quadtree mesh does not exactly conform to the boundary. Therefore, cells that

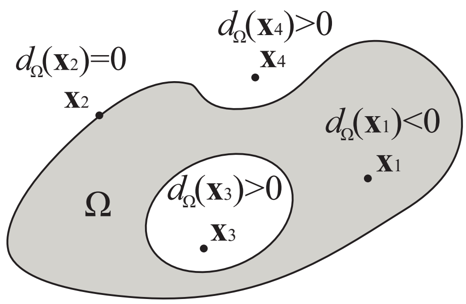

Figure 4.4: Signed distance function of a point inside the domain (X1), on the boundary (X2), and outside the domain (X3 and X4)

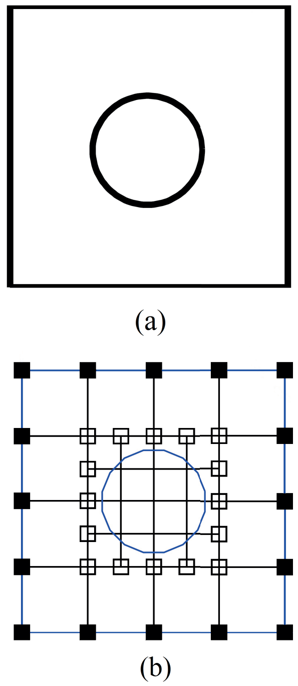

Figure 4.5: Square plate with circular hole (a) geometry, (b) initial quadtree grid mesh

intersect with the boundary are trimmed to form polygon shapes. The locations of vertices are determined by the signs and magnitudes of the signed distance functions; the vertices on the boundary are assigned with solid square markers, whilst those inside the boundary with open square markers.

It is noted that ill-shaped polygon cells, which contain much shorter edges as compared to the others, can be generated around the vertices close to the boundary. A threshold distance (e.g. 1/10 of the smallest cell edge attached to the vertex) determines whether those points are required to move to the boundary. In Fig. 4.6, the implementation of the quadtree SBFE model over a circular perforated plate is

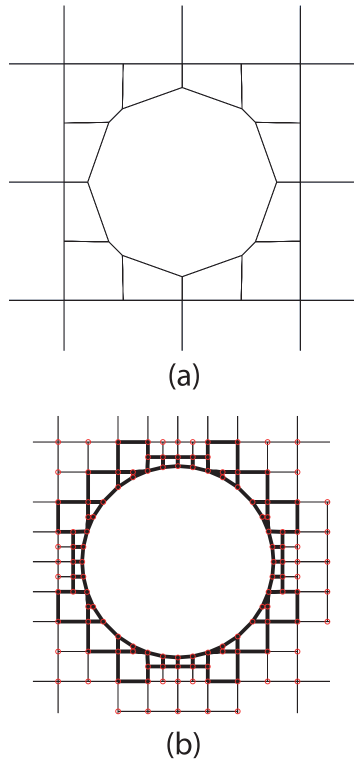

Figure 4.6: SBFE meshes around circular hole (a) standard polygon subdomains, (b) quadtree refinement

illustrated. In essence, Fig. 4.6a shows that coarse polygon cells are first assigned on the circular inner boundary. In Fig. 4.6b, the quadtree mesh is further refined to enhance the SBFE discretization around the circular hole using polygon-shape cells.

4.3.2 Polyhedral Octree Mesh Generation

In 3D problems, the typical elements available in the conventional FEM are limited to tetrahedrons and hexahedrons. Due to the limitations employed in these elements, the computer algorithms used for the analysis process are relatively simple. However, these restrictions shift the challenges to the meshing process. Therefore, the discretization of the problems with curved or complex geometrical features which cannot be easily modeled with tetrahedral or hexahedral elements, normally requires extensive pre-processing. This causes a tedious effort for mesh constructions of structures with complex geometries.

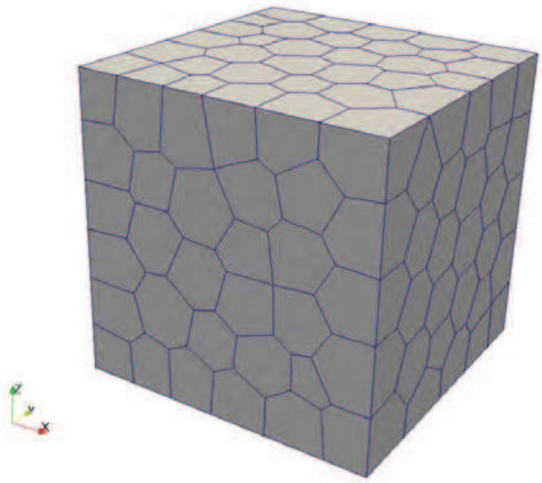

Figure 4.7: A cubic domain meshed with arbitrary polyhedral elements [4]

One solution to this problem is to relax the restrictions by using arbitrary polyhedral elements in the meshing process. An example showing the discretization of a cubic domain using polyhedral elements is provided in Fig. 4.7. With the new library of these polyhedral elements, the tetrahedral or hexahedral elements are automatically included. The use of polyhedral elements brings more flexibility in the meshing process. This is because a mesh for a complex boundary shapes can be constructed without the limitation of using very fine tetrahedral meshes.

In this section, the automatic octree mesh generation from CAD models by the use of scaled boundary polyhedral subdomains for 3D structures is explained. The basic idea of the ployhedral meshing method is to trim an octree grid by a CAD model and then converting the trimmed grid to a polyhedral mesh. In particular the STL surfaces, discussed in sections 4.1 and 4.3.2.1, are considered as the CAD input due to their popularity and ubiquitous applications in CAD software. The reader is referred to [5] for the comprehensive discussion on the method.

4.3.2.1 3D surface models in the STL format

An STL file describes the surface of a solid object in CAD software by using the unit normal and vertices of unstructured triangles. The simplicity of the STL model has

Figure 4.8: A surface model of a sphinx in the STL format [5]

made it one of the most popular formats for CAD software. Its simplicity is rooted in the fact that it does not enforce any closeness and connectedness requirements. Fig. 4.8 shows an example of an STL model of a sphinx [5]. The left model is the surface with shading features. The right model presents the the unstructured triangles.

With respect to the employed polyhedral mesh generation scheme, the STL model does not need to be flawless. Degenerated triangles, self-intersecting parts and overlapping facets are permitted in the input STL files, which makes the input of the polyhedral octree meshing technique simple and therefore universal.

4.3.2.2 Octree grid generation

Octree structure is first introduced by Meagher [117] for 3D computer graphics. Similar to the quadtree scheme, the generation procedure starts from a cube (cell), which is also known as the root. The root is recursively divided into 8 new cells until some stopping criteria are met (Fig. 4.9). The newly generated cells are called the children of the subdivided cell.

For an STL model, the entire domain is first covered by defining a bounding box. The minimum size of an octree cell, S_{min}, and the ratio between the maximum and minimum sizes of octree cells, S_{ratio}, are then defined. Therefore, the maximum size of an octree cell is equal to $S_{\text{max}} = S_{\text{min}} \times S_{\text{ratio}}$. The mesh generation is started by

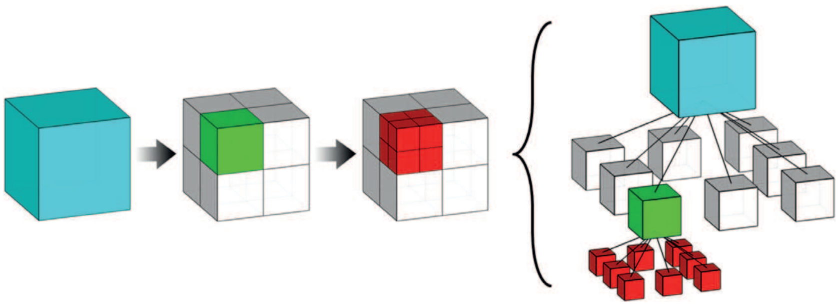

Figure 4.9: An octree grid with three levels [5]

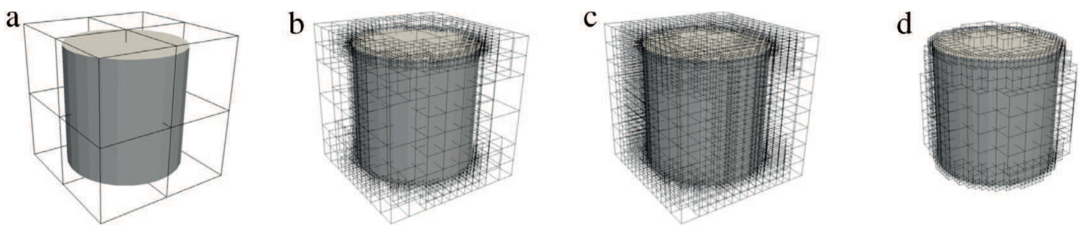

Figure 4.10: The octree generation of a cylinder (a) the initial subdivision (b) the subdivision considering high curvature (c) the 2:1 balanced octree grid and (d) the octree grid without external cells [5]

dividing the bounding box into smaller cubes with the size $S_{\max}$ as illustrated in Fig. 4.10a. Then, the cells intersecting the STL surface are identified and subdivided if their size are larger than $S_{\min}$ and the curvature of the cell surface is higher than the threshold (Fig. 4.10b). Additionally, the subdivisions are needed for the cells with multi-intersection edges. After completion of all the cells subdivisions, the 2:1 rule [118] is enforced on the octree grid to provide a balance grid (Fig. 4.10c). The cells outside the model are later removed in the meshing process. Fig. 4.10d demonstrates the octree grid which bounds the model.

4.3.2.3 Trimming an octree grid by an STL model

The octree grid bounding the STL model needs to be trimmed by the STL model to conform the boundary. The trimming process follows the bottom-up scheme shown in Fig. 4.11. It first splits edges and then trims faces, cells and octree grids sequentially.

Similar to the quadtree, the trimming operations are based on the signs of the points. As negative points are inside the model, they are naturally included in

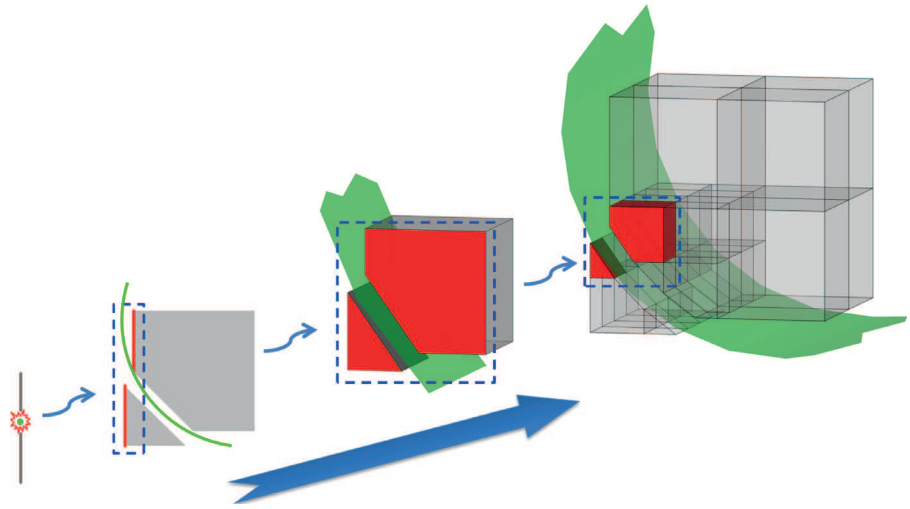

Figure 4.11: The bottom-up scheme for trimming an octree grid [5]

the polyhedral mesh as nodes. Positive points refer to the points outside the STL model. The points with the sign value of zero, i.e. the points on the STL surface, are conditionally included in the mesh as discussed below.

(a) Splitting an edge

For each edge only one intersection point is allowed. If it contains more intersection points, then the average location of these intersection points is used as the intersection point. For an intersection point on an edge, it is assembled into the mesh only if the edge has both positive and negative end points.

(b) Trimming a face

On a face, if a negative node exists, the edges with a negative point are kept and the others are removed. Otherwise, all the edges with zero nodes are kept and the others are removed. Then, the face is trimmed by linking the end nodes of a curve consisting of the kept edges. Fig. 4.12 shows the process of trimming a face.

(c) Trimming a cell

For trimming a cell, first, the associated surface boundary is detected and then the new face is constructed by combining the edges on the boundary. This process is shown on Fig. 4.13.

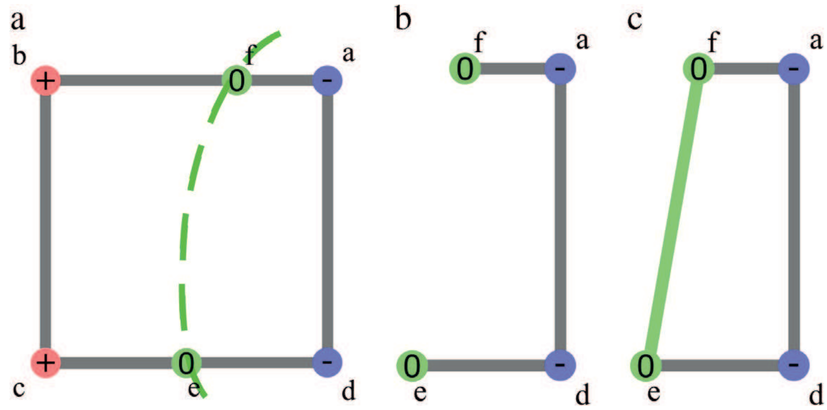

Figure 4.12: Trimming a face (a) a face with two intersection nodes, (b) edges with a negative node and (c) the trimmed face [5]

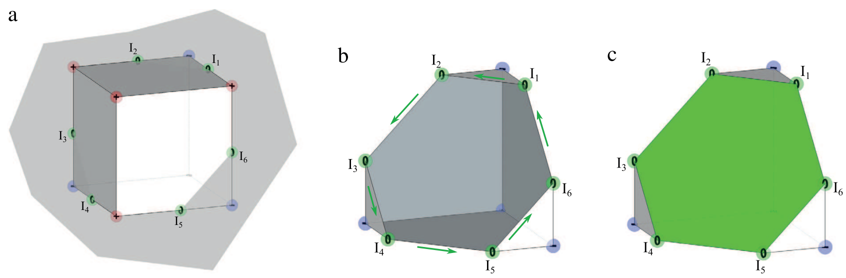

Figure 4.13: Trimming a cell (a) a surface passing through a face (b) trimmed faces and (c) the trimmed cell [5]

4.3.2.4 Trimming with the recovery of sharp edges

If the angle between the two facets is sharp, then the edge connecting the two facets is considered as a sharp feature. A sharp corner is the intersection of sharp edges. To precisely model the geometry, sharp edges need to be firstly extracted and then recovered in the corresponding meshes. Once these features are extracted [119, 120], the recovery of sharp edges can be done following a bottom-up scheme; the edges are first divided into two parts once they are intersected with these features. Then, the features on faces are recovered and remade in cells. The details are provided by Liu et al. [5].

4.4 Scaled Boundary Finite Element Implementation of MECM

The scaled boundary finite element implementation of MECM is similar to the finite element implementation of it discussed in section 3.4. The structural system is discretised into n SBFE subdomains, where each subdomain contains g integration points. At each iteration r, the equivalent stress resultants $\bar{\sigma}_{i,j}^{r}$ for all subdomains $i = 1$ to n are obtained at the integration points ($j = 1$ to g) to comply with the failure conditions imposed by the specific material properties, such as the von Mises (M) or Tresca (T) criteria (explained in Eqs. (3.1) to (3.6)). At the beginning of the next iteration $r+1$, stress distributions of some highly loaded subdomains whose averaged stress resultants $\bar{\sigma}_{i}^{r}$ (where $\bar{\sigma}_{i}^{r} = \sum\limits_{j=1}^{g} \bar{\sigma}_{i,j}^{r}/g$) sit above the nominal stress are performed using Eqs. (3.7) and (3.8) as in the FEM.

At the end of each iteration, the proposed algorithm imposes the yield conformity condition by determining the associated (positive scalar) load factor of $\alpha^{r} = \sigma_0/\bar{\sigma}_{\max}^{r}$ that adjusts the magnitude of stresses to lie within the maximum allowable yield stress σ_0. $\bar{\sigma}_{\max}^{r}$ is the maximum stress resultant of the whole structure at iteration r. The iterations are carried out for the total number of iterations (viz. $rmax$) and the collapse load limit α^{col} of the structure is defined by maximizing the load factor α^{r}, namely $\alpha^{\text{col}} = \max\{\alpha^{r} | r = 1, \ldots, rmax\}$.

The pseudo code summarizing the key steps underlying the proposed iterative elastic SBFE analysis procedure is presented in the following.

Step 0: Initialization

- At iteration $r = 0$, initialize: maximum number of iterations $rmax$, $\lambda \in (0,\, 1)$, yield limit σ_0, and elastic Young's modulus for all $i = 1$ to n SBFE subdomains.
- Construct a quadtree polygon/octree polyhedral SBFE model, and assemble the global nodal forces vector and global stiffness matrix associated with 2D (or 3D) structure.

Step 1: Iterative elastic analyses

- For $r = 1$ to $rmax$
  - Perform an elastic analysis
  - Determine the equivalent stress resultants using Eqs. (3.1) to (3.6) and the averaged stress resultants $\bar{\sigma}_i^r$ and $\bar{\sigma}_{\max}^r$.
  - Update the elastic modulus E_i^r for all subdomains using Eqs. (3.7) and (3.8).
  - Compute the load multiplier $\alpha^r = \sigma_0/\bar{\sigma}_{\max}^r$.
- end

Step 2: Termination

- Determine the collapse load $\alpha^{\text{col}} = \max\{\alpha^r | r = 1, \ldots, rmax\}$.

It is useful to make some additional remarks regarding the MECM algorithm using the SBFEM, as follows.

(1) As in the FEM, the subdomain stiffness matrices in the SBFEM are computed only once based on Eq. (4.30) at the first iteration and stored. In the subsequent iterations, these matrices for the subdomains whose elastic moduli are changed can be simply factored by the ratio of the new elastic modulus of the subdomain to the initial elastic modulus of it at the first iteration (i.e. $\frac{E_i^r}{E_i^{r=1}}$) to create the modified subdomain stiffness matrices required at iteration r. Similarly, for the calculation of stresses, the computations of the stress modes are not required to be done at every iterations; substituting the Eqs. (4.32) and (4.35) into Eq. (4.37) (for 2D) and the Eqs. (4.32) and (4.36) into Eq. (4.38) (for 3D) leads to

$$\boldsymbol{\sigma} = \mathbf{D}\bar{\mathbf{B}}\mathbf{u}_{\mathrm{b}} \tag{4.40}$$

, where

$$\bar{\mathbf{B}} = \left(-\mathbf{B}_1(\eta)\,\boldsymbol{\Phi}_{\mathrm{u}}^{(\mathrm{n})}\boldsymbol{\Lambda}^{(\mathrm{n})}\left(\boldsymbol{\Phi}_{\mathrm{u}}^{(\mathrm{n})}\right)^{-1} + \mathbf{B}_2(\eta)\right)\xi^{-(\boldsymbol{\Lambda}^{(\mathrm{n})}+\mathbf{I})} \tag{4.41}$$

in 2D spaces and

$$\bar{\mathbf{B}} = \left(-\mathbf{B}_1\left(\eta,\zeta\right)\mathbf{\Phi}_{\mathrm{u}}^{(\mathrm{n})}\left(\mathbf{\Lambda}^{(\mathrm{n})}+0.5\mathbf{I}\right)\left(\mathbf{\Phi}_{\mathrm{u}}^{(\mathrm{n})}\right)^{-1}+\mathbf{B}_2\left(\eta,\zeta\right)\right)\xi^{-\left(\mathbf{\Lambda}^{(\mathrm{n})}+1.5\mathbf{I}\right)} \tag{4.42}$$

in 3D spaces. In Eqs. (4.41) and (4.42), $\bar{\mathbf{B}}$ is independent of the elastic modulus of the element. Therefore, it is only computed once in the first iteration and stored, and will be used in other iterations along with Eq. (4.40) for stress computations.

(2) Similar to the FEM implementation of the MECM, the impressibility condition should be considered during the elastic analyses. As discussed before, the SBFEM is able to act sufficiently accurate to model nearly incompressible condition without any specific treatment [113]. In this study, the Poisson's ratio is taken as $\nu = 0.499$ to reflect the incompressible material. The accuracy of this assumption is further investigated in section 4.5.1.1 through the application of the proposed scheme on the well-known Prandtl's punch problem.

4.5 Numerical Examples

Seven numerical examples, three 2D benchmarks presented in Chapter 3 and four 3D examples, are presented to illustrate the application of the proposed iterative SBFE analyses for the determination of the collapse load. As in chapter 3, the accuracy of the results are validated through comparing them with the reported solutions. In all examples, the nearly incompressible condition is considered by using the Poisson's ratio $\nu = 0.499$. The numerical examples show that this value is close enough to 0.5 to estimate the collapse load limit sufficiently accurate. Plasticity was conformed solely at Gauss's integration points. In all examples, $\lambda = 0.05$ and $rmax = 300$ are considered. The analysis procedures were implemented within a MATLAB programming environment.

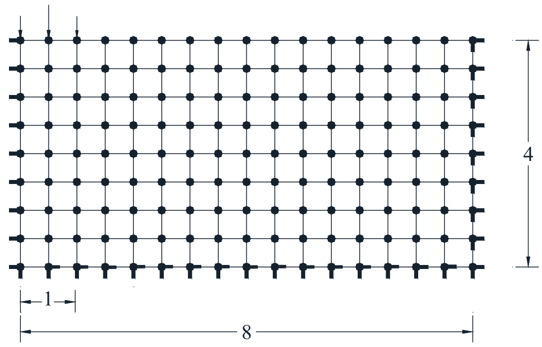

(a)

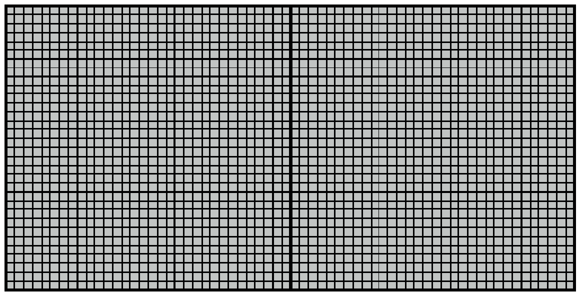

(b)

Figure 4.14: SBFE model of the Prandtl's punch problem (a) schematic model where thick solid lines denote nodal restrained directions (b) actual model

4.5.1 2D Examples

4.5.1.1 Prandtl's punch problem

The first example deals with the semi-infinite body under a punch load as in Fig. 3.1a, which was discussed in sections 2.2.7, 3.3, 3.4, and 3.5.1.1. The plain strain condition and the perfectly plastic Tresca material were adopted. The elastic modulus was given as $E = 10000$ whose unit is the same as the stress unit. The analytical solution of the ratio of the collapse load multiplier to the yield stress (i.e. $\frac{\alpha^{\mathrm{col}}}{\sigma_0}$) is 2.5708. Due to the symmetry, only half of the structure was modeled using the scaled boundary finite elements. The mesh was acquired quite automatically from a 2D solid. The schematic SBFE model is shown in Fig. 4.14a, where each subdomain was subdivided into 64 similar subdomains. In total, 2048 subdomains, 2145 nodes, 4290 DOFs, and 8192 integration points are utilized. Fig. 4.14b displays the actual SBFE model after subdivisions.

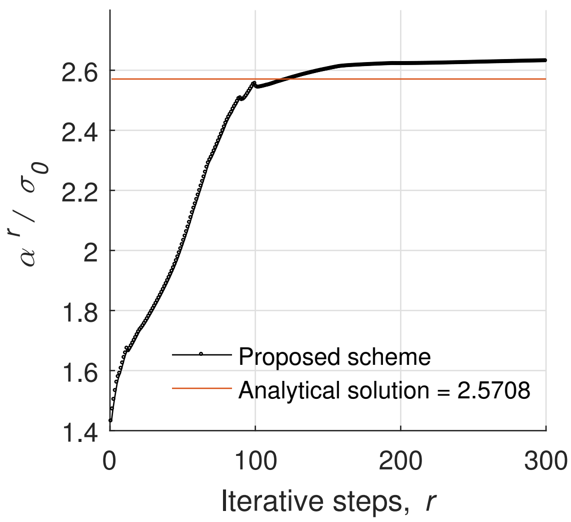

Figure 4.15: The iterative scheme for the Prandtl's punch problem with 2048 subdomains in the proposed MECM with SBFEM

The proposed MECM analysis of the structure was performed and $\frac{\alpha^{\mathrm{col}}}{\sigma_0}$ was obtained as 2.6302 which is some 2.31% higher than the analytical solution. Fig. 4.15 shows the changes of the normalized load multipliers during the iterations. The corresponding stress and elastic modulus distributions associated with the collapse load are also shown in Fig. 4.16. The schematic collapse mechanism is also displayed in Fig. 4.17.

The ability of the SBFEM in handling the incompressibility condition was also emphasized in this example by investigating the effect of different Poisson's ratios on the example. For this purpose, a sufficiently fine mesh was considered where 32768 subdomains, 33153 nodes, 66306 DOFs, and 131072 integration points were used. The reason that this mesh is chosen as a reasonably fine mesh is later explained in this section through a convergence study. The results are tabulated in Table 4.1 and compared with the analytical solution. Fig. 4.18 also shows the variations of the collapse load solution with different Poisson's ratios. As seen, the employed Poisson's ratio $\nu = 0.499$ can adequately represent the incompressiblility condition required for the MECM scheme. It should be noted that for the Poisson's ratio

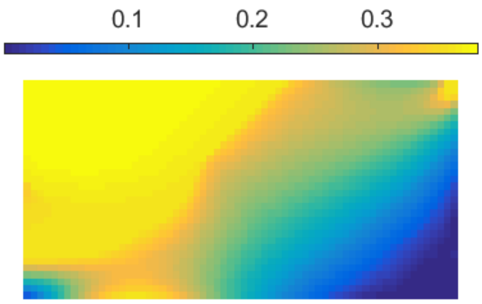

(a)

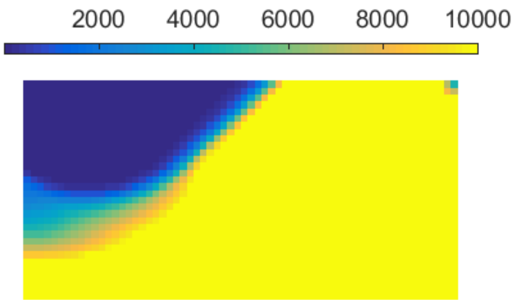

(b)

Figure 4.16: Stress and elastic modulus distributions for the Prandtl's punch problem using the proposed MECM with SBFEM (a) stress distribution (b) elastic modulus distribution

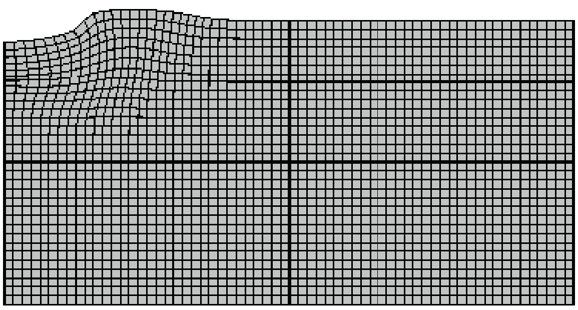

Figure 4.17: The schematic displacement field for the Prandtl's punch problem using the proposed MECM with SBFEM

Table 4.1: Variation of collapse load solutions with different Poisson's ratios for the Prandtl's punch problem using the proposed MECM with SBFEM

Poisson's ratio (ν)	$\alpha^{\mathrm{col}}/\sigma_0$	error %
0	1.2316	-52.09
0.1	1.2681	-50.67
0.2	1.3226	-48.55
0.3	1.5381	-40.17
0.4	2.1751	-15.39
0.45	2.5465	-0.95
0.49	2.5750	0.16
0.499	2.5768	0.23
0.4999	2.5769	0.24

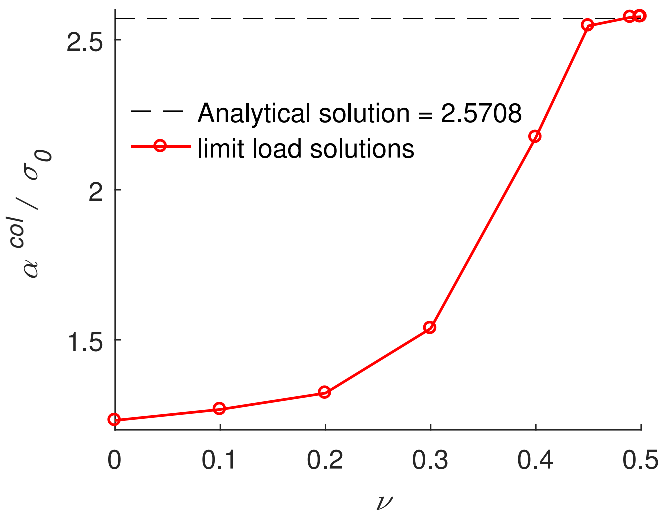

Figure 4.18: Variation of collapse load solutions with Poisson's ratio for the Prandtl's punch problem using the proposed MECM with SBFEM

values higher than 0.4999 the computations break down, as the constitutive matrix D is not finite. This agrees well with what stated in [113].

The influence of the total number of SBFE subdomains on the precision of the limit load solution $\frac{\alpha^{\mathrm{col}}}{\sigma_0}$ was also investigated using the proposed method. Six SBFE models are used, where the mesh is uniformly refined (ranging from coarse to fine). The results are reported in Table 4.2 under the title scheme A, where the error percentages between the analytical solution and the obtained collapse load solutions are also presented. The collapse load solutions corresponding to the variation of mesh sizes are also plotted in Fig. 4.19, where it can be seen that the values of $\frac{\alpha^{\mathrm{col}}}{\sigma_0}$

Table 4.2: The collapse load solutions of the Prandtl's punch problem for different discretizations using the proposed MECM with SBFEM

No. of subdomains	element mesh size	Scheme A		Scheme B	
(NS)	(h)	$\frac{\alpha^{col}}{\sigma_0}$	error%	$\frac{\alpha^{col}}{\sigma_0}$	error%
32	1.00000	3.3357	29.75	2.4007	-6.62
128	0.25000	2.9122	13.28	2.2873	-11.03
512	0.06250	2.7221	5.89	2.3292	-9.40
2048	0.01563	2.6302	2.31	2.3171	-9.87
8192	0.00391	2.5977	1.05	2.3183	-9.82
32768	0.00098	2.5768	0.24	2.3011	-10.49

decrease by increasing the number of subdomains. It should be emphasized that although the results reported here are above the true collapse loads, the proposed scheme should not be interpreted as an upper bound method. As explained in section 3.5.1.1, if sufficient number of element is used, the yield conformity is satisfied through the whole domain and the collapse load solution sits below the exact collapse load. In other words, the proposed method is a lower bound scheme as the MECM with the FEM described in chapter 3, but not a strict lower bound method. This matter is more clearly seen in sections 4.5.1.3 and 4.5.2.1.

Table 4.2 also shows the convergence study of the proposed iterative SBFE scheme for the Prandtl's punch problem where the maximum stress resultant (instead of the average stress resultant) in a subdomain is used for the modification of the elastic modulus of the subdomain (scheme B). As it can be seen, the computed collapse load solutions are much smaller than the reported analytical solution. This example illustrates the over conservative behavior of the MECM scheme when the maximum stress in a subdomain is used for the modification of the elastic modulus of the subdomain.

4.5.1.2 Double-edge notched specimen

The double edge notch tensile specimen under the plain strain and the von Mises conditions is considered as mentioned in the last chapter in section 3.5.1.2. The geometry and loading are shown in Fig. 3.13a. The schematic SBFE model is shown

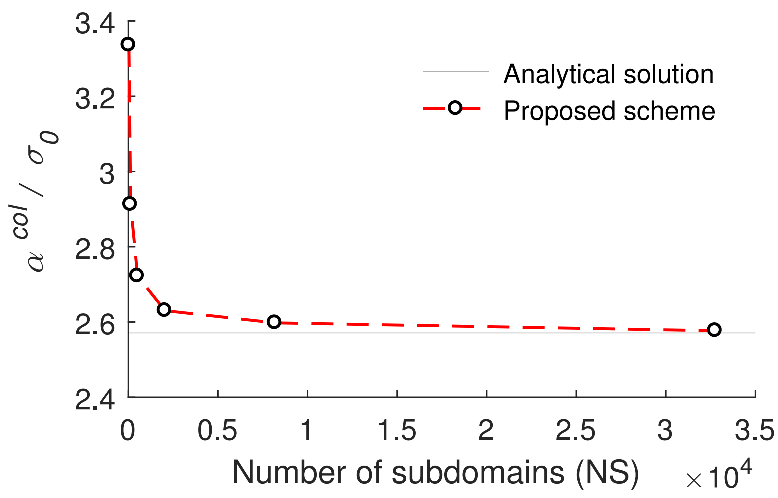

Figure 4.19: Variation of the collapse load solution with number of subdomains for Prandtl's punch problem using the proposed MECM with SBFEM

in Fig. 4.20a, where each subdomain is subdivided into 4 similar subdomains. In total, 1024 subdomains, 1089 nodes and 2178 DOFs and 4096 integration points were considered. Fig. 4.20b displays the actual mesh after these subdivisions.

The proposed MECM with SBFEM was applied to solve the problem and the collapse load solution $\frac{\alpha^{\mathrm{col}}}{\sigma_0}$ was obtained as 4.8055 which is 2.79% higher than the reported solution ($\left(\frac{\alpha^{\mathrm{col}}}{\sigma_0}\right)_{\mathrm{ref}} = 4.6749$). The iterative scheme is shown in Fig. 4.21. The corresponding stress and elastic modulus distributions are also depicted in Fig. 4.22. The associated collapse mechanism is plotted in Fig. 4.23.

The variations of the load multipliers with respect to the modification factor λ is studied in this example for the current mesh, and the results are shown in Fig. 4.24. As illustrated, the instability of the MECM with higher values of λ is evident, where the solutions are diverged before better results are obtained. However, $\lambda = 0.05$ still is offered an acceptable level of accuracy for this example.

The sensitivity of the method to the number of subdomains was also investigated through a convergence study. Seven models were used, where the mesh layout is uniformly changing from a coarse mesh to a fine mesh. The results are tabulated in Table 4.3 and plotted in Fig. 4.25. The differences between the reported solution and obtained results are also given. As expected, by increasing the number of

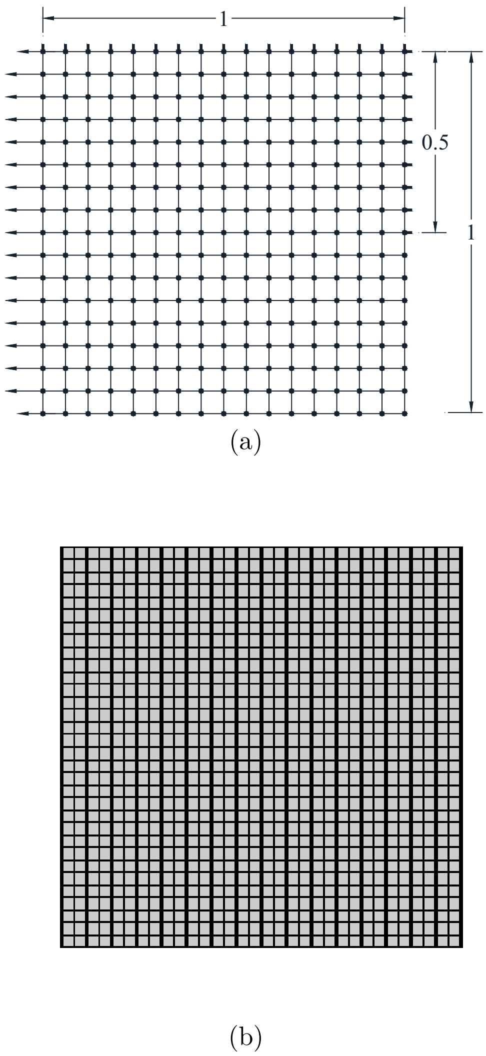

Figure 4.20: SBFE model of the double edge notched specimen (a) schematic model where thick solid lines denote nodal restrained directions (b) actual mesh

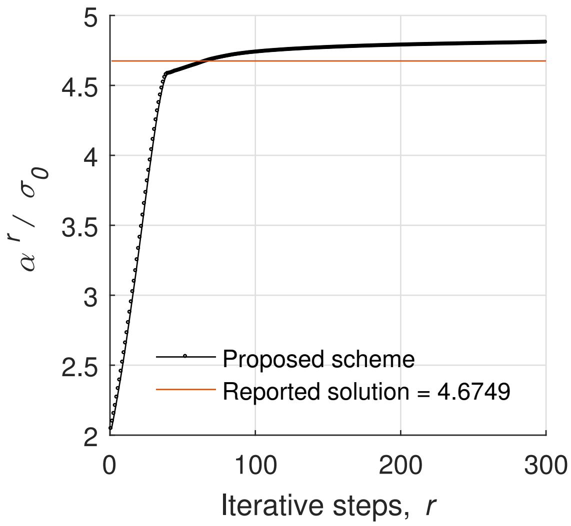

Figure 4.21: The iterative scheme for the double-edge notched specimen in the proposed MECM with SBFEM

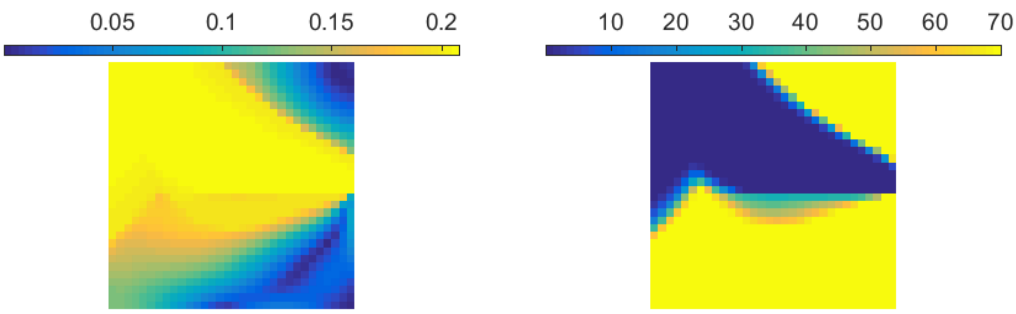

(a) (b)

Figure 4.22: Stress and elastic modulus distributions of the double-edge notched specimen using the proposed MECM with SBFEM (a) stress distribution (b) elastic modulus distribution

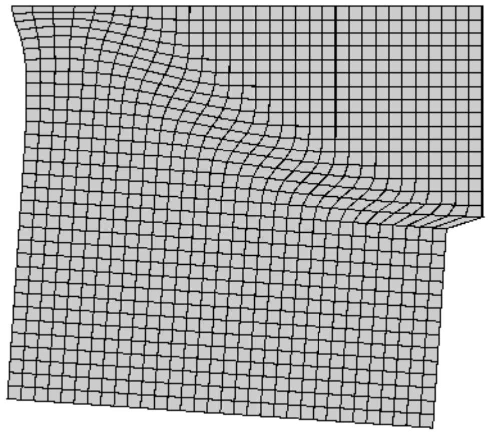

Figure 4.23: The schematic displacement field of the double-edge notched specimen using the proposed MECM with SBFEM

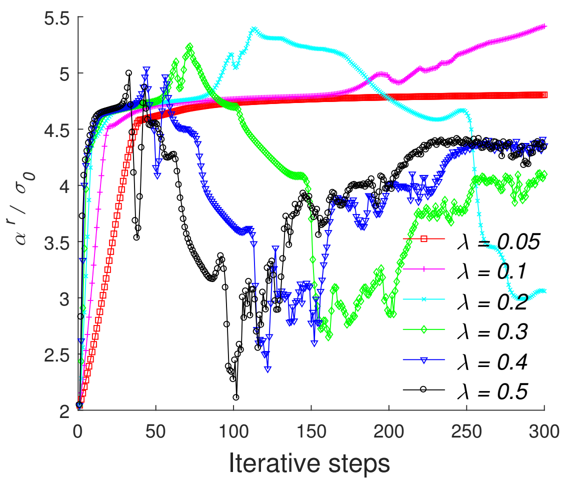

Figure 4.24: Variation of load multiplier solutions with λ for the double notched specimen using the MECM and FEM

Table 4.3: The collapse load solutions of the double-edge notched specimen for different discretizations using the proposed MECM and SBFEM

No. of subdomains (NS)	element mesh size (h)	$\frac{\alpha^{col}}{\sigma_0}$	difference%
4	0.5	7.1064	52.01
16	0.25	6.1365	31.26
64	0.125	5.4559	16.71
256	0.0625	5.0484	7.99
1024	0.03125	4.8055	2.79
4096	0.015625	4.6733	-0.03
16384	0.0078125	4.6020	-1.56

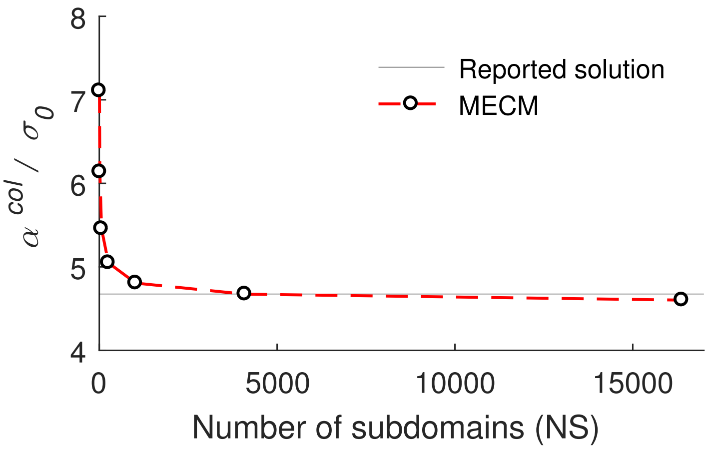

Figure 4.25: Variation of the collapse load solution with the number of elements for the double-edge notched specimen using the proposed MECM and SBFEM

subdomains the collapse load solutions decreased to a value below the reported solution. However, as the analytical solution is not available for this problem, a justification on whether the proposed method is a lower bound scheme or a strict method cannot be done.

4.5.1.3 Perforated plate problem

The third example is the plane stress perforated plate under the von Mises condition mentioned in section 3.5.1.3 of the last chapter. The geometry and loading are shown in Fig. 3.19a. Here, the problem was fully modeled with SBFEs (Fig. 4.26), where the advantage of the quadtree scheme can be seen. The use of polygonal subdomains allowed the circumference of the circle to be modeled efficiently and automatically out of a plane solid. Additionally, these type of subdomains allowed the hanging

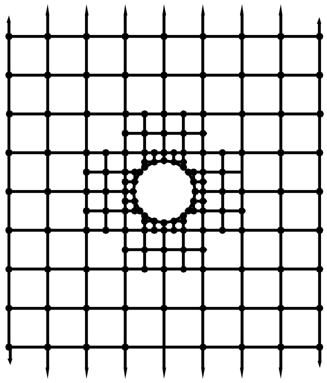

Figure 4.26: SBFE model of the perforated plate example

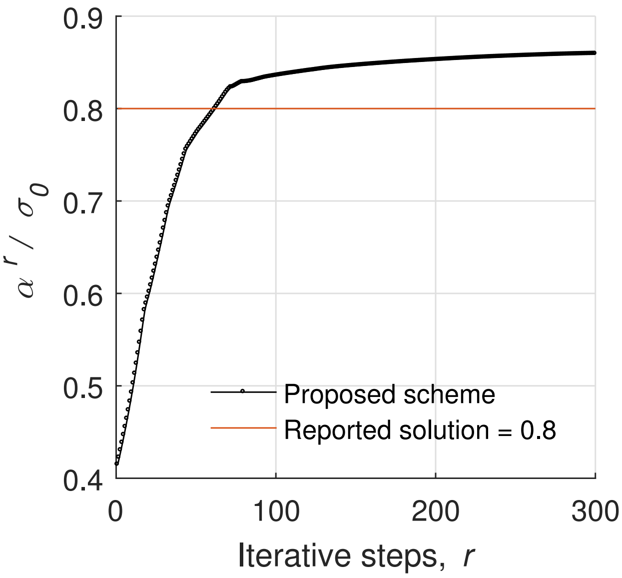

Figure 4.27: The iterative scheme for the perforated plate with 120 subdomains using the proposed MECM with SBFEM

nodes to be defined efficiently and hence the burden of the mesh generation was reduced significantly. In total, 112 subdomains, 152 nodes, 304 DOFs and 476 Gauss's points were utilized.

The MECM was performed on the structure and the collapse load solution $\frac{\alpha^{\mathrm{col}}}{\sigma_0}$ was computed as 0.8591, which is some 7.39% higher than the analytical solution, $\left(\frac{\alpha^{\mathrm{col}}}{\sigma_0}\right)_{\mathrm{ref}} = 0.8$. The iterative scheme is plotted in Fig. 4.27. The associated stress and elastic modulus distributions are also plotted in Fig. 4.28. The schematic mechanism is also shown in Fig. 4.29.

As the computed collapse load is considerably higher than the true collapse load solution, the uniform mesh refinement was performed on the structure, where each

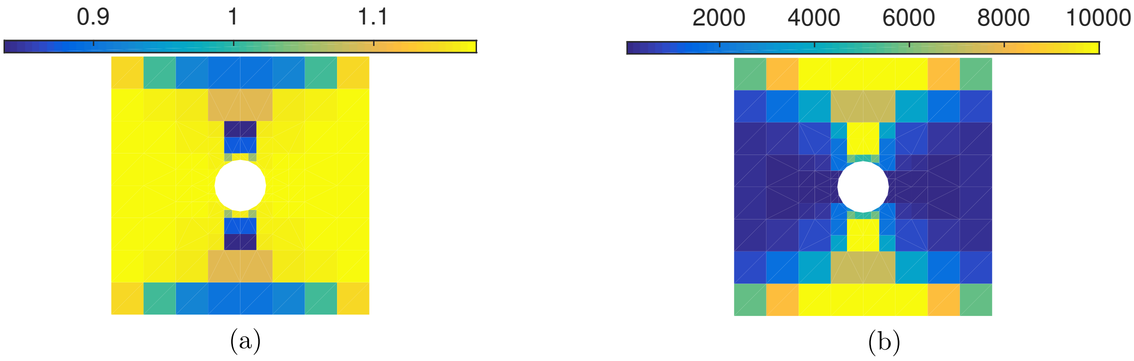

Figure 4.28: Stress and elastic modulus distributions of the perforated plate using the proposed MECM with SBFEM (a) stress distribution (b) elastic modulus distribution

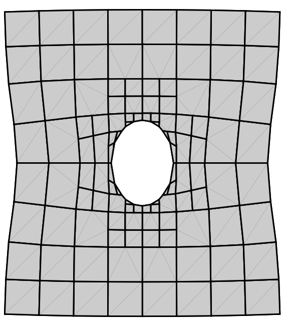

Figure 4.29: The schematic displacement field of the perforated plate using the proposed MECM with SBFEM

Table 4.4: The collapse load solutions of the perforated plate for different discretizations using the proposed MECM with SBFEM

Scheme A			Scheme B		
No. of subdomains (NS)	$\frac{\alpha^{col}}{\sigma_0}$	error %	No. of subdomains (NS)	$\frac{\alpha^{col}}{\sigma_0}$	error %
112	0.8591	7.39	1000	0.8280	3.51
424	0.8354	4.42	3976	0.8130	1.62
1704	0.8187	2.34	15908	0.8064	0.80
6724	0.8087	1.08	63536	0.8023	0.28
26744	0.8023	0.28			
106768	0.7980	-0.26			

subdomain was recursively subdivided into four smaller subdomains. The proposed MECM was performed on each of the acquired models, and the results are tabulated in Table 4.4 under the title scheme A. Fig. 4.30 also shows the influence of the number of subdomains on the collapse load solution. As shown, the lower strict bound solution was obtained by increasing the number of subdomains in media. This shows that although the proposed scheme is a lower bound scheme, it is not a strict lower bound method. In fact, the strict lower bound solution can be obtained only if sufficient number of elements is used in the domain. As discussed in chapter 3, this leads to the better satisfaction of the yield condition, as the number of integration points are increased too.

The results of the uniform refinements are also provided in Table 4.4 under the title scheme B. In constructing the uniform meshes, the size of the smallest subdomain, in the corresponding non-uniform mesh in scheme A, is chosen as the mesh size for the sake of comparison. As it can be seen, for the same level of accuracy, the use of non-uniform mesh is computationally advantageous, as it contains lower number of subdomains. For instance, the collapse load solution of 0.8023 with 0.28% error was achieved for both uniform and non-uniform mehses; nevertheless, the number of subdomains needed for this solution in the non-uniform mesh was 26744. This is almost 40% of the number of subdomains needed for the uniform mesh (i.e. 63536) and therefore computationally beneficial.

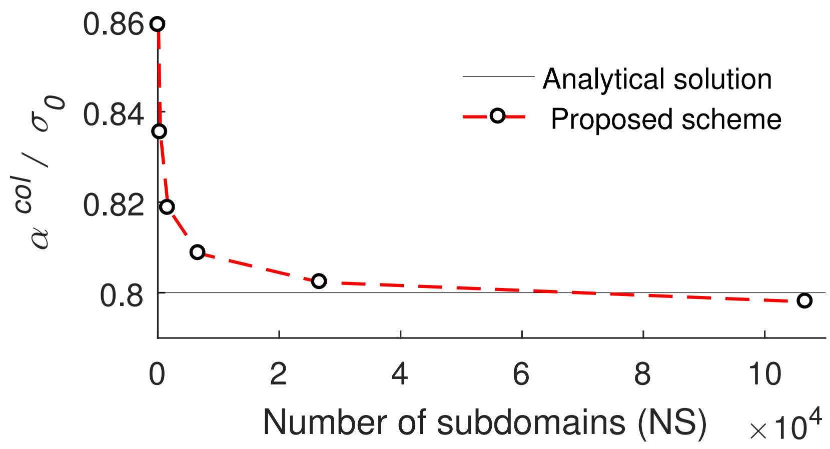

Figure 4.30: Variation of the collapse load solution with the number of subdomains for the perforated plate problem using the proposed MECM with SBFEM

4.5.2 3D Example

In this section, three 3D problems were modeled to illuminate the performance of the proposed MECM with SBFEM for structures in 3D spaces. In particular, the mesh generation for these examples were done fully automatically and out of the CAD (STL) models using the mentioned octree scheme.

4.5.2.1 Thick cylinder

The thick cylinder under the uniform pressure introduced in section 3.5.2.1 in last chapter was employed. Here, considering the fact that the effect of cylinder length is negligible on the true collapse load of the structure, it was reduced to 220 mm to accommodate more number of subdomains. The SBFE model with sharp features was generated by the explained octree meshing method and shown in Fig. 4.31. The model represents only a quarter of the cylinder due to the symmetric nature of the problem. In total, 1243 subdomains, 2007 nodes, and 6021 DOFs were defined.

The proposed MECM with SBFEM was carried out for 300 iterations (Fig. 4.32) and the collapse load solution $\frac{\alpha^{col}}{\sigma_0}$ was obtained as 0.8074, which is of 0.88% error in comparison to the analytical solution of $\frac{\alpha^{col}}{\sigma_0} = 0.8004$. The corresponding stress and elastic modulus distributions within the domain is also shown in Fig. 4.33.

The influence of the number of subdomains on the collapse load solution was

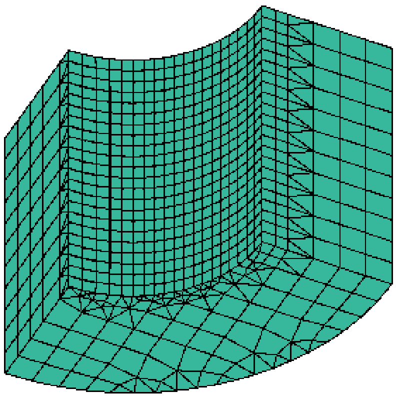

Figure 4.31: The SBFE model of the thick cylinder

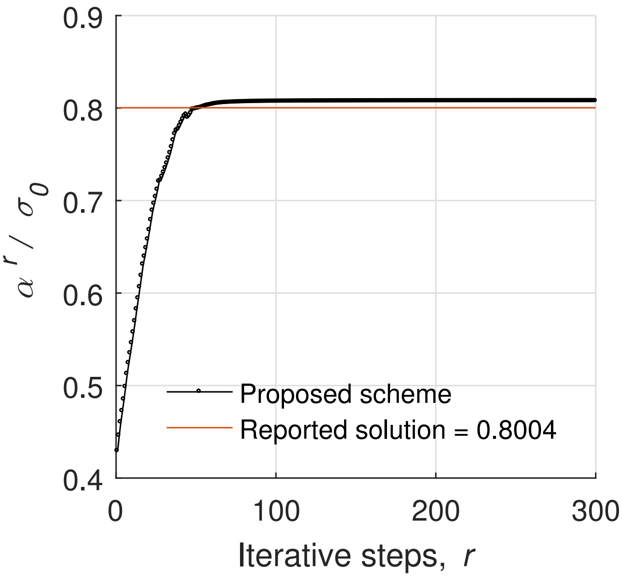

Figure 4.32: The iterative scheme for the thick cylinder with 1243 subdomains using the proposed MECM and SBFEM

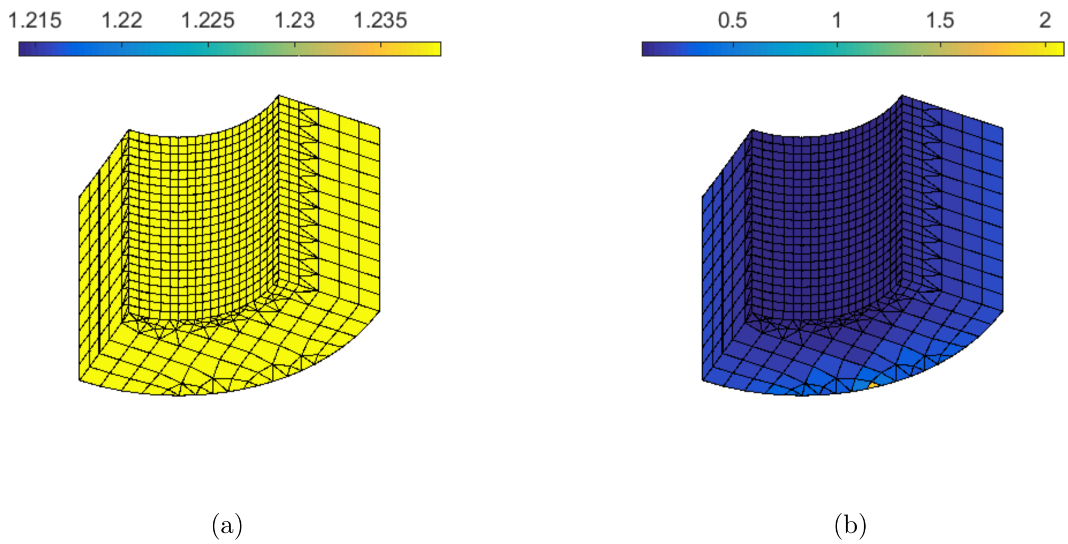

Figure 4.33: Stress and elastic modulus distributions of the thick cylinder using the proposed MECM with SBFEM (a) stress distribution (b) elastic modulus distribution

Table 4.5: The collapse load solutions of the thick cylinder for different discretizations using proposed MECM and SBFEM

No. of subdomains (NS)	$\frac{\alpha^{\text{col}}}{\sigma_0}$	error%
1243	0.8074	0.88
3632	0.8024	0.25
7832	0.7991	-0.16
22080	0.7989	-0.19

investigated by increasing the number of subdomains (reducing the minimum sizes, S_{min}). Four models were developed, and the proposed MECM with SBFEM was performed on them. The results are tabulated in Table 4.5. Fig. 4.34 also shows the variation of the collapse load solution with the number of subdomains. As illustrated, the lower bound solution is only obtainable if sufficient number of elements is used in the media. This shows that although the proposed scheme is a lower bound scheme (see Fig. 4.32), it is not a strict lower bound method.

4.5.2.2 Thick square plate with central elliptical flaw under axial tension

A square plate with a thickness of 5 mm and elliptical flaw at its center (Fig. 4.35a) was considered . The structure was subjected to a uniaxial uniform stresses of σ = 10 kPa. The von Mises material with $E = 207,000$ MPa and σ_0= 294 MPa was adopted. The collapse load solution of this problem $\frac{\alpha^{\text{col}}}{\sigma_0}$ is reported as 0.798 [17].

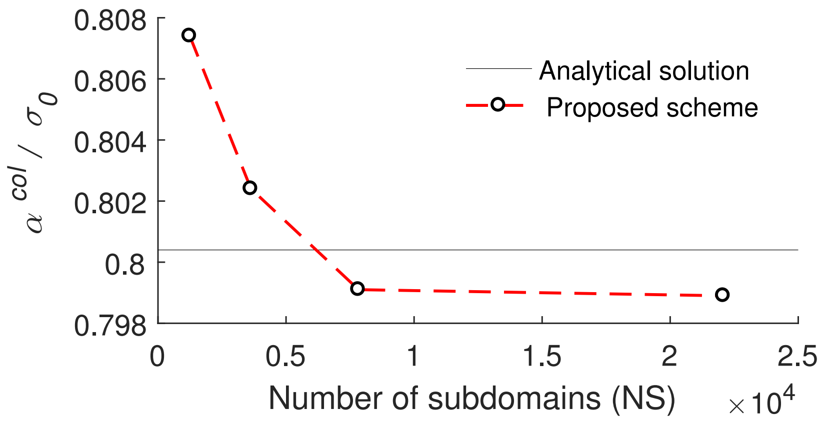

Figure 4.34: Variation of the collapse load solution with the number of subdomains for the thick cylinder problem using the proposed MECM with SBFEM

Due to its symmetry in all axes, only a quarter of the structure was modeled using SBFEs, as shown in Fig. 4.35b. The discrete model consisted of 1098 subdomains, 1885 nodes and 5655 DOFs.

The proposed MECM was performed on the model and the collapse load solution was obtained as $\frac{\alpha^{\text{col}}}{\sigma_0} = 0.8837$ with some 10.74 % difference with the reported solution. The amount of this relatively high difference is due to the low number of subdomains, and will be later improved by mesh refinement. The associated iterative scheme is shown in Fig. 4.36. The corresponding stress and elastic modulus distributions are also provided in Fig. 4.37.

The effect of the number of subdomains were also studied. Four different SBFE meshes were considered, ranging from a coarse mesh to a fine mesh. The proposed MECM was performed on them and the results are illustrated in Table 4.6. The differences between the reported solution [17] and obtained results are also given. Fig. 4.38 further shows the variation of the collapse load solution with the number of subdomains. As seen, the computed collapse load was reduced by refining the mesh. It should be noticed that no justification about the trend of the method (i.e a lower bound scheme or a strict lower bound) can be provided for this example, as the analytical solution is not available.

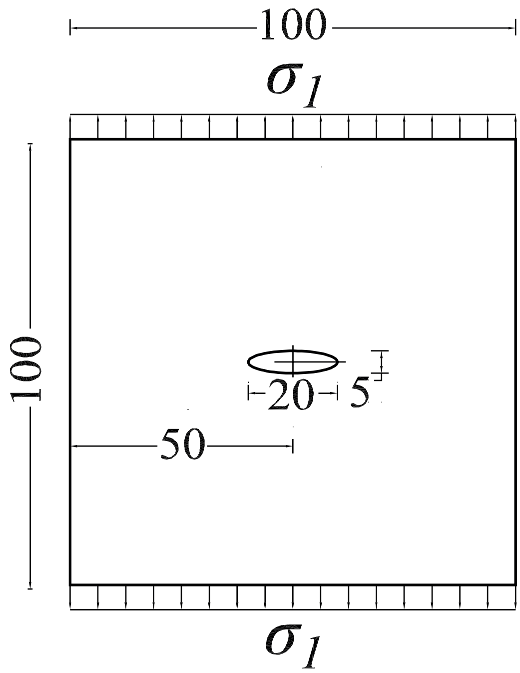

(a)

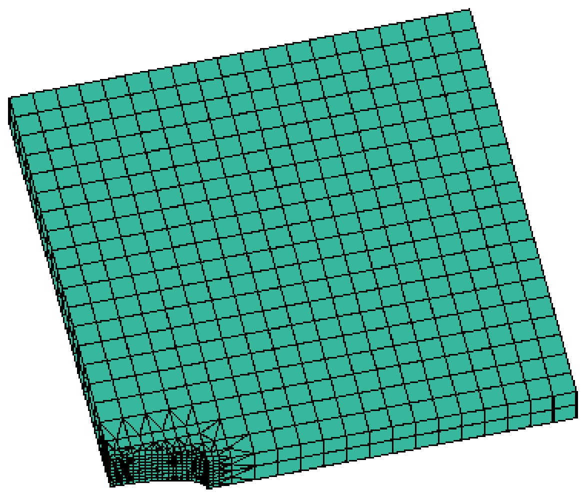

(b)

Figure 4.35: Square plate with a central ellipse flaw (a) geometry and loading (b) SBFE model

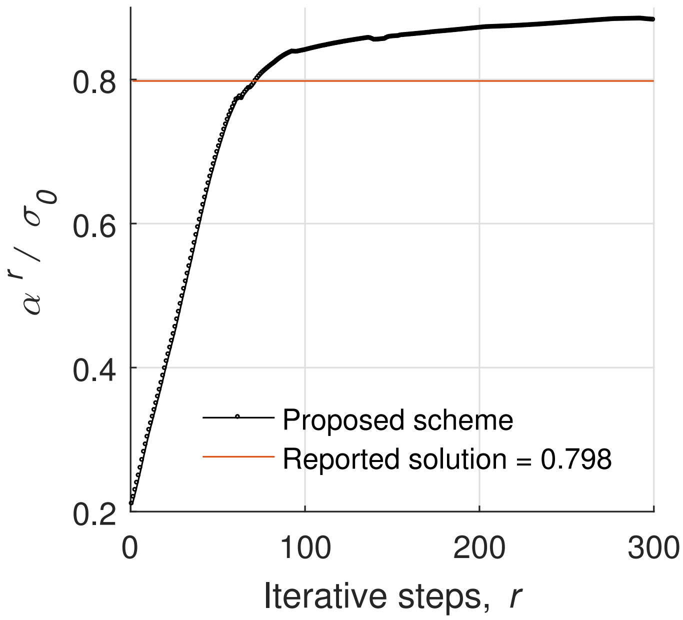

Figure 4.36: Iterative scheme for the perforated square plate with 1098 subdomains using the proposed MECM and SBFEM

Table 4.6: The collapse load solutions of the thick square plate for different discretizations using the proposed MECM and SBFEM

No. of subdomains (NS)	$\frac{\alpha^{col}}{\sigma_0}$	difference%
188	0.925	15.91
1098	0.8837	10.74
7505	0.8401	5.28
55512	0.8165	2.32

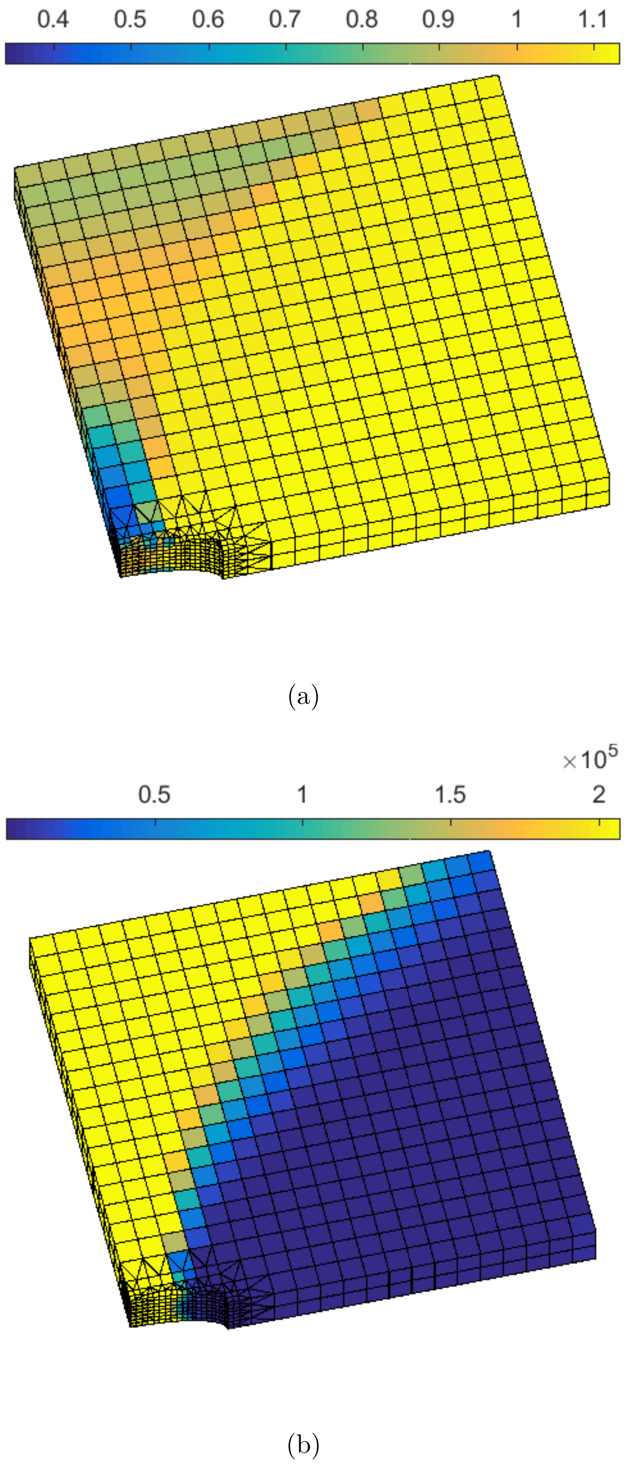

Figure 4.37: Stress and elastic modulus distributions of the perforated square plate using the proposed MECM with SBFEM (a) stress distribution (b) elastic modulus distribution

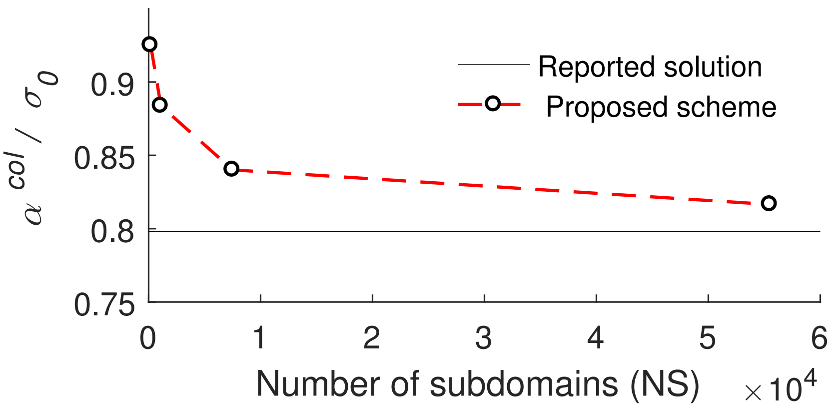

Figure 4.38: Variation of the collapse load solution with the number of subdomains for the thick square plate problem using the proposed MECM with SBFEM

4.5.2.3 Defected pipeline

The third 3D example is the defected pipeline discussed in section 3.5.2.3 in last chapter. The geometry and loading is given in Fig. 3.35. Two SBFE models were automatically generated to show the performance of the proposed method on this problem; case a consisting of 2216 subdomains, 3437 nodes, 9603 DOFs and a finer case b with 4734 subdomains, 6653 nodes, 19959 DOFs (Fig. 4.39).

The MECM successfully computed the collapse load solutions of $\alpha^{\mathrm{col}} = 69.5526$ in case a and $\alpha^{\mathrm{col}} = 67.5883$ in case b. Fig. 4.40 shows the employed iterative scheme for case b. The proposed approach provided good accuracy of collapse load results, as the solutions computed agree well with the reference values reported from various numerical algorithms, namely $\alpha^{\mathrm{col}}_{ref} = 64.05$ using the incremental method [92], $\alpha^{\mathrm{col}}_{ref} = 67.13$ using the kinematic method [86], and $\alpha^{\mathrm{col}}_{ref} = 63.42$ using the static method [92]. The diagrams in Fig. 4.41 depict the von Mises stress and elastic modulus distributions computed at α^{col} for case b. The schematic collapse mechanism associated at α^{col} is also plotted for case b in Fig. 4.42.

4.5.2.4 The leg of a chair

To highlight the advantageous performance of the SBFEM and its combination with the octree scheme for the automatic mesh generation, in this example, a ductile leg

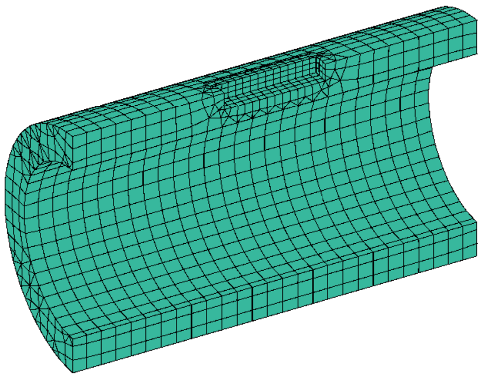

(a)

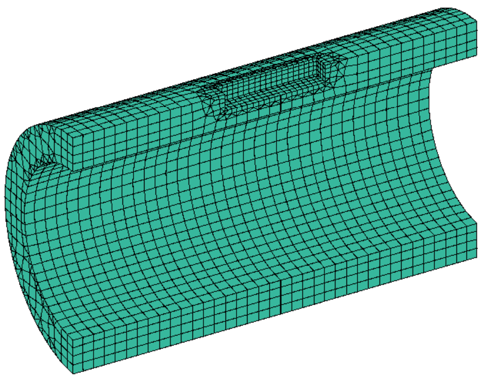

(b)

Figure 4.39: SBFE models for the defected pipeline (a) case a (b) case b

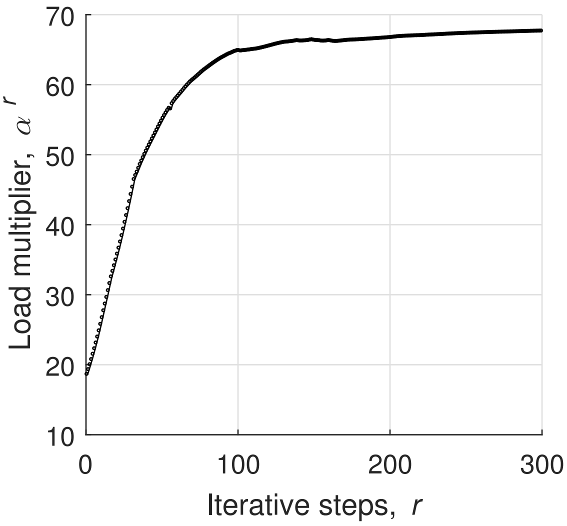

Figure 4.40: Iterative scheme for the defected pipeline (case b) using the proposed MECM and SBFEM

of a chair under the uniform pressure is considered. Fig. 4.43a shows the geometry of this example. The boundary conditions and loading are emphasized in Fig. 4.43b. The von Mises material properties used in this problem were E = 207 GPa, and σ_0 = 200 MPa. The SBFE mesh was automatically generated out of the STL file as per section 4.3.2. Fig. 4.44 shows the produced mesh. The final mesh contains 2730 subdomains, 4072 nodes, 12216 DOFs.

The MECM was performed on the structure and the normalized collapse load solution was obtained as $\frac{\alpha^{\mathrm{col}}}{\sigma_0} = 0.1310$. The iterative scheme is shown in Fig. 4.45. The von Mises stress and elastic moduli distributions associated with the collapse load are also shown in Fig. 4.46.

4.6 Conclusion and Remarks

In this chapter, the extension of the MECM to the SBFEM for using some of its advantages was explained. In particular, two merits of SBFEM suitable for MECM were discussed. First, the SBFEs satisfy from the nearly incompressible condition when Poisson's ratios of 0.499 was used without exhibiting volumetric locking. Second, the iterative elastic SBFE analysis adopted polygon-type (in 2D) or polyhedral

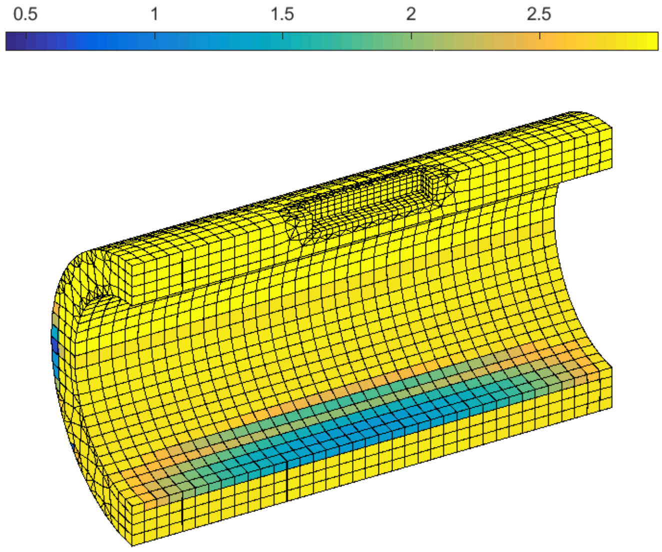

(a)

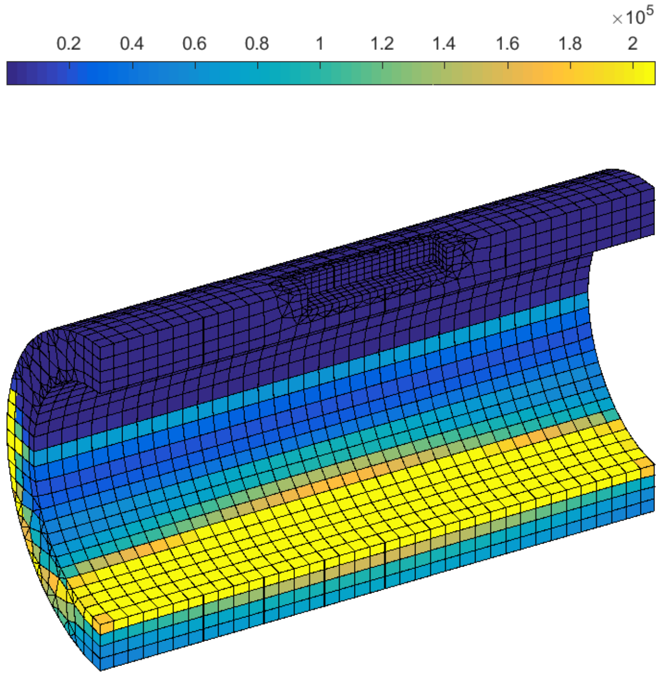

(b)

Figure 4.41: Stress and elastic modulus distributions of the defected pipeline problem (case b) using the proposed MECM and SBFEM (a) stress distribution (b) elastic modulus distribution

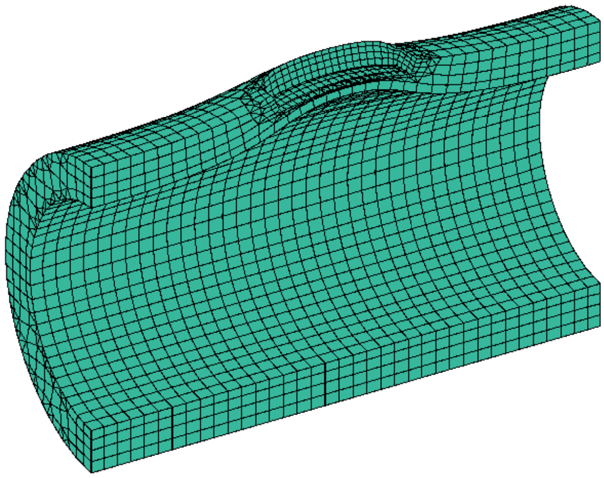

Figure 4.42: The collapse mechanism for the defected pipeline using the proposed MECM with SBFEM

(a)

(b)

Figure 4.43: The leg of a chair (a) geometry (b) loading and boundary conditions

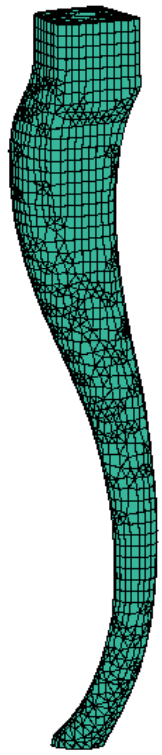

Figure 4.44: SBFE model for the leg of a chair

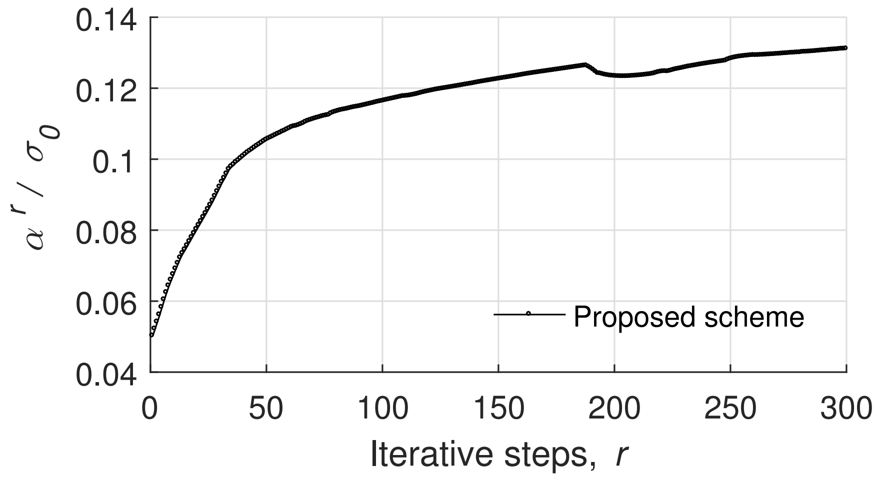

Figure 4.45: Iterative scheme for the leg of a chair using MECM and SBFEM

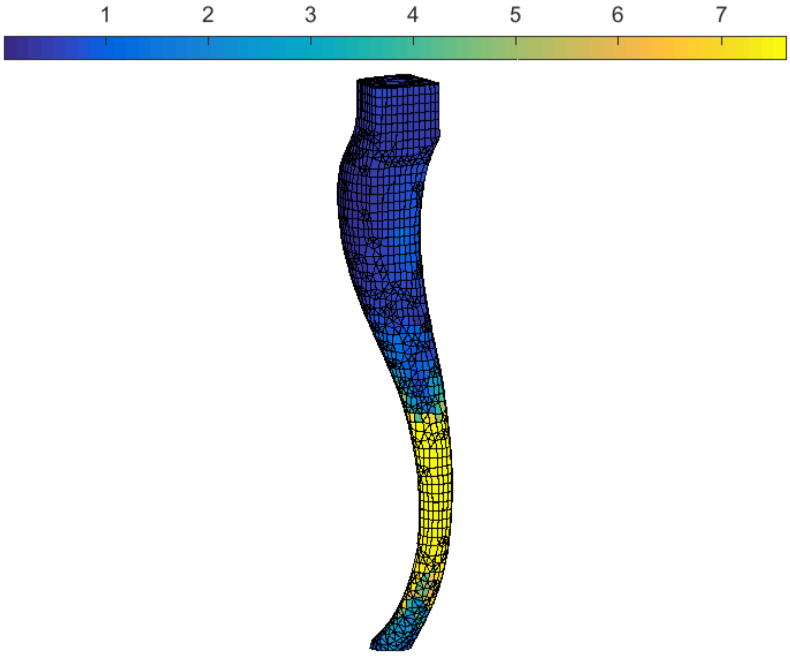

(a)

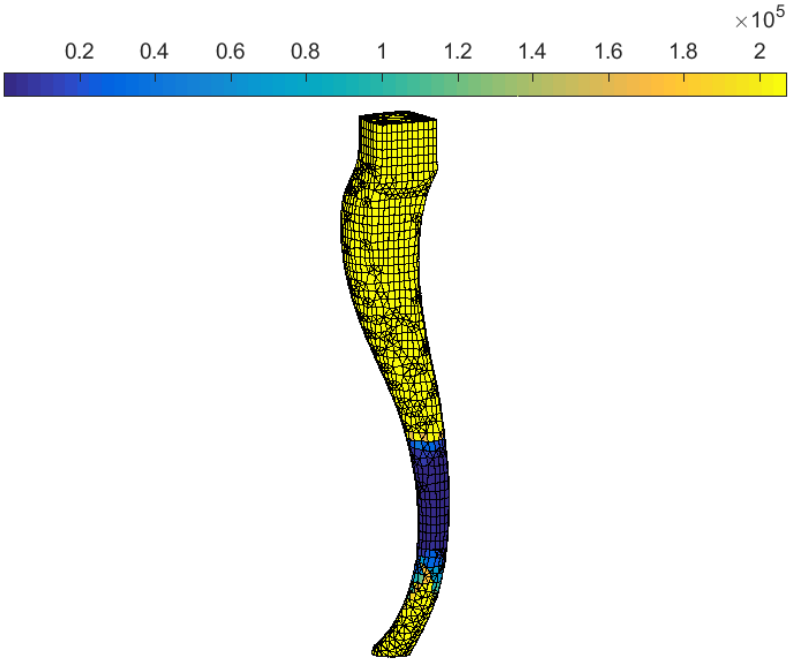

(b)

Figure 4.46: Equivalent stress and elastic modulus distributions of the leg of a chair using the proposed MECM and SBFEM (a) stress distribution (b) elastic modulus distribution

(in 3D) elements that enable structural modeling of problems with complex geometries. Automated quadtree/octree algorithms were incorporated directly within the SBFE framework, which gave it the capability to efficiently and automatically model the structural discretization of an in-plane solid (for 2D) or of CAD (STL) models (in 3D). This advantage alleviated the burden of the mesh generation required in the MECM. It also reduced the user interference in the mesh generation part and the associated errors arising from that. A number of numerical examples, ranging from benchmark tests, 2D and 3D solids, were studied to illustrate the performance of the proposed scheme. They also served as a platform that highlighted the influences of some key algorithmic parameters on the accuracy of the method.

Chapter 5

A NOVEL SENSITIVITY-BASED ECM FOR THE COLLAPSE LOAD DETERMINATION OF STRUCTURES USING THE FINITE ELEMENT METHOD

5.1 Introduction

The MECM uses the number of iterations selected by the user as the stopping criterion. When the maximum number of iterations is reached, the maximum load multiplier occurred during the iterations is selected as the solution. This allows some error to be included in the scheme whose value could vary from one problem to another or even from one mesh to another. The reason of using the number of iterations as the stopping criterion is the multiple oscillations which might happen for some structures during the iterations. Though the adjustable parameter λ, introduced in the MECM by Yang and Chen [16, 17] improved the convergence of the method, it does not completely solve the oscillation problem in the load multiplier.

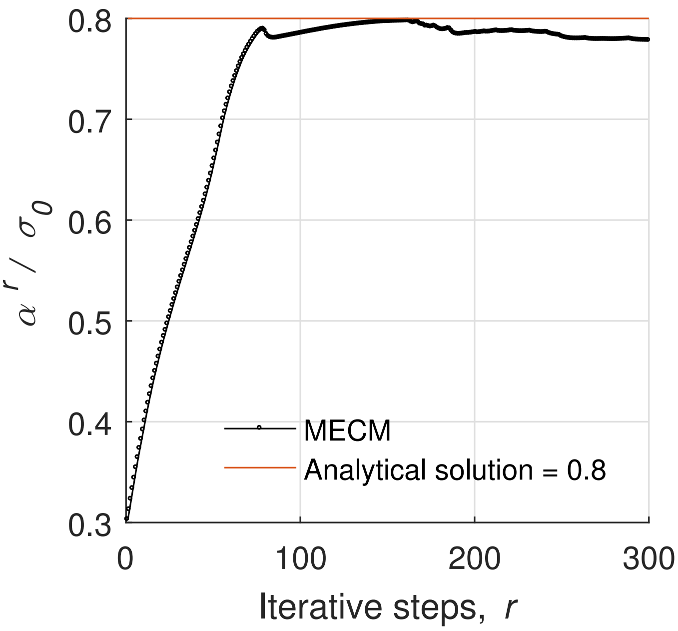

Figure 5.1: The oscillatory behavior of the limit load solutions for the perforated plate with 33280 FEs using the MECM

As an example, consider the perforated plate mentioned in section 3.5.1.3. Although the choice of $\lambda = 0.05$ has led to a convergence of the limit load multiplier for the chosen mesh with 120 elements, the limit load solution obtained for the same example using a mesh with 33280 elements and the same value of λ is of an oscillatory behavior as shown in Fig. 5.1. As it can be seen, the presence of multiple random oscillations with different amplitudes prevented the convergence to be defined on load multipliers. It is obvious that the use of higher values of λ exacerbates the oscillation as discussed before. The smaller values of λ might reduce (and not necessarily remove) the oscillatory behavior of the scheme; however, they demand more number of iterations, and hence more computational time. In addition, the input number of iterations set by the user might not be sufficient and therefore some time-consuming trial and error procedures are required to find the suitable number of iterations for obtaining a reasonable convergence.

In this chapter, a novel sensitivity-based ECM will be proposed which completely removes the oscillatory behavior of the limit load solution, and therefore the convergence will be defined directly on the limit load solution. In section 5.2, the reasons of these oscillations will be discussed in detail. A simple 2D truss is deployed to illustrate the source of oscillations. In section 5.3, a robust sensitivity-based ECM will be introduced which eliminates the oscillations by considering the contribution of all elements through the definition of a sensitivity matrix. Section 5.4 validates the proposed sensitive scheme through some 2D benchmarks and 3D numerical examples. The conclusions and remarks will be discussed in section 5.5 of this chapter.

5.2 Source of Oscillations

The main reason of oscillations is rested in the local elastic modulus modification scheme employed in the ECM, where the elastic modulus of each element is individually modified at each iteration r aiming to scale its equivalent stress down to the nominal stress. However, in the next iteration $r+1$, the equivalent stresses are computed with the contribution of all elements. Therefore, it is possible for an element, e.g. element k, to be loaded from other elements and its equivalent stress, namely $\bar{\sigma}_k^{r+1}$, exceeds the equivalent stress of element m ($\bar{\sigma}_m^{r+1}$), which has the maximum equivalent stress at the current iteration ($\bar{\sigma}_m^r = \bar{\sigma}_{\max}^r$). This phenomenon is called the stress overshooting in this thesis. If $\bar{\sigma}_k^{r+1}$ even becomes bigger than $\bar{\sigma}_{\max}^r$, a drop in the limit load curve happens. This matter is further illustrated through a simple example.

Consider the simple truss shown in Fig. 5.2 under reference loads, where $F = 1$ kN and $L = 4$m [121]. The truss consists of five elements, where the elastic modulus, E, and the cross section area, A, for all the members are taken as 1 kPa and 1m^2, respectively. The MECM with $\lambda = 0.5$ is performed on the structure. The normalized load multipliers are plotted for different iterations in Fig. 5.3. As seen, the drop in the limit load curve prevented the convergence to be defined on the collapse load solution, and therefore, the maximum number of iterations is used for stopping the iterations.

Fig. 5.4 shows the normalized stresses ($\frac{\sigma_i}{\sigma_0}$) for all the five truss elements. From

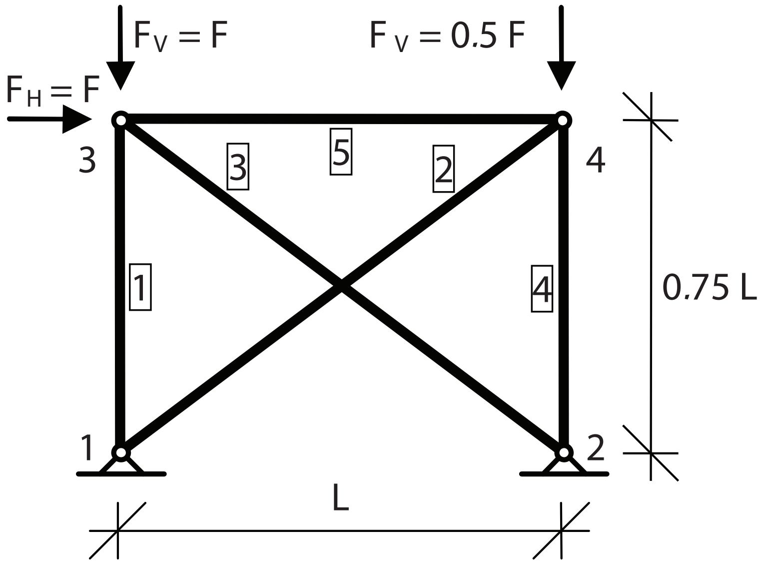

Figure 5.2: A simple truss - geometry and loading

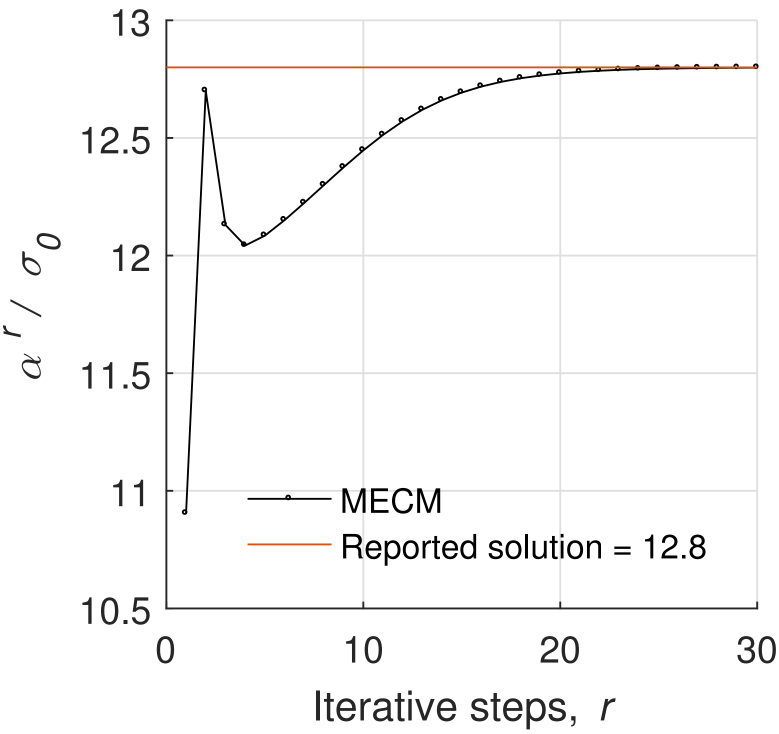

Figure 5.3: The iterative scheme for the considered truss using MECM

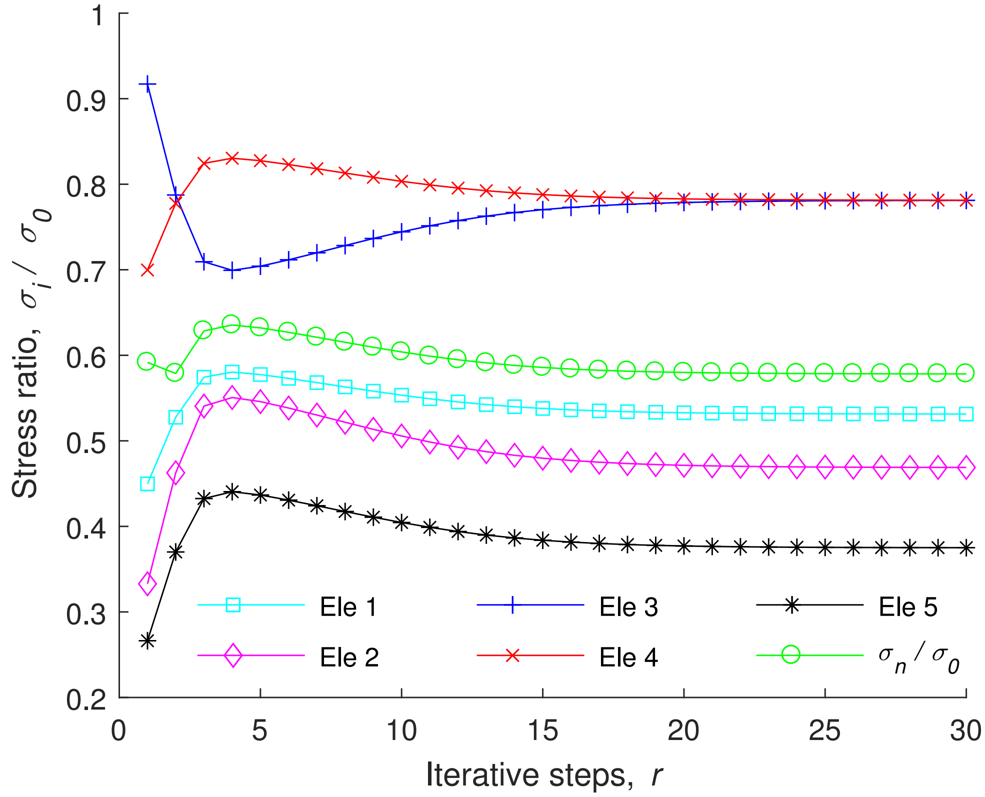

Figure 5.4: Variation of normalized stresses for the simple truss - $\lambda = 0.5$

this figure, it is obvious that the collapse of the structure occurs due to the yielding of both elements 3 and 4. The stresses of both of these elements sat above the nominal stress at the first iteration and the elastic moduli of them were reduced; however, the effect of the elastic modulus reduction in element 3 on element 4 had been more than the effect of the elastic modulus reduction of element 4 on itself and thus element 4 was loaded. This led to an increase in the stress of element 4. This loading on element 4 had been continued and led to stress overshooting in iteration 3, where a drop in the iterative scheme in Fig. 5.3 appeared.

The effect of the adjustment parameter λ on the stress overshooting phenomenon in this example is also investigated, where four smaller values for λ are considered (i.e. $\lambda = 0.1$, $\lambda = 0.05$, $\lambda = 0.01$, and $\lambda = 0.001$). The variations of normalized load multipliers and the associated normalized stresses for elements 3 and 4 are plotted in Fig. 5.5 and Fig. 5.6, respectively. Some graphs are zoomed-in to accentuate the drop and its associated stress overshooting. As seen, although the effect of the

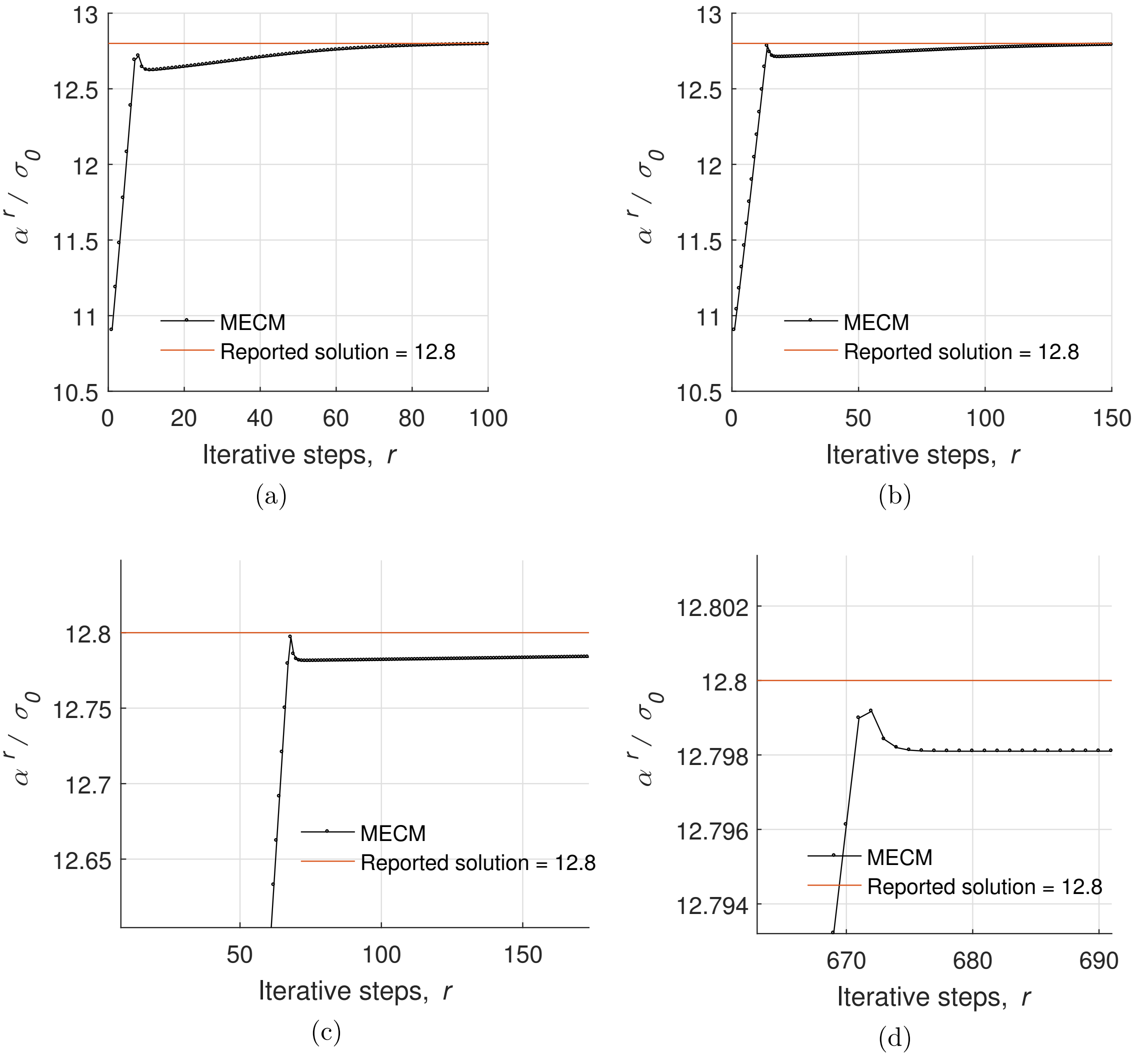

Figure 5.5: The presence of a drop in normalized load multipliers for the simple truss (a) $\lambda = 0.1$ (b) $\lambda = 0.05$ (c) $\lambda = 0.01$ (d) $\lambda = 0.001$

stress overshooting is reduced by decreasing the λ value, it is never vanished from the scheme.

5.3 Sensitivity-based ECM

In order to remove the oscillations in the local ECM or its modified versions, in this section the non-local sensitivity-based ECM is proposed. The proposed scheme predicts the stresses in the next iteration. The prediction is based on the first-order Taylor polynomial, where the effect of the elastic moduli changes of all elements is considered when the change of equivalent stress in an element is computed. In the

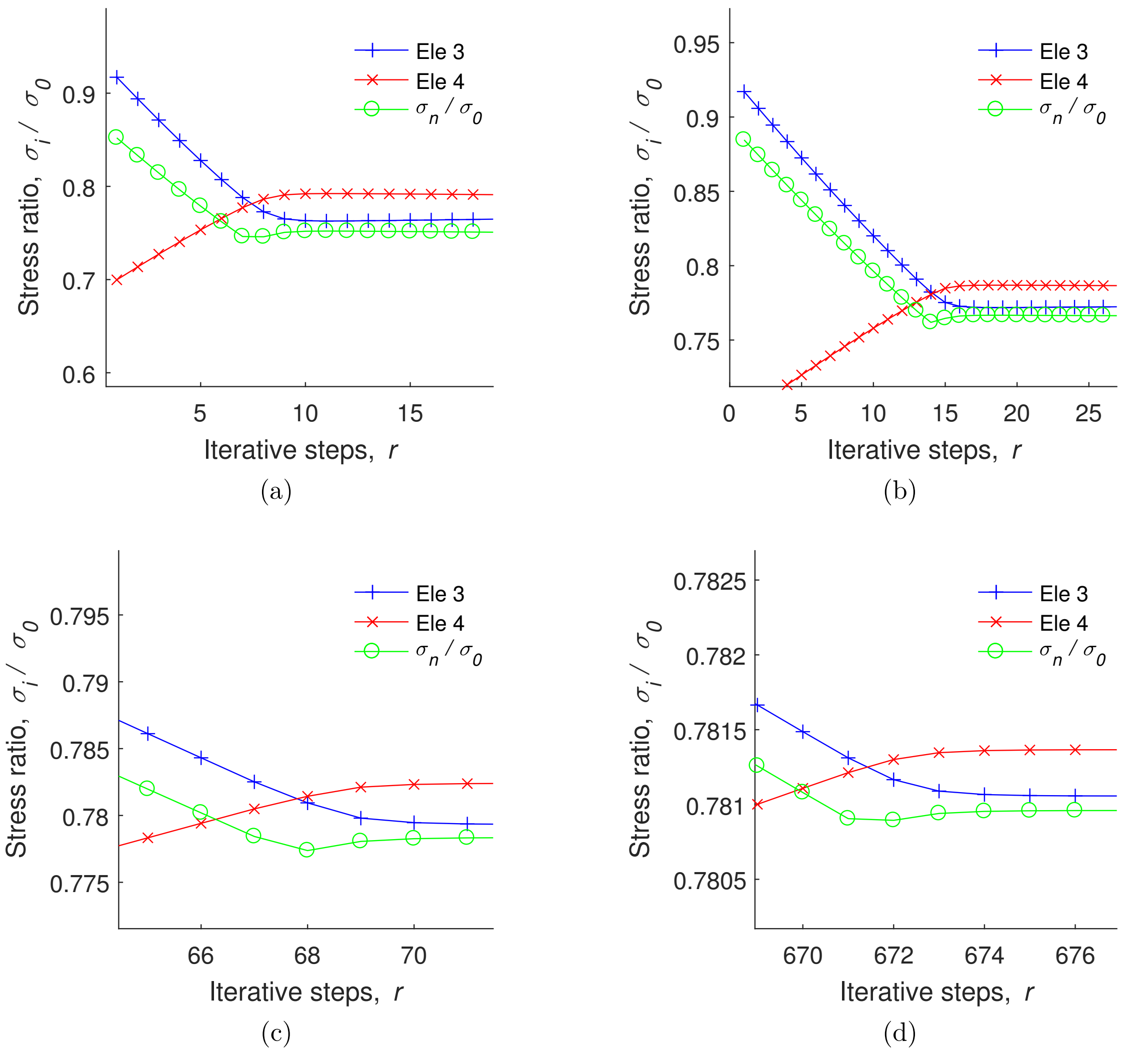

Figure 5.6: The stress overshootings for the simple truss (a) $\lambda = 0.1$ (b) $\lambda = 0.05$ (c) $\lambda = 0.01$ (d) $\lambda = 0.001$

case of stress overshooting, the proposed scheme simply scales the elastic moduli down to ensure the monotonic increase of load multipliers.

5.3.1 Stress Variations

Consider a structural system which is suitably discretised into n finite elements. In such a domain if forces, geometry and boundary conditions are kept constant, and the only quantity that varies is the elastic moduli, the equivalent stress $\bar{\sigma}_i$ in any discrete element i can be expressed as a multivariate function of the elastic modulus of every element in the domain. That is

$$\bar{\sigma}_i = f\left(E_1, E_2, \ldots, E_i, \ldots E_n\right) = f(\mathbf{E}) \tag{5.1}$$

, where E_j represents the elastic modulus of the j^{th} element in the domain, and $\mathbf{E}$ is the vector of elastic moduli of all elements.

Using the second-order Taylor series expansion, the equivalent stress variation $\Delta\bar{\sigma}_i$ in any discrete element i can be represented as

$$\Delta\bar{\sigma}_i = \left(\nabla\bar{\boldsymbol{\sigma}}_i\right)\left(\Delta\mathbf{E}\right) + \frac{1}{2}\left(\Delta\mathbf{E}\right)^{\mathrm{T}}\mathbf{H}_i\left(\Delta\mathbf{E}\right) \tag{5.2}$$

, where $\Delta\mathbf{E}$ represents the vector of elastic moduli changes. $\nabla\bar{\boldsymbol{\sigma}}_i$ shows the first-order derivative vector of the equivalent stress $\bar{\sigma}_i$ with respect to the vector of elastic moduli, and is defined as

$$\nabla\bar{\boldsymbol{\sigma}}_i = \frac{\partial\bar{\sigma}_i}{\partial\mathbf{E}} = \left\{\frac{\partial\bar{\sigma}_i}{\partial E_1}\ \frac{\partial\bar{\sigma}_i}{\partial E_2}\ \cdots\ \frac{\partial\bar{\sigma}_i}{\partial E_n}\right\}. \tag{5.3}$$

$\mathbf{H}_i$ is known as Hessian matrix and represents the second-order derivatives of the equivalent stress $\bar{\sigma}_i$ of the element i with respect to the vector of elastic moduli as

$$\mathbf{H}_i = \frac{\partial}{\partial \mathbf{E}}\left(\frac{\partial \bar{\sigma}_i}{\partial \mathbf{E}}\right)^{\mathrm{T}} = \begin{bmatrix} \frac{\partial^2 \bar{\sigma}_i}{\partial E_1^2} & \frac{\partial^2 \bar{\sigma}_i}{\partial E_1 \partial E_2} & \cdots & \frac{\partial^2 \bar{\sigma}_i}{\partial E_1 \partial E_n} \\ \frac{\partial^2 \bar{\sigma}_i}{\partial E_2 \partial E_1} & \frac{\partial^2 \bar{\sigma}_i}{\partial E_2^2} & \cdots & \frac{\partial^2 \bar{\sigma}_i}{\partial E_2 \partial E_n} \\ \vdots & \vdots & \ddots & \vdots \\ \frac{\partial^2 \bar{\sigma}_i}{\partial E_n \partial E_1} & \frac{\partial^2 \bar{\sigma}_i}{\partial E_n \partial E_2} & \cdots & \frac{\partial^2 \bar{\sigma}_i}{\partial E_n^2} \end{bmatrix}. \tag{5.4}$$

Assuming that the elastic moduli changes are sufficiently small, the equivalent stress variations for all elements can be approximated using the first-order Taylor series expansion as

$$\Delta \bar{\boldsymbol{\sigma}} = (\nabla \bar{\boldsymbol{\sigma}})(\Delta \mathbf{E}) \tag{5.5}$$

, where $\nabla \bar{\boldsymbol{\sigma}}$ shows the first derivatives of equivalent stresses for all elements with respect to elastic moduli changes. It is referred to as the sensitivity matrix in this thesis and is defined as

$$\nabla \bar{\boldsymbol{\sigma}} = \frac{\partial \bar{\boldsymbol{\sigma}}}{\partial \mathbf{E}} = \begin{bmatrix} \frac{\partial \bar{\sigma}_1}{\partial E_1} & \frac{\partial \bar{\sigma}_1}{\partial E_2} & \cdots & \frac{\partial \bar{\sigma}_1}{\partial E_n} \\ \frac{\partial \bar{\sigma}_2}{\partial E_1} & \frac{\partial \bar{\sigma}_2}{\partial E_2} & \cdots & \frac{\partial \bar{\sigma}_2}{\partial E_n} \\ \vdots & \vdots & \ddots & \vdots \\ \frac{\partial \bar{\sigma}_n}{\partial E_1} & \frac{\partial \bar{\sigma}_n}{\partial E_2} & \cdots & \frac{\partial \bar{\sigma}_n}{\partial E_n} \end{bmatrix}. \tag{5.6}$$

5.3.2 Derivation of the Sensitivity and Hessian Matrices

5.3.2.1 Sensitivity matrix

The sensitivity matrix can be computed from the equilibrium equation at the structural level. That is

$$\mathbf{F}_{\mathrm{G}} = \mathbf{K}_{\mathrm{G}} \mathbf{u}_{\mathrm{G}} \tag{5.7}$$

, where $\mathbf{F}_{\mathrm{G}}$, $\mathbf{K}_{\mathrm{G}}$, and $\mathbf{u}_{\mathrm{G}}$ show the global structural forces, structural stiffness matrix and structural displacements. Taking the derivatives of both sides with respect to the elastic modulus of an element j and using the chain rule lead to

$$\frac{\partial \mathbf{F}_{\mathrm{G}}}{\partial E_j} = \frac{\partial \mathbf{K}_{\mathrm{G}}}{\partial E_j}\mathbf{u}_{\mathrm{G}} + \mathbf{K}_{\mathrm{G}}\frac{\partial \mathbf{u}_{\mathrm{G}}}{\partial E_j}. \tag{5.8}$$

As the loads do not alter during the process of the elastic modulus adjustment, the left hand side of Eq. (5.8) is zero. $\frac{\partial \mathbf{K}_{\mathrm{G}}}{\partial E_j}$ shows the derivative of the global stiffness matrix with respect to the elastic modulus of the element j. It is simply obtained from the assembly of element stiffness matrix derivatives, $\frac{\partial \mathbf{K}}{\partial E_j}$. The derivative of the element stiffness matrix for an element i with respect to the elastic modulus of the element j can simply be obtained by taking the derivative of the definition of the stiffness matrix and is as

- In 2D spaces

$$\frac{\partial \mathbf{K}_i}{\partial E_j} = \int_S \mathbf{B}_i^{\mathrm{T}} \frac{\partial \mathbf{D}_i}{\partial E_j} \mathbf{B}_i \mathrm{d}S \tag{5.9}$$

- In 3D spaces

$$\frac{\partial \mathbf{K}_i}{\partial E_j} = \int_V \mathbf{B}_i^{\mathrm{T}} \frac{\partial \mathbf{D}_i}{\partial E_j} \mathbf{B}_i \mathrm{d}V \tag{5.10}$$

, where $\mathbf{B}_i$ is the strain-displacement matrix in the finite element method, and $\frac{\partial \mathbf{D}_i}{\partial E_j}$ shows the derivative of the elasticity matrix $\mathbf{D}$ of the element i with respect to the elastic modulus of the element j. Considering the fact that $\mathbf{D}_i$ has a linear relationship with the elastic modulus of the element i and using Eqs. (2.43) and (2.44), $\frac{\partial \mathbf{D}_i}{\partial E_j}$ can be obtained as

$$\frac{\partial \mathbf{D}_i}{\partial E_j} = \begin{cases} \frac{1}{E_i}\mathbf{D}_i & \text{if } i = j \\ \mathbf{O} & \text{if } i \neq j \end{cases} \tag{5.11}$$

, where $\mathbf{O}$ represents a null matrix of suitable size. Therefore, Eqs. (5.9) and (5.10) can be rewritten as

$$\frac{\partial \mathbf{K}_i}{\partial E_j} = \begin{cases} \frac{1}{E_i}\mathbf{K}_i & \text{if } i = j \\ \mathbf{O} & \text{if } i \neq j \end{cases} \tag{5.12}$$

Rearranging the Eq. (5.8) gives the changes of the displacements with respect to the change of the elastic modulus of the element j as

$$\frac{\partial \mathbf{u}_{\mathrm{G}}}{\partial E_j} = -\mathbf{K}_{\mathrm{G}}^{-1} \frac{\partial \mathbf{K}_{\mathrm{G}}}{\partial E_j} \mathbf{u}_{\mathrm{G}}. \tag{5.13}$$

Having $\frac{\partial \mathbf{u}_{\mathrm{G}}}{\partial E_j}$, the changes in strains in the element i due to changes of elastic modulus in the element j can be obtained by the definition of strains as

$$\frac{\partial \boldsymbol{\epsilon}_i}{\partial E_j} = \mathbf{B}_i \frac{\partial \mathbf{u}_i}{\partial E_j}. \tag{5.14}$$

, where $\mathbf{u}_i$ is the nodal displacements for the element i, which are extracted from the global displacements $\mathbf{u}_{\mathrm{G}}$ using the connectivity information of the elements. Finally, derivatives of stress tensors in the element i with respect to the elastic modulus of the element j can be computed using the Hook's law (Eq. (2.42)) and the use of the chain rule. Taking the derivatives of both sides of Eq. (2.42) for an element i with respect to the elastic modulus of element j leads to

$$\begin{gathered} \frac{\partial \boldsymbol{\sigma}_i}{\partial E_j} = \mathbf{D}_i \frac{\partial \boldsymbol{\epsilon}_i}{\partial E_j} + \frac{\partial \mathbf{D}_i}{\partial E_j} \boldsymbol{\epsilon}_i = \\ \begin{cases} \mathbf{D}_i \frac{\partial \boldsymbol{\epsilon}_i}{\partial E_i} + \frac{\mathbf{D}_i}{E_i} \boldsymbol{\epsilon}_i = \mathbf{D}_i \left(\frac{\partial \boldsymbol{\epsilon}_i}{\partial E_i} + \frac{\boldsymbol{\epsilon}_i}{E_i} \right) & \text{if } i = j \\ \mathbf{D}_i \frac{\partial \boldsymbol{\epsilon}_i}{\partial E_j} & \text{if } i \neq j \end{cases}. \end{gathered} \tag{5.15}$$

By having the stress tensors computed for elements based on the linear elastic analysis and their derivatives with respect to the elastic modulus of the j^{th} element (Eq. (5.15)), the changes in equivalent stresses can be derived from Eqs. (3.1) to (3.6) as

- **Plain strain**

$$\left(\frac{\partial \bar{\sigma}_i}{\partial E_j} \right)_M = \sqrt{\frac{3}{4}} \times \frac{\sigma_x \frac{\partial \sigma_x}{\partial E_j} + \sigma_y \frac{\partial \sigma_y}{\partial E_j} - \sigma_x \frac{\partial \sigma_y}{\partial E_j} - \sigma_y \frac{\partial \sigma_x}{\partial E_j} + 4\tau_{xy} \frac{\partial \tau_{xy}}{\partial E_j}}{\sqrt{\sigma_x^2 + \sigma_y^2 - 2\sigma_x \sigma_y + 4\tau_{xy}^2}} \tag{5.16}$$

$$\left(\frac{\partial \bar{\sigma}_i}{\partial E_j}\right)_T = \frac{\sigma_x \frac{\partial \sigma_x}{\partial E_j} + \sigma_y \frac{\partial \sigma_y}{\partial E_j} - \sigma_x \frac{\partial \sigma_y}{\partial E_j} - \sigma_y \frac{\partial \sigma_x}{\partial E_j} + 4\tau_{xy} \frac{\partial \tau_{xy}}{\partial E_j}}{\sqrt{\sigma_x^2 + \sigma_y^2 - 2\sigma_x \sigma_y + 4\tau_{xy}^2}} \tag{5.17}$$

- **Plain stress**

$$\left(\frac{\partial \bar{\sigma}_i}{\partial E_j}\right)_M = \frac{2\sigma_x \frac{\partial \sigma_x}{\partial E_j} + 2\sigma_y \frac{\partial \sigma_y}{\partial E_j} - \sigma_x \frac{\partial \sigma_y}{\partial E_j} - \sigma_y \frac{\partial \sigma_x}{\partial E_j} + 6\tau_{xy} \frac{\partial \tau_{xy}}{\partial E_j}}{2\sqrt{\sigma_x^2 + \sigma_y^2 - \sigma_x \sigma_y + 3\tau_{xy}^2}} \tag{5.18}$$

- **3D Space**

$$\left(\frac{\partial \bar{\sigma}_i}{\partial E_j}\right)_M = \frac{A\sigma_x + B\sigma_y + C\sigma_z + 6\left(\tau_{xy} \frac{\partial \tau_{xy}}{\partial E_j} + \tau_{xz} \frac{\partial \tau_{xz}}{\partial E_j} + \tau_{yz} \frac{\partial \tau_{yz}}{\partial E_j}\right)}{(\bar{\sigma}_i)_M} \tag{5.19}$$

, where

$$(\bar{\sigma}_i)_M = \sqrt{\sigma_x^2 + \sigma_y^2 + \sigma_z^2 - \sigma_x\sigma_y - \sigma_y\sigma_z - \sigma_x\sigma_z + 3\left(\tau_{xy}^2 + \tau_{xz}^2 + \tau_{yz}^2\right)} \tag{5.20}$$

$$A = 2\frac{\partial \sigma_x}{\partial E_j} - \frac{\partial \sigma_y}{\partial E_j} - \frac{\partial \sigma_z}{\partial E_j} \tag{5.21}$$

$$B = 2\frac{\partial \sigma_y}{\partial E_j} - \frac{\partial \sigma_x}{\partial E_j} - \frac{\partial \sigma_z}{\partial E_j} \tag{5.22}$$

$$C = 2\frac{\partial \sigma_z}{\partial E_j} - \frac{\partial \sigma_x}{\partial E_j} - \frac{\partial \sigma_y}{\partial E_j}. \tag{5.23}$$

In Eqs. (5.16) to (5.23), $\{\sigma_x, \sigma_y, \sigma_z, \tau_{xy}, \tau_{xz}, \tau_{yz}\}$ are the standard set of stress tensors for the element i. Computing $\frac{\partial \bar{\sigma}_i}{\partial E_j}$ for all $i = 1, 2, \ldots, n$ and $j = 1, 2, \ldots, n$ leads to the sensitivity matrix shown in Eq. (5.6). It should be noticed that due to the non-smooth behavior of the Tresca yielding criterion in plain stress and 3D cases, the derivatives of the Tresca yielding condition for these two cases are not considered.

5.3.2.2 Hessian matrix

Similar to the sensitivity matrix, the Hessian matrix can be computed from the equilibrium equation in the structural level (Eq. (5.7)). Taking the derivatives of

Eq. (5.8) with respect to the elastic modulus of the element k leads to:

$$\frac{\partial^2 \mathbf{K}_\mathrm{G}}{\partial E_j \partial E_k}\mathbf{u}_\mathrm{G} + \frac{\partial \mathbf{K}_\mathrm{G}}{\partial E_j}\frac{\partial \mathbf{u}_\mathrm{G}}{\partial E_k} + \frac{\partial \mathbf{K}_\mathrm{G}}{\partial E_k}\frac{\partial \mathbf{u}_\mathrm{G}}{\partial E_j} + \mathbf{K}_\mathrm{G}\frac{\partial^2 \mathbf{u}_\mathrm{G}}{\partial E_j \partial E_k} = 0 \tag{5.24}$$

, where $\frac{\partial^2 \mathbf{K}_\mathrm{G}}{\partial E_j \partial E_k}$ and $\frac{\partial^2 \mathbf{u}_\mathrm{G}}{\partial E_j \partial E_k}$ show the derivatives of $\frac{\partial \mathbf{K}_\mathrm{G}}{\partial E_j}$ and $\frac{\partial \mathbf{u}_\mathrm{G}}{\partial E_j}$ with respect to E_k. The term $\frac{\partial^2 \mathbf{K}_\mathrm{G}}{\partial E_j \partial E_k}$, obtained by the assembly of $\frac{\partial^2 \mathbf{K}_i}{\partial E_j \partial E_k}$ for all $i = \{1, 2, \ldots, n\}$, is a null matrix with the same size of $\mathbf{K}_\mathrm{G}$. This is due to the fact that each of $\frac{\partial^2 \mathbf{K}_i}{\partial E_j \partial E_k}$ matrices is a null matrix with the same size of $\mathbf{K}_i$. This is proved using Eq. (5.12) and considering five conditions.

- $i \neq j \neq k$ and $i \neq j = k$

$$\frac{\partial^2 \mathbf{K}_i}{\partial E_j \partial E_k} = \frac{\partial}{\partial E_j}\left(\frac{\partial \mathbf{K}_i}{\partial E_k}\right) = \frac{\partial \mathbf{O}}{\partial E_j} = \mathbf{O} \tag{5.25}$$

- $i = j \neq k$

$$\frac{\partial^2 \mathbf{K}_i}{\partial E_j \partial E_k} = \frac{\partial}{\partial E_j}\left(\frac{\partial \mathbf{K}_i}{\partial E_k}\right) = \frac{\partial \mathbf{O}}{\partial E_j} = \mathbf{O} \tag{5.26}$$

- $i = k \neq j$

$$\frac{\partial^2 \mathbf{K}_i}{\partial E_j \partial E_k} = \frac{\partial}{\partial E_j}\left(\frac{\partial \mathbf{K}_i}{\partial E_k}\right) = \frac{1}{E_i}\frac{\partial \mathbf{K}_i}{\partial E_j} = \frac{1}{E_i}\mathbf{O} = \mathbf{O} \tag{5.27}$$

- $i = j = k$

$$\frac{\partial^2 \mathbf{K}_i}{\partial E_j \partial E_k} = \frac{\partial}{\partial E_j}\left(\frac{\partial \mathbf{K}_i}{\partial E_k}\right) = \frac{\partial}{\partial E_i}\left(\frac{\mathbf{K}_i}{E_i}\right) = \frac{-\mathbf{K}_i}{E_i^2} + \frac{\mathbf{K}_i}{E_i^2} = \mathbf{O} \tag{5.28}$$

The second derivatives of the global displacements can be obtained by rearranging of Eq. (5.24) as

$$\frac{\partial^2 \mathbf{u}_\mathrm{G}}{\partial E_j \partial E_k} = -\mathbf{K}_\mathrm{G}^{-1}\left(\frac{\partial \mathbf{K}_\mathrm{G}}{\partial E_j}\frac{\partial \mathbf{u}_\mathrm{G}}{\partial E_k} + \frac{\partial \mathbf{K}_\mathrm{G}}{\partial E_k}\frac{\partial \mathbf{u}_\mathrm{G}}{\partial E_j}\right). \tag{5.29}$$

The second derivatives of strains of the element i can be derived by using the strain-displacement matrix. That is

$$\frac{\partial^2 \boldsymbol{\epsilon}_i}{\partial E_j \partial E_k} = \mathbf{B}_i \frac{\partial^2 \mathbf{u}_{\mathrm{G}}}{\partial E_j \partial E_k}. \tag{5.30}$$

The second derivatives of stress tensors for an element i can be obtained by making making use of the stress-strain relationship and chain rule. Considering the fact that the second derivative of elasticity matrix $\frac{\partial^2 \mathbf{D}_i}{\partial E_j \partial E_k}$ is a null matrix, $\frac{\partial^2 \boldsymbol{\sigma}_i}{\partial E_j \partial E_k}$ is obtained from

$$\frac{\partial^2 \boldsymbol{\sigma}_i}{\partial E_j \partial E_k} = \mathbf{D}_i \frac{\partial^2 \boldsymbol{\epsilon}_i}{\partial E_j \partial E_k} + \frac{\partial \mathbf{D}_i}{\partial E_j}\frac{\partial \boldsymbol{\epsilon}_i}{\partial E_k} + \frac{\partial \mathbf{D}_i}{\partial E_k}\frac{\partial \boldsymbol{\epsilon}_i}{\partial E_j}. \tag{5.31}$$

The second derivative of equivalent stress for the element i can be obtained by differentiating the Eqs. (5.16) to (5.19) with respect to the elastic modulus of the element k. This leads to the following equations:

- **Plain strain**

$$\begin{aligned}
\left(\frac{\partial^2 \bar{\sigma}_i}{\partial E_j \partial E_k}\right)_M = \\
\frac{3}{4(\bar{\sigma}_i)_M}\{ & \frac{-(\frac{\partial \bar{\sigma}_i}{\partial E_k})_M(\sigma_x \frac{\partial \sigma_x}{\partial E_j} + \sigma_y \frac{\partial \sigma_y}{\partial E_j} - \sigma_x \frac{\partial \sigma_y}{\partial E_j} - \sigma_y \frac{\partial \sigma_x}{\partial E_j} + 4\tau_{xy}\frac{\partial \tau_{xy}}{\partial E_j})}{(\bar{\sigma}_i)_M} \\
& + \frac{\partial \sigma_x}{\partial E_k}\frac{\partial \sigma_x}{\partial E_j} + \sigma_x \frac{\partial^2 \sigma_x}{\partial E_j \partial E_k} + \frac{\partial \sigma_y}{\partial E_k}\frac{\partial \sigma_y}{\partial E_j} + \sigma_y \frac{\partial^2 \sigma_y}{\partial E_j \partial E_k} \\
& - (\frac{\partial \sigma_x}{\partial E_k}\frac{\partial \sigma_y}{\partial E_j} + \sigma_x \frac{\partial^2 \sigma_y}{\partial E_j \partial E_k}) - (\frac{\partial \sigma_y}{\partial E_k}\frac{\partial \sigma_x}{\partial E_j} + \sigma_y \frac{\partial^2 \sigma_x}{\partial E_j \partial E_k}) + \\
& 4(\frac{\partial \tau_{xy}}{\partial E_k}\frac{\partial \tau_{xy}}{\partial E_j} + \tau_{xy}\frac{\partial^2 \tau_{xy}}{\partial E_j \partial E_k})\}
\end{aligned} \tag{5.32}$$

$$\left(\frac{\partial^2\bar{\sigma}_i}{\partial E_j \partial E_k}\right)_T = \frac{1}{(\bar{\sigma}_i)_T}\{\frac{-(\frac{\partial\bar{\sigma}_i}{\partial E_k})_T(\sigma_x\frac{\partial\sigma_x}{\partial E_j}+\sigma_y\frac{\partial\sigma_y}{\partial E_j}-\sigma_x\frac{\partial\sigma_y}{\partial E_j}-\sigma_y\frac{\partial\sigma_x}{\partial E_j}+4\tau_{xy}\frac{\partial\tau_{xy}}{\partial E_j})}{(\bar{\sigma}_i)_T} + \frac{\partial\sigma_x}{\partial E_k}\frac{\partial\sigma_x}{\partial E_j}+\sigma_x\frac{\partial^2\sigma_x}{\partial E_j\partial E_k}+\frac{\partial\sigma_y}{\partial E_k}\frac{\partial\sigma_y}{\partial E_j}+\sigma_y\frac{\partial^2\sigma_y}{\partial E_j\partial E_k} - (\frac{\partial\sigma_x}{\partial E_k}\frac{\partial\sigma_y}{\partial E_j}+\sigma_x\frac{\partial^2\sigma_y}{\partial E_j\partial E_k}) - (\frac{\partial\sigma_y}{\partial E_k}\frac{\partial\sigma_x}{\partial E_j}+\sigma_y\frac{\partial^2\sigma_x}{\partial E_j\partial E_k}) + 4(\frac{\partial\tau_{xy}}{\partial E_k}\frac{\partial\tau_{xy}}{\partial E_j}+\tau_{xy}\frac{\partial^2\tau_{xy}}{\partial E_j\partial E_k})\} \quad (5.33)$$

- **Plain stress**

$$\left(\frac{\partial^2\bar{\sigma}_i}{\partial E_j \partial E_k}\right)_M = \frac{1}{2(\bar{\sigma}_i)_M}\{\frac{-(\frac{\partial\bar{\sigma}_i}{\partial E_k})_M(2\sigma_x\frac{\partial\sigma_x}{\partial E_j}+2\sigma_y\frac{\partial\sigma_y}{\partial E_j}-\sigma_x\frac{\partial\sigma_y}{\partial E_j}-\sigma_y\frac{\partial\sigma_x}{\partial E_j}+6\tau_{xy}\frac{\partial\tau_{xy}}{\partial E_j})}{(\bar{\sigma}_i)_M} + 2(\frac{\partial\sigma_x}{\partial E_k}\frac{\partial\sigma_x}{\partial E_j}+\sigma_x\frac{\partial^2\sigma_x}{\partial E_j\partial E_k})+2(\frac{\partial\sigma_y}{\partial E_k}\frac{\partial\sigma_y}{\partial E_j}+\sigma_y\frac{\partial^2\sigma_y}{\partial E_j\partial E_k}) - (\frac{\partial\sigma_x}{\partial E_k}\frac{\partial\sigma_y}{\partial E_j}+\sigma_x\frac{\partial^2\sigma_y}{\partial E_j\partial E_k}) - (\frac{\partial\sigma_y}{\partial E_k}\frac{\partial\sigma_x}{\partial E_j}+\sigma_y\frac{\partial^2\sigma_x}{\partial E_j\partial E_k}) + 6(\frac{\partial\tau_{xy}}{\partial E_k}\frac{\partial\tau_{xy}}{\partial E_j}+\tau_{xy}\frac{\partial^2\tau_{xy}}{\partial E_j\partial E_k})\} \quad (5.34)$$

, where $\{\sigma_x, \sigma_y, \tau_{xy}\}$ are the standard set of stress tensors for the element i in 2D cases. $(\bar{\sigma}_i)_M$ and $(\bar{\sigma}_i)_T$ are the von Mises and Tresca equivalent stress resultants of the element i, respectively. $(\frac{\partial\bar{\sigma}_i}{\partial E_k})_M$ and $(\frac{\partial\bar{\sigma}_i}{\partial E_k})_T$ are the equivalent stress derivatives for the von Mises and Tresca yielding conditions obtained from Eqs. (5.16) to (5.18).

- **3D spaces**

$$
\begin{aligned}
&\left(\frac{\partial^2 \bar{\sigma}_i}{\partial E_j \partial E_k}\right)_M = \\
&\frac{1}{(\bar{\sigma}_i)_M}\{\frac{-(\frac{\partial \bar{\sigma}_i}{\partial E_k})_M (A\sigma_x + B\sigma_y + C\sigma_z + 6(\tau_{xy}\frac{\partial \tau_{xy}}{\partial E_j} + \tau_{xz}\frac{\partial \tau_{xz}}{\partial E_j} + \tau_{yz}\frac{\partial \tau_{yz}}{\partial E_j}))}{(\bar{\sigma}_i)_M} \\
&\qquad + \frac{\partial A}{\partial E_k}\sigma_x + A\frac{\partial \sigma_x}{\partial E_k} + \frac{\partial B}{\partial E_k}\sigma_y + B\frac{\partial \sigma_y}{\partial E_k} + \frac{\partial C}{\partial E_k}\sigma_z + C\frac{\partial \sigma_z}{\partial E_k} \\
&\qquad + 6(\frac{\partial \tau_{xy}}{\partial E_k}\frac{\partial \tau_{xy}}{\partial E_j} + \tau_{xy}\frac{\partial^2 \tau_{xy}}{\partial E_j \partial E_k} + \frac{\partial \tau_{xz}}{\partial E_k}\frac{\partial \tau_{xz}}{\partial E_j} + \tau_{xz}\frac{\partial^2 \tau_{xz}}{\partial E_j \partial E_k} + \\
&\qquad\qquad \frac{\partial \tau_{yz}}{\partial E_k}\frac{\partial \tau_{yz}}{\partial E_j} + \tau_{yz}\frac{\partial^2 \tau_{yz}}{\partial E_j \partial E_k})\}
\end{aligned} \tag{5.35}
$$

, where $\{\sigma_x, \sigma_y, \sigma_z, \tau_{xy}, \tau_{xz}, \tau_{yz}\}$ are the standard set of stress tensors for the element i in 3D spaces. $(\bar{\sigma}_i)_M$ and $(\frac{\partial \bar{\sigma}_i}{\partial E_k})_M$ are the equivalent von Mises stress and first derivative if it, which are defined in Eqs. (5.20) and (5.19), respectively. The factors A, B, and C are based on Eqs. (5.21) to (5.23), whose first derivatives can be obtained as follows

$$\frac{\partial A}{\partial E_k} = 2\frac{\partial^2 \sigma_x}{\partial E_j \partial E_k} - \frac{\partial^2 \sigma_y}{\partial E_j \partial E_k} - \frac{\partial^2 \sigma_z}{\partial E_j \partial E_k} \tag{5.36}$$

$$\frac{\partial B}{\partial E_k} = 2\frac{\partial^2 \sigma_y}{\partial E_j \partial E_k} - \frac{\partial^2 \sigma_x}{\partial E_j \partial E_k} - \frac{\partial^2 \sigma_z}{\partial E_j \partial E_k} \tag{5.37}$$

$$\frac{\partial C}{\partial E_k} = 2\frac{\partial^2 \sigma_z}{\partial E_j \partial E_k} - \frac{\partial^2 \sigma_x}{\partial E_j \partial E_k} - \frac{\partial^2 \sigma_y}{\partial E_j \partial E_k}. \tag{5.38}$$

5.3.3 Finite Element Implementation of the Sensitivity-based ECM

Similar to the local ECM, the non-local sensitivity-based ECM performs a series of linear elastic analyses of sufficiently ductile structures that are modeled within the finite element framework to determine the maximum load capacity at the plastic collapse. The structural system is suitably discretised into n finite elements. At each iteration, r, an elastic analysis is performed and the nodal displacements for all nodes, $\mathbf{u}_\mathrm{G}$, strain and stress tensors (viz, $\boldsymbol{\epsilon}_i$ and $\boldsymbol{\sigma}_i$, respectively) are computed for all of the elements $i = \{1, 2, \ldots, n\}$. The equivalent stresses $\bar{\boldsymbol{\sigma}}^r$ for the von Mises or Tresca yielding conditions are only computed at the first iteration, and for other iterations, they are already estimated in the previous iteration as discussed below. By having these information, the sensitivity matrix of all elements ($\nabla\bar{\boldsymbol{\sigma}}$) in Eq. (5.6) is derived as discussed in section 5.3.2.1.

As in the ECM, the sensitivity-based ECM carries out the stress redistribution of some critical elements with high stresses by systematically adjusting the stiffness properties(i.e. Young's modulus) of them. Therefore, the methodology firstly selects the critical elements j whose equivalent stresses $\bar{\sigma}_j^r$ are greater than the nominal stress σ_n^r. These elements are included in a set known as the active set, $\mathbf{S}_{active}$. The complementary set of $\mathbf{S}_{active}$, which includes all of the other elements, is called the non-active set, $\mathbf{S}_{non-active}$, representing non-selected elements. The definition of the nominal stress is similar to the MECM and follows

$$\sigma_n^r = \bar{\sigma}_{\max}^r - \lambda \left(\bar{\sigma}_{\max}^r - \bar{\sigma}_{\min}^r\right). \tag{5.39}$$

λ is a modification factor, $\bar{\sigma}_{\max}^r$ and $\bar{\sigma}_{\min}^r$ are the maximum and minimum stress resultants developed at iteration r in the whole structure, namely $\bar{\sigma}_{\max}^r = \max\left(\bar{\sigma}_i^r\right)$ and $\bar{\sigma}_{\min}^r = \min\left(\bar{\sigma}_i^r\right)$ for all $i = 1$ to n elements, respectively.

To include the contribution of the other elements, the variation of elastic moduli of elements, $\Delta\mathbf{E}$, can be estimated by rearranging Eq. (5.5), following

$$\Delta\mathbf{E} = \left(\nabla\bar{\boldsymbol{\sigma}}\right)^{-1}\left(\Delta\bar{\boldsymbol{\sigma}}\right) \tag{5.40}$$

, where $\Delta\bar{\boldsymbol{\sigma}}$ is the stress difference vector and can be computed as follows

$$\left(\Delta\bar{\sigma}\right)_i = \begin{cases} \sigma_n^r - \bar{\sigma}_i^r & \text{if } i \in \mathbf{S}_{active} \\ 0 & \text{if } i \in \mathbf{S}_{non-active} \end{cases}. \tag{5.41}$$

It should be noticed that, similar to the MECM, the elastic moduli of the elements in the non-active set should not be altered. This is imposed to the Eq. (5.40) as initial boundary values (i.e. $(\Delta E)_{i\in\mathbf{S}_{non-active}} = 0$). Therefore, Eq. (5.40) is solved similar to the equilibrium equation in the FEM ($\mathbf{u}_{\mathrm{G}} = \mathbf{K}_{\mathrm{G}}^{-1}\mathbf{F}_{\mathrm{G}}$).

The variation of the elastic moduli obtained from Eq. (5.40) can be used for approximating the equivalent stresses in the next iteration using the first term of Taylor series, providing that $\Delta\mathbf{E}$ is sufficiently small. The proposed sensitivity-based ECM considers this matter through defining β_i factor for each element by comparing the linear approximation of its equivalent stress variation ($(\Delta\bar{\sigma}_i)_1 = (\nabla\bar{\boldsymbol{\sigma}}_i)(\Delta\mathbf{E})$) and the second term of the second-order approximation for its equivalent stress variation ($(\Delta\bar{\sigma}_i)_2 = \frac{1}{2}(\Delta\mathbf{E})^{\mathrm{T}}\mathbf{H}_i(\Delta\mathbf{E})$). If the ratio of $\bar{\beta}_i = |\frac{(\Delta\bar{\sigma}_i)_2}{(\Delta\bar{\sigma}_i)_1}|$ for the element is less than a predefined tolerance, ε_1, then β_i is unit; otherwise, β_i is defined to scale down this ratio to ε_1. That is

$$\beta_i = \begin{cases} 1 & \text{if } \bar{\beta}_i \leq \varepsilon_1 \\ \\ \frac{\varepsilon_1}{\bar{\beta}_i} & \text{if } \bar{\beta}_i > \varepsilon_1 \end{cases} \tag{5.42}$$

By having the β coefficients for all elements, $\Delta\mathbf{E}$ can be scaled down by the factor $\beta_{\min}$ to ensure the accuracy of the linear approximation of the equivalent stresses for all elements. $\beta_{\min}$ is the minimum amount between the computed β factors (i.e. $\beta_{\min} = \min(\beta_i)$, $i = 1, 2, \ldots, n$).

The predefined tolerance ε_1 should be taken sufficiently small to ensure the accuracy of the explicit scheme. However, very small values of it are likely to impose a larger number of numerical iterations for a solution convergence. Our numerical experience indicates that the value of $\varepsilon_1 = 2.5\times10^{-2}$ can be taken adequately small to ensure the validity of the explicit scheme, yet sufficiently large to consider the efficiency of the method.

By having the updated elastic moduli variations for all elements, the equivalent stresses can be linearly estimated and used as the prediction of stresses in the next iteration. That is

$$\bar{\boldsymbol{\sigma}}^{r+1} = \bar{\boldsymbol{\sigma}}^{r} + \beta_{\min} \times (\nabla \bar{\boldsymbol{\sigma}}) (\Delta \mathbf{E}) . \tag{5.43}$$

In order to prevent the stress overshooting, the predicted stresses are divided into the active and non-active sets, $\bar{\boldsymbol{\sigma}}^{r+1}_{\mathbf{S}_{active}}$ and $\bar{\boldsymbol{\sigma}}^{r+1}_{\mathbf{S}_{non-active}}$, respectively. We define the maximum predicted equivalent stress for the active set as

$$\bar{\sigma}_{m}^{r+1} = \max\left(\bar{\boldsymbol{\sigma}}^{r+1}_{\mathbf{S}_{active}}\right) \tag{5.44}$$

, where m is the element having this maximum stress.

To avoid the stress overshooting in the next iteration, the predicted equivalent stresses in the non-active set should not exceed $\bar{\sigma}_{m}^{r+1}$. If this happens, the proposed scheme simply reduces the elastic moduli by a factor less than 1. Therefore, the factor γ_j is defined for all elements $j \in \mathbf{S}_{non-active}$ as follows

$$\gamma_j = \begin{cases} 1 & \text{if } \bar{\sigma}_{j}^{r+1} \leq \bar{\sigma}_{m}^{r+1} \\ \frac{\bar{\sigma}_{m}^{r} - \bar{\sigma}_{j}^{r}}{\beta_{\min} [\nabla \bar{\boldsymbol{\sigma}}_j - \nabla \bar{\boldsymbol{\sigma}}_m] (\Delta \mathbf{E})} & \text{if } \bar{\sigma}_{j}^{r+1} > \bar{\sigma}_{m}^{r+1} \end{cases} \tag{5.45}$$

Eq. (5.45) is defined so that in case of stress overshooting of the element $j \in \mathbf{S}_{non-active}$, the predicted equivalent stresses of elements m and j become equal. Therefore, the most suitable factor to be multiplied by $\Delta \mathbf{E}$ for prevention of stress overshooting is the minimum of all γ factors. That is

$$\gamma_{min} = \min(\gamma_j) \ \text{ for all}\, j \in \mathbf{S}_{non-active} \tag{5.46}$$

Finally, the final linear approximation of the equivalent stresses in the next iteration can be obtained as follows

$$\bar{\boldsymbol{\sigma}}^{r+1} = \bar{\boldsymbol{\sigma}}^{r} + \beta_{\min} \times \gamma_{min} \times (\nabla \bar{\boldsymbol{\sigma}}) (\Delta \mathbf{E}) . \tag{5.47}$$

, where $\bar{\boldsymbol{\sigma}}^{r+1}$ shows the estimation of equivalent stresses in the next iteration. Use of these stresses in the next iteration guarantees the oscillation free scheme for load multipliers. The elastic moduli of all elements to be used in the next iteration can also be obtained as

$$\mathbf{E}^{r+1} = \mathbf{E}^{r} + \beta_{\min} \times \gamma_{min} \times \Delta\mathbf{E} \tag{5.48}$$

At each iteration, the load multiplier, α^r, is then obtained by making use of the estimated stresses as

$$\alpha^r = \sigma_0 / \bar{\sigma}^r_{\max} \tag{5.49}$$

, where σ_0 is the predefined yield stress of the material, and $\bar{\sigma}^r_{\max}$ is the maximum estimated stress in the whole domain. Considering the fact that there is no stress overshooting, and consequently no drop in the limit load curve, the convergence of the scheme can be defined directly on load multipliers as follows

$$\Delta = \frac{\alpha^r - \alpha^{r-1}}{\alpha^r} < \varepsilon_2 \tag{5.50}$$

where Δ shows the normalized difference in load multipliers between iterative steps r and $r-1$, and ε_2 is a predefined tolerance.

It is useful to make some additional remarks regarding our sensitivity-based ECM, as follows:

- The elastic moduli computed based on Eq. (5.40) do not allow unloading to be considered for the elements in active set. This is due to the fact that the final equivalent stresses obtained by this set of elastic moduli are either equal to the nominal stress σ^r_n ,if $\Delta\mathbf{E}$ is small enough (i.e. $\beta_{\min} = 1$), or greater than σ^r_n, if $\Delta\mathbf{E}$ is not small enough (i.e. $\beta_{\min} < 1$). Hence, they will be included in the active set in the next iteration as $\sigma^{r+1}_n < \sigma^r_n$. In other words, the unloading of the assumed yielded elements in the active set cannot be seen. This might be true for many structures; however, for some structures, some active elements might be unloaded due the yielding of some other elements. Our proposed sensitivity-based ECM is able to identify these elements by the unique characteristic of the sensitivity matrix. After the computation of the elastic moduli based on Eq. (5.40), the associated hollow matrix of the sensitivity matrix can be defined as follows

$$(\nabla\bar{\boldsymbol{\sigma}})_{\mathrm{H}} = \nabla\bar{\boldsymbol{\sigma}} - (\nabla\bar{\boldsymbol{\sigma}})_{\mathrm{D}} \tag{5.51}$$

, where $(\nabla\bar{\boldsymbol{\sigma}})_{\mathrm{H}}$ only considers the contribution of all the other elements on the stress variation of each of the element. The matrix $(\nabla\bar{\boldsymbol{\sigma}})_{\mathrm{D}}$ shows the diagonal matrix of the sensitivity matrix, and is defined as follows

$$(\nabla\bar{\boldsymbol{\sigma}})_{\mathrm{D}} = \mathrm{diag}\,(\nabla\bar{\boldsymbol{\sigma}}) = \begin{bmatrix} \frac{\partial\bar{\sigma}_1}{\partial E_1} & 0 & \cdots & 0 \\ 0 & \frac{\partial\bar{\sigma}_2}{\partial E_2} & \cdots & 0 \\ \vdots & \vdots & \ddots & \vdots \\ 0 & 0 & \cdots & \frac{\partial\bar{\sigma}_n}{\partial E_n} \end{bmatrix}. \tag{5.52}$$

The matrix $(\nabla\bar{\boldsymbol{\sigma}})_{\mathrm{D}}$ is basically the matrix which is implicitly used in the ECM, and as can be seen, it does not consider the contribution of the other elements. Therefore, based on Eq. (5.51) the hollow sensitivity matrix is of the form of

$$(\nabla\bar{\boldsymbol{\sigma}})_{\mathrm{H}} = \begin{bmatrix} 0 & \frac{\partial\bar{\sigma}_1}{\partial E_2} & \cdots & \frac{\partial\bar{\sigma}_1}{\partial E_n} \\ \frac{\partial\bar{\sigma}_2}{\partial E_1} & 0 & \cdots & \frac{\partial\bar{\sigma}_2}{\partial E_n} \\ \vdots & \vdots & \ddots & \vdots \\ \frac{\partial\bar{\sigma}_n}{\partial E_1} & \frac{\partial\bar{\sigma}_n}{\partial E_2} & \cdots & 0 \end{bmatrix}. \tag{5.53}$$

By having the hollow sensitivity matrix, the direction of the loading for each of the elements due to the presence of the other elements can be obtained as

$$(\Delta\bar{\boldsymbol{\sigma}})^{\mathrm{dir.}} = (\nabla\bar{\boldsymbol{\sigma}})_{\mathrm{H}}\,(\Delta\mathbf{E}) \tag{5.54}$$

, where $(\Delta\bar{\boldsymbol{\sigma}})^{\mathrm{dir.}}$ shows the direction of loading for all the elements imposed from the other elements. $(\Delta\bar{\sigma})_i^{\mathrm{dir}} > 0$ represents loading of the element i from the other elements, and $(\Delta\bar{\sigma})_i^{\mathrm{dir}} < 0$ shows the unloading of the element i from the other elements. Therefore, to include the unloading of the elements whose $(\Delta\bar{\sigma})_i^{\mathrm{dir}} < 0$, the sensitivity matrix, only in Eq. (5.40) is replaced with the modified sensitivity matrix, $(\nabla\bar{\boldsymbol{\sigma}})_{\mathrm{M}}$, whose rows ($i$) are defined as follows

$$(\nabla\bar{\boldsymbol{\sigma}})_{\mathrm{M}_i} = \begin{cases} (\nabla\bar{\boldsymbol{\sigma}})_i & \text{if } (\Delta\bar{\sigma})_i^{\mathrm{dir}} > 0 \\ (\nabla\bar{\boldsymbol{\sigma}})_{\mathrm{D}_i} & \text{if } (\Delta\bar{\sigma})_i^{\mathrm{dir}} < 0 \end{cases}. \tag{5.55}$$

Definition of the modified sensitivity matrix as in Eq. (5.55) permits the equivalent stresses of the unloaded elements to sit below the nominal stress. The updated elastic moduli is then obtained as

$$\Delta\mathbf{E} = \left((\nabla\bar{\boldsymbol{\sigma}})_{\mathrm{M}}\right)^{-1}(\Delta\bar{\boldsymbol{\sigma}}). \tag{5.56}$$

Eqs. (5.54) to (5.56) are repeated until no difference between two consecutive sets of $\Delta\mathbf{E}$ is seen. Thereafter, the final updated set of elastic moduli will be used in Eqs. (5.42) to (5.48).

- In the control of the stress overshooting, there is a possibility that the factor γ_{min} becomes very small if the stress overshooting for an element k whose equivalent stress is slightly below the nominal stress occurs. This might have a negative effect on the convergence of the method. To prevent this, another condition is considered. When γ_{min} is computed as less than $0.001\beta_{\min}$, which represents the occurrence of the mentioned stress overshooting, the nominal stress is decreased by slightly increasing the parameter λ such that the element k is included in the active set. Thereafter, this iteration is repeated once more. This prevents the sudden changes of γ_{min} factor, and allows a smooth monotonic limit load curve to be obtained.

- Similar to the ECM, the Poisson's ratio should be taken as close to 0.5 to represent the incompressibility. This is achieved by implementing the selective integration scheme for the low-order elements and by the use of $\nu = 0.499$ as in the MECM described in chapter 3.

- Similar to the ECM, the suitable choice of the parameter λ is also of importance. Though, all choices of $\lambda \in (0,\ 1)$ lead to a smooth monotonic limit load solutions, the values of converged solutions are different for different values of λ. High values of λ result in the lower converged collapse loads which are far away from the actual collapse load, However, the small values of it lead to converged solutions which are close enough to the true collapse load of the structure. In this thesis the value of 0.01 for λ is proposed, which makes the scheme suitable for practical engineering application. More discussions are provided in the section 5.4.1.1.

The pseudo code summarizing key steps underlying the sensitivity-based ECM is prescribed below:

Step 0: Initialization

- At iteration $r = 1$, initialize: tolerances ε_1 and ε_2, $\lambda = 0.01$, yielding limit σ_0, and the elastic Young's modulus vector $\mathbf{E}^1$
- Construct a finite element model, and assemble the global nodal forces vector and global stiffness matrix associated with 2D (or 3D) structure.

Step 1: Iterative elastic analyses

- If $r = 1$ obtain the equivalent stresses $\bar{\boldsymbol{\sigma}}^{r=1}$ from a linear elastic analysis; otherwise use the estimated $\bar{\boldsymbol{\sigma}}^{r}$.
- Using the finite element solution and $\bar{\boldsymbol{\sigma}}^{r}$, obtain/update the variables $\{\sigma_n^r$ (Eq. (5.39)), $\mathbf{S}_{active}$, $\mathbf{S}_{non-active}$, $\nabla\bar{\boldsymbol{\sigma}}$ (Eq. (5.6)), $\mathbf{H}_i$ (Eq. (5.4)) for all $i = 1$ to n finite elements, $\Delta\bar{\boldsymbol{\sigma}}$ (Eq. (5.41)), $(\nabla\bar{\boldsymbol{\sigma}})_{\mathrm{D}}$ (Eq. (5.52)), $(\nabla\bar{\boldsymbol{\sigma}})_{\mathrm{H}}$ (Eq. (5.53))$\}$ in order.

- Compute $\Delta\mathbf{E}$ based on Eq. (5.40).

- Compute $(\Delta\bar{\boldsymbol{\sigma}})^{\text{dir.}}$ (Eq. (5.54)) and $(\nabla\bar{\boldsymbol{\sigma}})_{\text{M}}$ (Eq. (5.55)) and update $\Delta\mathbf{E}$ based on Eqs. (5.54) to (5.56); repeat the step until no difference between two consecutive sets of $\Delta\mathbf{E}$ is seen.

- Compute the variables ($\beta_{\min}$, $\bar{\boldsymbol{\sigma}}^{r+1}$, $\bar{\sigma}_m^{r+1}$, γ_{min}) in order and based on Eqs. (5.42) to (5.46).

- Update the variables ($\bar{\boldsymbol{\sigma}}^{r+1}$ and $\mathbf{E}^{r+1}$) using Eqs. (5.47) and (5.48).

- Compute α^r, and update Δ using Eqs. (5.49) and (5.50).

Step 2: Termination

- If $\Delta < \varepsilon_2$, terminate. Take $\alpha^{\text{col}} = \alpha^r$.

- Else, update $r = r + 1$ and go to step 1.

It is useful to make some remarks regarding the MATLAB implementation of our proposed sensitivity-based ECM as follows.

- The constructions of the sensitivity and Hessian matrices are the most time-consuming parts of the proposed scheme and require high amount of computational resources. This is due to two reasons. First, the derivatives of stresses depend on the nodal displacement derivatives. In computation of nodal displacements derivatives, Eq. (5.13) should be solved for all of the finite elements (or at least for the elements in the active set) at each iteration. In other words, at each iteration, a large number of additional systems of linear equations, whose quantity is proportional to the number of elements (or at least to the number of elements in active set), needs to be solved. This imposes a lot of computational cost at each iteration, especially for systems with large number of elements. Secondly, the computation of the sensitivity matrix from the nodal displacement derivatives is also time consuming, as calculating of equivalent stress derivatives from Eqs. (5.16) to (5.19) is computationally taxing. The computations of the Hessian matrix is even significantly more time consuming, as for each of the elements, an $n \times n$ matrix (or at least $l \times l$ matrix, where l shows the number of elements in the active set) should be obtained at each iteration. Therefore, for the full calculation of the Hessian matrices n^3 terms (or at least nl^2 terms) need to be computed which is l times more than the computations of the sensitivity matrix.

In this thesis a significant reduction in computational time is enforced in calculation of these two matrices. For the sensitivity matrix, considering the fact that only the elastic moduli of the elements in the active set are changing, the derivatives are only obtained with respect to the elastic moduli of these activated elements. The set of additional systems of linear equations imposed by Eq. (5.13) are efficiently solved by the use of the backslash "\" command and in a matrix form. That is

$$\nabla \mathbf{u}_{\mathrm{G}} = \mathbf{K}_{\mathrm{G}} \backslash \bar{\mathbf{F}}_{\mathrm{G}} \tag{5.57}$$

, where $\nabla \mathbf{u}_{\mathrm{G}}$ is the matrix of derivatives of nodal displacements with respect to the elastic moduli of elements in the active set and in a system with d degrees of freedom is as follows

$$\nabla \mathbf{u}_{\mathrm{G}} = \frac{\partial \mathbf{u}_{\mathrm{G}}}{\partial \mathbf{E}} = \begin{bmatrix} \frac{\partial u_1}{\partial E_{\mathbf{S}_{active}(1)}} & \frac{\partial u_1}{\partial E_{\mathbf{S}_{active}(2)}} & \cdots & \frac{\partial u_1}{\partial E_{\mathbf{S}_{active}(l)}} \\ \frac{\partial u_2}{\partial E_{\mathbf{S}_{active}(1)}} & \frac{\partial u_2}{\partial E_{\mathbf{S}_{active}(2)}} & \cdots & \frac{\partial u_2}{\partial E_{\mathbf{S}_{active}(l)}} \\ \vdots & \vdots & \ddots & \vdots \\ \frac{\partial u_d}{\partial E_{\mathbf{S}_{active}(1)}} & \frac{\partial u_d}{\partial E_{\mathbf{S}_{active}(2)}} & \cdots & \frac{\partial u_d}{\partial E_{\mathbf{S}_{active}(l)}} \end{bmatrix}. \tag{5.58}$$

$\bar{\mathbf{F}}_{\mathrm{G}}$ in Eq. (5.57) is the matrix of pseudo forces defined as

$$\bar{\mathbf{F}}_{\mathrm{G}} = \begin{bmatrix} \frac{\partial \mathbf{K}_{\mathrm{G}}}{\partial E_{\mathbf{S}_{active}(1)}} \mathbf{u}_{\mathrm{G}} & \frac{\partial \mathbf{K}_{\mathrm{G}}}{\partial E_{\mathbf{S}_{active}(2)}} \mathbf{u}_{\mathrm{G}} & \cdots & \frac{\partial \mathbf{K}_{\mathrm{G}}}{\partial E_{\mathbf{S}_{active}(l)}} \mathbf{u}_{\mathrm{G}} \end{bmatrix} \tag{5.59}$$

, where each term of $\frac{\partial \mathbf{K}_{\mathrm{G}}}{\partial E_{\mathbf{S}_{active}(k)}}\mathbf{u}_{\mathrm{G}}$ is a vector of pseudo forces. The computation of these pseudo forces are also quick, as for each vector k only the values of the element $\mathbf{S}_{active}(k)$ need to be obtained; the rest of the entries are zero. That is

$$\frac{\partial \mathbf{K}_{\mathrm{G}}}{\partial E_{\mathbf{S}_{active}(k)}}\mathbf{u}_{\mathrm{G}} = \sum_{i=1}^{n} \bar{\mathbf{f}}^{i}_{\mathbf{S}_{active}(k)} \tag{5.60}$$

, where

$$\bar{\mathbf{f}}^{i}_{\mathbf{S}_{active}(k)} = \begin{cases} \frac{\partial \mathbf{K}_{i}}{\partial E_{\mathbf{S}_{active}(k)}}\mathbf{u}_{i} & \text{if } i = k \\ \mathbf{O} & \text{if } i \neq k \end{cases} \tag{5.61}$$

Computations of the nodal displacement derivatives with respect to all the elastic moduli in the active set in the form of 5.57 is much faster than obtaining individual vectors of $\frac{\partial \mathbf{u}_{\mathrm{G}}}{\partial E_{\mathbf{S}_{active}(k)}}$ for all $k = 1$ to l in a loop, and saves computing time.

For further reduction in computing time, the nodal displacement derivatives $\nabla \mathbf{u}_{\mathrm{G}}$ obtained at each time is stored and overwritten at each iteration and used later for computations of the sensitivity matrix. Although this action reduces the computing time of the sensitivity matrix significantly, it increases the computational resources demand at each iteration.

To reduce the computational cost of the Hessian matrix, in addition to the similar actions applied on calculation of the sensitivity matrix, a simple assumption is made and only the diagonal terms of the Hessian matrices are obtained at each iteration. This assumption is acceptable with high level of precision, as the effect of the off-diagonal terms in each Hessian matrix in computing the second order term of Taylor series expansion is quite small and therefore negligible. This reduces the number of computation terms from nl^2 to nl, which is the same as for the sensitivity matrix.

- Similar to the MECM described in chapter 3, the element stiffness matrices are computed only once in the first iteration, and stored. In the subsequent iterations, their factored matrices will be used for assembling the total stiffness matrix. Similarly, the element stiffness matrix derivatives can be obtained for all elements only once at the first iteration and stored. However, in case of the need for computational resources, they can be simply obtained at each iteration based on Eq. (5.12) by simply dividing the previously stored element stiffness matrices by the elastic modulus of the elements.

5.4 Numerical Examples

To illustrate the performance of the proposed non-local sensitivity-based ECM, three 2D benchmarks and three 3D examples used in chapter 3 are considered. The accuracy of the results is validated by comparing them with the reported solutions. In all examples, $\lambda = 0.01$, and the incompressibility is considered by the use of $\nu = 0.499$. The low-order four-node elements in case of 2D problems and the eight-node brick elements in case of 3D problems are employed. To reduce the burden of computations, the selective one-point integration scheme is implemented. The tolerance for stopping the iteration is considered as $\varepsilon_2 = 1 \times 10^{-6}$. The analysis procedures are implemented within a MATLAB programming environment.

5.4.1 2D Examples

5.4.1.1 Prandtl's punch problem

The first example is the well-known Prandtl's punch problem dealing with the semi-infinite body under a punch load as in Fig. 3.1a, which was discussed in sections 2.2.7, 3.3, 3.4, and 3.5.1.1. The perfectly plastic Tresca material and plain strain condition were adopted. The initial elastic modulus was $E = 10000$ whose unit is the same as the stress unit. The ratio of the analytical collapse load multiplier to the yield stress (i.e. $\frac{\alpha^{\text{col}}}{\sigma_0}$) is given as 2.5708.

Due to the symmetry, only half of the structure was modeled using low order

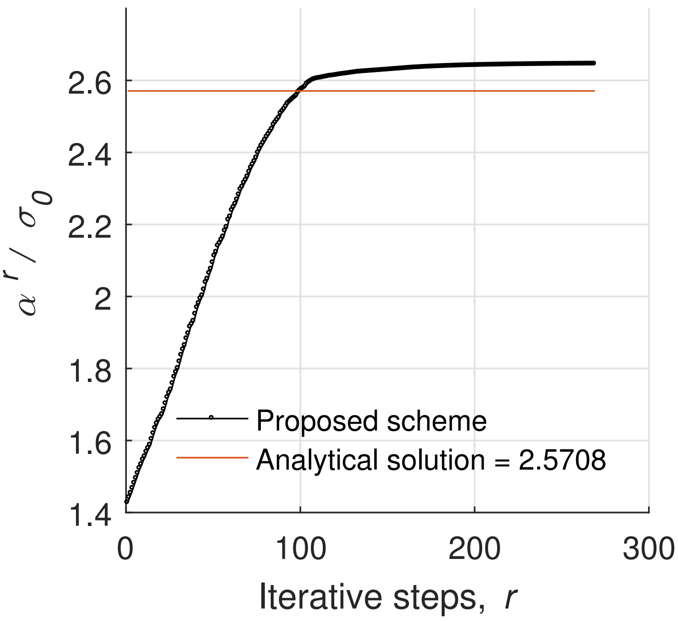

Figure 5.7: Iterative scheme for the Prandtl's punch problem with 2048 finite elements using the proposed sensitivity-based ECM

four-node finite elements. The model is exactly the same model used in chapter 3, and its schematic figure is illustrated in Fig. 3.6b, where each element was further subdivided into 16 similar elements (Fig. 3.6c). In total, 2048 elements, 2145 nodes, 4290 DOFs and 2048 integration points were used. The mesh convergence study will be later performed.

The proposed sensitivity-based ECM was implemented on the problem, and the normalized load multipliers $\frac{\alpha^r}{\sigma_0}$ were monotonically increased and converged to the normalized collapse load solution of $\frac{\alpha^{\text{col}}}{\sigma_0} = 2.6449$, which is 2.88% higher than the analytical solution. The iterative scheme is also plotted in Fig. 5.7. As seen, the curve is monotonically increasing and there is no drops in the curve anymore (in comparison to Fig. 3.7 in chapter 3), which led the convergence to be defined on the load multipliers directly.

The plots of stress and elastic modulus distributions corresponding to the collapse load solution are displayed in Fig. 5.8, where the smallest values of the elastic moduli belong to the elements contributing to the collapse mechanism. The scaled displacement field is also displayed in Fig. 5.9.

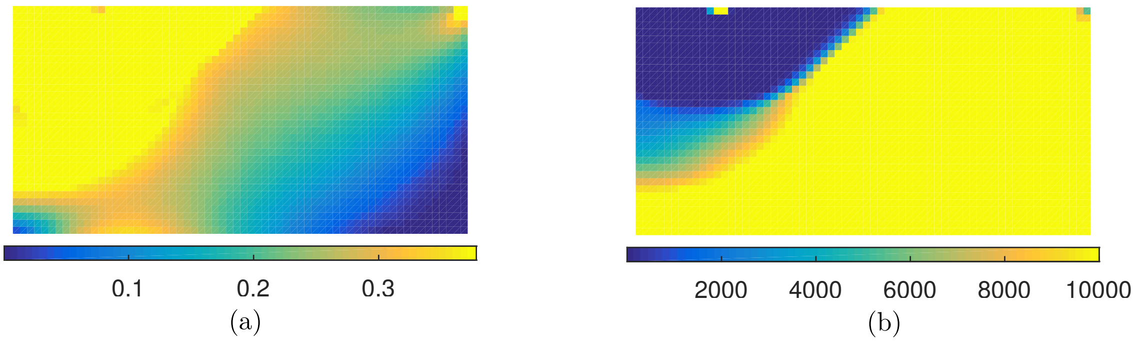

Figure 5.8: Stress and elastic modulus distributions for the Prandtl's punch problem with 2048 finite elements using the proposed sensitivity-based ECM (a) stress distribution (b) elastic modulus distribution

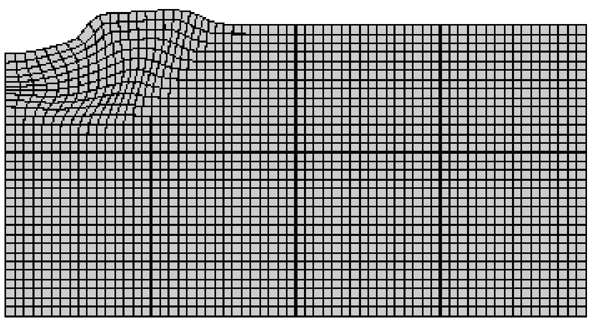

Figure 5.9: The schematic displacement field for the Prandtl's punch problem with 2048 finite elements using the proposed sensitivity-based ECM

The effect of the parameter λ on the collapse load solutions was also investigated for this problem. Fig. 5.10 shows the iterative scheme for different values of λ. As illustrated, the increasingly monotonic trend is achieved regardless of the value of λ. However, the larger values of λ lead to the collapse load solutions which are smaller than the true collapse load. As the λ values are decreased, the collapse load solutions are increased and the maximum collapse load solution is obtained for the smallest value of $\lambda = 0.001$. However, this maximum collapse load is obtained at the expense of the high computational cost due to the high number of iterations (viz. roughly 950 iterations). The collapse load solution for the proposed $\lambda = 0.01$ is only 0.42% less than this maximum collapse load solution (i.e. $\left(\frac{\alpha^{\text{col}}}{\sigma_0}\right)_{\lambda=0.01} \cong 0.994 \left(\frac{\alpha^{\text{col}}}{\sigma_0}\right)_{\lambda=0.001}$, but requires almost one-thirds of the number of iterations required for $\lambda = 0.001$ (viz. 340 iterations). The collapse load solution for $\lambda = 0.05$ is also close enough to $\left(\frac{\alpha^{\text{col}}}{\sigma_0}\right)_{\lambda=0.001}$, however it almost demands the same number of iterations required for $\lambda = 0.01$ (i.e. 320 iterations), and therefore $\lambda = 0.01$ is superior. The precision of the accuracy reduces for larger values of λ.

The variation of the collapse load multiplier with respect to different FE discretizations was also investigated. The results are tabulated in Table 5.1, where the last column shows the error between the obtained collapse load solution and the analytical one. As seen, by increasing the number of elements, the element mesh size is reduced, and the collapse load solution is decreased. This is due to the fact that the yield conformity is better satisfied as the number of elements (and therefore the integration points) are increased. Fig. 5.11 also displays this variation. Considering the robust behavior of the sensitivity-based ECM, a two-term power series is fit on the obtained collapse load solutions, and its equation is shown on the Fig. 5.11a. Based on the fit curve, the collapse load solution is converged to the final collapse load solution of $\left(\frac{\alpha^{\text{col}}}{\sigma_0}\right)_{conv.} = 2.57$, which is 0.03% lower than the analytical solution and therefore safe. Fig. 5.11b also plots the error, e_α, between this converged solution and the collapse load solutions obtained for different FE discretizations, where

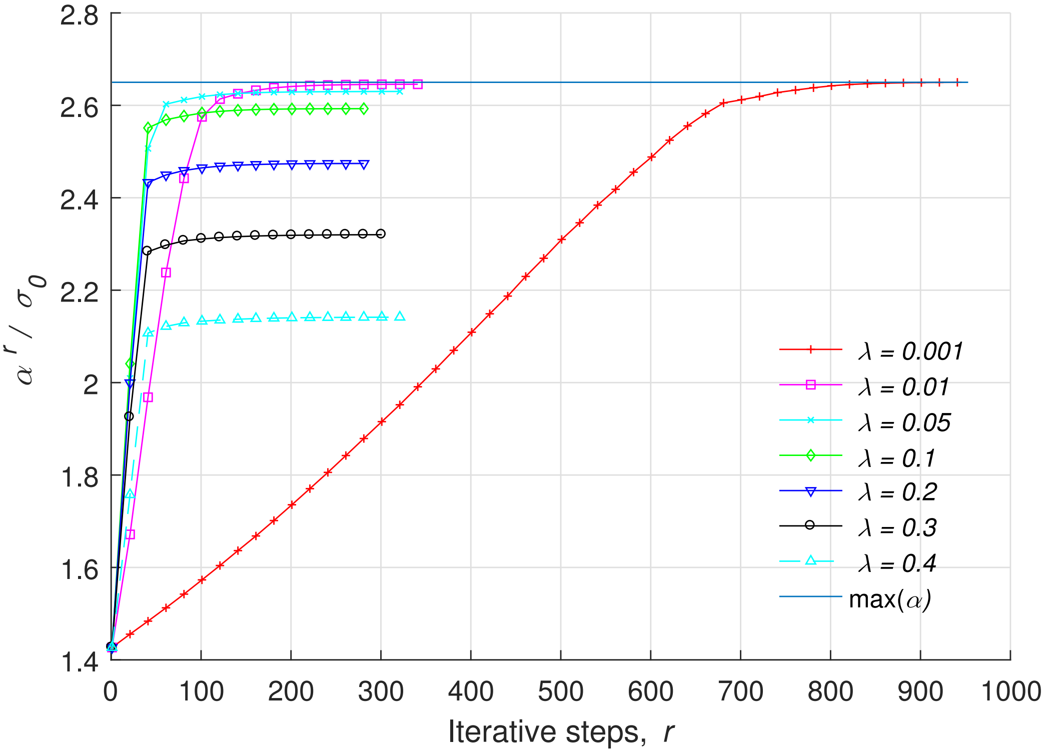

Figure 5.10: The influence of λ on the iterative scheme of the proposed sensitivity-based ECM

e_α is defined as

$$e_\alpha = \frac{\left| \left(\frac{\alpha^{\text{col}}}{\sigma_0}\right)_{conv.} - \frac{\alpha^{\text{col}}}{\sigma_0} \right|}{\left(\frac{\alpha^{\text{col}}}{\sigma_0}\right)_{conv.}} \tag{5.62}$$

Fig. 5.11 also shows that although the proposed sensitivity-based ECM is a lower bound method, it is not a strict lower bound scheme (similar to the MECM). However, the converged collapse load solution shows that the strict lower bound solution is obtainable only if sufficient number of elements is used.

Table 5.1: The collapse load solutions of the Prandtl's punch problem for different FE discretizations using the proposed sensitivity-based ECM

No. of elements (NE)	element mesh size (h)	$\frac{\alpha^{\text{col}}}{\sigma_0}$	error%
32	1.00000	3.1912	24.13
128	0.25000	2.8627	11.35
512	0.06250	2.7234	5.94
2048	0.01563	2.6449	2.88
8192	0.00391	2.6069	1.40
32768	0.00098	2.5804	0.37

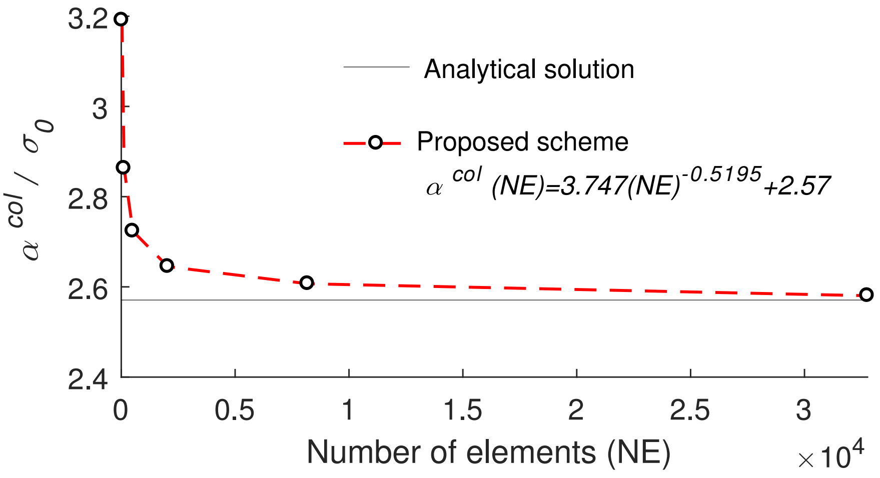

(a)

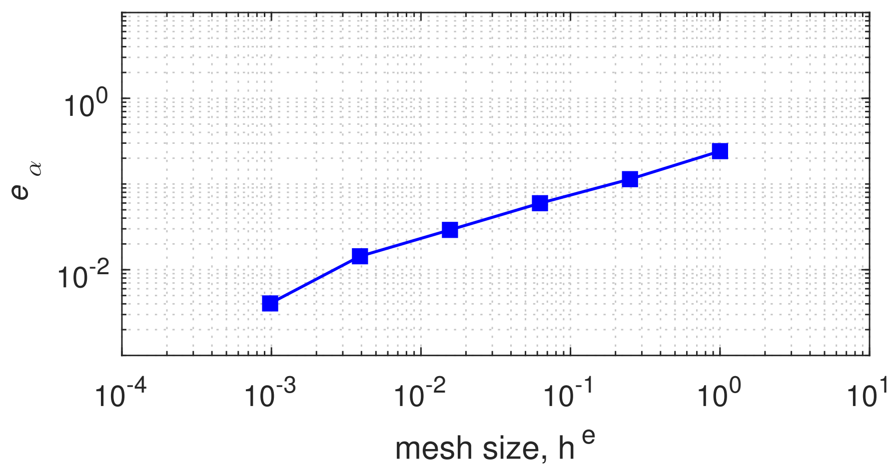

(b)

Figure 5.11: Variation of collapse load solutions of the Prandtl's punch problem for different FE discretizations using the proposed sensitivity-based ECM (a) variation with the number of elements (b) error with respect to the extrapolated converged solution

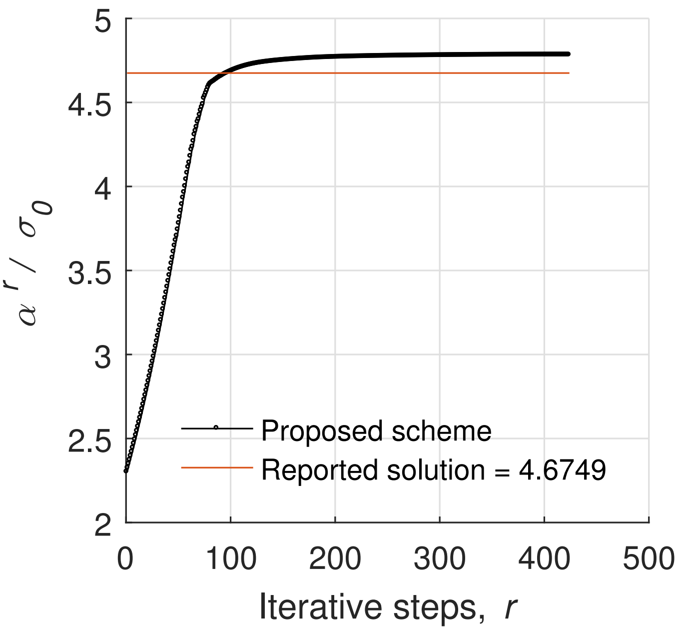

Figure 5.12: Iterative scheme for the notched specimen with 1024 finite elements using the proposed sensitivity-based ECM

5.4.1.2 Double-edge notched specimen

The second 2D example is the double edge notch tensile specimen under the plain strain and perfectly-plastic von Mises conditions, which was described in chapter 3 in section 3.5.1.2. The geometry and loading conditions are shown in Fig. 3.13a. The ratio of the collapse load multiplier to the yield stress (i.e. $\frac{\alpha^{\text{col}}}{\sigma_0}$) is reported as 4.6749 [89]. The schematic and actual structural finite element models are also shown in Figs. 3.13b and 3.13c, respectively. Due to the symmetric nature of the problem, only a quarter of the problem was modeled. In total, 1024 elements, 1089 nodes, 2178 DOFs and 1024 integration points were considered.

The proposed sensitivity-based ECM was performed on the model, and the iterative scheme as shown in Fig. 5.12 is free from oscillation. The normalized load multipliers are monotonically increased and converged to the normalized collapse load solution with the value of $\frac{\alpha^{\text{col}}}{\sigma_0} = 4.7812$, which is some 2.27% higher than the reported solution.

The equivalent stress and elastic moduli distributions associated with the collapse load are also plotted in Fig. 5.13, which agree well with the reported mechanism

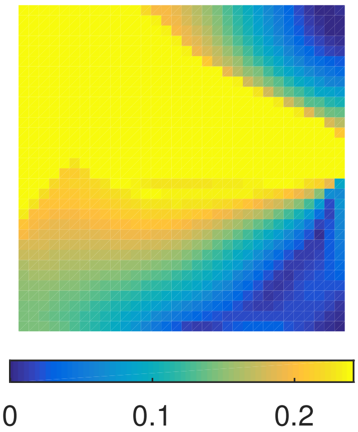

(a)

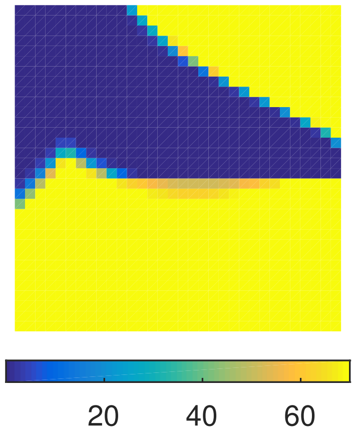

(b)

Figure 5.13: Stress and elastic modulus distributions for the notched specimen with 1024 finite elements using the proposed sensitivity-based ECM (a) stress distribution (b) elastic modulus distribution

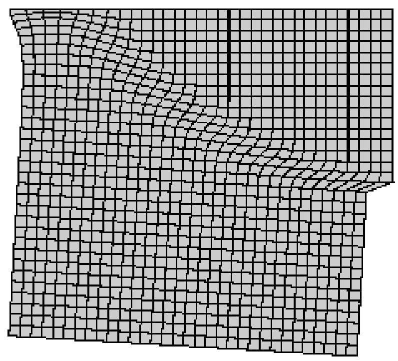

Figure 5.14: The schematic displacement field for the notched specimen with 1024 finite elements using the proposed sensitivity-based ECM

[87]. The related displacement field is also plotted in Fig. 5.14.

The influence of the FE discretizations on the collapse load solution was also investigated on the problem. The results are shown in Table 5.2. As seen, the collapse load solutions are decreased and converged to a value below the reported collapse load solution, due to the better satisfaction of the yield conformity in fine meshes. Fig. 5.15 also displays these variations. Fig. 5.15a shows the two-term power series fitted to the obtained scattered collapse load solutions, and Fig. 5.15b presents the error of the solutions with respect to the converged collapse load solution, $\left(\frac{\alpha^{\text{col}}}{\sigma_0}\right)_{conv.} = 4.602$, which is some 1.56% lower than the reported solution.

Table 5.2: The collapse load solutions of double-edge notched specimen for different FE discretizations using the proposed sensitivity-based ECM

No. of subdomains (NE)	element mesh size (h)	$\frac{\alpha^{\text{col}}}{\sigma_0}$	difference%
4	0.5	7.2569	55.23
16	0.25	5.8766	25.70
64	0.125	5.2982	13.33
256	0.0625	4.9687	6.28
1024	0.03125	4.7812	2.27
4096	0.015625	4.6714	-0.07
16384	0.0078125	4.6231	-1.11

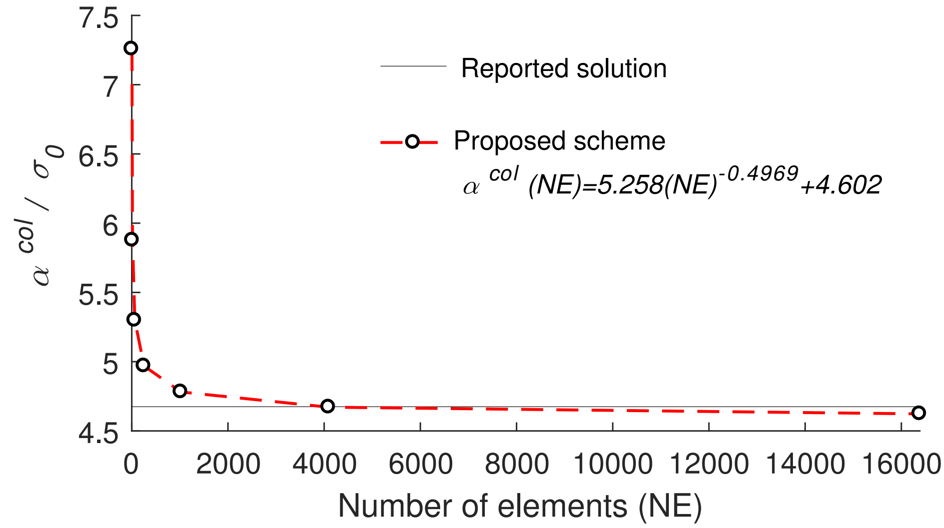

(a)

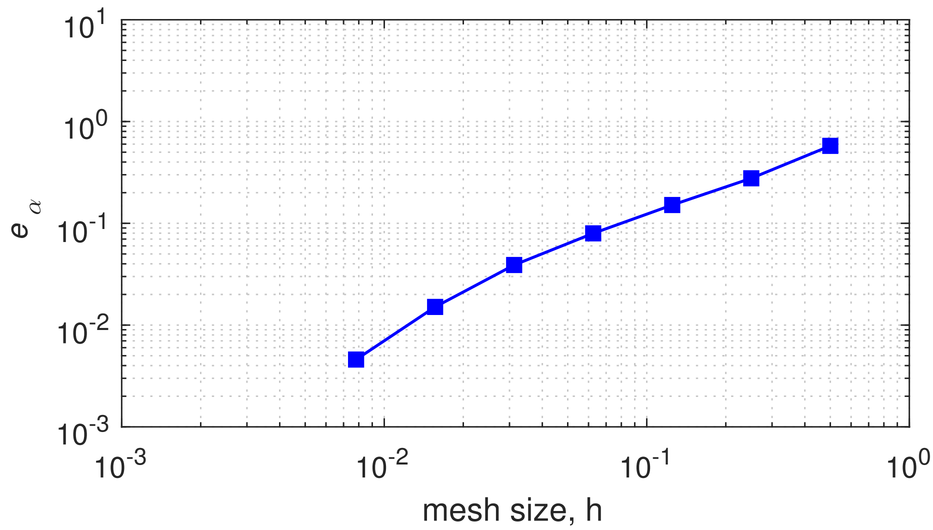

(b)

Figure 5.15: Variation of collapse load solutions of the notched specimen for different FE discretizations using the proposed sensitivity-based ECM (a) variation with the number of elements (b) error with respect to the extrapolated converged solution

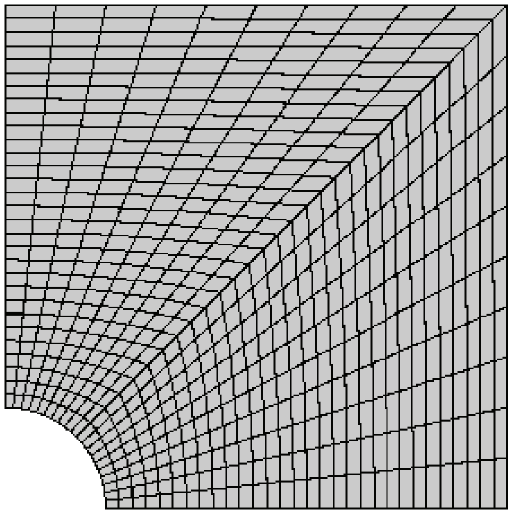

Figure 5.16: The FE model of the perforated plate with 600 elements

5.4.1.3 Perforated plate problem

The third 2D example is the plain stress perforated plate mentioned in section 3.5.1.3 under the perfectly plastic von Mises condition. The geometry and loading are shown in Fig. 3.19a. Here, a finite element model with 600 elements, 651 nodes, 1302 DOFs, and 600 integration points was considered. Fig 5.16 shows this finite element model. A convergence study will be later performed for this example.

The sensitivity-based ECM was performed on the model. The iterative scheme is plotted in Fig. 5.17. As illustrated, the normalized load multipliers are monotonically increased and converged to the collapse load solution of $\frac{\alpha^{\mathrm{col}}}{\sigma_0} = 0.8076$, which is just some 0.95% higher than the analytical solution $\left(\frac{\alpha^{\mathrm{col}}}{\sigma_0}\right)_{\mathrm{ref}} = 0.8$.

The equivalent stresses and elastic moduli distributions for the problem are also displayed in Fig. 5.18. The scaled displacement field representing the schematic collapse mechanism is also shown in Fig. 5.19.

To compare the non-local sensitivity-based ECM and the local MECM in distributing the plasticity in the domain, contour plots of normalized stiffness (E_i/E_0), with E_0 being the original elastic modulus of the material) at a few iterations for both methods are shown in Fig. 5.20. As seen, the MECM has produced more heterogeneous contour plots for all shown iterations in comparison to the propo-

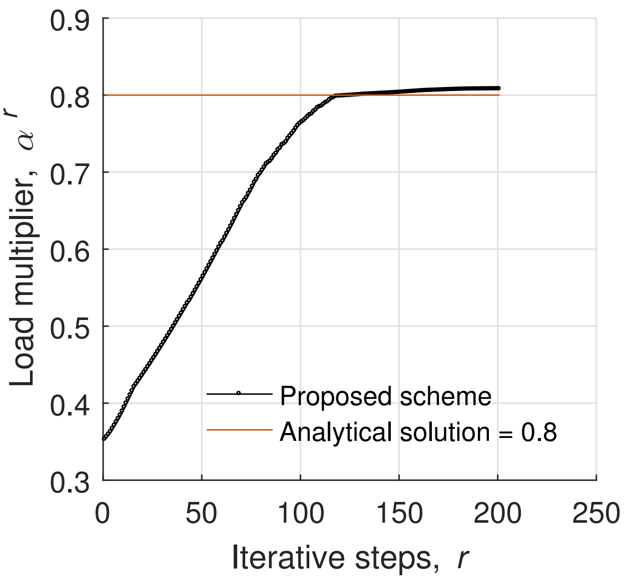

Figure 5.17: Iterative scheme for the perforated plate with 600 finite elements using the proposed sensitivity-based ECM

sed sensitivity-based ECM. Additionally, the collapse shear band in the non-local sensitivity-based ECM is captured better compared to the local MECM.

The effect of the number of elements on the final collapse load solution was also studied. Five uniform discretizations were considered ranging from a coarse mesh (with 120 elements) to a fine mesh (with 33280 elements). The results are illustrated in Table 5.3. As expected, the collapse load solutions are decreased by increasing the number of elements. This is because of the better satisfaction of the yield conformity throughout the whole domain. Fig. 5.21 also shows this pattern. Fig. 5.21a displays the fitted two-term power series on the obtained collapse load solutions, and Fig. 5.21b shows the error between these solutions and the converged collapse load solution, $\left(\frac{\alpha^{\mathrm{col}}}{\sigma_0}\right)_{conv.} = 0.7994$, which is 0.075% lower than the analytical solution, and therefore safe.

Fig. 5.21 also illustrates that although the proposed sensitivity-based ECM is a lower bound scheme (see Fig. 5.17), it is not a strict lower bound method (similar to the MECM). However, the converged collapse load solution shows that the strict lower bound solution is obtainable only if sufficient number of elements is used.

To show the advantageous performance of the proposed sensitivity-based ECM

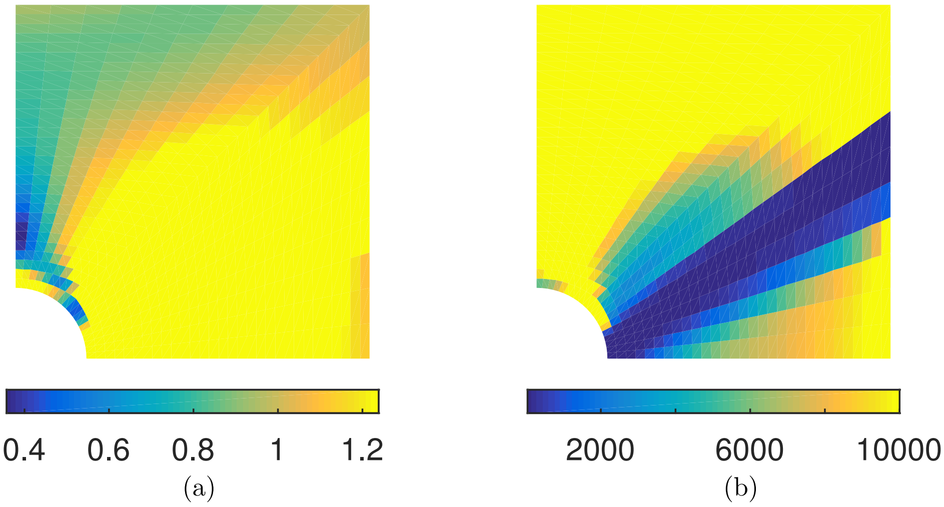

Figure 5.18: Stress and elastic modulus distributions for the perforated plate with 600 finite elements using the proposed sensitivity-based ECM (a) stress distribution (b) elastic modulus distribution

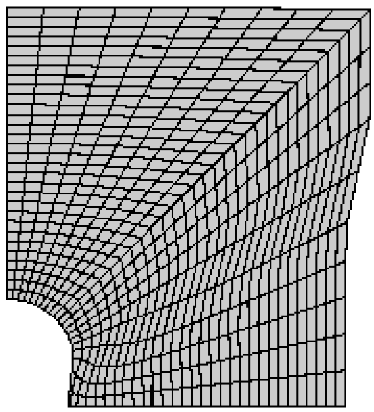

Figure 5.19: The scaled displacement field for the perforated plate with 600 finite elements using the proposed sensitivity-based ECM

Table 5.3: The collapse load solutions of the perforated plate for different FE discretizations using the proposed sensitivity-based ECM

No. of elements (NE)	$\frac{\alpha^{col}}{\sigma_0}$	error%
120	0.8168	2.10
600	0.8076	0.95
2080	0.8041	0.51
8320	0.8019	0.24
33280	0.8007	0.09

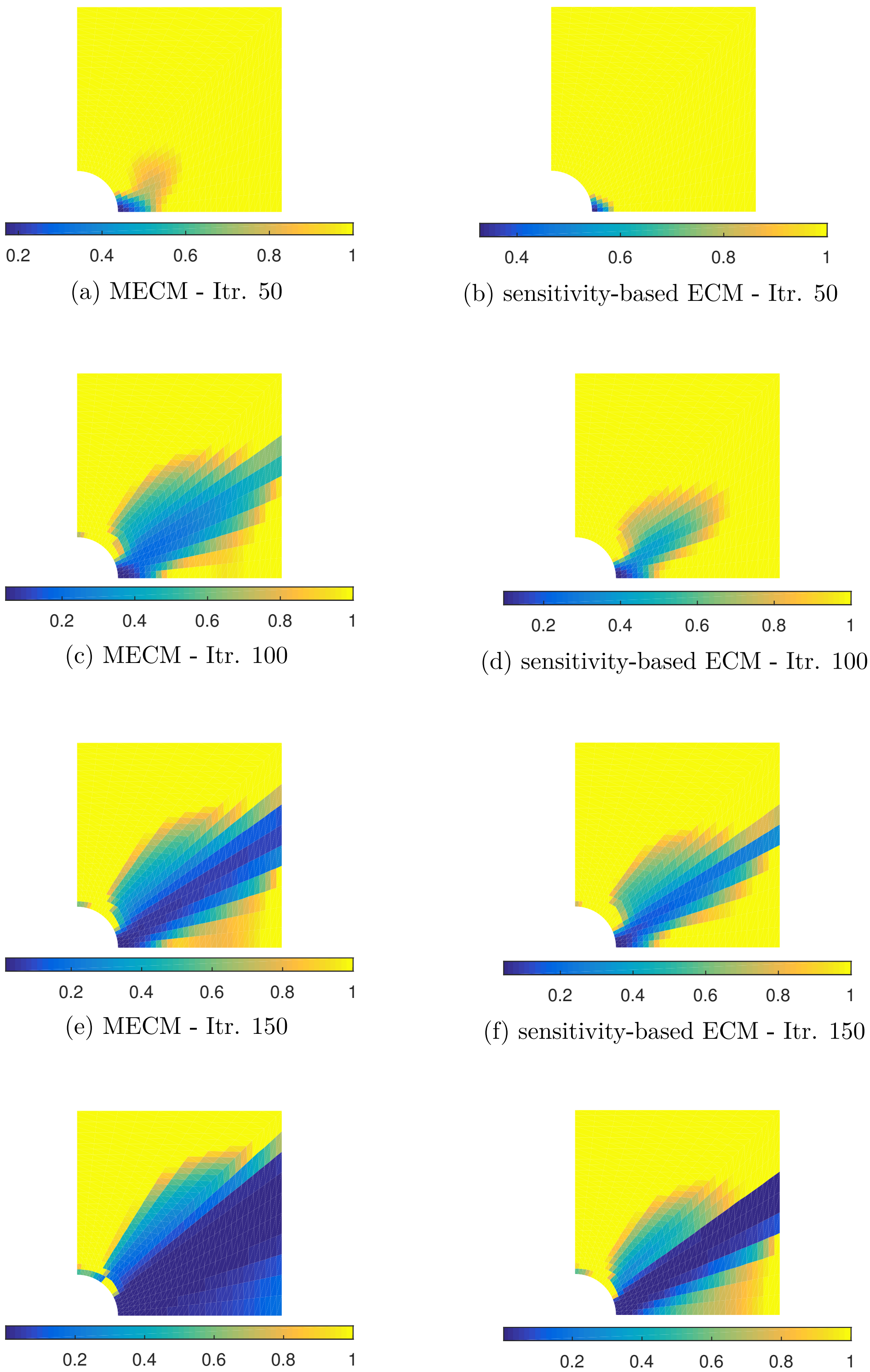

(a) MECM - Itr. 50

(b) sensitivity-based ECM - Itr. 50

(c) MECM - Itr. 100

(d) sensitivity-based ECM - Itr. 100

(e) MECM - Itr. 150

(f) sensitivity-based ECM - Itr. 150

(g) MECM - Itr. 200

(h) sensitivity-based ECM - Itr. 200

Figure 5.20: Normalized elastic moduli distribution for both MECM and sensitivity-based ECM for the perforated plate with 600 finite elements at different iterations

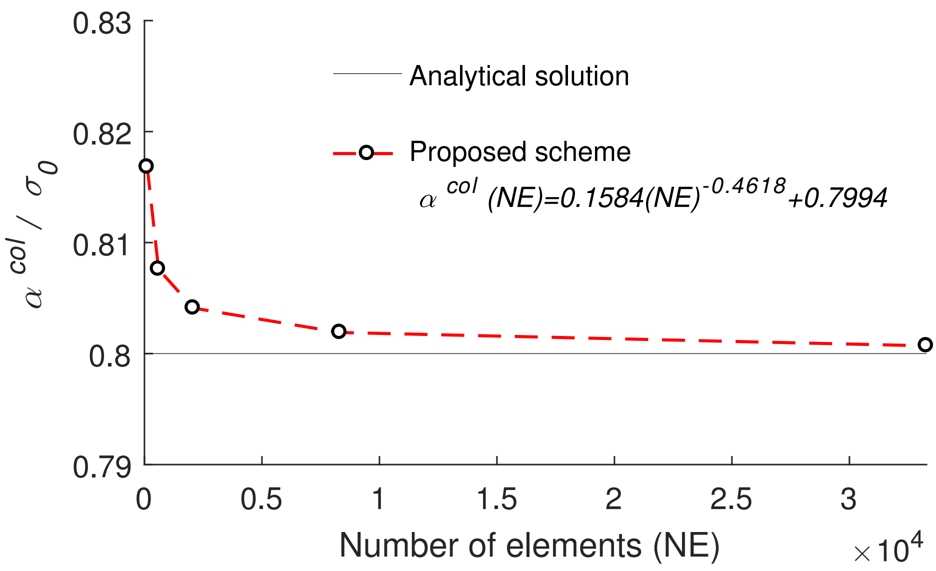

(a)

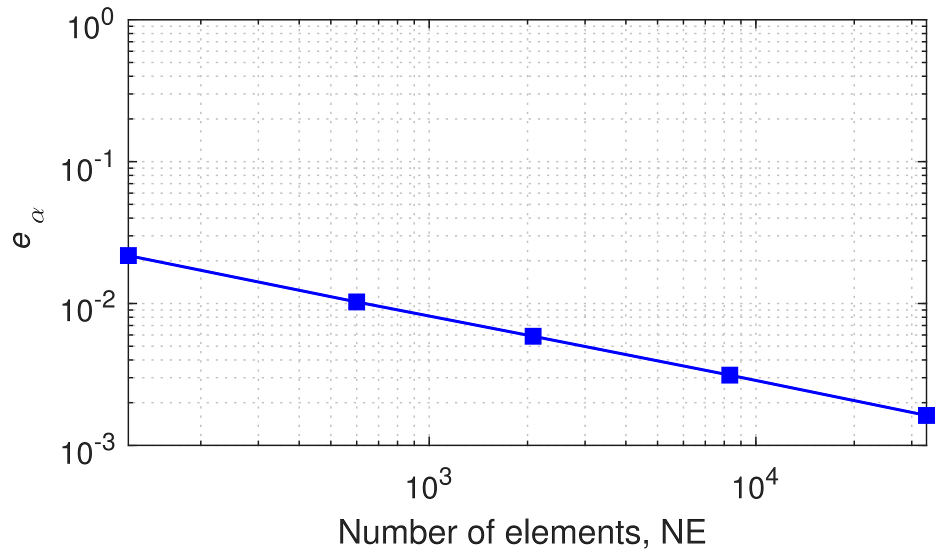

(b)

Figure 5.21: Variation of collapse load solutions of the perforated plate problem for different FE discretizations using the proposed sensitivity-based ECM (a) variation with the number of elements (b) error with respect to the extrapolated converged solution

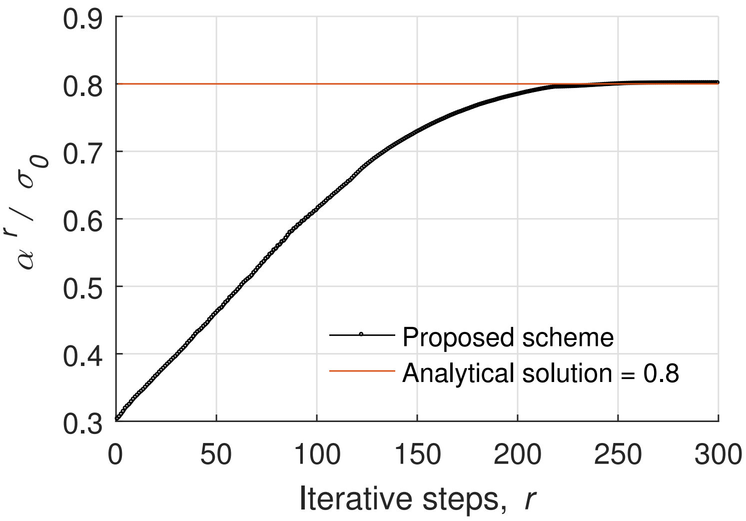

Figure 5.22: Iterative scheme for the perforated plate with 33280 finite elements using the proposed sensitivity-based ECM

in controlling the oscillations, the iterative sensitivity-based ECM for the same finite element model used at the beginning of this chapter in section 5.1 is also shown in Fig. 5.22, where 33280 elements, 33649 nodes, 67298 DOFs, and 33280 integration points were considered. As illustrated, the oscillations in Fig. 5.1 do not appear anymore. The equivalent stresses and elastic moduli distributions for this mesh are also displayed in Fig. 5.23.

5.4.2 3D Examples

5.4.2.1 Thick cylinder

The first 3D example considers the mentioned thick cylinder in section 3.5.2.1 in chapter 3 under the uniform pressure. The geometry and mesh are shown in Fig. 3.25. In total 2016 elements, 2639 nodes, 7917 DOFs and 2016 integration points were considered.

The proposed sensitivity-based ECM was performed on the model, and the iterative scheme is shown in Fig. 5.24. The ratio of the load multiplier to the yield stress is monotonically increased and converged to the value of $\frac{\alpha^{\mathrm{col}}}{\sigma_0} = 0.8023$, which is only some 0.24% higher than the analytical solution of $\frac{\alpha^{\mathrm{col}}}{\sigma_0} = 0.8003$.

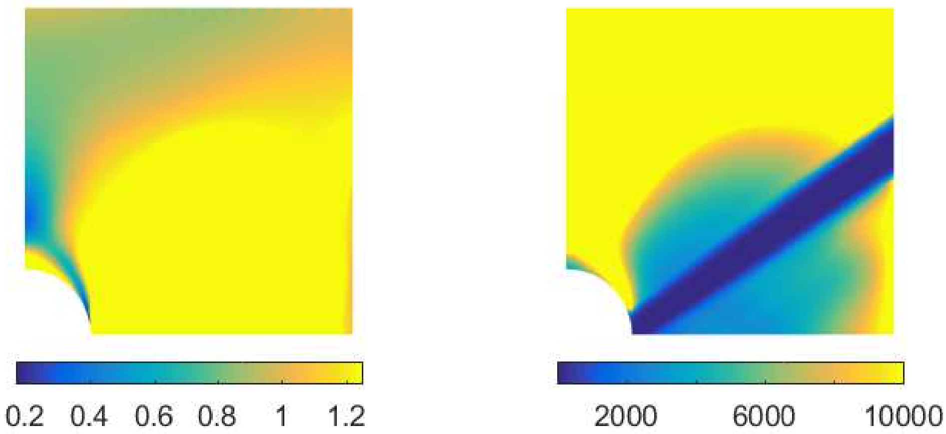

(a) (b)

Figure 5.23: Stress and elastic modulus distributions for the perforated plate with 33280 finite elements using the proposed sensitivity-based ECM (a) stress distribution (b) elastic modulus distribution

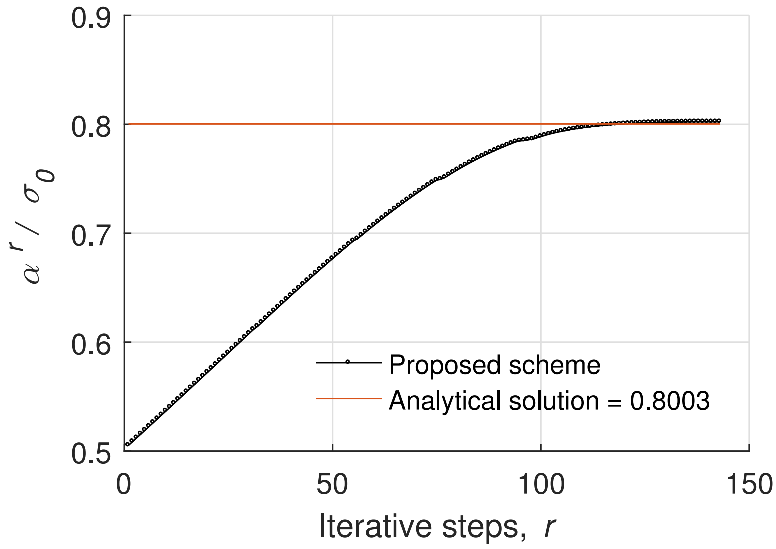

Figure 5.24: Iterative scheme for the thick cylinder with 2016 elements using the proposed sensitivity-based ECM

Table 5.4: The collapse load solutions of the thick cylinder for different FE discretizations using the proposed sensitivity-based ECM

No. of elements (NE)	$\frac{\alpha^{\text{col}}}{\sigma_0}$	error%
252	0.8076	0.91
756	0.8056	0.65
2016	0.8023	0.24
4725	0.8019	0.19

The equivalent stress and elastic moduli distributions are also plotted for the problem in Fig. 5.25, which agree well with the theoretical collapse mechanism, where the collapse happens due to the yielding of all elements.

The effect of the number of elements on the collapse load solution is also tabulated in Table 5.4. The results are also shown in Fig. 5.26, where the collapse load solutions are decreased by increasing the number of elements due to the better satisfaction of the yield condition. The curve fitting is not implemented on the scattered obtained solutions, as only the results of four meshes were obtained due to the high computational time and resources needed for finer uniform meshes.

5.4.2.2 Hollow sphere

The second 3D example considers a homogeneous hollow sphere under the uniform pressure mentioned in section 3.5.2.2 in chapter 3. The geometry and loading and the associated finite element model are all shown in Fig. 3.30. Due to the symmetric nature of the problem only an octant of it was modeled. In total, 2916 elements, 3523 nodes, 10569 DOFs and 2916 integration points were employed.

The proposed sensitivity-based ECM was implemented, and the normalized load multipliers were monotonically increased and converged to the value of $\frac{\alpha^{\text{col}}}{\sigma_0} = 2.2045$, which is some 0.34% higher than the analytical solution $\left(\frac{\alpha^{\text{col}}}{\sigma_0}\right)_{\text{ref}} = 2.197$. The iterative scheme of the method is shown in Fig. 5.27

The variation of the collapse load solution with the number of elements was also investigated. Four meshes ranging from a course mesh to a relatively fine mesh were considered, where the meshes were uniformly discretized. The sensitivity-based

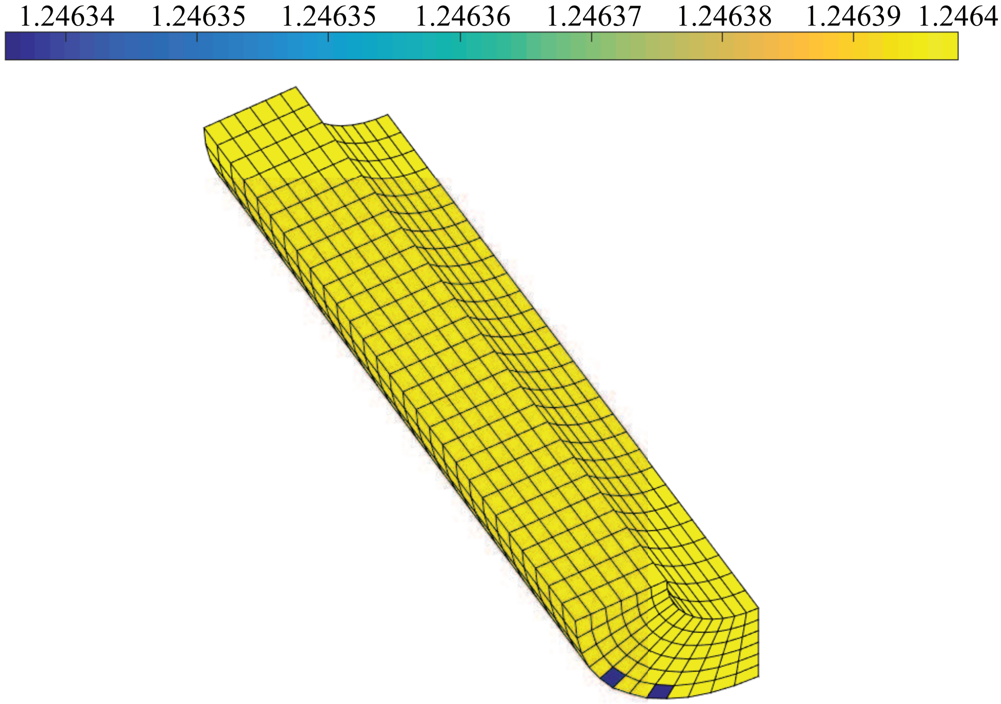

(a)

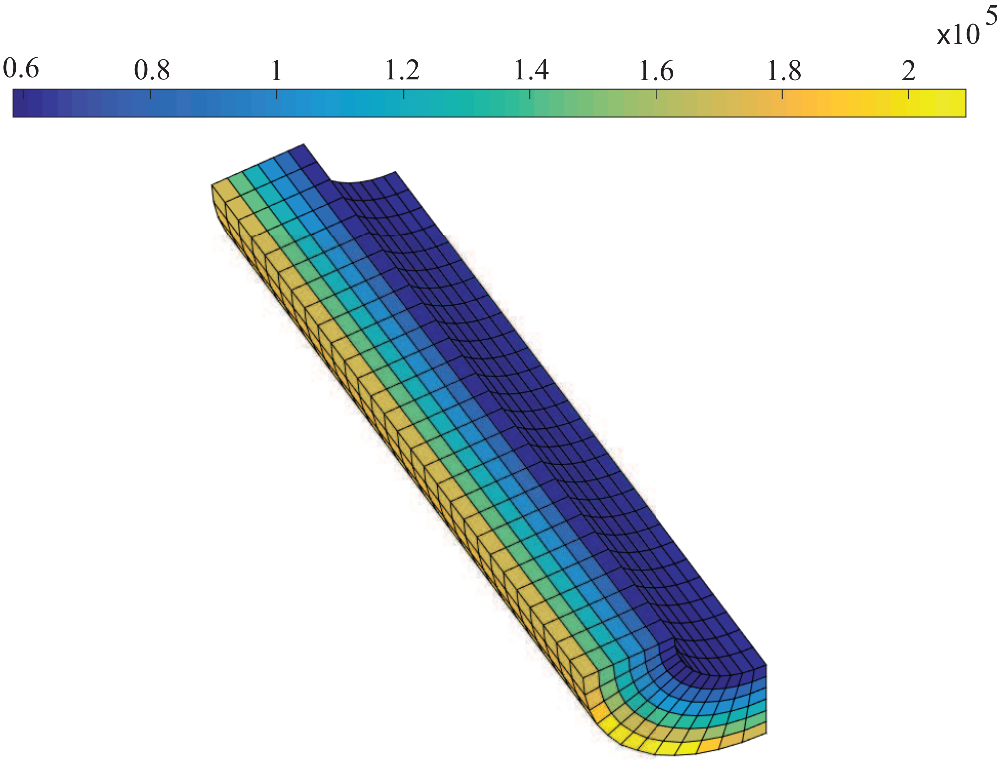

(b)

Figure 5.25: Stress and elastic modulus distributions for the thick cylinder with 2016 finite elements using the proposed sensitivity-based ECM (a) stress distribution (b) elastic modulus distribution

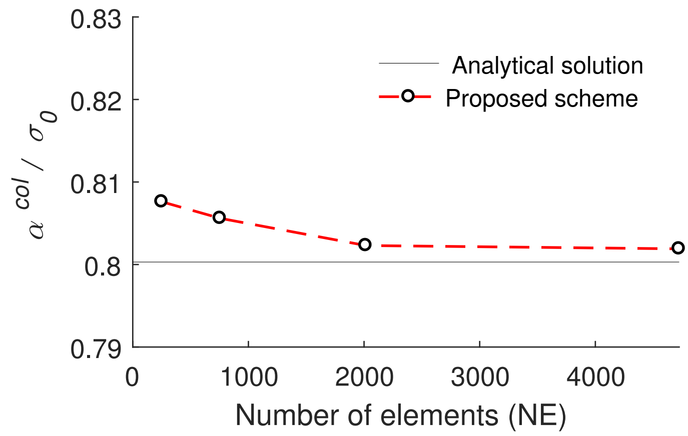

Figure 5.26: Variation of collapse load solutions of the thick cylinder for different FE discretizations using the proposed sensitivity-based ECM

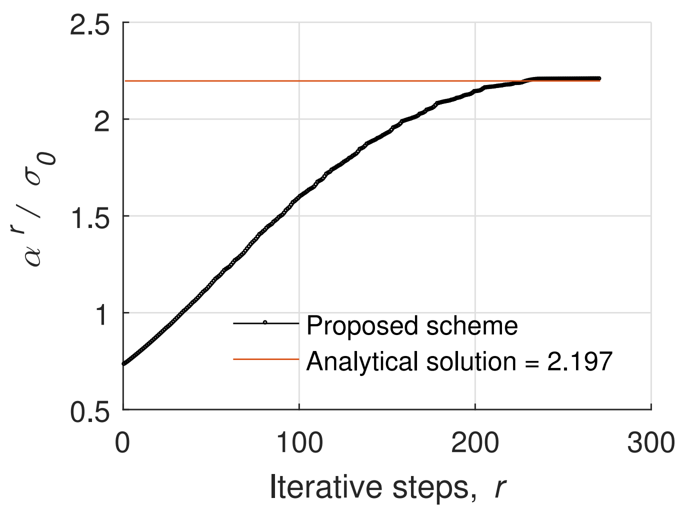

Figure 5.27: Iterative scheme for the hollow sphere with 2916 elements using the proposed sensitivity-based ECM

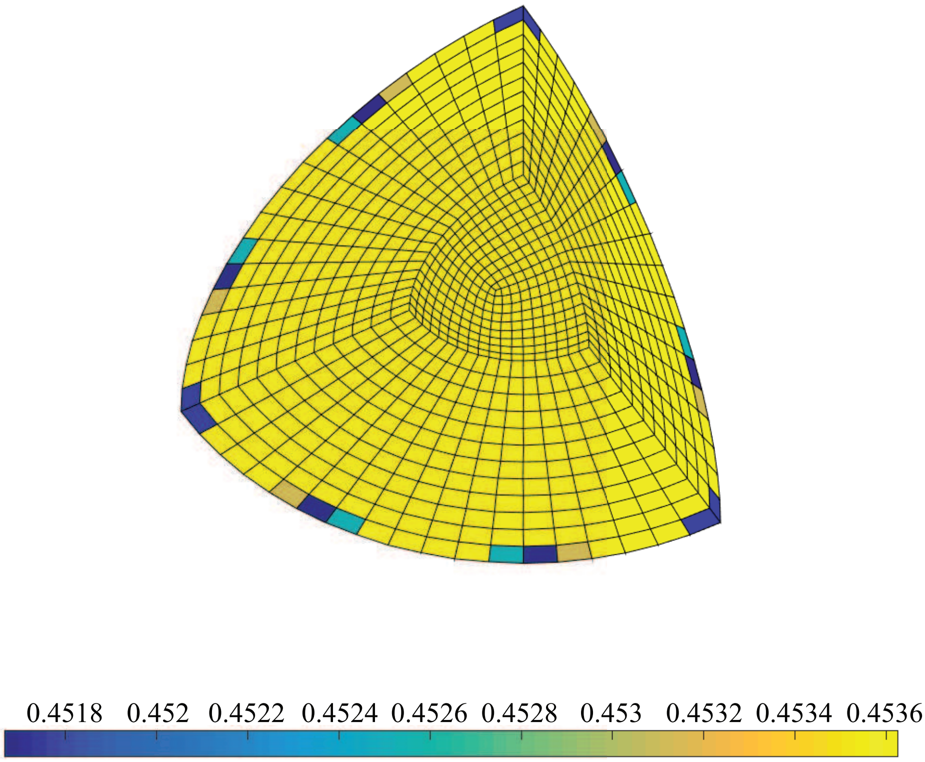

(a)

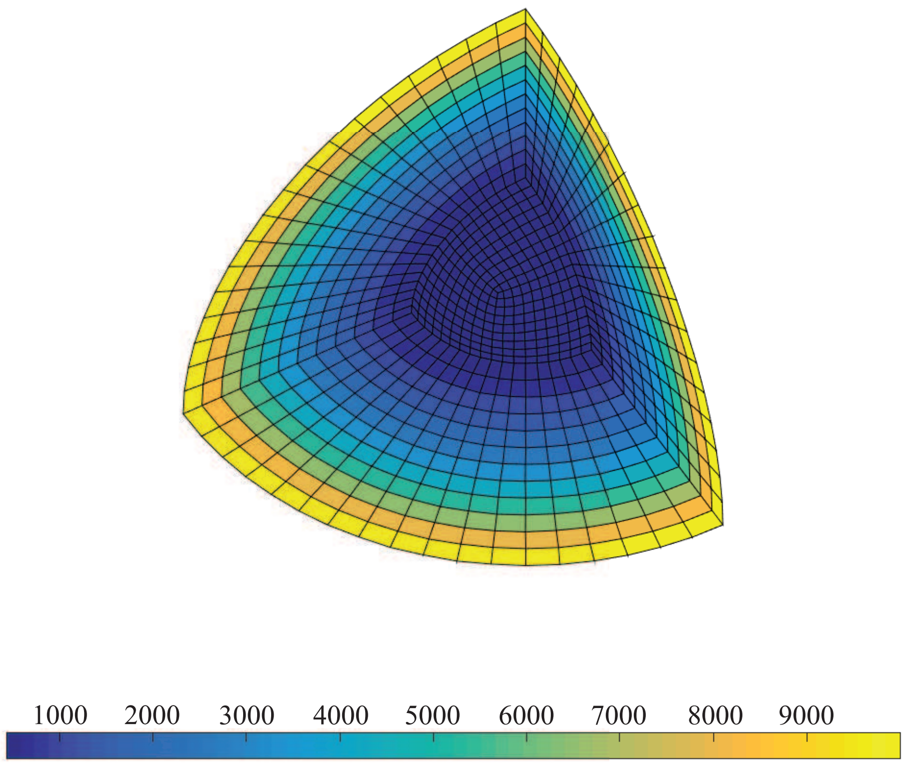

(b)

Figure 5.28: Stress and elastic modulus distributions for the hollow sphere with 2916 finite elements using the proposed sensitivity-based ECM (a) stress distribution (b) elastic modulus distribution

Table 5.5: The collapse load solutions of the hollow cylinder for different FE discretizations using the sensitivity-based ECM

No. of elements (NE)	$\frac{\alpha^{\mathrm{col}}}{\sigma_0}$	error%
252	2.2541	2.60
864	2.2103	0.61
2916	2.2045	0.34
6912	2.2000	0.14

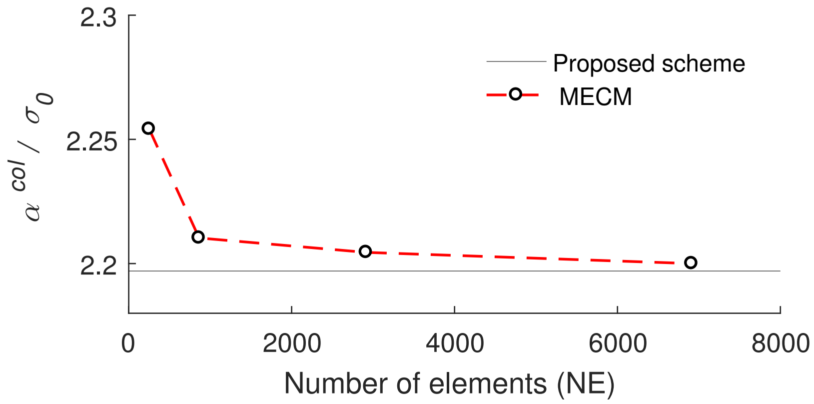

Figure 5.29: Variation of collapse load solutions for the hollow cylinder for different FE discretizations using the sensitivity-based ECM

ECM was performed on each of them and the results are presented in Table 5.5. As seen, the collapse load solution is decreased by increasing the number of elements due to the better satisfaction of yield conformity in the domain. Fig. 5.29 also plots this variation. It should be noted that the curve fitting is not implemented on this 3D example due to the lack of sufficient meshes. The reason for this, is the high amount of the computational time and more importantly resources required for the finer meshes.

5.4.2.3 Defected pipeline

The third 3D example is the defected pipeline used in section 3.5.2.3. The geometry and loading is presented in Fig. 3.35. Two finite element models of the problem are also shown in Fig. 3.36, where the course mesh (case a) consists of 316 elements, 558 nodes, 1674 DOFs and 316 integration points and the finer mesh (case b) considers 2528 elements, 3437 nodes, 10311 DOFs, and 2528 integration points.

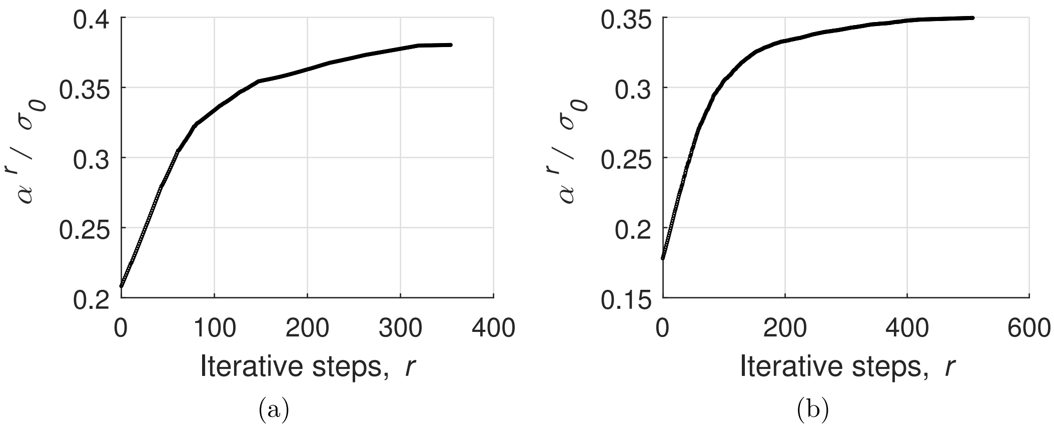

Figure 5.30: The iterative schemes for the defected pipeline using the proposed sensitivity-based ECM (a) case a with 316 FEs (b) case b with 2528 FEs

The proposed sensitivity-based ECM was performed on both of the finite element models, and the iterative scheme is plotted for both of the meshes in Fig. 5.30. The load multipliers for both of the discretizations are monotonically increased and converged to $\alpha^{\text{col}} = 75.9201$ in case a and $\alpha^{\text{col}} = 69.7553$ in case b. The proposed approach provides good accuracy of the collapse load results, as the solutions computed agree well with the reference values reported from various numerical algorithms, namely $\alpha^{\text{col}}_{ref} = 64.05$ using the incremental method [92], $\alpha^{\text{col}}_{ref} = 67.13$ the kinematic method [86], and $\alpha^{\text{col}}_{ref} = 63.42$ the static method [92].

The equivalent stress and elastic modulus distributions for the mesh in case b are displayed in Fig. 5.31, where the elastic modulus adjustment is started from the elements in the defected area and then distributed to the adjacent elements. The schematic collapse mechanism for the structure in case b is also plotted in Fig. 5.32.

5.5 Conclusion and Remarks

In this chapter, the source of the oscillations in the MECM described in chapter 3 was presented. In particular, the stress overshooting phenomenon, which might lead to drops in the limit load curve, was investigated. The presence of drops in the limit load curve prevents the convergence to be defined in the limit load, explaining why the number of iterations is used as the convergence criterion for the ECM or

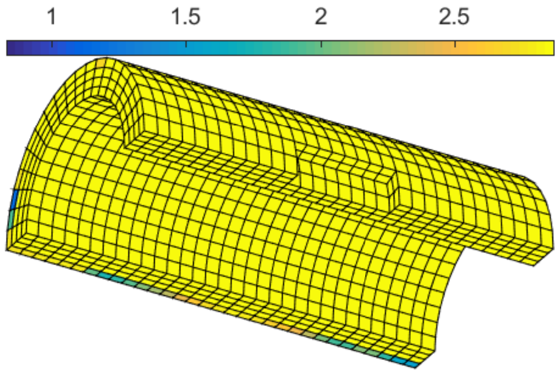

(a)

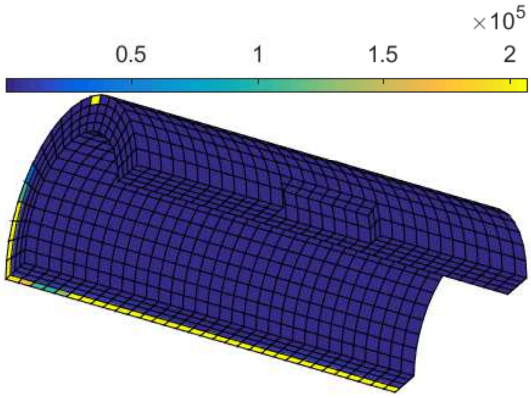

(b)

Figure 5.31: Stress and elastic modulus distributions for the defected pipeline with 2528 finite elements using the proposed sensitivity-based ECM (a) stress distribution (b) elastic modulus distribution

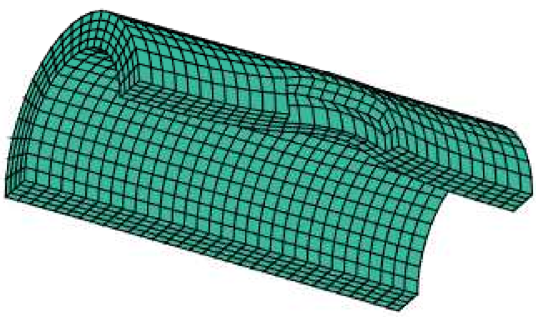

Figure 5.32: The collapse mechanism for the defected pipeline with 2528 finite elements using the proposed sensitivity-based ECM

MECM.

The robust sensitivity-based ECM was then proposed and explained, which produces an oscillation-free scheme for the determination of the collapse load multiplier. The contribution of all elements in each iteration is considered through the definition of the sensitivity matrix, and the equivalent stresses of all elements in the next iteration are linearly estimated at the current iteration. By having the predicted equivalent stresses, the overshooting of them can be prevented by multiplying the vector of elastic moduli changes by a factor less than 1. This guarantees the non-oscillatory behavior of obtained load multipliers. A number of 2D and 3D examples were provided, which verify the robustness and accuracy of the proposed scheme.

The sensitivity-based ECM is robust, and therefore superior to the MECM. It, however, demands more computational time and resources in comparison to the ECM and MECM due to the fact that the equivalent stress derivatives for all the elements are required to be obtained at each iteration. Although a significant reduction in computing time was achieved in the MATLAB implementation of the methodology; however, it is still computationally demanding for large-size structures.

In the next chapter, the sensitivity-based ECM is extended to the SBFEM to use the advantages it offers such as auto-mesh construction for 2D and 3D structures. In particular, the adaptive sensitivity-based ECM is proposed which reduces the need for the computational resources by the use of adaptive meshes produced by the SBFEM.

Chapter 6

A SENSITIVITY-BASED ECM FOR THE COLLAPSE LOAD DETERMINATION OF STRUCTURES USING THE SCALED BOUNDARY FINITE ELEMENT METHOD

6.1 Introduction

The sensitivity-based ECM introduced in last chapter was found to be robust and accurate for the collapse load determination of structures using the FEM. It was observed that the level of the accuracy of the results is dependent on the quality of the employed mesh. In general, a more accurate (and safer) collapse load solution can be obtained by using uniform fine meshes. The use of uniform mesh in the sensitivity-based ECM does incur a computing cost, primarily in the effort required for the calculation of derivatives for all elements. Additionally, construction of a high quality uniform fine mesh, specifically for 3D structures, is a tedious and time-consuming task.

In the present chapter, firstly, the sensitivity-based ECM is extended to employ the SBFEM described in chapter 4. This allows the use of automatic (quadtree/octree) mesh generator schemes. Therefore, a high quality mesh from an in-plane solid (in 2D problems) or of a solid 3D CAD (STL) model (in 3D problems) can be automatically constructed, which effectively reduces the burden of the mesh generation. This leads to a two-part fully automatic scheme which can robustly determine the collapse load of the structures and minimizes the need for the user to interfere. In the first part, the mesh is automatically generated to comply with the geometry and loading of the structures using quadtree/octree frameworks and the SBFEM. In the second part, the collapse load of the structure, for the generated mesh, is automatically and robustly computed using the sensitivity-based ECM. This allows the definition of the convergence criterion directly on the limit load curve, removing the need of the user for finding the right number of iterations required for traditional ECMs.

Secondly, an adaptive sensitivity-based ECM is proposed for 2D problems to reduce the demands for computational resources associated with the uniform refinement. This is achieved by the use of polygonal scaled boundary finite elements along with the quadtree framework, which allows the efficient construction of adaptive meshes. The use of these adaptive meshes leads to a reduction in the size of the problem and leads to a significant gain in computational resources required for the sensitivity-based ECM.

The organization of this chapter is as follows. Section 6.2 explains the SBFE implementation of the sensitivity-based ECM for 2D and 3D structures. The development of the adaptive sensitivity-based ECM is described in section 6.3. The numerical examples are then presented in section 6.4 which validate the accuracy and efficiency of the proposed schemes. Finally, conclusions of the present chapter are stated in section 6.6.

6.2 SBFE Implementation of the Sensitivity-based ECM

The scaled boundary finite element implementation of the sensitivity-based ECM is similar to its finite element implementation discussed in last chapter. The structural system is automatically discretized into n subdomains using the quadtree or octree framework described in chapter 4 of this thesis, where each subdomain is constructed by some line elements (in 2D spaces) or some surface elements (in 3D). At each iteration r, an elastic SBFE analysis is carried out and the nodal displacements $\mathbf{u}_{\mathrm{G}}$ are obtained, and then the stress and strain tensors (i.e. $\boldsymbol{\epsilon}_i$ and $\boldsymbol{\sigma}_i$, respectively) for all of the subdomains $i = \{1, 2, \ldots, n\}$ are computed. To reduce the cost of the computations, the stresses and strains are only obtained at the scaling center of the subdomains. The equivalent stresses at the scaling center of subdomains $\bar{\boldsymbol{\sigma}}^r$ for the von Mises or Tresca yielding conditions are only computed at the first iteration.

By having this information, the sensitivity matrix $\nabla\bar{\boldsymbol{\sigma}}$ and the Hessian matrices $\mathbf{H}_i$ of all subdomains $i = \{1, 2, \ldots, n\}$ can be obtained as per section 5.3.2.1 with two minor justifications as follows:

(1) Eq. (5.10) is not applicable to the SBFE formulation for obtaining the subdomain stiffness matrix. However, the derivative of the stiffness matrix of the subdomain i with respect to the change in elastic modulus of the subdomain j can still be obtained from Eq. (5.12). As discussed in chapter 4, this is due to the fact that the stiffness matrix of a subdomain has linear relationship with its elastic modulus. Accordingly, the discussion provided for the second derivatives of the element stiffness matrix for the calculation of the Hessian matrices of elements in Eqs. (5.25) to (5.28) is also valid for the calculation of Hessian matrices for subdomains in the SBFEM.

(2) The derivatives of strains of the subdomain i with respect to the elastic modulus of the subdomain j in the SBFEM is similar to Eq. (5.14), and are defined

as follows

$$\frac{\partial \boldsymbol{\epsilon}_i}{\partial E_j} = \bar{\mathbf{B}}_i \frac{\partial \mathbf{u}_i}{\partial E_j} \tag{6.1}$$

, where $\bar{\mathbf{B}}_i$ is a matrix representing the strain-displacement relationship for the subdomain i and is defined as per Eqs. (4.41) and (4.42) for 2D and 3D spaces, respectively. Similarly, the second derivatives of strains in a typical subdomain i with respect to changes in elastic moduli of elements j and k can be obtained as

$$\frac{\partial^2 \boldsymbol{\epsilon}_i}{\partial E_j \partial E_k} = \bar{\mathbf{B}}_i \frac{\partial^2 \mathbf{u}_{\mathrm{G}}}{\partial E_j \partial E_k}. \tag{6.2}$$

The stress distributions in the domain is then carried out by changing the elastic moduli of the subdomains in the active set, $\mathbf{S}_{active}$, whose equivalent stresses sit above the nominal stress σ_n^r at iteration r, defined in Eq. (5.39). The complementary set of the active set, is the non-active set, $\mathbf{S}_{non-active}$, including all subdomains whose equivalent stresses sit below the nominal stress. The change of elastic moduli in subdomains, $\Delta\mathbf{E}$, is initially obtained from Eqs. (5.40) and (5.41), and then is recursively updated based on Eqs. (5.51) to (5.56) to consider the probable unloading of some subdomains. The repetitions are continued until no difference between two consecutive $\Delta\mathbf{E}$ is observed.

By having the elastic moduli of the subdomains, the equivalent stresses of all subdomains at their scaling centers in the next iteration can be initially obtained as follows

$$\bar{\boldsymbol{\sigma}}^{r+1} = \bar{\boldsymbol{\sigma}}^{r} + \beta_{\min} \times (\nabla \bar{\boldsymbol{\sigma}})\,(\Delta \mathbf{E}) \tag{6.3}$$

, where $\beta_{\min}$ is the minimum amount of β_i coefficients obtained from Eq. (5.42), ensuring that all computed elastic moduli are sufficiently small for the linear approximation of the equivalent stresses. The factor ε_1 in Eq. (5.42) is taken as 2.5×10^{-2} as in the finite element implementation of the sensitivity-based ECM. To prevent the stress overshooting, the predicted equivalent stresses of the non-active subdomains should be less than the predicted equivalent stress of the subdomain m having the maximum predicted equivalent stress of the subdomains in the active set (i.e. $\bar{\sigma}_m^{r+1} = \max\left(\bar{\boldsymbol{\sigma}}^{r+1}_{\mathbf{S}_{active}}\right)$). The scheme simply imposes this condition by reducing the vector of elastic moduli changes by the factor $\gamma_{\min}$ defined in Eqs. (5.45) and (5.46). The final predicted equivalent stresses and elastic moduli for all of the subdomains, which will be used in the next iterations are defined as

$$\bar{\boldsymbol{\sigma}}^{r+1} = \bar{\boldsymbol{\sigma}}^r + \beta_{\min} \times \gamma_{min} \times (\nabla\bar{\boldsymbol{\sigma}})\,(\Delta\mathbf{E})\,, \tag{6.4}$$

and

$$\mathbf{E}^{r+1} = \mathbf{E}^r + \beta_{\min} \times \gamma_{min} \times \Delta\mathbf{E}. \tag{6.5}$$

Finally, the load multipler α^r and the convergence criterion at iteration r, can be defined based on the Eqs. (5.49) and (5.50) as per the finite element implementation of the sensitivity-based ECM.

The pseudo code summarizing the key steps underlying the sensitivity-based ECM is prescribed below:

Step 0: Initialization

- At iteration $r = 1$, initialize: tolerances ε_1 and ε_2, $\lambda = 0.01$, yield limit σ_0, and elastic Young's modulus vector $\mathbf{E}^1$.
- Construct the SBFE model using the quadtree/octree framework, and assemble the global nodal forces vector and global stiffness matrix associated with 2D (or 3D) structure.

Step 1: Iterative elastic analyses

- If $r = 1$ obtain the equivalent stresses $\bar{\boldsymbol{\sigma}}^{r=1}$; otherwise, use the estimated $\bar{\boldsymbol{\sigma}}^r$.
- Using the scaled boundary finite element solution and $\bar{\boldsymbol{\sigma}}^r$, obtain/update the variables $\{\sigma_n^r$ (Eq. (5.39)), $\mathbf{S}_{active}$, $\mathbf{S}_{non-active}$, $\nabla\bar{\boldsymbol{\sigma}}$ (Eq. (5.6)), $\mathbf{H}_i$ (Eq. (5.4)) for all $i = 1$ to n SBFEs, $\Delta\bar{\boldsymbol{\sigma}}$ (Eq. (5.41)), $(\nabla\bar{\boldsymbol{\sigma}})_{\mathrm{D}}$ (Eq. (5.52)), $(\nabla\bar{\boldsymbol{\sigma}})_{\mathrm{H}}$) (Eq. (5.53)) $\}$ in order.

- Compute $\Delta\mathbf{E}$ based on Eq. (5.40).
- Compute $(\Delta\bar{\boldsymbol{\sigma}})^{\text{dir.}}$ (Eq. (5.54)) and $(\nabla\bar{\boldsymbol{\sigma}})_{\text{M}}$ (Eq. (5.55)) and update $\Delta\mathbf{E}$ based on Eqs. (5.54) to (5.56); repeat the step until no difference between two consecutive sets of $\Delta\mathbf{E}$ is seen.
- Compute the variables (β_{min}, $\bar{\boldsymbol{\sigma}}^{r+1}$, $\bar{\sigma}_m^{r+1}$, γ_{min}) in order and based on Eqs. (5.42) to (5.46).
- Update the variables ($\bar{\boldsymbol{\sigma}}^{r+1}$ and $\mathbf{E}^{r+1}$) using Eqs. (6.4) and (6.5).
- Compute α^r, and update Δ using Eqs. (5.49) and (5.50).

Step 2: Termination

- If $\Delta < \varepsilon_2$, terminate. Take $\alpha^{\text{col}} = \alpha^r$.
- Else, update $r = r + 1$ and go to step 1.

6.3 Adaptive Sensitivity-based ECM Using the SBFEM

Use of adaptive strategies, involving the capability of employing a non-uniform mesh obtained based on the solution of a numerical scheme, for computation of the limit load has been the subject of considerable and successful researches (e.g. [122, 123, 124, 125, 126]). Adaptive improvement of the solution obtained by finite element methods (SBFEM in this chapter) is achieved by enrichment of the estimated solution in some way, such as refining the mesh, so that the best solution for a given computational effort can be obtained [127]. The procedure is carried out after an initial solution is obtained through finding the regions of the domain where the accuracy is not yet satisfied, and then refining them.

In the proposed adaptive sensitivity-based ECM, initially a basic uniform coarse mesh is constructed using the SBFEM. Thereafter, the sensitivity-based ECM is performed on the mesh to estimate the collapse load solution. In the process, all the subdomains (cells) which have undergone yielding are identified. These subdomains are the cells whose elastic moduli are changed during the iterations. A better level of accuracy, therefore, can be obtained by refining these parent cells into 4 equal children quadtree cells. This action imposes a hanging node on the adjacent cells, if they are not identified to be refined too. However, the presence of the hanging node does not pose a problem to the employed quadtree mesh in the SBFEM, since, as discussed in chapter 4, each cell is treated as a polygon having an arbitrary number of sides (Fig. 4.1). Therefore, the imposed hanging node is treated as a normal corner node in the adjacent polygonal cell. This ability in the quadtree implementation of the SBFEM allows an efficient adaptive mesh generation and reduces the need for the high computational resources of it. After the completion of identified parent cells subdivisions, the 2:1 rule is enforced on the mesh to ensure the balanced grid. The forces and boundary conditions are applied on the mesh, and the sensitivity-based ECM is again performed on the structure. The process can be repeated until a convergence on the collapse load solutions is obtained.

6.4 Numerical Examples

In this section, four 2D problems and five 3D problems were used to illustrate the performance of the proposed sensitivity-based ECM using SBFEM. In case of 2D problems, the adaptive sensitivity-based ECM was also implemented to highlight the superior performance of it in comparison to the uniform refinement and the efficiency of the SBFEM in handling the hanging nodes. In all examples, $\lambda = 0.01$, and the incompressibility was considered by use of $\nu = 0.499$. The tolerance for stopping the iterations of sensitivity-based ECM was considered as $\varepsilon_2 = 1 \times 10^{-6}$. The analysis procedures were implemented within a MATLAB programming environment.

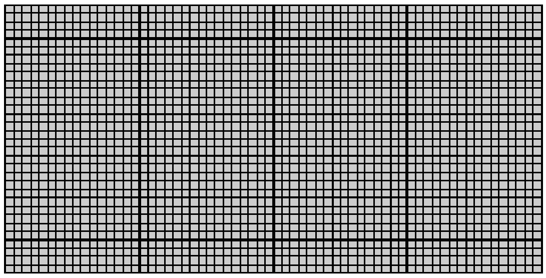

Figure 6.1: Prandtl's punch problem - actual SBFE model

6.4.1 2D Examples

6.4.1.1 Prandtl's punch problem

The first 2D problem addresses the Prandtl's punch problem mentioned in sections 2.2.7, 3.3, 3.4, 3.5.1.1, 3.5.1.1, and 5.4.1.1. The geometry and loading are shown in Fig. 3.1a. The ratio of the analytical collapse load multiplier to the yield stress ($\frac{\alpha^{\text{col}}}{\sigma_0}$) is 2.5708. Due to the symmetry, only half of the structure was modeled using the scaled boundary finite elements. The schematic model is shown in Fig. 4.14a. Each subdomain is subdivided into 16 similar subdomains. The actual model is shown in Fig. 6.1. The model was acquired quite automatically from a 2D solid. In total, 2048 subdomains, 2145 nodes, 4290 DOFs, and 2048 integration points were utilized.

The sensitivity-based ECM was performed on the SBFE model and the normalized load multipliers were monotonically increased and converged to the collapse load solution of $\frac{\alpha^{\text{col}}}{\sigma_0} = 2.6743$, which is 4.03% higher than the analytical solution. The iterative scheme is shown in Fig. 6.2.

The plots of equivalent stress and elastic modulus distributions corresponding to the collapse load solution are displayed in Fig. 6.3. The scaled displacement field is also displayed in Fig. 6.4.

The influence of the number of subdomains on the collapse load solution was also investigated. Six discretizations are uniformly developed ranging from a coarse

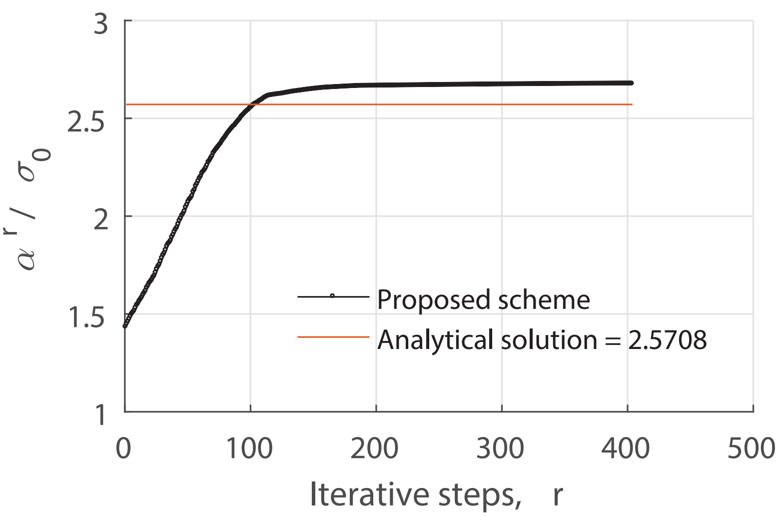

Figure 6.2: Iterative scheme for the Prandtl's punch problem with 2048 SBFEs using the sensitivity-based ECM

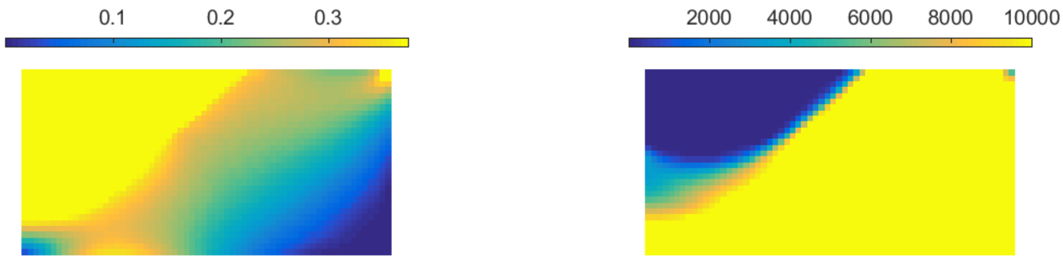

(a) (b)

Figure 6.3: Stress and elastic modulus distributions for the Prandtl's punch problem with 2048 SBFEs using the sensitivity-based ECM (a) stress distribution (b) elastic modulus distribution

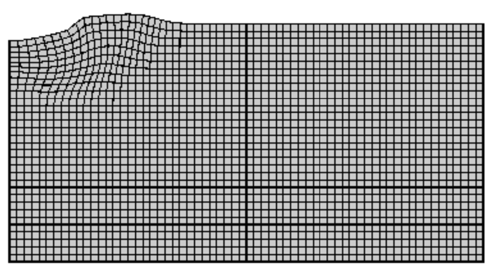

Figure 6.4: The schematic displacement field for the Prandtl's punch problem with 2048 SBFEs using the sensitivity-based ECM

Table 6.1: The collapse load solutions of the Prandtl's punch problem for different SBFE discretizations using the sensitivity-based ECM

Uniform refinement			Adaptive refinement		
No. of subdomains	$\frac{\alpha^{\text{col}}}{\sigma_0}$	error%	No. of subdomains	$\frac{\alpha^{\text{col}}}{\sigma_0}$	error%
32	3.5593	38.45	32	3.5593	38.45
128	3.0056	16.91	101	3.0116	17.15
512	2.7803	8.15	308	2.7833	8.27
2048	2.6743	4.03	887	2.6772	4.14
8192	2.6113	1.58	2783	2.6133	1.65
32768	2.5876	0.65	9323	2.5826	0.46

mesh to a fine mesh. The sensitivity-based ECM was carried out on each of the models and the final collapse load solutions are shown in Table 6.1. As expected, the collapse load solutions are reduced by increasing the number of subdomains due to the better satisfaction of the yield conformity in the whole domain. The variation of the collapse load solutions for different discretizations is also shown in Fig. 6.5. A two-term power series was fit on the scattered collapse load solutions in Fig. 6.5b, which converges to the collapse load solution of $\left(\frac{\alpha^{\text{col}}}{\sigma_0}\right)_{conv.} = 2.576$. The variation of the errors between this converged solution and the obtained collapse load solutions, e_α defined in Eq. (5.62), with respect to the different mesh sizes is also shown in Fig. 6.5.

The proposed adaptive sensitivity-based ECM was also performed on the example. The produced adaptive SBFE meshes are shown in Fig. 6.6, which are correspondent to the elastic moduli distributions shown in Fig. 6.7. As seen, the ability of handling the hanging nodes allowed efficient local refinements. The final collapse load solutions are also tabulated in Table 6.1 for the sake of comparison with the uniform refinements. In all instances, the adaptive sensitivity-based ECM requires less computational resources, represented by the number of elements. For example, the last adaptive mesh with 9323 subdomains converged to the collapse load solution of $\frac{\alpha^{\text{col}}}{\sigma_0} = 2.5826$, which is only 0.46% higher than the true collapse load solution. However, the corresponding collapse load solution for the uniform mesh with almost 3.5 times more number of subdomains is $\frac{\alpha^{\text{col}}}{\sigma_0} = 2.5876$, which is 0.65%

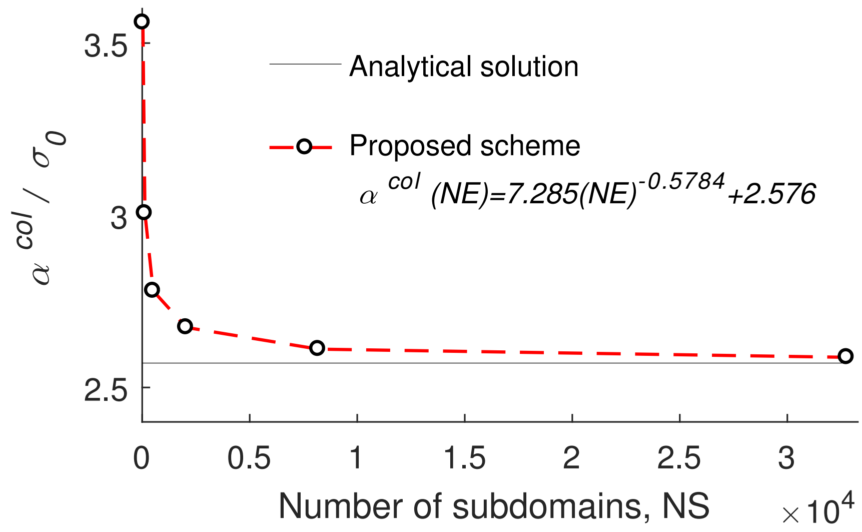

(a)

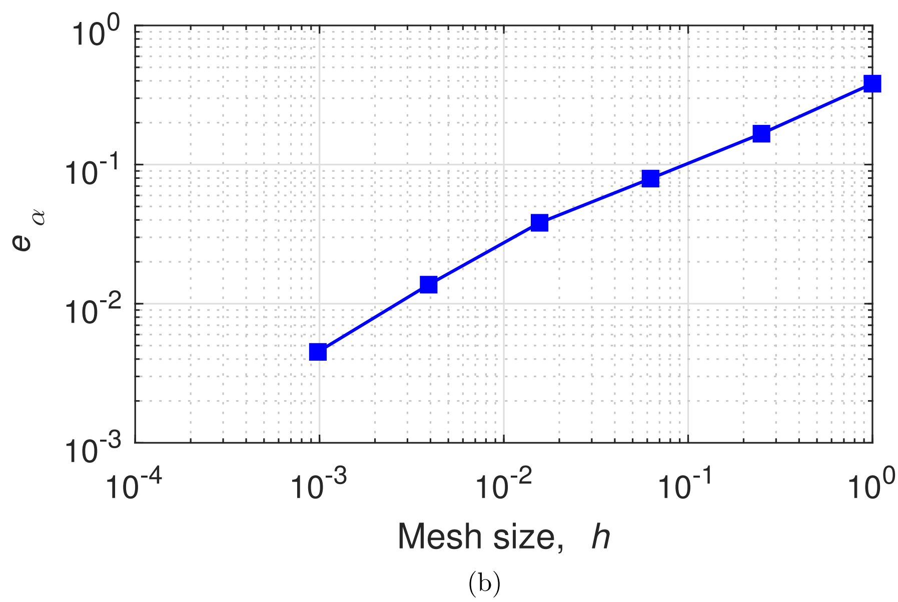

(b)

Figure 6.5: Variation of collapse load solutions of Prandtl's punch problem for different SBFE discretizations using the sensitivity-based ECM (a) variation with the number of subdomains (b) error with respect to the extrapolated converged solution

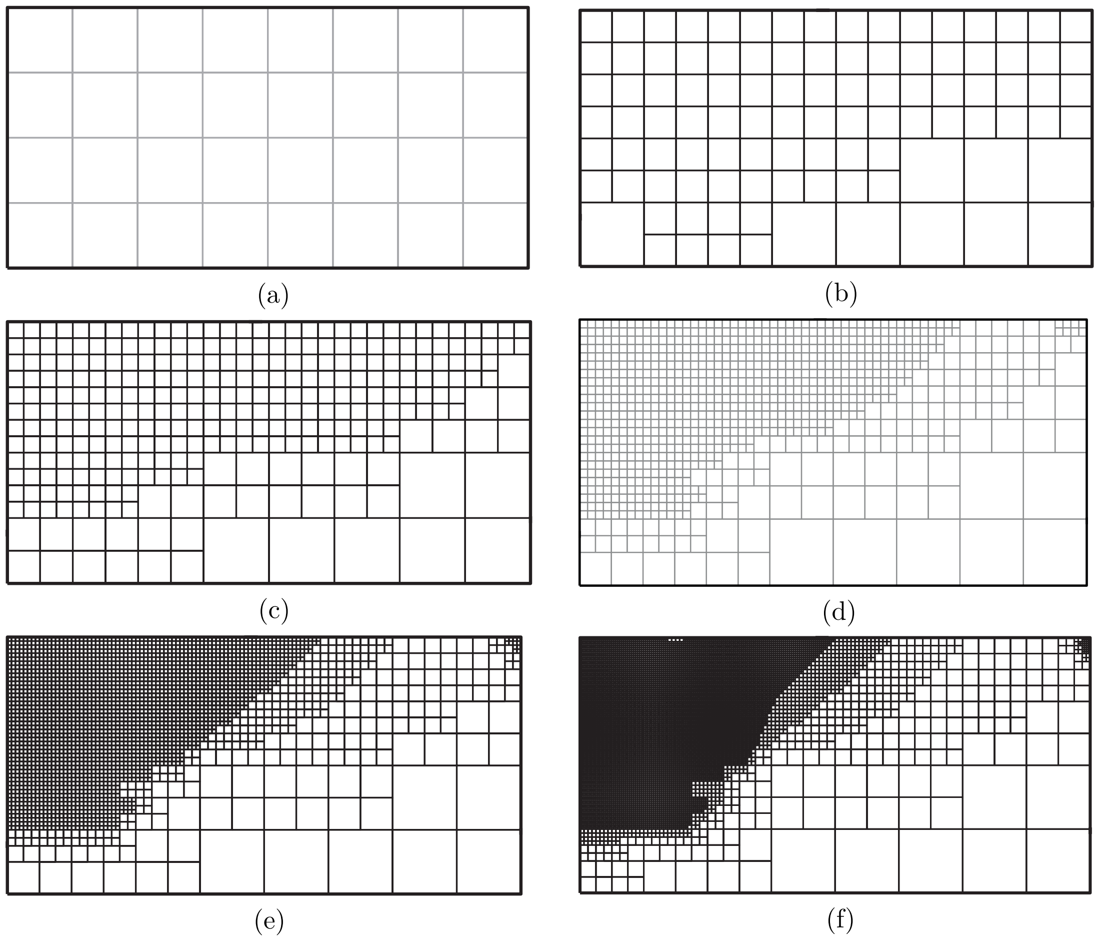

Figure 6.6: The produced adaptive meshes for the Prandtl's punch problem; a) 32 subdomains b) 101 subdomains c) 308 subdomains d) 887 subdomains e) 2783 subdomains f) 9323 subdomains

higher than the analytical solution.

Fig. 6.8 shows the variation of the errors e_α between the converged solution and the obtained collapse load solutions for the adaptive meshes. The graph is also shown for the uniform mesh. The advantageous behavior of using the adaptive sensitivity-based ECM over its uniform approach is obvious, as almost the same level of accuracy is achieved using less computational resources.

6.4.1.2 Double-edge notched specimen

The second 2D example considers the double-edge notched specimen provided in section 3.5.1.2. The geometry and loading are shown in Fig. 3.13a. The normalized collapse load multiplier for the problem under the shown reference load is reported

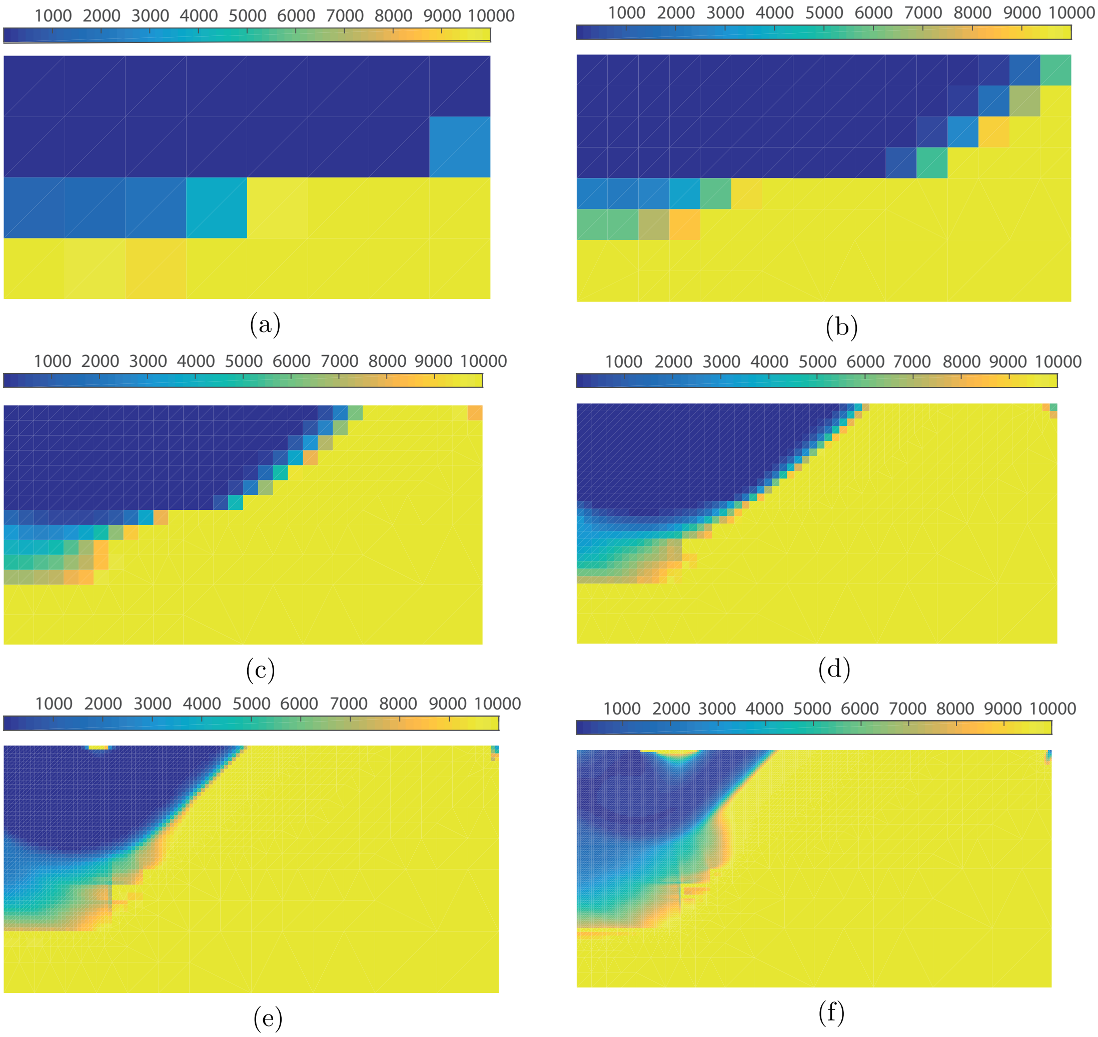

Figure 6.7: The corresponding elastic moduli distributions of the adaptive meshes produced for the Prandtl's punch problem; a) 32 elements b) 101 subdomains c) 308 subdomains d) 887 subdomains e) 2783 subdomains f) 9323 subdomains

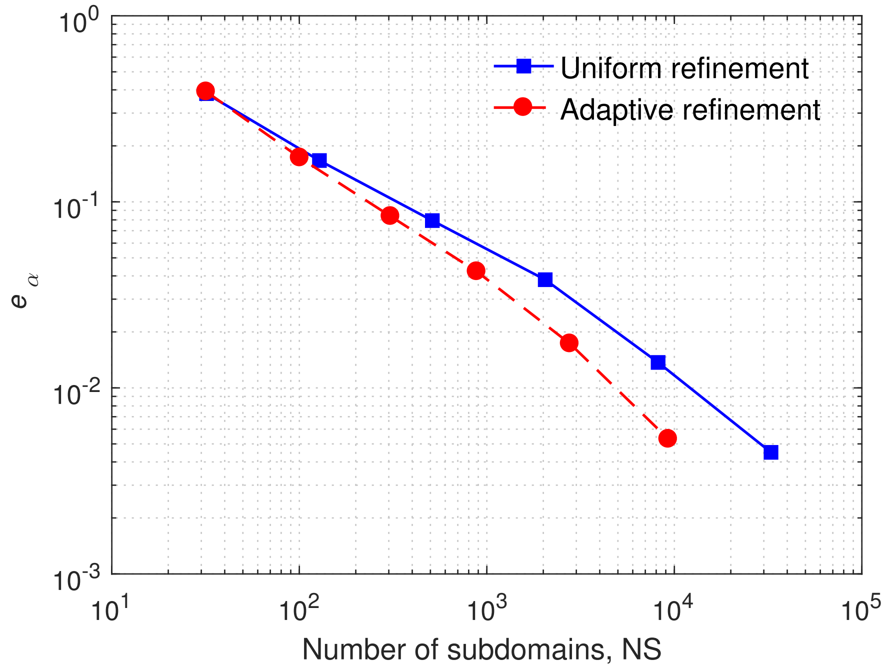

Figure 6.8: Variation of the error e_α with the number of subdomains for the Prandtl's punch problem using adaptive and uniform refinements

as $\left(\frac{\alpha^{\text{col}}}{\sigma_0}\right)_{\text{ref}} = 4.6749$ [89]. Due to the symmetric nature of the problem in load and geometry, only a quarter of it was automatically modeled using SBFEs. The schematic uniform mesh is shown in Fig. 4.20a, where each subdomain is subdivided into 16 similar subdomains (Fig. 6.9). In total, 4096 subdomains, 4225 nodes and 8450 DOFs and 4096 integration points were considered.

The proposed sensitivity-based ECM was implemented on the model. The normalized load multipliers were increased monotonically and converged to the normalized collapse load multiplier of $\frac{\alpha^{\text{col}}}{\sigma_0} = 4.6588$, which is almost 0.34% lower than the reported collapse load solution. The iterative scheme is plotted in Fig. 6.10.

The equivalent stress and elastic moduli distribution in domain are also displayed in Fig. 6.11. The schematic displacement field showing the collapse mechanism is also plotted in Fig. 6.12.

The effect of the number of subdomains on the collapse load solution was also studied. Table 6.2 shows the results of this mesh investigation, where the difference percentages between the computed solutions and the reported solution are

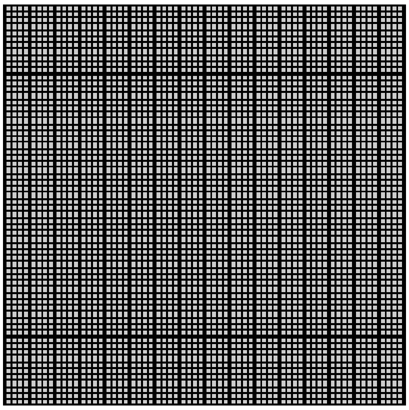

Figure 6.9: Double-edge notched specimen - actual SBFE model

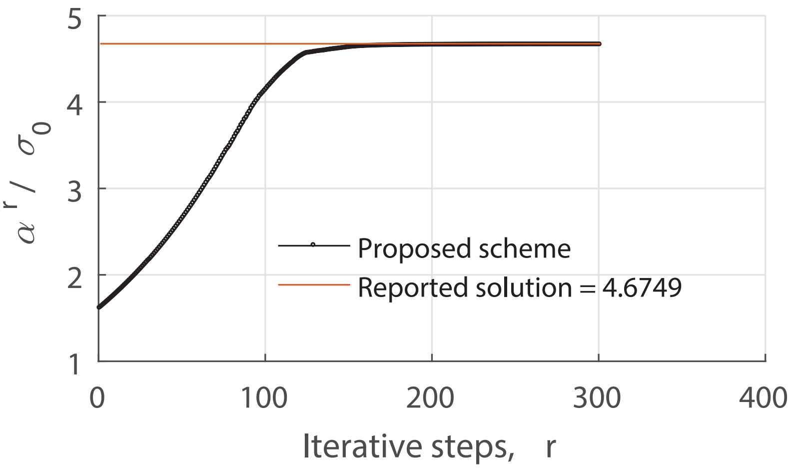

Figure 6.10: Iterative scheme for the notched specimen with 4096 SBFEs using the sensitivity-based ECM

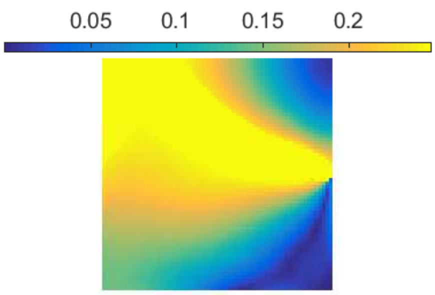

(a)

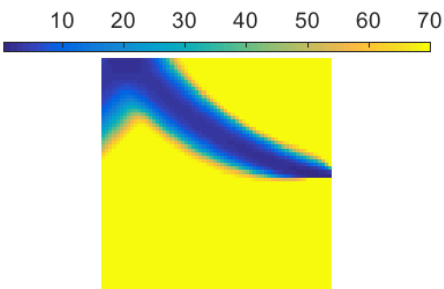

(b)

Figure 6.11: Equivalent stress and elastic modulus distributions for the notched specimen with 4096 SBFEs using the sensitivity-based ECM (a) stress distribution (b) elastic modulus distribution

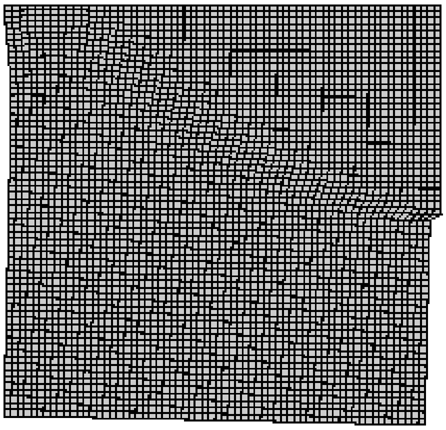

Figure 6.12: The schematic displacement field of the double-edge notched specimen with 4096 SBFEs using the sensitivity-based ECM

Table 6.2: The collapse load solutions of the double-edge notched specimen for different SBFE discretizations using the sensitivity-based ECM

Uniform refinement			Adaptive refinement		
No. of subdomains	$\frac{\alpha^{\text{col}}}{\sigma_0}$	difference%	No. of subdomains	$\frac{\alpha^{\text{col}}}{\sigma_0}$	difference%
16	6.2601	33.91	16	6.2601	33.91
64	5.5140	17.95	55	5.5234	18.15
256	5.0630	8.30	193	5.0715	8.48
1024	4.8049	2.78	604	4.8146	2.99
4096	4.6588	-0.34	1882	4.6761	0.03
16384	4.5844	-1.94	5758	4.5845	-1.93

also presented. As expected, the collapse load solution is decreased by increasing the number of elements (reducing the mesh size). Fig. 6.13 also shows this variation. Fig. 6.13a plots the variation of collapse load solutions with the number of subdomains, where a two-term power series is fitted to them. The fitted plot converges to the collapse load solution of $\left(\frac{\alpha^{\text{col}}}{\sigma_0}\right)_{conv.} = 4.458$, which is some 4.64% less than the reported solution. Fig. 6.13b also plots the error e_α between the converged solution and the obtained scattered collapse load solutions with the mesh size. As expected, this error is almost linearly reduced by reduction in mesh size.

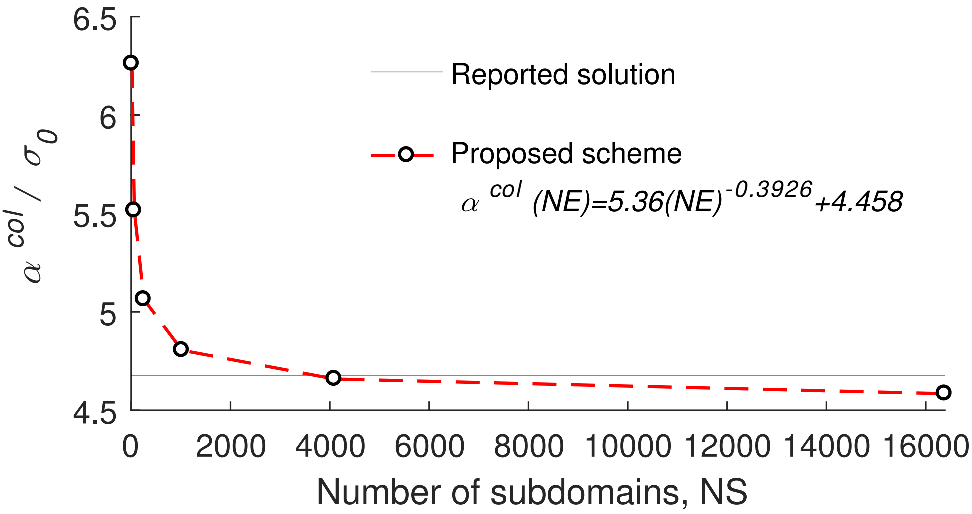

(a)

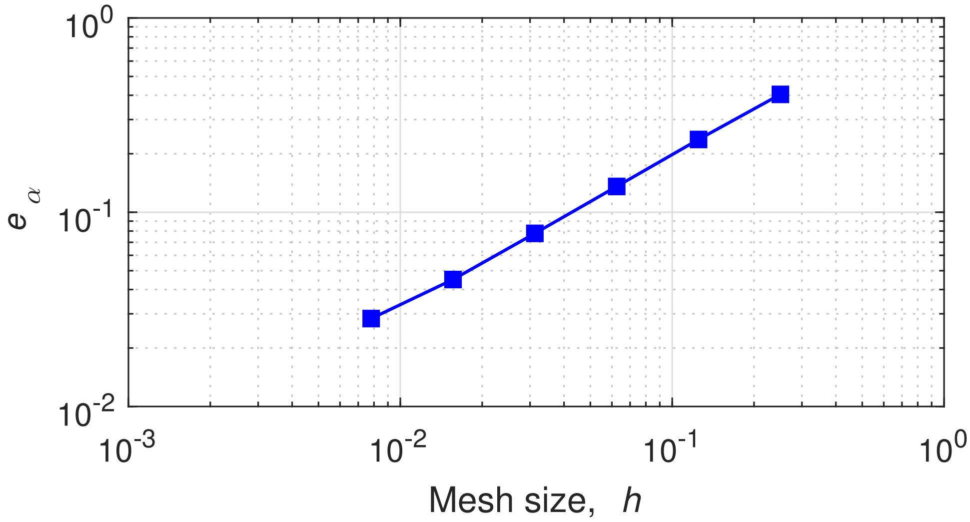

(b)

Figure 6.13: Variation of collapse load solutions of the double-edge notched specimen for different SBFE discretizations using the sensitivity-based ECM (a) variation with the number of subdomains (b) error with respect to the extrapolated converged solution

The adaptive sensitivity-based ECM was also performed on the structure. The produced adaptive meshes are shown in Fig. 6.14. The corresponding elastic moduli distributions are also plotted in Fig. 6.15. The collapse load solutions are tabulated in Table 6.2, where the results for uniform discretizations are also shown. Similar to the uniform refinements, the collapse load solutions are reduced by increasing the number of subdomains. However, for obtaining approximately the same level of accuracy, less computational resources, shown by the number of subdomains, are needed.

The error e_α between the converged collapse load solution and the scattered collapse load solutions were also obtained for both uniform and adaptive produced meshes and plotted in Fig. 6.16. As seen, the error is reduced by increasing the number of elements for both approaches. However, the rate of this reduction is higher for the adaptive scheme, which saves more computational resources for the user.

6.4.1.3 Perforated plate problem

This 2D example considers the perforated plate problem mentioned in section 3.5.1.3 of chapter 3. The geometry and loading are illustrated in Fig. 3.19a. The plain stress condition and the von Mises yield criterion were considered. The analytical normalized collapse load solution is $\left(\frac{\alpha^{\mathrm{col}}}{\sigma_0}\right)_{\mathrm{ref}} = 0.8$. The uniform structural SBFE model is shown in Fig. 6.17. In total, 3976 subdomains, 4295 nodes, 8590 DOFs, and 3976 integration points were utilized.

The proposed sensitivity-based ECM was performed on the structure and the normalized load multipliers were monotonically increased and converged to the normalized collapse load multiplier of $\frac{\alpha^{\mathrm{col}}}{\sigma_0} = 0.8215$, which is some 2.62% higher than the analytical solution. The iterative scheme is also shown in Fig. 6.18. The equivalent stress and elastic moduli distributions corresponding to the obtained collapse load are also displayed in Fig. 6.19. The associated schematic displacement field corresponding to the collapse mechanism is also shown in Fig. 6.20.

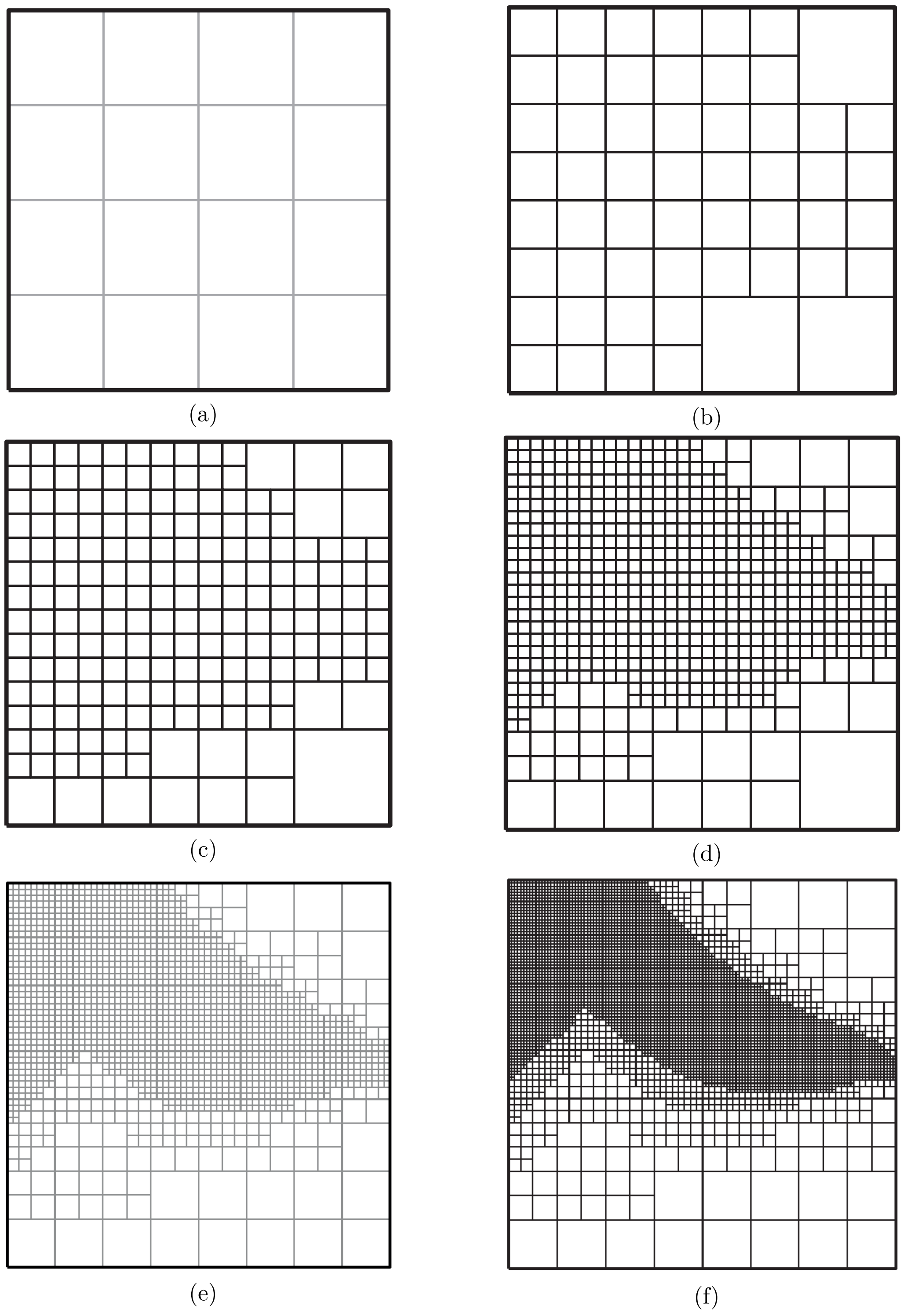

Figure 6.14: The produced adaptive meshes for the double-edge notched specimen; a) 16 subdomains b) 55 subdomains c) 193 subdomains d) 604 subdomains e) 1882 subdomains f) 5758 subdomains

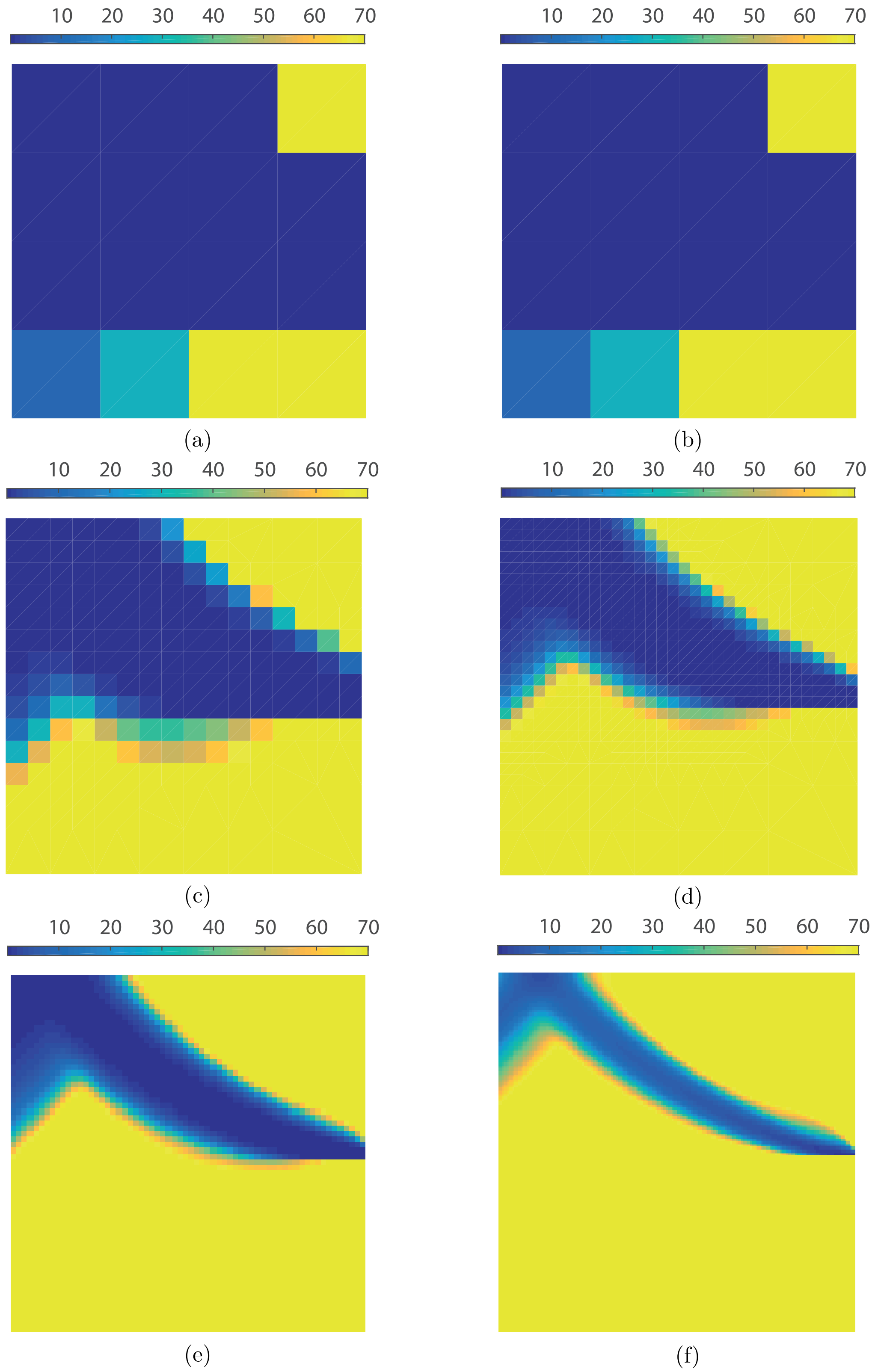

Figure 6.15: The corresponding elastic moduli distributions of the adaptive meshes produced for the double-edge notched specimen; a) 16 subdomains b) 55 subdomains c) 193 subdomains d) 604 subdomains e) 1882 subdomains f) 5758 subdomains

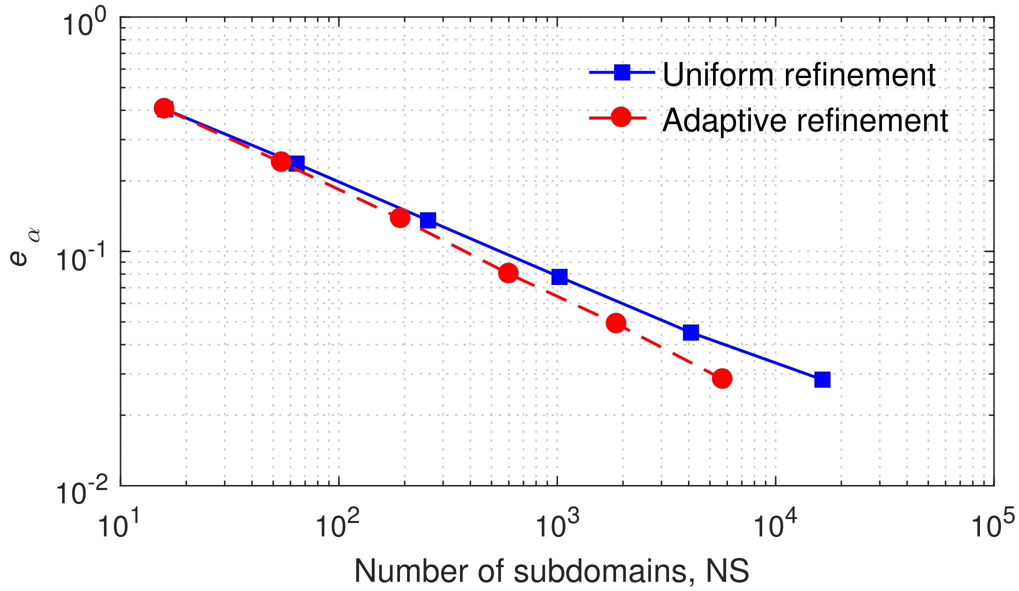

Figure 6.16: Variation of the error e_α with the number of subdomains for the double-edge notched specimen using the adaptive and uniform refinements

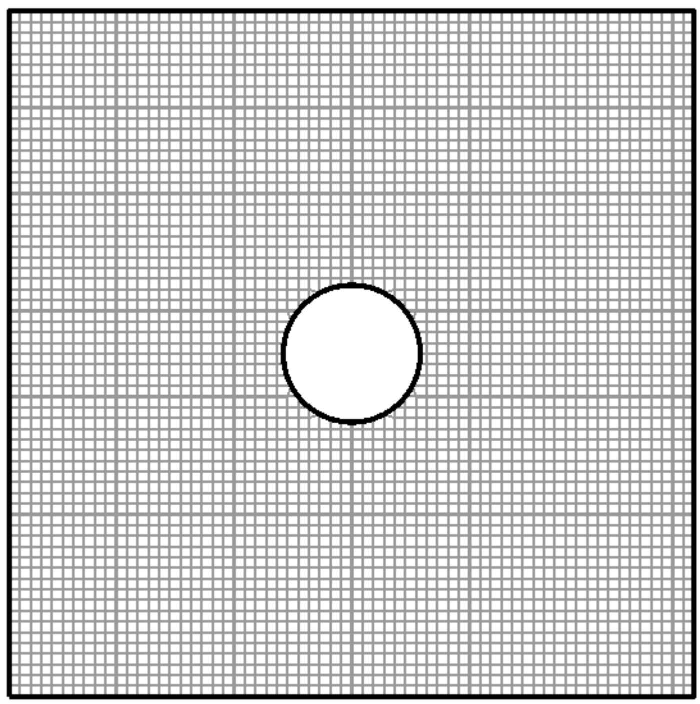

Figure 6.17: The uniform SBFE model with 3976 subdomains for the perforated plate

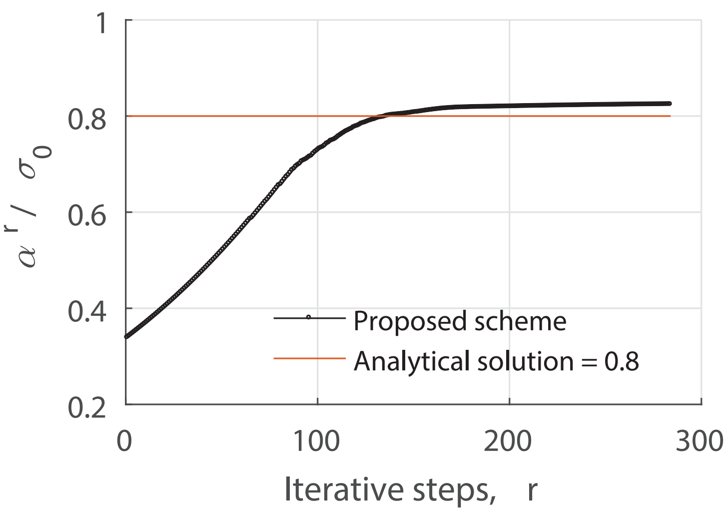

Figure 6.18: Iterative scheme for the perforated plate problem with 3976 SBFEs using the sensitivity-based ECM

The influence of the number of subdomains on the collapse load solution was also investigated. Four discretizations were considered, where the models are uniformly refined to develop coarse to fine meshes. The sensitivity-based ECM using the SBFEM was applied on each of the discretizations and the results are summarized in Table 6.3. As can be seen, the collapse load solution is decreased by increasing the number of subdomains due to the better satisfaction of the yield conformity in the domain. Fig. 6.21 also shows the variation of the normalized collapse load solution with respect to the number of subdomains. In Fig. 6.21a a two-term power-series is fitted to the scattered obtained data, whose equation is shown. The converged solution based on this fit is $\left(\frac{\alpha^{\mathrm{col}}}{\sigma_0}\right)_{conv.} = 0.7858$, which is some 1.13% less than the analytical solution. The error between this converged collapse load solution and the obtained collapse load solutions for the uniform discretizations are also depicted in Fig. 6.21b.

The adaptive sensitivity-based ECM was also performed on the structure. In addition to the first uniform mesh, three other adaptive meshes produced automatically are shown in Fig. 6.22. The corresponding elastic moduli distribution for each of the discretizations are also shown in Fig. 6.23. The results of the computed collapse load solution for each of the cases are also tabulated in Table 6.3. Similar

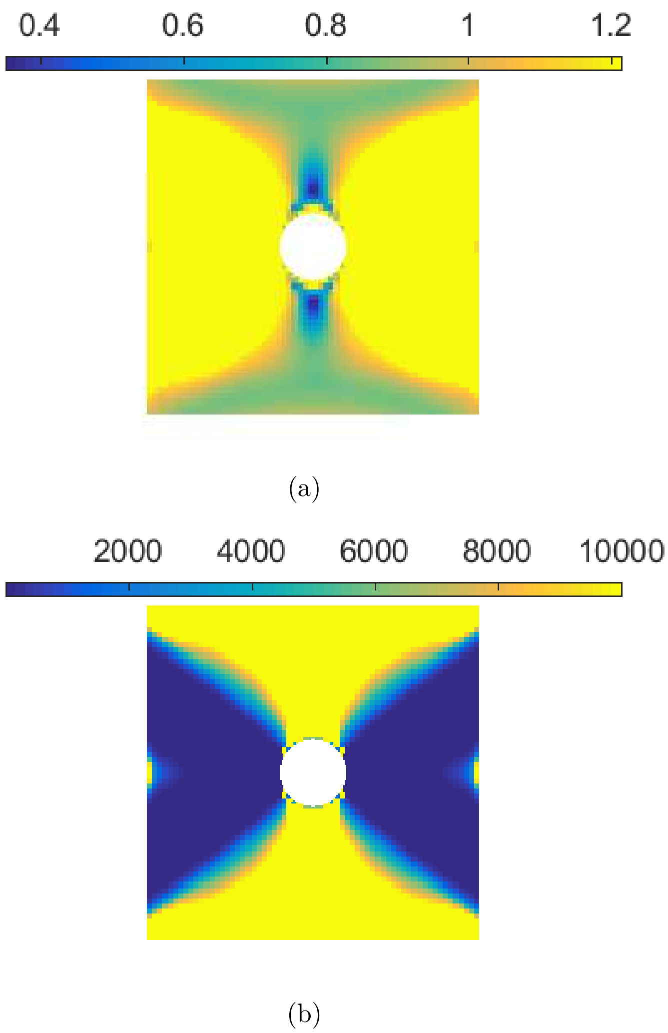

Figure 6.19: Stress and elastic modulus distributions for the perforated plate problem with 3976 SBFEs using the sensitivity-based ECM (a) stress distribution (b) elastic modulus distribution

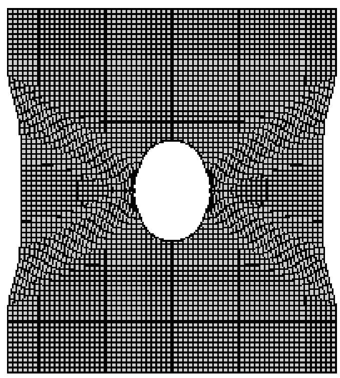

Figure 6.20: The schematic displacement field of the perforated plate problem with 3976 SBFEs using the sensitivity-based ECM

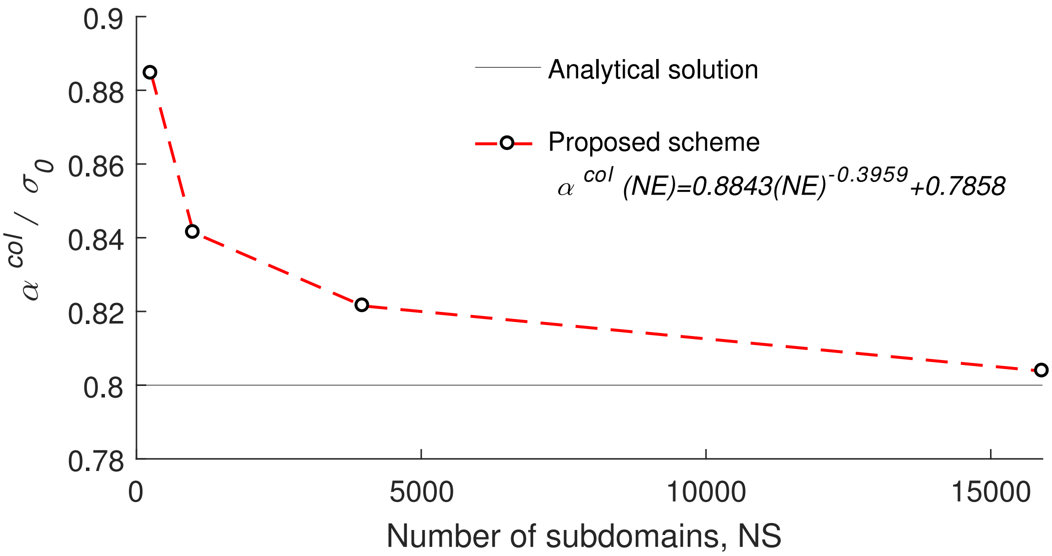

(a)

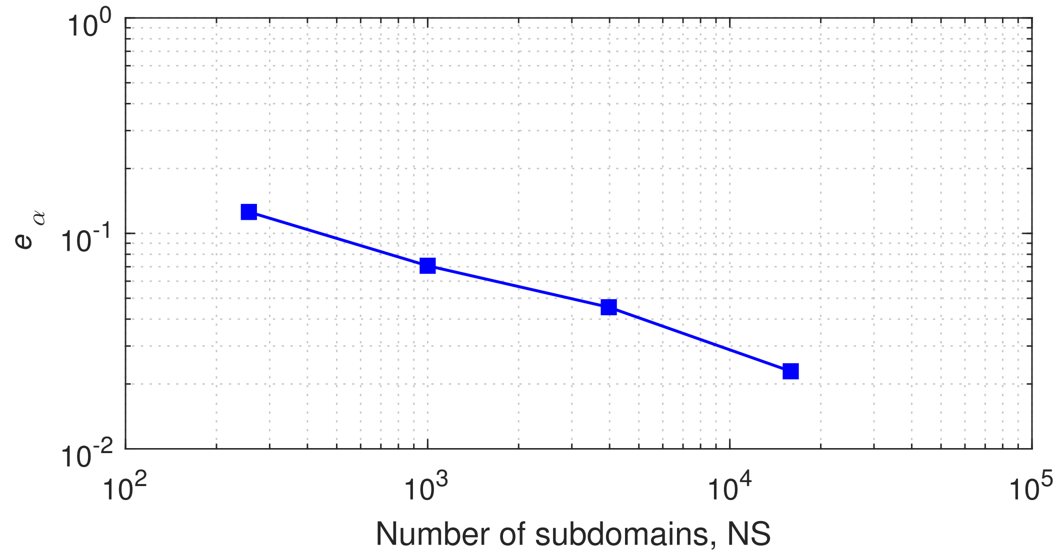

(b)

Figure 6.21: Variation of collapse load solutions of the perforated plate problem for different SBFE discretizations using the sensitivity-based ECM (a) variation with the number of subdomains (b) error with respect to the extrapolated converged solution

Table 6.3: The collapse load solutions of the perforated plate problem for different SBFE discretizations using the sensitivity-based ECM

Uniform refinement			Adaptive refinement		
No. of subdomains	$\frac{\alpha^{\mathrm{col}}}{\sigma_0}$	error%	No. of subdomains	$\frac{\alpha^{\mathrm{col}}}{\sigma_0}$	error%
256	0.8846	9.56	256	0.8846	9.56
1000	0.8414	4.92	868	0.8418	4.97
3976	0.8215	2.62	2980	0.8201	2.45
15908	0.8038	0.47	10268	0.8023	0.29

to the uniform refinements, the collapse load solutions are decreased by increasing the number of subdomains. However, in all instances, the adaptive sensitivity-based ECM requires less computational resources, represented by the number of elements. Fig. 6.24 also shows the variation of the errors e_α between the converged solution and the obtained collapse load solutions for the produced adaptive meshes. The graph is also shown for the uniform refinements for the sake of comparison. The advantageous behavior of using the adaptive sensitivity-based ECM over its uniform approach is obvious. Almost the same level of accuracy is achieved using less computational resources.

6.4.1.4 The square plate with asymmetric penetrations

The final 2D example considers an in-plane square plate with asymmetric penetrations, where its dimensions in mm and uniformly applied loads of P = 1 N/mm are shown in Fig. 6.25. The structure employed the von Mises materials. The elastic modulus was initially taken as 2000 MPa whose unit is the same as the stress unit.

This structure was initially implemented by Díez et al. [128] to study the strain localization in softening viscoplastic solids undergoing large deformations, and later by Zouain et al. [129] in the context of the shakedown analysis. Makrodimopoulos and Matrin [130] employed a second-order cone program to capture the strict lower bound limit, and concluded that the accuracy of the collapse load depends on the efficiency of the structural discretization around the circumference area of complex

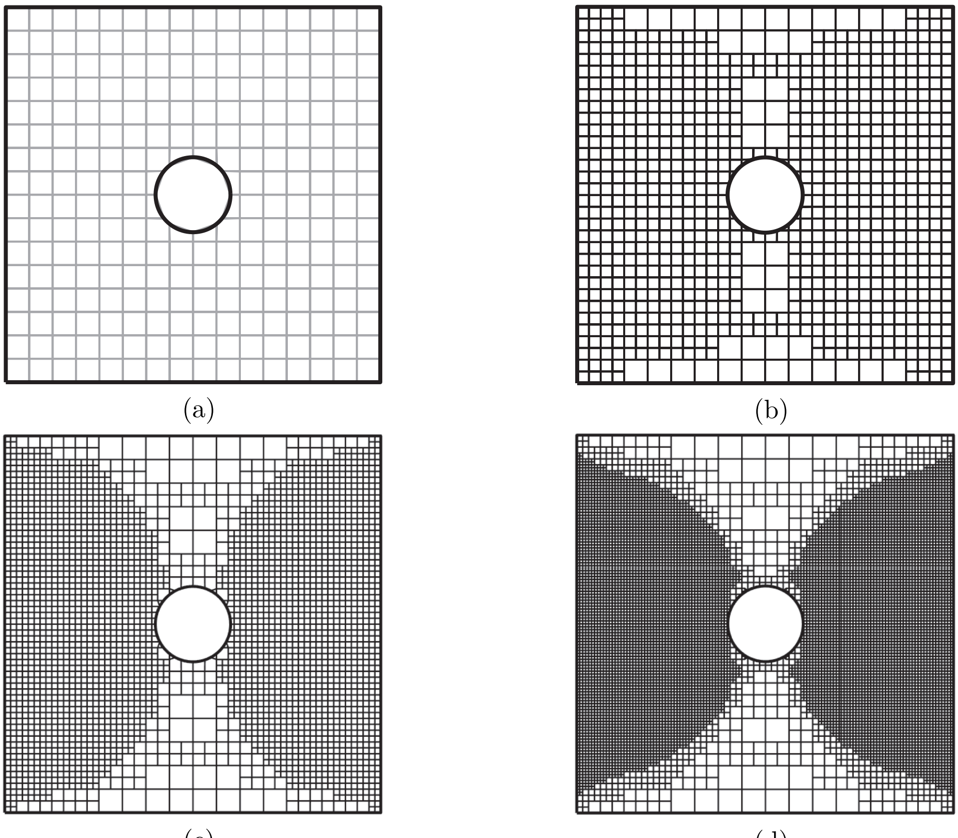

(a) (b) (c) (d)

Figure 6.22: The produced adaptive meshes for the perforated plate problem; a) 256 subdomains b) 868 subdomains c) 2980 subdomains d) 10268 subdomains

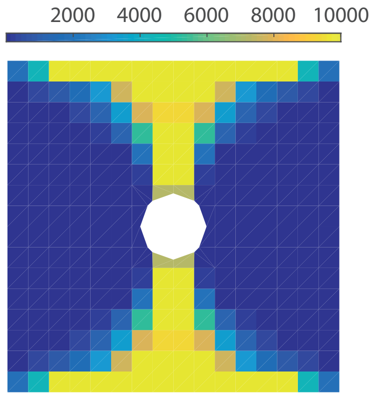

(a)

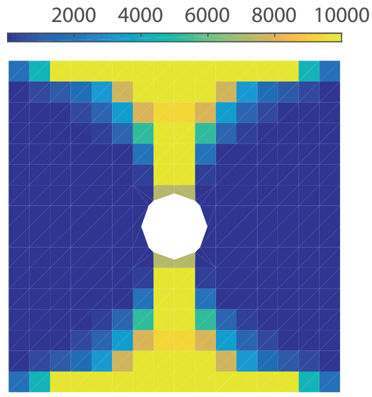

(b)

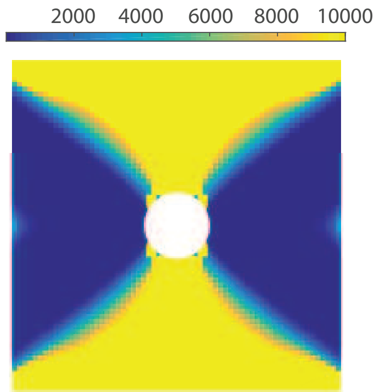

(c)

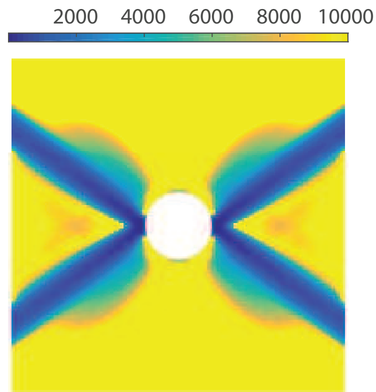

(d)

Figure 6.23: The corresponding elastic moduli distributions of the adaptive meshes produced for the perforated plate problem; a) 256 subdomains b) 868 subdomains c) 2980 subdomains d) 10268 subdomains

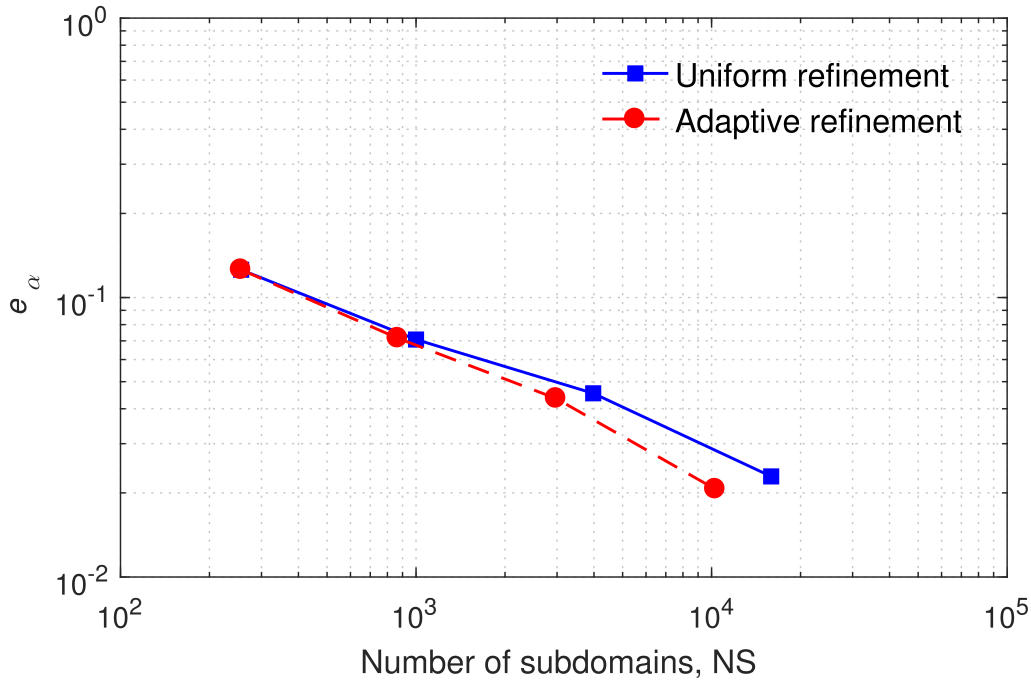

Figure 6.24: Variation of the error e_α with the number of subdomains for the perforated plate problem using adaptive and uniform refinements

holes. Muñoz et al [131] implemented an automated adaptive (triangular) finite element model in the context of the lower bound limit analysis, and highlighted the difficulties associated with the construction of the structural discrete model.

In the light of the above comments, this example was initially modeled using a uniform SBFE discretizations. The mesh was automatically constructed out of an in-plane solid and is shown in Fig. 6.26. The use of polygonal subdomains efficiently facilitated the discretization around the circumference area of the complex holes, as the challenges associated with the construction of a mapped mesh were removed.

The sensitivity-based ECM was performed on the model. The normalized load multipliers were monotonically increased and converged to the normalized collapse load multiplier of $\frac{\alpha^{\text{col}}}{\sigma_0} = 1.0733$, which is 2.02% higher than the reported collapse load solution $\left(\frac{\alpha^{\text{col}}}{\sigma_0}\right)_{\text{ref}} = 1.052$ [129]. The iterative scheme is also plotted in Fig. 6.27. The equivalent stress and elastic moduli distributions corresponding to the collapse load solutions are also displayed in Fig. 6.28. The schematic displacement field corresponding to the collapse mechanism is also shown in Fig. 6.29.

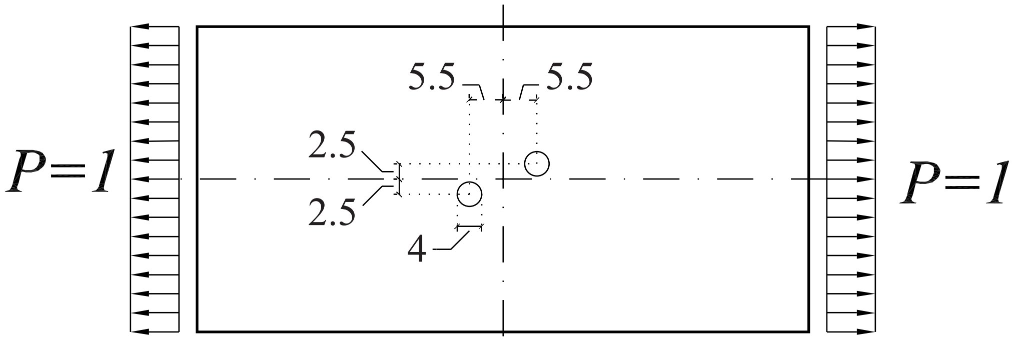

Figure 6.25: The square plate with asymmetric penetrations - geometry and loading

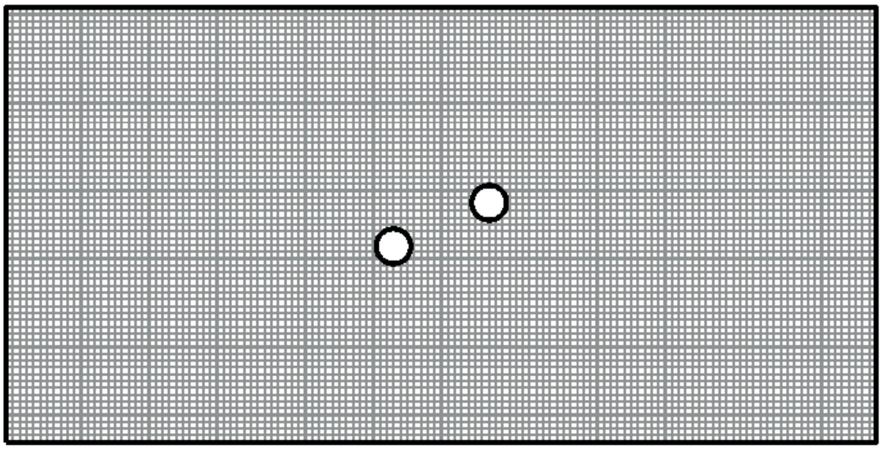

Figure 6.26: The square plate with asymmetric penetrations - SBFE uniform model

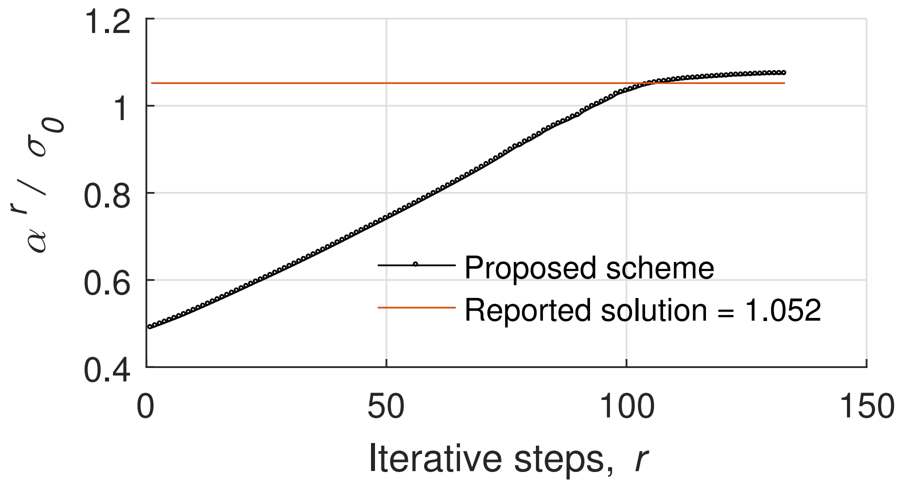

Figure 6.27: Iterative scheme for the square plate with asymmetric penetrations with 8168 SBFEs using the sensitivity-based ECM

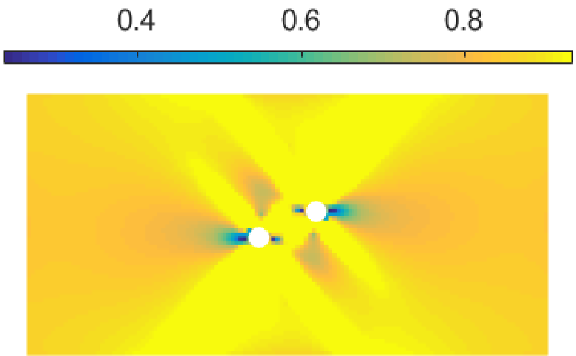

(a)

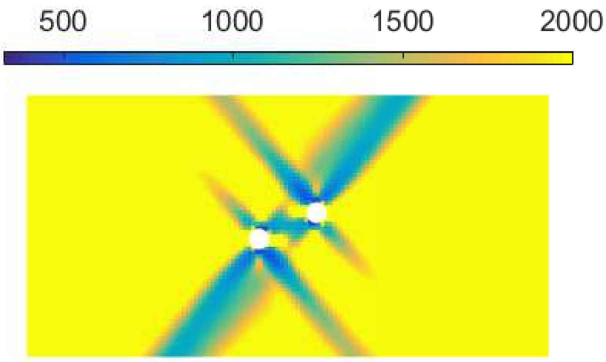

(b)

Figure 6.28: Equivalent stress and elastic modulus distributions for the square plate with asymmetric penetrations with 8168 SBFEs using the sensitivity-based ECM (a) stress distribution (b) elastic modulus distribution

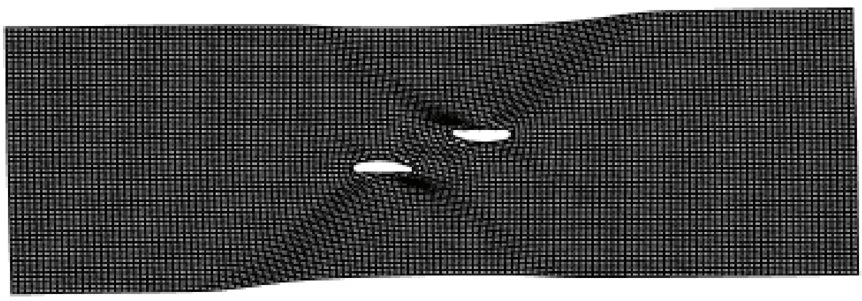

Figure 6.29: The schematic displacement field for the square plate with asymmetric penetrations with 8168 SBFEs using the sensitivity-based ECM

Table 6.4: The collapse load solutions of the square plate with asymmetric penetrations problem for different SBFE discretizations using the sensitivity-based ECM

Uniform refinement			Adaptive refinement		
No. of subdomains	$\frac{\alpha^{col}}{\sigma_0}$	difference%	No. of subdomains	$\frac{\alpha^{col}}{\sigma_0}$	difference%
2046	1.1330	7.70	2046	1.1330	7.70
8168	1.0733	2.02	6871	1.0737	2.06
32634	1.0523	0.02	12575	1.0542	0.20

The effect of the number of subdomains on the collapse load solution was investigated. Due to the high computational costs involved in this problem, three uniform discretizations were automatically constructed, and the sensitvity-based ECM was performed on them. The normalized collapse load solutions are computed for each of the discretizations and the results are tabulated in Table 6.4. As expected, the collapse load solutions are decreased by increasing the number of subdomains and the number of integration points consequently. It should be noticed that due to the insufficient number of uniform samples, caused by high computational costs involved, the curve fitting process is not carried out for this example; performing the curve fitting process with inadequate samples might overestimate the the collapse load in the sensitivity-based ECM.

The adaptive sensitivity-based ECM was also conducted for this problem. In addition to the first uniform mesh, two other adaptive non-uniform meshes produced automatically are shown in Fig. 6.30. The corresponding elastics moduli distributions of these discretizations obtained for the collapse load solutions are shown in Fig. 6.31. The collapse load solutions are also tabulated in Table 6.4. As seen, the collapse load solutions are reduced by increasing the number of subdomains. However, the number of subdomains (computational resources) required for almost the same level of accuracy is lower than the corresponding uniform refinements. Fig. (6.32) also shows the variation of these collapse load solutions for both uniform and adaptive discretizations.

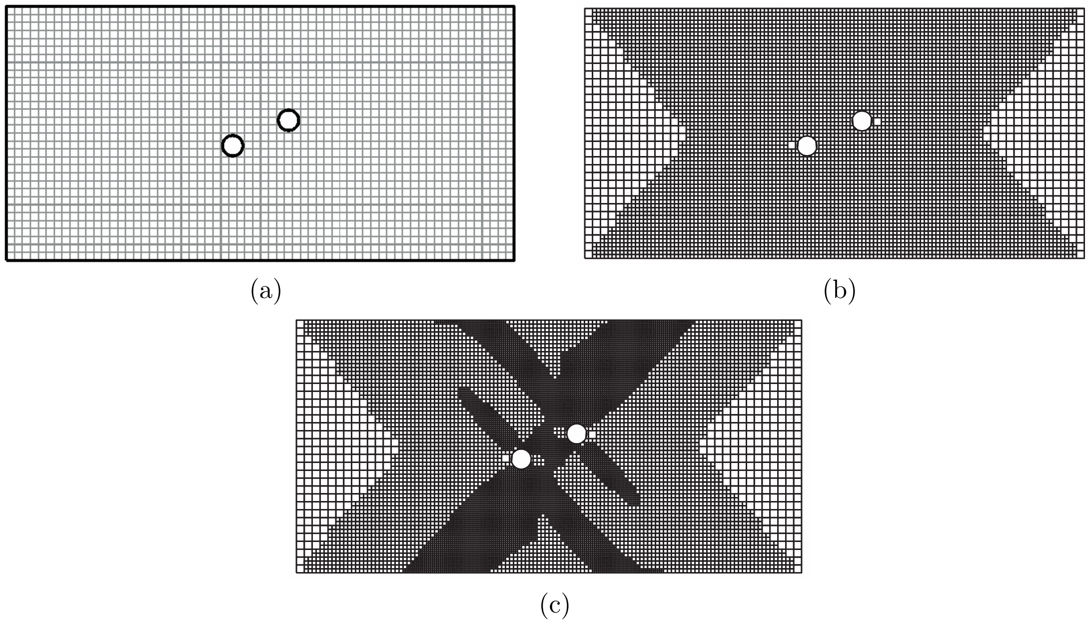

Figure 6.30: The produced adaptive meshes for the square plate with asymmetric penetrations problem; a) 2046 subdomains b) 6871 subdomains c) 12575 subdomains

It should be emphasized that the adaptive scheme discretises the yielded elements only. For the first uniform mesh used in this example, many elements experienced yielding. This is why the difference between the uniform and adaptive refinements is not so significant in the second step of refinement. However, for the next step of refinement, the difference is more obvious, as almost 40% of the number of DOFs employed in the uniform refinement is used in the adaptive scheme. This amount of reduction in number of DOFs is useful when sufficient computational resources for uniform refinement are not available.

6.4.2 3D Examples

6.4.2.1 Thick cylinder

The first 3D example involves the thick cylinder under the uniform pressure introduced in section 3.5.2.1 of chapter 3. Here, considering the fact that the effect of the cylinder length is negligible on the true collapse load of the structure, it is reduced to 220 mm to accommodate more number of subdomains. The SBFE model was generated quite automatically and out of the CAD (STL) model directly, and is

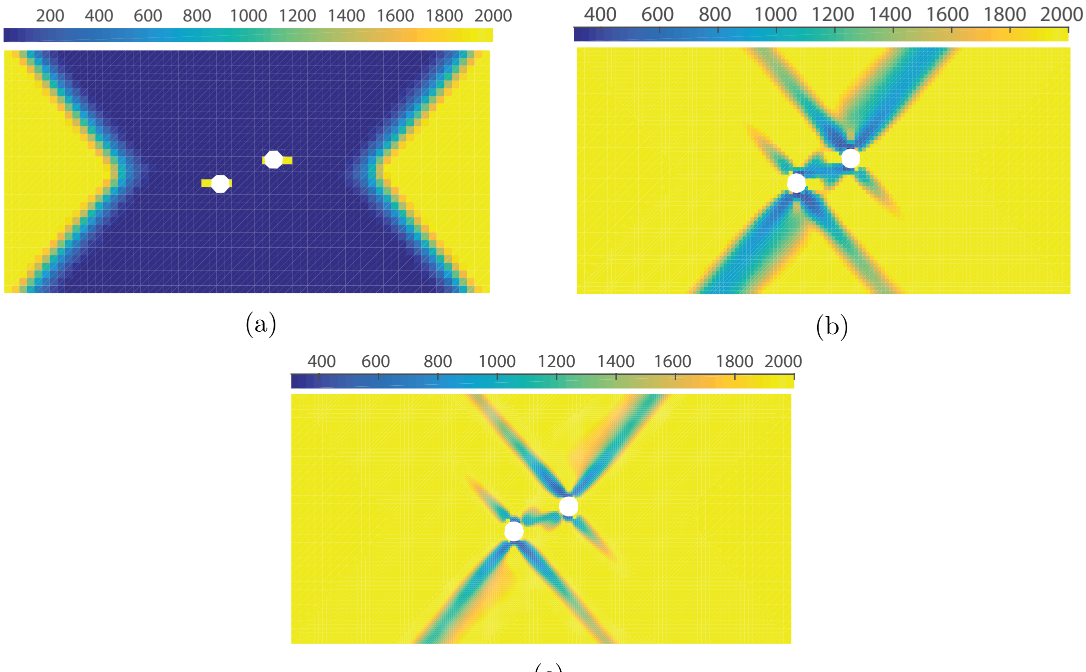

Figure 6.31: The corresponding elastic moduli distributions of the adaptive meshes produced for the square plate with asymmetric penetrations problem; a) 2046 subdomains b) 6871 subdomains c) 12575 subdomains

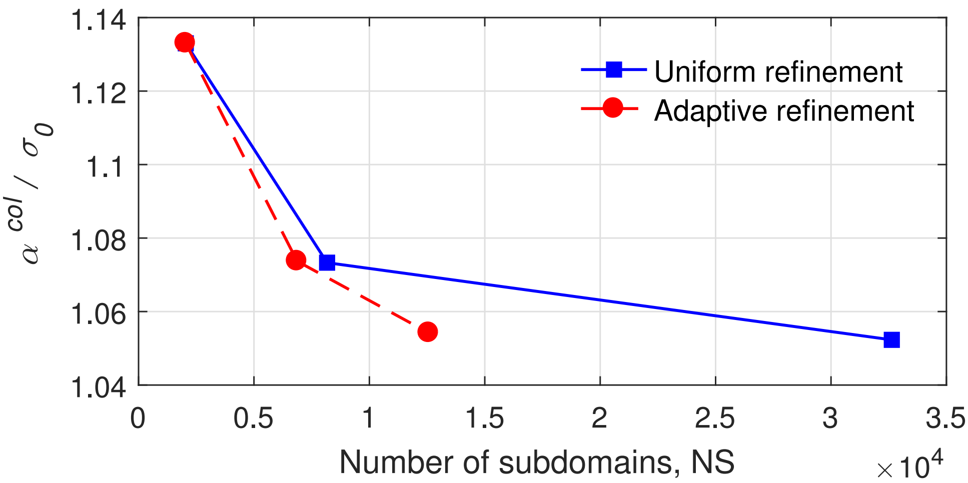

Figure 6.32: Variation of the the normalized collapse load solutions with the number of subdomains for the square plate with asymmetric penetrations plate problem using the adaptive and uniform refinements

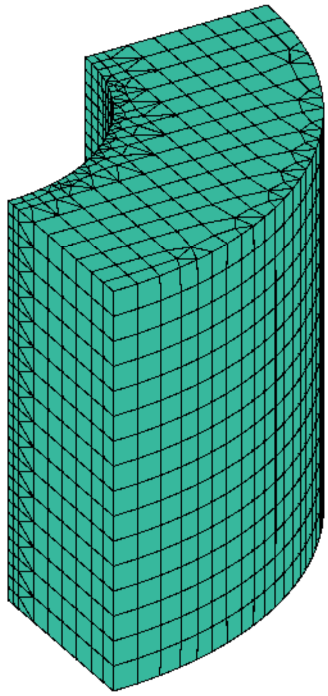

Figure 6.33: The SBFE model of the thick cylinder with 3632 subdomains

shown in Fig. 6.33. In total, 3632 subdomains, 5188 nodes, 15564 DOFs, and 3632 integration points were employed.

The sensitivity-based ECM was performed on the model, and the load multipliers were monotonically increased. The converged normalized collapse load solution $\frac{\alpha^{\text{col}}}{\sigma_0}$ was obtained as 0.8036, which is some 0.4% higher than the analytical solution of 0.8004. The iterative scheme of the proposed method is shown in Fig. 6.34 The corresponding von Mises stress and elastic moduli distribution to this collapse load solution are also depicted in Fig. 6.35.

The effect of the number of subdomains were also investigated on the problem. Due to the high computational costs involved in this 3D problem, only three discretizations were automatically produced from the STL format of the CAD model. The normalized collapse load results and their errors with respect to the analytical solution are provided in Table (6.5). As expected, the collapse load solutions are reduced by increasing the number of subdomains, due to the better satisfaction of

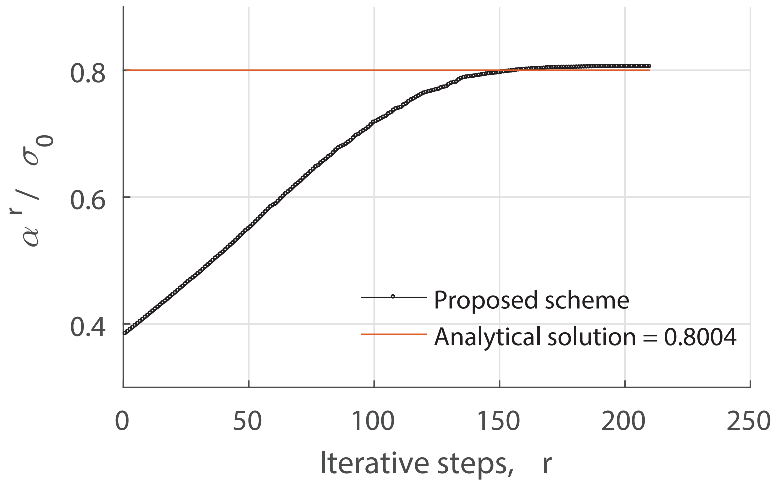

Figure 6.34: Iterative scheme for the thick cylinder with 3632 SBFEs using the sensitivity-based ECM

Table 6.5: The collapse load solutions of the thick cylinder for different SBFE discretizations using the sensitivity-based ECM

No. of subdomains	$\frac{\alpha^{col}}{\sigma_0}$	error%
1243	0.8075	0.89
3632	0.8036	0.40
7832	0.8029	0.31

the yield condition.

6.4.2.2 Thick square plate with central elliptical flaw under axial tension

The second example considers the thick square plate with a thickness of 5 mm and an elliptical flaw at its center, mentioned earlier in section 4.5.2.2. The geometry and loading is shown in Fig. 4.35a. The collapse load solution of this problem $\frac{\alpha^{col}}{\sigma_0}$ is reported as 0.798. Due to its symmetry in all axes, only a quarter of the structure was modeled using SBFEs. The model was automatically constructed based on the geometry of the STL format of the CAD model, and shown in Fig. 4.35b. In total, 1098 subdomains, 1885 nodes, 5655 DOFs, and 1098 integration points were utilized.

The proposed sensitivity-based ECM was conducted on the SBFE model and the load multipliers were monotonically increased and converged. The normalized collapse load solution was obtained as $\frac{\alpha^{col}}{\sigma_0} = 0.8746$, which is some 9.61% higher than the reported collapse load solution. The iterative scheme for the proposed

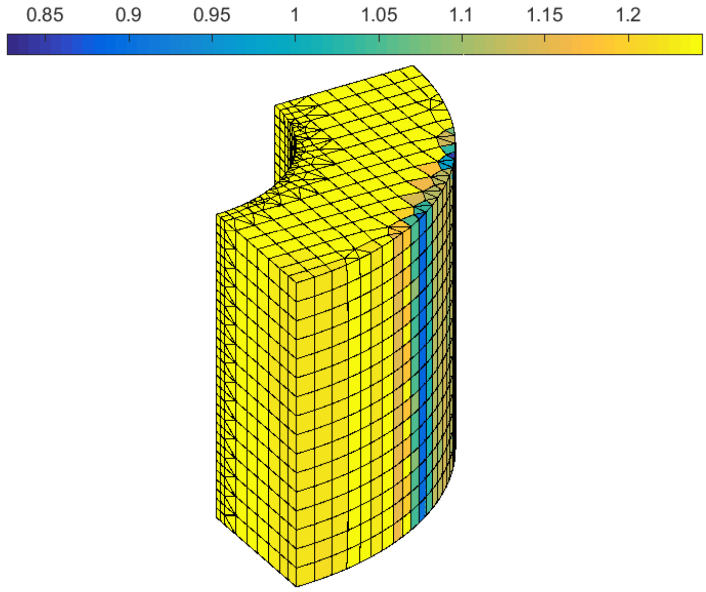

(a)

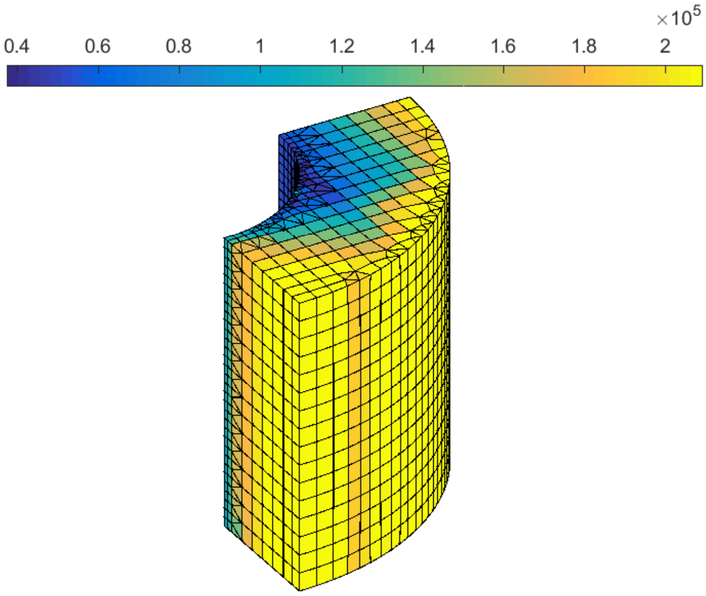

(b)

Figure 6.35: The von Mises stress and elastic modulus distributions for the thick cylinder with 3632 SBFEs using the sensitivity-based ECM (a) stress distribution (b) elastic modulus distribution

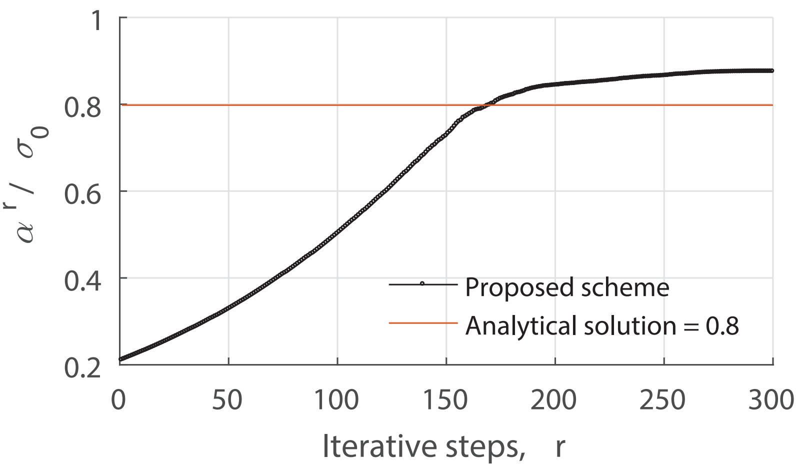

Figure 6.36: Iterative scheme for the thick square plate with central elliptical flaw using 1098 SBFEs and the sensitivity-based ECM

Table 6.6: The collapse load solutions of the thick square plate with central elliptical flaw for different SBFE discretizations using the sensitivity-based ECM

No. of subdomains	$\frac{\alpha^{\mathrm{col}}}{\sigma_0}$	difference%
188	0.9036	13.23
1098	0.8747	9.61
7505	0.8434	5.69

method is shown in Fig. 6.36, where the oscillations in Fig. 4.36 are removed. The corresponding von Mises stress and elastic moduli distributions are also derived for the collapse load solution and are shown in Fig. 6.37.

The variation of the collapse load solutions with respect to the number of subdomains was also derived by considering three discretizations. Only three different refinement was used, as the high imposed computational costs prevented the scheme to be implemented on finer discretizations. The collapse load solutions are provided in Table (6.6), where the differences between the reported solution and the obtained results are also given. As seen, the collapse load solutions are reduced by increasing the number of subdomains. The curve fitting process is not implemented on the obtained data, due to the lack of sufficient results.

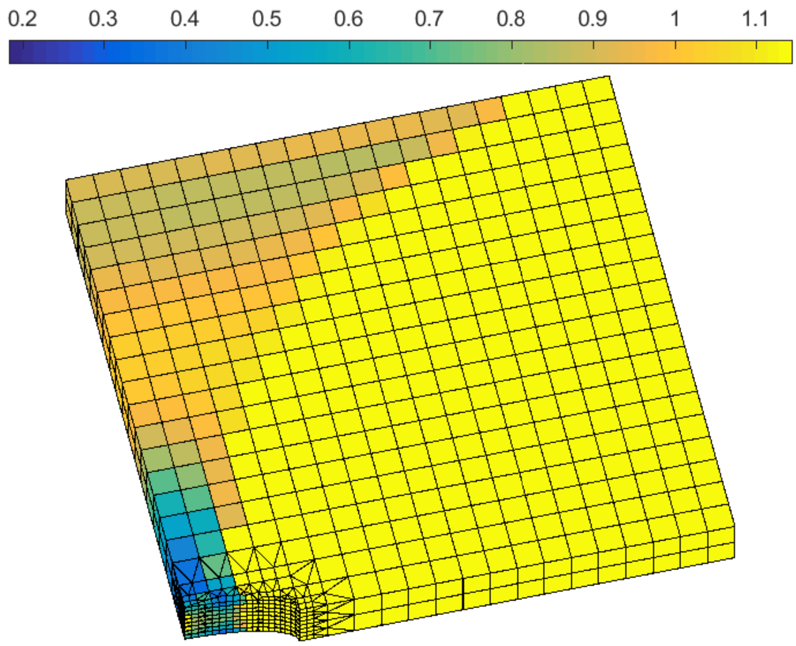

(a)

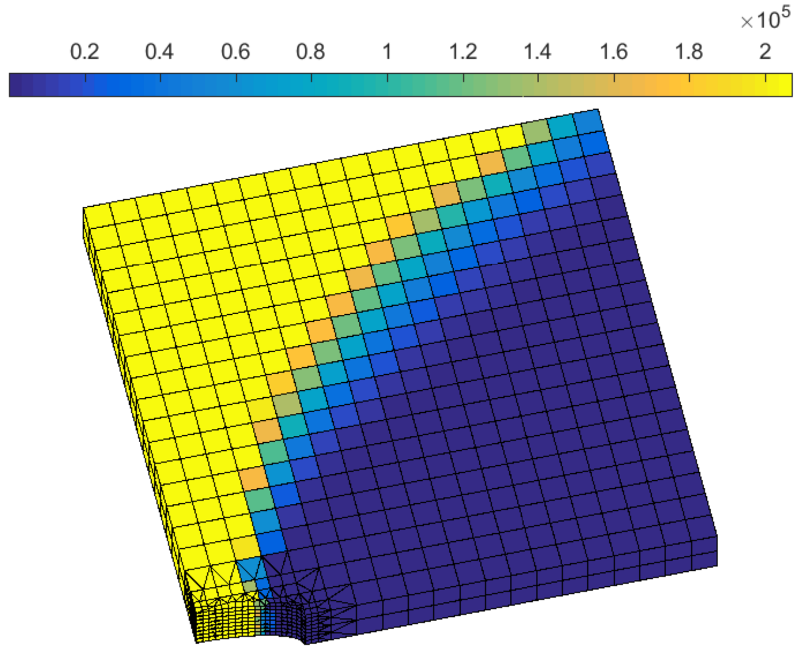

(b)

Figure 6.37: The von Mises stress and elastic modulus distributions for the thick square plate with central elliptical flaw using 1098 SBFEs and the sensitivity-based ECM (a) stress distribution (b) elastic modulus distribution

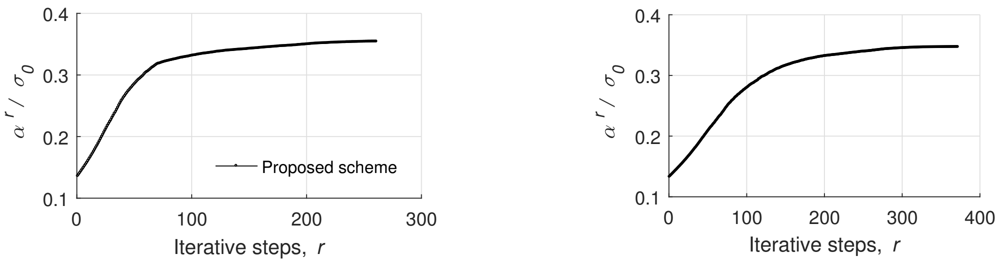

(a) (b)

Figure 6.38: Iterative scheme for the defected pipeline using SBFEM and sensitivity-based ECM (a) case a (b) case b

6.4.2.3 Defected pipeline

The third 3D example is the defected pipeline employed in section 3.5.2.3 . The geometry and loading is presented in Fig. 3.35. Two SBFE models were automatically generated to show the performance of the proposed method on this problem; case a consisting of 2216 subdomains, 3437 nodes, 9603 DOFs and a finer case b with 4734 subdomains, 6653 nodes, 19959 DOFs (Fig. 4.39).

The sensitivity-based ECM was performed on both SBFE models. The load multipliers for both of the discretizations were monotonically increased and converged to $\alpha^{\mathrm{col}} = 70.8126$ in case a and $\alpha^{\mathrm{col}} = 68.9292$ in case b. The iterative plots for both cases are shown in Fig.6.38. The proposed approach provided good accuracy of the collapse load results, as the solutions computed agree well with the reference values reported from various numerical algorithms, namely $\alpha^{\mathrm{col}}_{ref} = 64.05$ using the incremental method [92], $\alpha^{\mathrm{col}}_{ref} = 67.13$ using the kinematic method [86], and $\alpha^{\mathrm{col}}_{ref} = 63.42$ using the static method [92]. The von Mises stress and elastic moduli distributions corresponding to the collapse load solution for case b is also shown in Fig. 6.39.

6.4.2.4 The leg of a chair

To show the advantages of the SBFEM in automatic polyhedral mesh generation, in this example, the ductile leg of a chair under uniform surface load, discussed in section 4.5.2.4, is considered. The geometry is shown in Fig. 4.43a. Fig. 4.43b shows

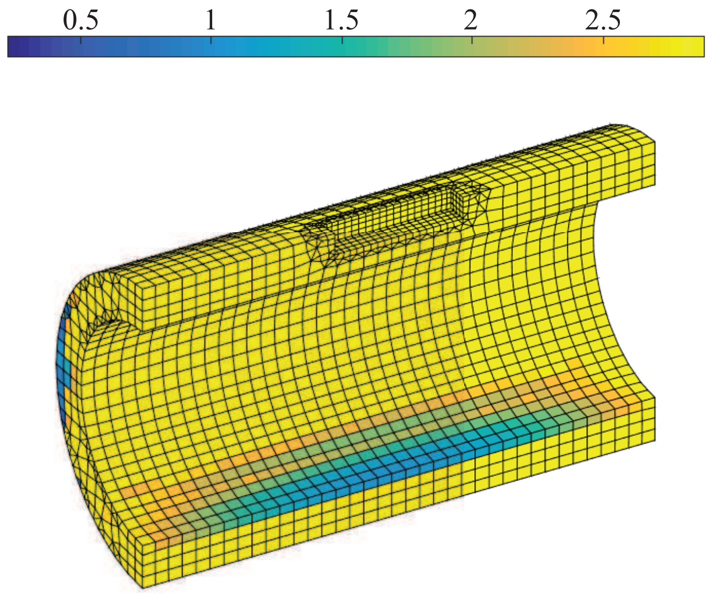

(a)

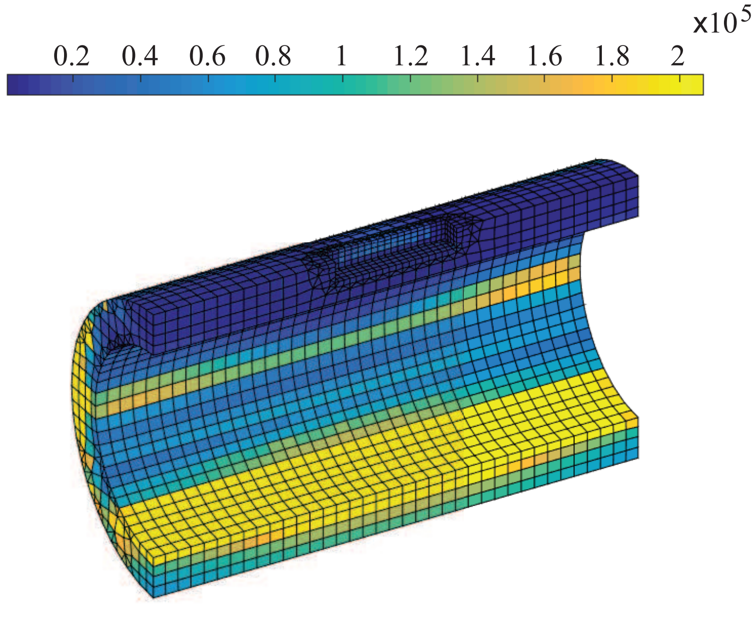

(b)

Figure 6.39: The von Mises stress and elastic modulus distributions for the defected pipeline using 4734 SBFEs and the sensitivity-based ECM (a) stress distribution (b) elastic modulus distribution

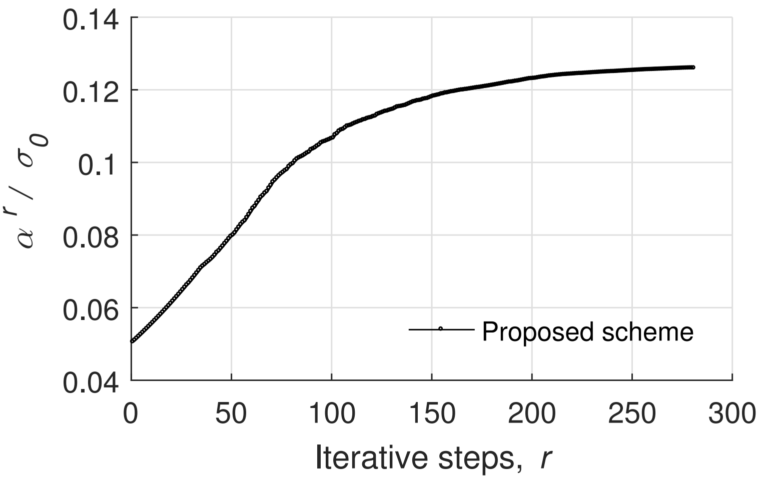

Figure 6.40: Iterative scheme for the leg of a chair using the SBFEM and sensitivity-based ECM

the loading and boundary conditions. The von Mises material properties utilized were $E = 207$ GPa, and $\sigma_0 = 200$ MPa. The mesh generation was automatically conducted out of the STL file as per section 4.3.2. The final mesh contains 2730 subdomains, 4072 nodes, 12216 DOFs, and 2730 integration points.

The sensitivity-based ECM was performed on the structure and the iterative scheme is given in Fig. 6.40. As illustrated, the normalized load multipliers are monotonically increased and converged to the normalized collapse load of $\frac{\alpha^{\mathrm{col}}}{\sigma_0} = 0.1259$. The associated von Mises stress and elastic modulus distributions at the collapse load are shown in Fig. 6.41.

6.4.2.5 The bottle cap

The last example involves a ductile bottle cap to show the advantage of the proposed method in the automatic collapse load determination of structures with complex geometries. In the first part, SBFEM in combination with the octree scheme is used for the automatic mesh generation of this complex geometry. In the next part, the produced mesh is employed in the sensitivity-based ECM for the automatic collapse load determination.

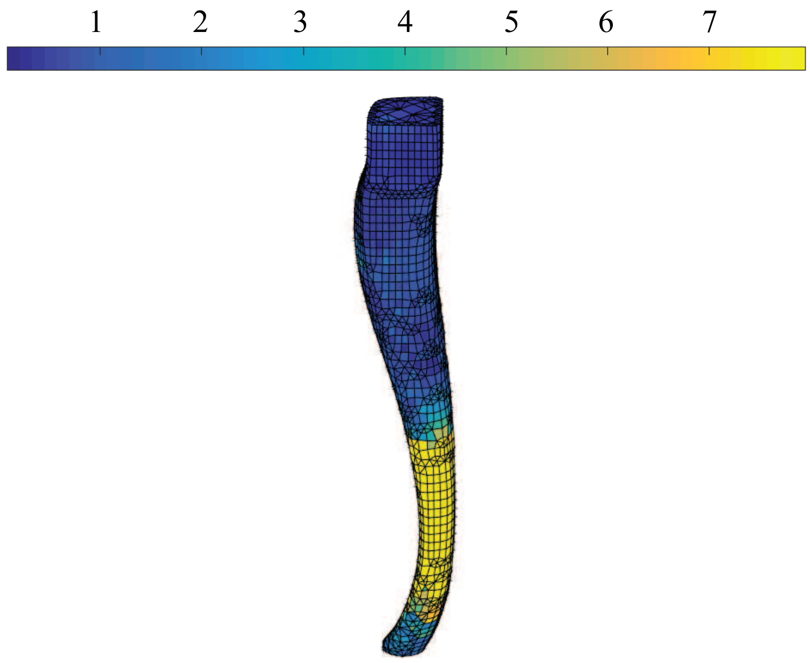

(a)

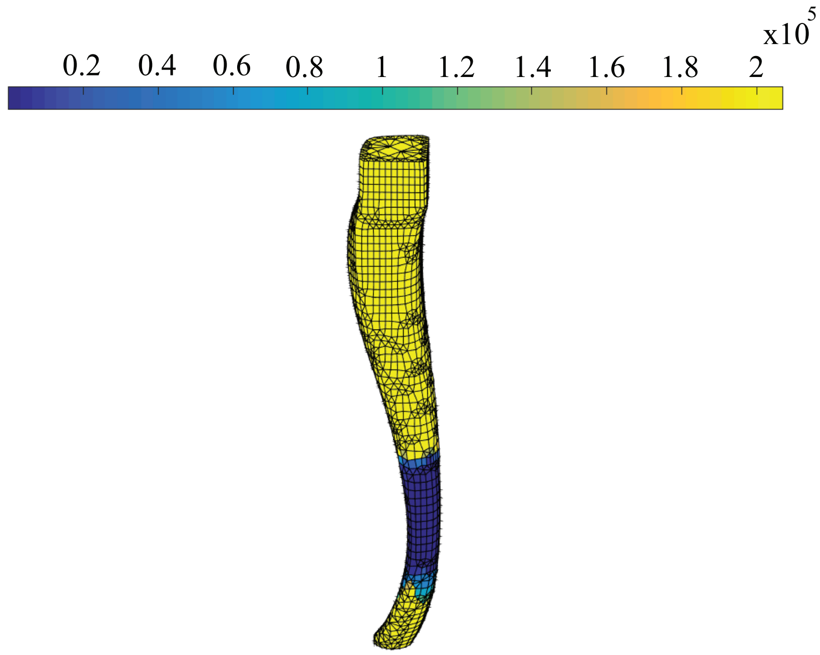

(b)

Figure 6.41: Equivalent stress and elastic modulus distributions of the leg of a chair using the SBFEM and sensitivity-based ECM (a) stress distribution (b) elastic modulus distribution

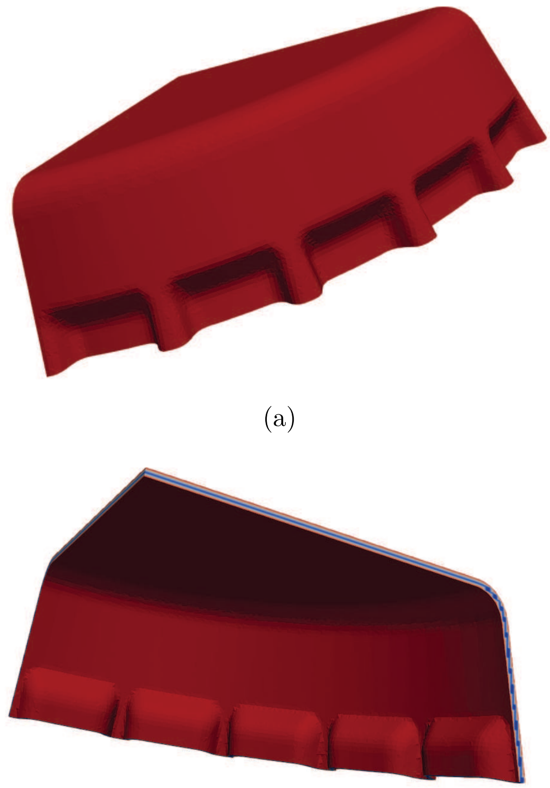

(a)

(b)

Figure 6.42: The surface model of a quarter of a bottle cap in STL format (a) view 1 (b) view 2

Due to the symmetric nature of the problem only a quarter of the cap is considered. Fig. 6.42 shows the surface models of this quarter in STL format from two different views. The loading and boundary conditions in the direction of loading are illustrated in Fig. 6.43. The cap is subjected to a uniform pressure, where it is assumed that the pressure is only applied on the upper part of the cap. The upper parts of the teeth (shown in purple triangles) are fixed in the direction of the pressure to resist it. The von Mises material properties were taken as $E = 207$ GPa, and $\sigma_0 = 294$ MPa.

The construction of an accurate mesh using conventional finite elements requires tedious human efforts and is time-consuming. Here, the mesh was produced automatically using the STL file as an input, and is shown in Fig. 6.44. In total, 27112 subdomains, 41660 nodes, 124980 DOFs were used. The modified elastic compensation method was performed on the produced mesh. The iterations were

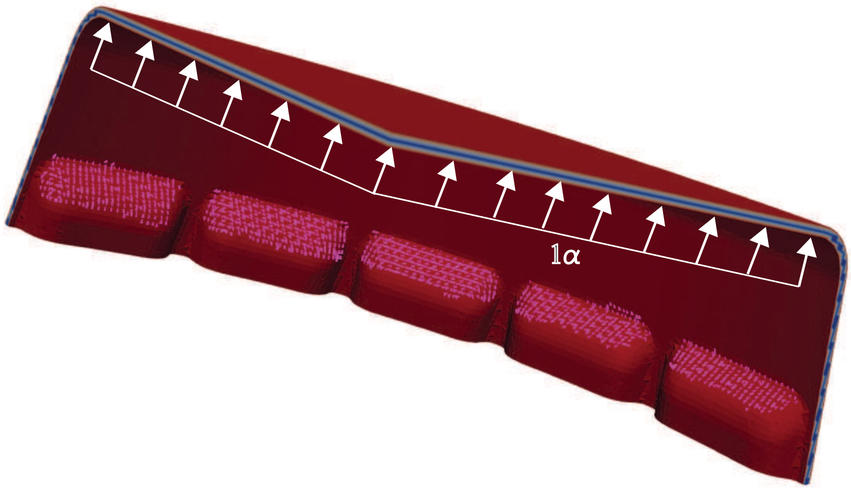

Figure 6.43: A quarter of a bottle cap - loading and boundary conditions in the direction of loading

continued until the convergence was met on the load multipliers. The final normalized collapse load was obtained as $\frac{\alpha^{\text{col}}}{\sigma_0} = 0.0028$. The iterative scheme for the proposed method is given in Fig. 6.45. The corresponding von Mises stress and elastic moduli distributions for the collapse load is also plotted in Fig. 6.46.

6.5 Comparison Between Different Proposed Schemes

To provide the additional information to readers to justify the technique of their own choice, in this section a full comparison between the different proposed schemes in terms of accuracy, computational time, and number of iterations is conducted. The Prandtl's punch problem is chosen because of two reasons. First, the analytical solution for its collapse load is available. Second, the geometry of this example allows the use of the same DOFs for all the proposed methods. This permits a sound comparison to be done between all the schemes. The proposed schemes are as follows.

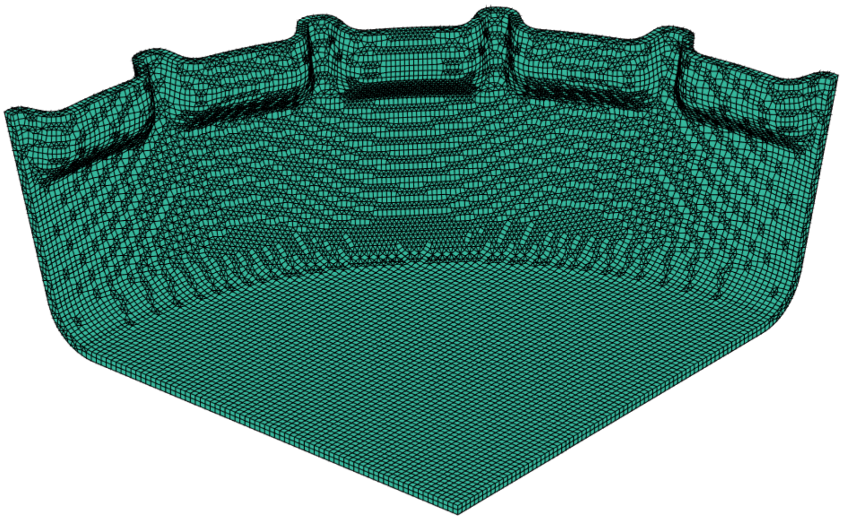

Figure 6.44: SBFE model for a quarter of the bottle cap

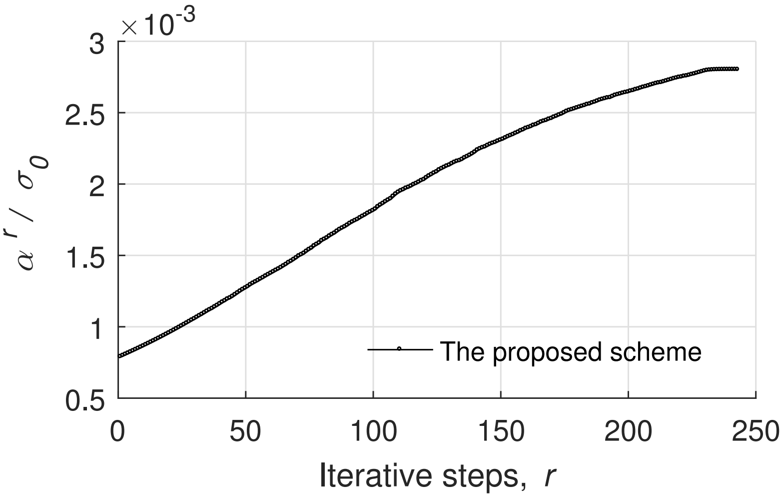

Figure 6.45: Iterative scheme for the quarter of the bottle cap using the SBFEM and sensitivity-based ECM

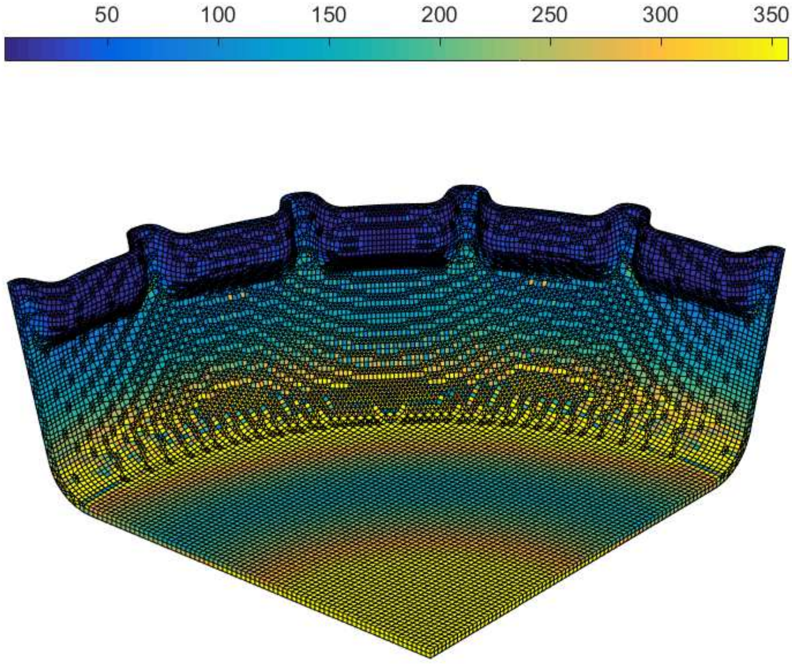

(a)

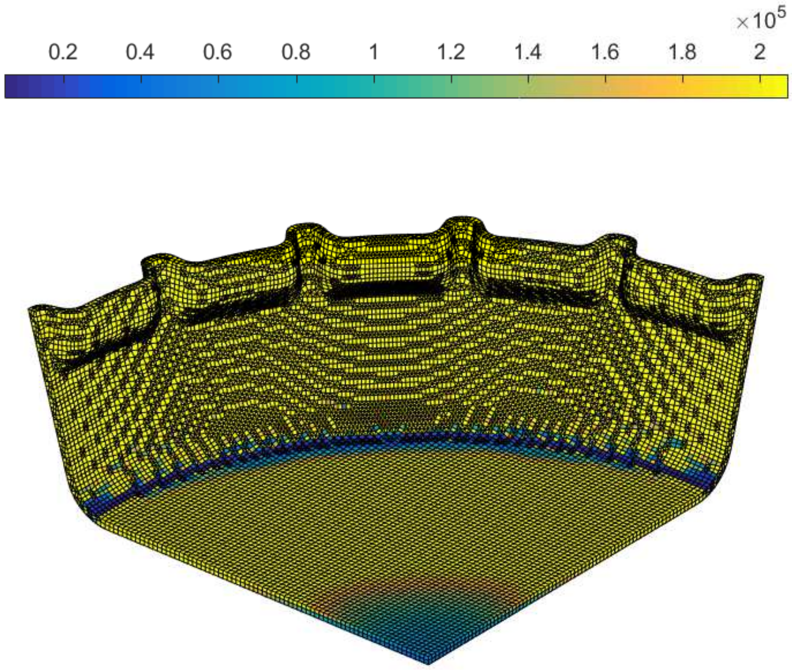

(b)

Figure 6.46: Equivalent stress and elastic modulus distributions for the quarter of the bottle cap using the SBFEM and sensitivity-based ECM (a) stress distribution (b) elastic modulus distribution

(i) The MECM for collapse load determination of structures using finite element method proposed in chapter 3 (MECM+FEM)

(ii) The MECM for collapse load determination of structures using the scaled boundary finite element method proposed in chapter 4 (MECM+SBFEM)

(iii) The sensitivity-based ECM for the collapse load determination of structures using the finite element method proposed in chapter 5 (sensitivity-based ECM+FEM)

(iv) The sensitivity-based ECM for the collapse load determination of structures using the scaled boundary finite element method proposed in chapter 6 (sensitivity-based ECM+SBFEM)

(v) The adaptive sensitivity-based ECM for the collapse load determination of structures using the scaled boundary finite element method proposed in chapter 6 (adaptive sensitivity-based ECM+SBFEM)

It should be noticed that the main advantage of using the SBFEM, which is the convenient and automatic mesh generation, is not considered in this section and the focus is on the analysis part. However, it should be emphasized that the main purpose of using the SBFEM was the ease and automation in mesh generation. For some examples, the generation of a sound and robust mesh in the FEM is highly time-consuming (i.e. the bottle cap in section 6.4.2.5) and might be even impossible.

The final normalized collapse loads of the structure captured by each of the methods are shown in Fig. 6.47 for a range of mesh sizes. As seen, for all the methods, the normalized collapse loads are decreased by increasing the number of elements/sumdomains. For this example, the accuracy level for (iv) and (v) are less compared to the other methods. This is due to the fact that for decreasing the computational time of these schemes, the equivalent stresses are only computed in the scaling center of the subdoamins, whereas for the other methods, the averaged equivalent stresses from stresses obtained at the integration points are used. It should be noticed that if sufficient number of elements/subdomains is used, the accuracy level for all the proposed methods are roughly the same.

Another important note is the fact that although all methods for this example

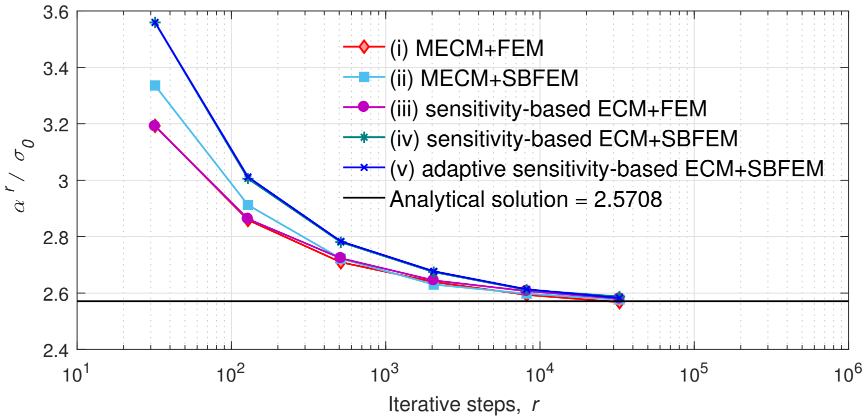

Figure 6.47: Variation of the collapse load multipliers for the Prandtl's punch problem using different proposed schemes for a range of mesh sizes

provided sufficient accuracy, the key merit of the sensitivity-based schemes over the MECMs is its stability and robustness as stated before in chapters 5 and 6. The results obtained by sensitivity-based schemes are based on the convergence on the load multipliers while in the MECMs the results are obtained after a specified number of iterations (300 in this case) and might not necessarily be of sufficient accuracy for other examples.

To provide an idea of the computational efforts for the user in different schemes, the number of iterations and computational time for this example are reported. It should be considered that the computational time for the sensitivity-based ECMs highly depends on the number of elements in the active set (undergoing yielding) as discussed in section 5.3.3. Therefore, the computational time for other examples might be quite different from what is reported here and should be taken into account during the interpretation of the results.

Table 6.7 shows the computational effort for all the five proposed schemes in terms of the number of iterations, where NE and NS indicate the number of elements and number of subdomains respectively. The number of iterations in the MECM is input by the user and in this thesis is taken as 300. The number of iterations for the sensitivity based ECM depends on the convergence tolerance. It is generally seen that as the number of elements/subdomains increases, the sensitivity based ECMs

Table 6.7: Required number of iterations for different proposed schemes

NE/NS	NE/NS	No. of iterations				
uniform	adaptive	i	ii	iii	iv	v
32	32	300	300	153	224	224
128	101	300	300	203	216	440
512	308	300	300	257	277	719
2048	887	300	300	269	404	1127
8192	2783	300	300	362	315	1447
32768	9323	300	300	373	321	1918

require more number of iterations. The number of iterations reported here for the adaptive scheme indicates the accumulated iterations for all the meshes generated adaptively, and therefore more than the iterations required for the corresponding uniform meshes as expected. However, it should be noticed that the main advantage of the adaptive scheme its more efficiency as discussed in the next paragraph.

The computational time spent for the analysis part of all the proposed schemes in this thesis is tabulated in Table 6.8. As evident, the proposed sensitivity-based ECM generally induces more time on the scheme, compared to the original MECM in both FEM and SBFEM. As discussed before in section 5.3.3, this is mainly due to the time spent on the construction of sensitivity and Hessian matrices. Additionally, the difference in time between the MECMs and the proposed sensitivity-based ECMs is increased as the number of elements/subdomains increases. For example, the computational time for both the MECM in case (ii) and the sensitivity-based ECM in case (iv) is similar when 32 subdomains are utilized. However, the consumed time in (iv) when 32768 subdomains are used is almost 38 times more than the corresponding MECM in (ii) on the same mesh. In comparison of FEM and SBFEM schemes for uniform meshes, no significant difference is seen, and the minor differences between these two methods ((ii) compared to (i) and (iv) compared to (v)) arise from programming the codes in MATLAB.

Another interesting point is the time consumed in the normal uniform refinement and the adaptive refinement when sensitivity based ECM is used with the SBFEM (i.e. (iv) and (v) respectively). Although the adaptive scheme requires more number

Table 6.8: Consumed computational times for different proposed schemes

NE/NS	NS	computational time (sec.)				
uniform	adaptive	i	ii	iii	iv	v
32	32	2.4	2.9	2.07	2.34	2.34
128	101	5.82	7.05	6.35	5.31	5.8
512	308	18.53	22.71	41.09	32.01	24.08
2048	887	80.26	101.65	436.92	353.06	201.47
8192	2783	383.64	475.13	6531.82	5441.2	2376.2
32768	9323	2137.75	2641.32	105201	82772	47597

of iterations (Table 6.7) for providing almost the same level of accuracy (Fig. 6.47), it requires less computational time and resources (NS); for instance, the computational time for almost the same level of accuracy in collapse load when uniform mesh with 8192 subdomains is employed, is almost 60% less in the corresponding adaptive scheme. Additionally, the adaptive scheme only requires 2783 subdomains for almost the same solution and therefore computationally advantageous in terms of consumed computational resources.

6.6 Conclusion and Remarks

In this chapter, the sensitivity-based ECM proposed in chapter 5 was extended to be implemented with the SBFEM. This allowed some advantages of SBFEM, such as the automatic mesh construction and the adaptive mesh generation, to be used with the proposed sensitivity-based ECM. Firstly, the implementation of the automatic mesh generator, allowed the SBFE meshes to be constructed from an in-plane solid (in 2D problems) or of a solid 3D CAD (STL) model (in 3D problems). This effectively reduced the burden of the fine mesh generation often needed for the sensitivity-based ECM. Secondly, an adaptive sensitivity-based ECM for 2D problems was proposed, which reduces the size of the problem (in comparison to the use of uniform refinements) and led to a gain in computational time and resources required for the sensitivity-based ECM. The adaptive refinement was performed through the use of the quadtree scheme and the ability of the SBFEM in handling the hanging nodes. Initially, a uniform coarse mesh is produced using polygonal SBFEs. The sensitivity-based ECM is performed on this mesh and the initial collapse load solution is obtained. The yielded subdomains are then identified and efficiently refined into smaller subdomains. The generated hanging nodes are considered as regular corner nodes in polygonal SBFEs. This process is repeated recursively until the convergence on the limit load is achieved. This scheme allowed almost the same level of accuracy to be obtained more efficiently.

The use of automatic mesh generators and the adaptive scheme were verified by some numerical examples. The results showed the robustness and efficiency of the proposed schemes.

Chapter 7

CONCLUSIONS AND RECOMMENDATIONS FOR FUTURE STUDIES

7.1 Concluding Remarks

In this thesis a comprehensive study on the ECM by emphasis on its updated and modified version, the MECM, for the collapse load determination of engineering structures was performed. In particular, the study was motivated by two main aims; (1) to develop a new and robust scheme based on the ECM to remove the oscillations happening in the limit load curve, which leads to the convergence directly on the limit load, and (2) to remove the mesh-related challenges to solve the problem more efficiently and conveniently. This leads to a simple, robust and automatic scheme for the collapse load determination, which minimizes the need for the user interference and therefore mostly reduces the errors which might be caused by the user. The key contributions and conclusions are summarized as follows.

(a) The finite element implementations of the MECM was described in details for a range of 2D and 3D structures. The importance of using the (nearly) incompressible condition for accurate collapse load determinations was emphasized. The value of $\nu = 0.499$ was shown to be close enough to 0.5 to satisfy this condition. It was shown that the popular widely-used low order displacement-based finite elements can be used along with the MECM when the selective integration scheme is applied to allow justification of element stiffness matrices under nearly incompressible condition. The important role of the mesh density in the method was investigated and it is concluded that all of the estimated collapse load results tend to converge to the lower bound limits when the sufficient number of structural discretization has been attained.

(b) The MECM was extended to the SBFEM to use its advantages in automatic mesh construction. The use of SBFEM along with the quadtree or octree schemes allowed the SBFE discretizations to be automatically constructed from an in-plane solid (in 2D problems) or of a solid 3D CAD model (in 3D problems). Such technique automatically handles structures with complex geometries (e.g. curved boundaries, holes, etc.), as compared to standard finite element methods. This effectively reduced the burden of fine mesh generation required for the MECM. Additionally, it is shown that the SBFEs do not suffer from the required nearly incompressible condition when Poisson's ratios of 0.499 was used. In contrast to the low-order finite elements, this is achieved directly and without the specific treatment (i.e. use of selective or reduced integration methods) for subdomain stiffness matrices. A number of numerical examples, ranging from benchmark tests, 2D and 3D solids, were studied to illustrate the performance and accuracy of the proposed scheme.

(c) The main shortcoming of the ECM or MECM was described which is the convergence criterion. The convergence criterion in these methods is the number of the iterations input by the user, which could be insufficient for a structure. The reason of using the number of iterations as the convergence criterion is the multiple oscillations with unknown amplitudes happening in the limit load curve. The reason of these oscillation was investigated as the stress overshooting phenomenon happening during the iterative scheme. A robust and novel sensitivity-based ECM was then introduced which prevents the stress overshooting phenomenon by considering the contribution of all elements, and therefore is oscillation-free. This allowed the convergence to be defined directly on the limit load of the structure, and therefore, the need for the user interference and its judgment is eliminated.

(d) The proposed sensitivity-based ECM was extended to be used with the SBFEM and quadtree/octree schemes to use their advantages in mesh generation and to reduce the burden of mesh generation. This allowed the automatic process of the collapse load determination of structures in both mesh generation part and analysis part. This convenient automatic scheme minimizes the user interference and its associated errors.

(e) The proposed sensitivity-based ECM may be computationally demanding when uniform (or approximately uniform) refined meshes are used. Therefore, an automatic adaptive sensitivity-base ECM was introduced, which generates adaptive non-uniform meshes automatically based on the results of the sensitivity-based ECM at each step. This guarantees the required level of accuracy using less number of elements (in comparison to its equivalent uniform mesh), and therefore demands less computational resources.

(f) The efficiency of the proposed techniques in the analysis part was investigated using the well-known Prandtl's punch problem. It reveals that the computational time for the proposed sensitivity-based schemes is more in comparison to the MECMs under both FEM and SBFEM frameworks. Although this difference is negligible when coarse meshes are used, it becomes noticeable as the number of elements/subdomains increases. The proposed adaptive scheme is found to be to computationally efficient (in terms of time and resources) compared to the uniform mesh, and hence superior.

(g) A number of numerical examples, in 2D and 3D spaces, have been provided throughout the thesis to illustrate the performance of all the proposed schemes and to show the validity of the approaches.

7.2 Recommendation for Future Studies

The following suggestions are recommended for further research works on this topic.

(a) Considering the fact that the proposed sensitivity-based ECM only involves a series of linear elastic analysis, its finite element implementation can be extended to be integrated with the available computer software which are superior and convenient in elastic analysis, such as ANSYS and ABAQUS. This allows an extensive library of element types, pre-processors and post-processors, defined in these software, to be directly used for the collapse load determination of ductile structures.

(b) The proposed extensions of the MECM and the sensitivity-based ECM to the SBFEM allow the use of some other advantages of it such as the efficient and automatic image-based stress analysis for 2D [132] or 3D [112] structures. This leads to an attracting efficient way to perform virtual testing of sufficiently ductile materials and structures for their collapse load determination.

(c) The computations of the sensitivity and Hessian matrices as parts of the required computation for the proposed sensitivity-based ECM induces more time on the scheme, compared to the original ECM/MECM. It is reasonable as any non-local techniques will require such extra computations for better convergence and stability/accuracy. However instead of taking into account the effects of all "yielded" elements in the whole structure, it seems the same procedure can be applied to yielded elements in a local neighborhood of the considered element. Then there will be several small operations like involved. This process could be less "non-local" while still not the strictly local one in the original ECM/MECM. This approach could be less computationally expensive, as instead of solving a large matrix equation like Eq. (5.13) and (5.29) for the whole structure, inverting several much smaller ones separately would help reduce the computational time. However, the level of accuracy and an appropriate scheme for defining the neighbor elements should be studied.

(d) This thesis only investigated the proposed method as a basic standard scheme for the collapse load determination, as other special effects such as hardening, geometric, temperature, etc. or the possibility of the approximation of the displacements for a better illustration of the failure pattern were not taken into account. It would be worthwhile to include such effects/possibilities in the sensitivity-based ECM.

REFERENCES

[1] R. Seshadri, C. P. Fernando, Limit load of mechanical components and structures using the GLOSS r-node method, in: ASME Pressure Vessels and Piping Conference, American Society of Mechanical Engineering, ASME, San Diego, California, 1991, pp. 125 –134.

[2] R. Seshadri, S. Mangalaramanan, Lower bound limit loads using variational concepts: the m_α-method, International Journal of Pressure Vessels and Piping Volume 71 (1997) 93–106.

[3] E. Ooi, H. Man, S. Natarajan, C. Song, Adaptation of quadtree meshes in the scaled boundary finite element method for crack propagation modelling, Engineering Fracture Mechanics 144 (2015) 101–117.

[4] A. A. Saputra, A scaled boundary polyhedral element for three-dimensional analyses, Ph.D. thesis, School of Civil and Environmental Engineering, University of New South Wales, Sydney, Ausralia (2015).

[5] Y. Liu, A. A. Saputra, J. Wang, F. Tin-Loi, C. Song, Automatic polyhedral mesh generation and scaled boundary finite element analysis of STL models, Computer Methods in Applied Mechanics and Engineering 313 (2017) 106 – 132.

[6] J. C. McCormac, Structural steel design, Pearson Prentice Hall, 2008.

[7] D. Nethercot, Limit states design of structural steelwork, 3rd Edition, CRC Press, 2001.

[8] G. Maier, D. E. Grierson, M. J. Best, Mathematical programming methods for deformation analysis at plastic collapse, Computers & Structures 7 (1977) 599–612.

[9] S. W. Sloan, Lower bound limit analysis using finite elements and linear programming, International Journal for Numerical and Analytical Methods in Geomechanics 12 (1988) 61–77.

[10] G.-l. Jiang, Non-linear finite element formulation of kinematic limit analysis, International Journal for Numerical Methods in Engineering 38 (1995) 2775–2807.

[11] D. Mackenzie, J. Shi, J. Boyle, Finite element modelling for limit analysis by the elastic compensation method, Computers & Structures 51 (1994) 403–410.

[12] D. Mackenzie, J. T. Boyle, R. Hamilton, The elastic compensation method for limit and shakedown analysis: a review, The Journal of Strain Analysis for Engineering Design 35 (2000) 171–188.

[13] D. Mackenzie, J. T. Boyle, A method of estimating limit loads by iterative elastic analysis. I-simple examples, International Journal of Pressure Vessels and Piping 53 (1993) 77–95.

[14] R. Hamilton, D. Mackenzie, J. Shi, J. Boyle, Simplified lower bound limit analysis of pressurised cylinder/cylinder intersections using generalised yield criteria, International Journal of Pressure Vessels and Piping 67 (1996) 219–226.

[15] A. Ponter, K. Carter, Shakedown state simulation techniques based on linear elastic solutions, Computer Methods in Applied Mechanics and Engineering 140 (1997) 259–279.

[16] P. Yang, Y. Liu, Y. Ohtake, H. Yuan, Z. Cen, Limit analysis based on a modified elastic compensation method for nozzle-to-cylinder junctions, International Journal of Pressure Vessels and Piping 82 (10) (2005) 770–776.

[17] L. Chen, Y. Liu, P. Yang, Z. Cen, Limit analysis of structures containing flaws based on a modified elastic compensation method, European Journal of Mechanics - A/Solids 27 (2008) 195–209.

[18] W. D. Reinhardt, R. Seshadri, Limit load bounds for the m_α multiplier, Journal of Pressure Vessel Technology 125 (2003) 11–18.

[19] J. P. Wolf, C. Song, The scaled boundary finite-element method - a primer: derivations, Computers & Structures 78 (2000) 191–210.

[20] C. Song, J. P. Wolf, The scaled boundary finite-element method - a primer: solution procedures, Computers & Structures 78 (2000) 211–225.

[21] E. T. Ooi, C. Song, F. Tin-loi, Z. Yang, Polygon scaled boundary finite elements for crack propagation modelling, International Journal for Numerical Methods in Engineering 91 (2012) 319–342.

[22] E. T. Ooi, M. Shi, C. Song, F. Tin-Loi, Z. Yang, Dynamic crack propagation simulation with scaled boundary polygon elements and automatic remeshing technique, Engineering Fracture Mechanics 106 (2013) 1–21.

[23] J. B. Martin, Plasticity fundamentals and general results, MIT Press, 1975.

[24] S. Kaliszky, Plasticity: Theory and engineering applications, Elsevier, 1989.

[25] M. B. Wong, Plastic Analysis and Design of Steel Structures, Butterworth-Heinemann, 2008.

[26] En 13445-3 : Unfired pressure vessels - part 3: Design.

[27] R. E. Smallman, R. J. Bishop, Modern Physical Metallurgy and Materials Engineering, Elsevier, 1999.

[28] R. D. Cook, Concepts and applications of finite element analysis: a treatment of the finite element method as used for the analysis of displacement, strain, and stress, John Wiley & Sons, 1974.

[29] M. A. Crisfield, Non-Linear Finite Element Analysis of Solids and Structures: Essential, John Wiley & Sons, 1991.

[30] M. A. Crisfield, Non-Linear Finite Element Analysis of Solids and Structures, Volume 2, Advanced Topics, John Wiley & Sons, 1997.

[31] R. Borst, M. A. Crisfield, J. J. C. Remmers, C. V. Verhoosel, Nonlinear Finite Element Analysis of Solids and Structures, 2nd Edition, John Wiley & Sons, 2012.

[32] J. Kamenjarzh, Limit Analysis of Solids and Structures, Boca Raton: CRC Press, 1996.

[33] G. Maier, A matrix structural theory of piecewise linear elastoplasticity with interacting yield planes, Meccanica 5 (1970) 54–66.

[34] G. Cocchetti, G. Maier, Elastic-plastic and limit-state analyses of frames with softening plastic-hinge models by mathematical programming, International Journal of Solids and Structures 40 (2003) 7219–7244.

[35] S. Tangaramvong, F. Tin-loi, Extended limit analysis of strain softening frames involving 2nd-order geometric nonlinearity and limited ductility, CMES-Computer Modeling in Engineering and Sciences 42 (2009) 217–256.

[36] S. Tangaramvong, F. Tin-Loi, Collapse load evaluation of structures with frictional contact supports under combined stresses, Computers & Structures 89 (2011) 1050–1058.

[37] S. Tangaramvong, F. Tin-Loi, An FE-MPEC approach for limit load evaluation in the presence of contact and displacement constraints, International Journal of Solids and Structures 49 (2012) 1753–1763.

[38] G. Bolzon, Complementarity problems in structural engineering: an overview, Archives of Computational Methods in Engineering (2015) 1–14.

[39] S. Tangaramvong, F. Tin-Loi, T. Senjuntichai, An MPEC approach for the critical post-collapse behavior of rigid-plastic structures, International Journal of Solids and Structures 48 (2011) 2732–2742.

[40] Z. Luo, J. Pang, D. Ralph, Mathematicalprograms with equilibrium constraints, Cambridge University Press, 1996.

[41] M. Gilbert, C. Casapulla, H. Ahmed, Limit analysis of masonry block structures with non-associative frictional joints using linear programming. Computers & Structures, Computers & Structures 84 (2006) 873–887.

[42] Y. Kanno, J. A. C. Martins, Arc-length method for frictional contact problems using mathematical programming with complementarity constraints, Journal of Optimization Theory and Applications 131 (2006) 89–113.

[43] Y. Kanno, J. A. C. Martins, A. Pinto da Costa, Three-dimensional quasi-static frictional contact by using second-order cone linear complementarity problem, International Journal for Numerical Methods in Engineering 65 (2006) 62–83.

[44] G. L. Jones, A. K. Dhalla, Classification of clamp-induced stresses in thin-walled pipe, in: Proceedings of the ASME Pressure Vessel and Piping Conference, no. April, American Society of Mechanical Engineers, Denver, 1981, pp. 17–23.

[45] A. K. Dhalla, A simplified procedure to classify stresses for elevated temperature service, in: ASME Pressure Vessels and Piping Conference, 1987, pp. 177–188.

[46] D. L. Marriott, Evaluation of deformation or load control of stresses under inelastic condition using elastic finite element stress analysis, in: ASME Pressure

Vessels and Piping Conference, American Society of Mechanical Engineering, ASME, Pittsburgh, Pennsylvania, 1988, pp. 3–9.

[47] R. Seshadri, Classification of stresses in pressure components using the GLOSS diagram, in: ASME Pressure Vessels and Piping Conference, American Society of Mechanical Engineering, ASME, Honolulu, Hawaii, 1990, pp. 115–123.

[48] R. Seshadri, Generalized local stress strain (gloss) analysis. theory and applications, Journal of Pressure Vessel Technology 113 (1991) 219–227.

[49] R. Seshadri, S. Babu, Extended gloss method for determining inelastic effects in mechanical components and structures: Isotropic materials, Journal of Pressure Vessel Technology 114 (2000) 201–208.

[50] S. Babu, P. K. Iyer, Inelastic analysis of components using a modulus adjustment scheme, Journal of Pressure Vessel Technology 120 (1998) 1–5.

[51] S. Babu, P. K. Iyer, A robust method for inelastic analysis of components made of anisotropic material, Journal of Pressure Vessel Technology 121 (1999) 154–159.

[52] D. Mackenzie, J. T. Boyle, Simple method of estimating shakedown loads for complex structures 265 (1993) 89–94.

[53] D. Mackenzie, J. T. Boyle, R. Hamilton, J. Shi, Secondary stress and shakedown in axisymmetric nozzles 313 (1995) 409–413.

[54] A. R. Ponter, M. Engelhardt, Shakedown limits for a general yield condition: implementation and application for a Von Mises yield condition, European Journal of Mechanics - A/Solids 19 (2000) 423–445.

[55] A. Ponter, H. Chen, A minimum theorem for cyclic load in excess of shakedown, with application to the evaluation of a ratchet limit, European Journal of Mechanics - A/Solids 20 (2001) 539–553.

[56] H. Chen, A. R. Ponter, A method for the evaluation of a ratchet limit and the amplitude of plastic strain for bodies subjected to cyclic loading, European Journal of Mechanics - A/Solids 20 (2001) 555–571.

[57] H. F. Chen, A. R. S. Ponter, Shakedown and limit analyses for 3-D structures using the linear matching method, International Journal of Pressure Vessels and Piping 78 (6) (2001) 443–451.

[58] H. F. Chen, A. R. S. Ponter, The Linear Matching Method for Shakedown and Limit Analyses Applied to Rolling and Sliding Point Contact Problems, Road Materials and Pavement Design 6 (2005) 9–30.

[59] H. Chen, A. R. S. Ponter, A Direct Method on the Evaluation of Ratchet Limit, Journal of Pressure Vessel Technology 132 (2010) 0412021–8.

[60] R. Seshadri, C. P. D. Fernando, Limit loads of mechanical components and structures using the GLOSS R-Node method, Journal of Pressure Vessel Technology 114 (1992) 201–208.

[61] C. A. Schulte, Predicting creep deflections of plastic beams, in: American Society for Testing and Materials, Vol. 60, 1960, pp. 895–904.

[62] D. L. Marriott, F. A. Leckie, Some observations on the deflections of structures during creep, in: Proceedings of the Institution of Mechanical Engineers, Vol. 178, 1964, pp. 115–125.

[63] R. Seshadri, D. Marriott, On relating the reference stress, limit load and the asme stress classification concepts, International Journal of Pressure Vessels and Piping 56 (1993) 387–408.

[64] S. P. Mangalaramanan, R. Seshadri, Minimum weight design of pressure components using r-nodes, Pressure Vessel Technology 119 (1997) 224–231.

[65] S. Mangalaramanan, Conceptual models for understanding the role of the r-nodes in plastic collapse, Pressure Vessel Technology 119 (1997) 374–378.

[66] T. Mura, W. H. Rimawi, S. L. Lee, Extended theorems of limit analysis, Quarterly of Applied Mathematics 23 (1965) 171–179.

[67] C. R. Calladine, D. C. Drucker, Nesting surfaces of constant rate of energy dissipation in creep, Quarterly of Applied Mathematics 20 (1962) 79–84.

[68] J. T. Boyle, The theorem of nesting surfaces in steady creep and its application to generalized models and limit reference stress, Res Mechanica 4 (1982) 275–294.

[69] D. Mackenzie, C. Nadarajah, J. Shi, J. Boyle, Simple bounds on limit loads by elastic finite element analysis, Journal of Pressure Vessel Technology 115 (1993) 27–31.

[70] C. Nadarajah, D. Mackenzie, J. T. Boyle, A method of estimating limit loads by iterative elastic analysis. II - nozzle sphere intersections with internal pressure and radial load, International Journal of Pressure Vessels and Piping 53 (1992) 97–119.

[71] J. Shi, D. Mackenzie, J. T. Boyle, A method of estimating limit loads by iterative elastic analysis. III - torispherical heads under internal pressure, International Journal of Pressure Vessels and Piping 53 (1992) 121–142.

[72] R. Adibi-Asl, I. F. Z. Fanous, R. Seshadri, Elastic modulus adjustment procedures - improved convergence schemes, International Journal of Pressure Vessels and Piping 83 (2006) 154–160.

[73] K. Molski, G. Glinka, A method of elastic-plastic stress and strain calculation at a notch root, Materials Science and Engineering 50 (1981) 93–100.

[74] B. Yu, L. Yang, Elastic modulus reduction method for limit analysis of thin plate and shell structures, Thin-Walled Structures 48 (2010) 291–298.

[75] L. Yang, B. Yu, Y. Qiao, Elastic modulus reduction method for limit load evaluation of frame structures, Acta Mechanica Solida Sinica 22 (2009) 109–115.

[76] A. Capsoni, L. Corradi, A mixed finite element model for plane strain elastic-plastic analysis. part i: formulation and assessment of the overall behaviour., Computer Methods in Applied Mechanics and Engineering 141 (1997) 67–79.

[77] A. Capsoni, L. Corradi, A mixed finite element model for plane strain elastic-plastic analysis Part II. Application to the 4-node bilinear element, Computer Methods in Applied Mechanics and Engineering 141 (1997) 81–93.

[78] A. Capsoni, A mixed finite element model for plane strain limit analysis computations, Communications in numerical methods in engineering 15 (1999) 101–112.

[79] D. Mackenzie, R. Hamilton, J. T. Boyle, Using the ansys apdl macro language to calculate limit loads from elastic finite element analysis, in: Sixth international ANSYS conference, Pittsburgh, Pennsylvania, Vol. 3, 1994, pp. 14.31–14.38.

[80] A. Ponter, K. Carter, Limit state solutions, based upon linear elastic solutions with a spatially varying elastic modulus, Computer Methods in Applied Mechanics and Engineering 140 (1997) 237–258.

[81] A. R. Ponter, P. Fuschi, M. Engelhardt, Limit analysis for a general class of yield conditions, European Journal of Mechanics - A/Solids 19 (3) (2000) 401–421.

[82] D. S. Malkus, T. J. R. Hughes, Mixed finite element methods - reduced and selective integration techniques: A unification of concepts, Computer Methods in Applied Mechanics and Engineering 15 (1978) 63–81.

[83] T. J. R. Hughes, Generalization of selective integration procedures to anisotropic and nonlinear media, International Journal for Numerical Methods in Engineering 15 (1980) 1413–1418.

[84] A. F. Bower, Applied Mechanics of Solids, Taylor & Francis Inc, 2009.

[85] S. W. Sloan, P. W. Kleeman, Upper bound limit analysis using discontinuous velocity fields, Computer Methods in Applied Mechanics and Engineering 127 (1995) 293–314.

[86] M. V. Da Silva, A. N. Antão, A non-linear programming method approach for upper bound limit analysis, International Journal for Numerical Methods in Engineering 72 (2007) 1192–1218.

[87] S. Tangaramvong, F. Tin-Loi, C. Song, A direct complementarity approach for the elastoplastic analysis of plane stress and plane strain structures, International Journal for Numerical Methods in Engineering 90 (2012) 838–866.

[88] J. C. Nagtegaal, D. M. Parks, J. R. Rice, On numerically accurate finite element solutions in the fully plastic range, Computer Methods in Applied Mechanics and Engineering 4 (1974) 153–177.

[89] E. Christiansen, K. D. Andersen, Computation of collapse states with von Mises type yield condition, International Journal for Numerical Methods in Engineering 46 (1999) 1185–1202.

[90] F. Tin-Loi, N. Ngo, Performance of the p-version finite element method for limit analysis, International Journal of Mechanical Sciences 45 (2003) 1149–1166.

[91] A. Mendelson, Plasticity: Theory and applications, MacMilan Company, 1968.

[92] Y. Liu, X. Zhang, Z. Cen, Numerical determination of limit loads for three-dimensional structures using boundary element method, European Journal of Mechanics - A/Solids 23 (1) (2004) 127–138.

[93] D. F. Watson, Computing the n-dimensional delaunay tessellation with application to voronoi polytopes, The Computer Journal 24 (1981) 167–172.

[94] J. Shewchuk, Delaunay refinement mesh generation, Ph.D. thesis, School of Computer Science, Carnegie Mellon University (1997).

[95] R. Löhner, P. Parikh, Generation of three-dimensional unstructured grids by the advancing-front method, International Journal for Numerical Methods in Fluids 8 (1988) 1135–1149.

[96] T. D. Blacker, R. J. Meyers, Seams and wedges in plastering: A 3-d hexahedral mesh generation algorithm, Engineering with Computers 9 (1993) 83–93.

[97] M. O. Freitas, P. A. Wawrzynek, J. B. Cavalcante-Neto, C. A. Vidal, L. F. Martha, A. R. Ingraffea, A distributed-memory parallel technique for two-dimensional mesh generation for arbitrary domains, Advances in Engineering Software 59 (2013) 38 – 52.

[98] X. Liang, M. S. Ebeida, Y. Zhang, Guaranteed-quality all-quadrilateral mesh generation with feature preservation, Computer Methods in Applied Mechanics and Engineering 199 (2010) 2072 – 2083.

[99] F. B. Atalay, S. Ramaswami, D. Xu, Quadrilateral meshes with provable angle bounds, Engineering with Computers 28 (2012) 31–56.

[100] T. Hughes, J. Cottrell, Y. Bazilevs, Isogeometric analysis: Cad, finite elements, nurbs, exact geometry and mesh refinement, Computer Methods in Applied Mechanics and Engineering 194 (2005) 4135 – 4195.

[101] H.-J. Kim, Y.-D. Seo, S.-K. Youn, Isogeometric analysis for trimmed cad surfaces, Computer Methods in Applied Mechanics and Engineering 198 (2009) 2982 – 2995.

[102] Y. Bazilevs, V. Calo, J. Cottrell, J. Evans, T. Hughes, S. Lipton, M. Scott, T. Sederberg, Isogeometric analysis using t-splines, Computer Methods in Applied Mechanics and Engineering 199 (2010) 229 – 263.

[103] J. Cottrell, A. Reali, Y. Bazilevs, T. Hughes, Isogeometric analysis of structural vibrations, Computer Methods in Applied Mechanics and Engineering 195 (2006) 5257 – 5296.

[104] L. De Lorenzis, . Temizer, P. Wriggers, G. Zavarise, A large deformation frictional contact formulation using nurbs-based isogeometric analysis, International Journal for Numerical Methods in Engineering 87 (2011) 1278 – 1300.

[105] Y. Bazilevs, V. M. Calo, Y. Zhang, T. J. R. Hughes, Isogeometric fluid–structure interaction analysis with applications to arterial blood flow, Computational Mechanics 38 (4) (2006) 310–322.

[106] E. Bassoli, A. Gatto, L. Iuliano, M. G. Violante, 3D printing technique applied to rapid casting, Rapid Prototyping Journal 13 (2007) 148–155.

[107] F. Rengier, A. Mehndiratta, H. von Tengg-Kobligk, C. M. Zechmann, R. Unterhinninghofen, H.-U. Kauczor, F. L. Giesel, 3D printing based on imaging data: review of medical applications, International Journal of Computer Assisted Radiology and Surgery 5 (4) (2010) 335–341.

[108] E. Bechet, J.-C. Cuilliere, F. Trochu, Generation of a finite element mesh from stereolithography (stl) files, Computer-Aided Design 34 (2002) 1–17.

[109] D. Wang, O. Hassan, K. Morgan, N. Weatherill, Enhanced remeshing from stl files with applications to surface grid generation, Communications in Numerical Methods in Engineering 23 (2006) 227 – 239.

[110] M. Attene, M. Campen, L. Kobbelt, Polygon mesh repairing: An application perspective, ACM Computing Surveys (CSUR) 45.

[111] G. Legrain, R. Allais, P. Cartraud, On the use of the extended finite element method with quadtree/octree meshes, International Journal for Numerical Methods in Engineering 86 (2011) 717–743.

[112] A. Saputra, H. Talebi, D. Tran, C. Birk, C. Song, Automatic image-based stress analysis by the scaled boundary finite element method, International Journal for Numerical Methods in Engineering 109 (2017) 697–738.

[113] E. T. Ooi, C. Song, F. Tin-Loi, A scaled boundary polygon formulation for elasto-plastic analyses, Computer Methods in Applied Mechanics and Engineering 268 (2014) 905–937.

[114] C. Song, A matrix function solution for the scaled boundary finite-element equation in statics, Computer Methods in Applied Mechanics and Engineering 193 (2004) 2325–2356.

[115] C. Song, J. P. Wolf, The scaled boundary finite-element method-alias consistent, Computer Methods in Applied Mechanics and Engineering 147 (1997) 329–355.

[116] C. Talischi, G. H. Paulino, A. Pereira, I. F. M. Menezes, PolyMesher: a general-purpose mesh generator for polygonal elements written in Matlab, Structural and Multidisciplinary Optimization 45 (2012) 309–328.

[117] D. Meagher, Geometric modeling using octree encoding, Computer Graphics and Image Processing 19 (2) (1982) 129 – 147.

[118] H. Sundar, R. Sampath, G. Biros, Bottom-up construction and 2:1 balance refinement of linear octrees in parallel, SIAM Journal on Scientific Computing 30 (2008) 2675–2708.

[119] S.-K. Kim, C.-H. Kim, Finding ridges and valleys in a discrete surface using a modified mls approximation, Computer-Aided Design 37 (2005) 1533 – 1542.

[120] Y. Ohtake, A. Belyaev, H.-P. Seidel, Ridge-valley lines on meshes via implicit surface fitting, ACM Transactions on Graphics 23 (2004) 609–612.

[121] Z. Petrovic, B. Milosevic, M. Mijalkovic, S. Brcic, Determination of the limit load of statically indeterminate truss girders, Facta universitatis - series: Architecture and Civil Engineering 9 (2) (2011) 217–229.

[122] J. R. Q. Franco, J. Oden, A. R. Ponter, F. B. Barros, A posteriori error estimator and adaptive procedures for computation of shakedown and limit loads on pressure vessels, Computer Methods in Applied Mechanics and Engineering 150 (1997) 155 – 171.

[123] L. Borges, R. Feijó, N. Zouain, A directional error estimator for adaptive limit analysis, Mechanics Research Communications 26 (1999) 555 – 563.

[124] L. Borges, N. Zouain, C. Costa, R. Feijó, An adaptive approach to limit analysis, International Journal of Solids and Structures 38 (2001) 1707–1720.

[125] J. R. Q. Franco, A. R. Ponter, F. B. Barros, Adaptive f.e. method for the shakedown and limit analysis ofÂ pressure vessels, European Journal of Mechanics - A/Solids 22 (2003) 525 – 533.

[126] F. Tin-Loi, N. Ngo, Performance of a p-adaptive finite element method for shakedown analysis, International Journal of Mechanical Sciences 49 (10) (2007) 1166–1178.

[127] A. K. Noor, I. Babuska, Quality assessment and control of finite element solutions, Finite Elements in Analysis and Design 3 (1987) 1 – 26.

[128] P. Díez, M. A. Balaguer, A. Huerta, Adaptivity based on error estimation for viscoplastic softening materials, Mechanics of Cohesive-Frictional Materials (2000) 87–112.

[129] N. Zouain, L. Borges, J. L. Silveira, An algorithm for shakedown analysis with nonlinear yield functions, Computer Methods in Applied Mechanics and Engineering 191 (23-24) (2002) 2463–2481.

[130] A. Makrodimopoulos, C. M. Martin, Lower bound limit analysis of cohesive-frictional materials using second-order cone programming, International Journal for Numerical Methods in Engineering 66 (2006) 604–634.

[131] J. Munoz, J. Bonet, A. Huerta, J. Peraire, Upper and lower bounds in limit analysis: adaptive meshing strategies and discontinuous loading, International Journal for Numerical Methods in Engineering 77 (2009) 471–501.

[132] C. Song, Automatic image-based stress analysis by the scaled boundary polytope elements, in: 23^{rd} Australasian Conference on the Mechanics of Structures and Materials (ACMSM23), Byron Bay, Australia, 2014.